

Star Formation History of Low Surface Brightness Galaxies in the HDF–S

Dissertation

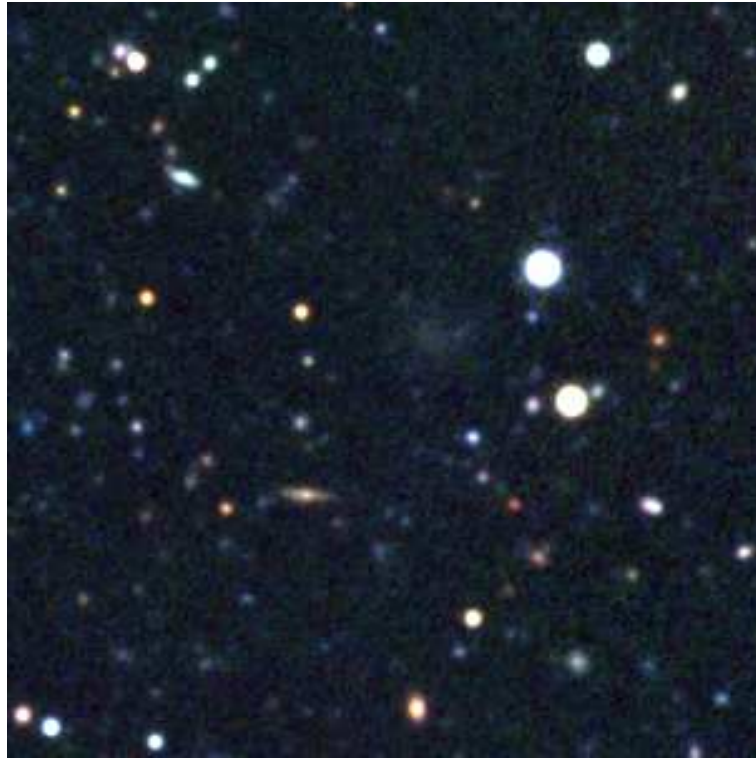
zur Erlangung des Grades
“Doktor der Naturwissenschaften”
der Fakultät für Physik und Astronomie
an der Ruhr-Universität Bochum



von
Dipl. Phys. Lutz Haberzettl

13. Mai 2005

1. Gutachter: Prof. Dr. Ralf-Jürgen Dettmar
2. Gutachter: Priv. Doz. Dr. Dominik J. Bomans



Three color composite image of the very faint Low Surface Brightness galaxy HBDP22320-60381 found in the HDF-S.

"Life must be lived forward, but could be understood backwards"

Soeren Kierkegaard

"If we remember we are all mad, the mystery disappears and life stands explained"

Mark Twain

Contents

1	Motivation	1
2	Introduction	3
2.1	Low Surface Brightness Galaxies	3
2.2	Properties of galaxies: LSB vs. HSB	8
2.3	Formation and Evolution Scenarios	11
2.4	Basic Physical Equations	12
3	LSB Galaxies in the HDF–S	17
3.1	Sample selection	17
3.2	Observations and Data Reduction	24
3.2.1	Observations	24
3.2.2	Reduction and calibration	26
3.3	Results and Discussion	27
3.3.1	Physical Parameters of the LSB Sample	27
3.3.2	The HDF–S LSB Galaxies in the Color–Color Space	30
3.3.3	Volume densities of the HDF–S LSB galaxies	33
3.4	Conclusions and Summary	37
4	SFH of LSB galaxies in the HDF–S	39
4.1	Data and sample selection	39
4.2	PÉGASE	40
4.2.1	Stellar Population Synthesis	40
4.2.2	Parameter Study	41
4.3	Results	57
4.3.1	SFH of LSB Galaxies	58
4.3.2	SFH of HSB Galaxies	66
4.4	Discussion	70
4.5	Conclusion	74

5 Summary	77
6 Outlook	79
A HDF–S Sample	85
B PÉGASE parameter study	97
C HSB galaxy sample	127

List of Figures

2.1	Freeman Law	4
2.2	Visibility	6
2.3	HSB and LSB galaxy examples	9
2.4	Large Scale Structure Formation	12
2.5	Hierarchical Clustering Model	13
3.1	BTC and B_W Filter	19
3.2	Color–color diagram	21
3.3	Color evolution	22
3.4	Detection limits	23
3.5	Color–color diagrams	34
3.6	Volume distribution	36
4.1	IMFs – Numerical Solutions	44
4.2	IMFs – Analytical Solutions	45
4.3	IMF–HBDP22325-60155	46
4.4	Mass limit – HBDP22325-60155	48
4.5	Star Formation Law	49
4.6	Constant Star Formation Rate	50
4.7	Exponential decreasing Star Formation Rate	51
4.8	Power Law SFR 1	52
4.9	Power Law SFR 2	53
4.10	Power Law SFR 3	54
4.11	Dust Model	55
4.12	SFH of HBDP22300-60300	58
4.13	SFH of HBDP22302-60352	59
4.14	SFH of HBDP22325-60155	61
4.15	SFH of HBDP22330-60543	62
4.16	SFH of HBDP22343-60222	63
4.17	SFH of HBDP22352-60420	64

4.18 SFH of HBDP22353-60311	65
4.19 HDF-S LSB galaxy images	67
4.20 SFH of NGC2903 and NGC3627	71
4.21 Distribution of Galaxy Ages	72
4.22 SFH of IC1613	73
4.23 Hubble Type – Age Relation	74
4.24 LSS	75
6.1 CDF-S surface brightness distribution	81
6.2 LSB candidates in the CDF-S	83
A.1 HBDP22300-60300	86
A.2 HBDP22302-60352	87
A.3 HBDP22311-60503	88
A.4 HBDP22325-60155	89
A.5 HBDP22330-60543	90
A.6 HBDP22343-60222	91
A.7 HBDP22352-60420	92
A.8 HBDP22353-60311	93
A.9 HBDP22354-60122	94
A.10 HBDP22355-60183	95
A.11 HBDP22324-60520	96
B.1 IMF + const. SFR	98
B.2 IMF + star burst	99
B.3 IMF + exponential SFR	100
B.4 IMF + power law	101
B.5 Mass + constant SFR	102
B.6 Mass limit + star burst	103
B.7 Mass limit + exponential SFR	104
B.8 Mass limit + power law	105
B.9 Star Formation Law	106
B.10 Constant Star Formation Rates	107
B.11 Exponential decreasing Star Formation Rates	108
B.12 SFR Power Law	109
B.13 Extinction + star burst	110
B.14 Extinction constant SFR	111
B.15 Extinction + exponential decreasing SFR	112
B.16 Extinction + power law SFR	113
B.17 SNII model + star burst	114
B.18 SNII model + constant SFR	115
B.19 SNII model + exponential decreasing SFR	116
B.20 SNII model + power law SFR	117

B.21	Fraction of binary systems + star burst	118
B.22	Fraction of binary systems const. SFR	119
B.23	Fraction of binary systems + exponential decreasing SFR	120
B.24	Fraction of binary systems + power law SFR	121
B.25	Mass fraction of substellar objects + star burst	122
B.26	Mass fraction of substellar objects + constant SFR	123
B.27	Mass fraction of substellar objects + exponential decreasing SFR	124
B.28	Mass fraction of substellar objects + power law SFR	125
C.1	Spectra: NGC1375, NGC1832, NGC2775, NGC2903	128
C.2	Spectra: NGC3034, NGC3077, NGC3147, NGC3245	129
C.3	Spectra: NGC3368, NGC3379, NGC3471, NGC3516	130
C.4	Spectra: NGC3623, NGC3627, NGC3941, NGC4449	131
C.5	Spectra: NGC4631, NGC4648, NGC4775, NGC5248	132
C.6	Spectra: NGC5548, NGC5866, NGC5996, NGC6181	133
C.7	Spectra: NGC6217, NGC6643, NGC6764	134

List of Tables

3.1	GSFC exposures times	20
3.2	Color indices of the GSFC subsample	25
3.3	Spectroscopic Observation	26
3.4	Redshift determination	29
3.5	Physical Parameter	31
3.6	LSB candidates	32
4.1	PÉGASE Parameter	56
4.2	SFH of LSB galaxies	66
4.3	SFH of HSB galaxies	69

Chapter 1

Motivation

Galaxies represent gravitational bound islands in the Universe. Built out of Dark Matter, stars, gas, and dust they belong to the oldest systems known today. The evolution of these systems also reflects the evolution of the whole Universe. All models describing the formation and evolution of galaxies are based on the study of bright galaxies. In order to understand the evolution of the Universe as a whole all populations of galaxies must be included in these studies.

In order to do so this thesis is aimed at the study of the evolution of Low Surface Brightness (LSB) galaxies. Using multi color data a new selection method will be presented. This method is based on differences in the stellar population mix between High Surface Brightness (HSB) and LSB galaxies. The different stellar population mix results in different locations of the LSB galaxies in the color-color diagrams. Spectroscopic follow up data for the derived LSB sample in the HDF-S (Hubble Deep Field- South) will be used in order to derive the Star Formation History (SFH). Therefore the flux calibrated spectra will be compared to a library of several thousands synthetic Spectral Energy Distributions (SEDs) composed with the synthesis evolution model PÉGASE. From the estimated SFHs predictions will be made about the evolution paths taken by the LSB galaxies. The same analysis will be done for a sample of HSB galaxies. By comparing the SFHs of the LSB and HSB galaxies assumptions will be made about the differences between both galaxy populations resulting in such low surface brightnesses as seen for the LSB galaxies. Finally, the evolutionary scenarios for the LSB galaxies will be brought in coherence with existing formation and evolution models (e.g. "Cold Dark Matter" –model).

Introduction

2.1 Low Surface Brightness Galaxies

The existence of a population of galaxies showing low central surface brightnesses became more and more accepted in the last 20 years. In this context the central surface brightness is the surface brightness extrapolated to a radius of $r=0$ arcsec (see Eqn. 2.6 and 2.7). In the last couple of years extended searches for so-called Low Surface Brightness (LSB) galaxies have shown that the LSBs represent an important part of the galaxy population. They may account for up to 50% of the local galaxy population (McGaugh, 1996; O'Neil & Bothun, 2000). It is known today that the Freeman Law (Freeman, 1970, see Fig 2.1) – which indicates that all galaxies have nearly the same central surface brightness of about $\mu_{0,B} \sim 21.65 \pm 0.3$ mag arcsec⁻² – was the result of observational selection effects. Due to these selection effects, until a few years ago the LSB galaxies were missed in most galaxy catalogs. Nevertheless the selection effects – defining the composition of the galaxy catalogs – could be quantified having in mind that galaxies are diffuse objects and that they are only detectable down to a certain percentage of the night sky surface brightness.

The composition of galaxy catalogs are defined by three parameters. These parameters are the limiting surface brightness μ_l , the limiting magnitude m_l , and the limiting angular diameter θ_l . The latter is the diameter at which the surface brightness of the selected galaxies is still consistent with the limiting surface brightness μ_l of the survey. Selection effects now result in a different composition of catalogs using different selection criteria. The existence of selection effects was first stated by Zwicky (1957). A first formal description was published by Disney (1976) and Disney & Phillipps (1983). They showed that the apparent radius $R_{app}(\mu_0)$ and apparent luminosity $L_{app}(\mu_0)$ are sensitive functions of the central surface brightness μ_0 , e.g. for disk galaxies:

$$\frac{R_{app}}{R_L} = \left[0.4 \frac{\ln(10)}{\sqrt{2}} \right] [\mu_L - \mu_0] 10^{-0.2[\mu_L - \mu_0]} \quad (2.1)$$

$$\frac{L_{app}}{L_T} = 1 - (1 + 0.4 \ln(10) (\mu_L - \mu_0)) 10^{-0.4(\mu_L - \mu_0)} \quad (2.2)$$

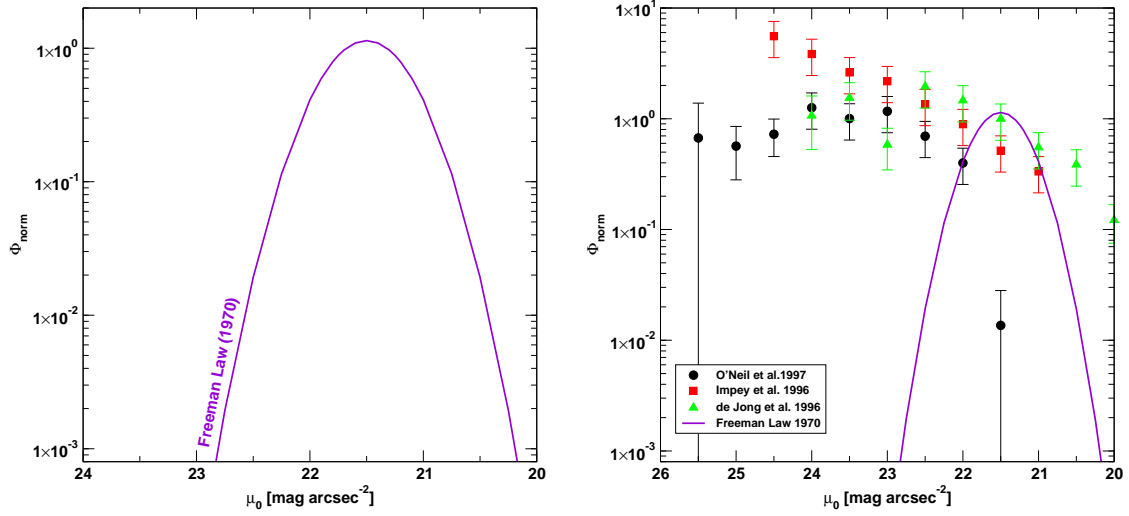


Figure 2.1: The Freeman Law (left panel) indicates that all disk galaxies have nearly the same central surface brightness. The central surface brightness should follow a Gaussian distribution. More sensitive galaxy surveys showed that the true distribution (right panel) is not represented by a Gaussian function. The distribution stays flat down to very low central surface brightnesses more than 3σ below the maximum of the Freeman distribution ($\mu_{0,\text{max}} = 21.65 \pm 0.3 \text{ mag arcsec}^{-2}$).

The two equations (Eqn. 2.1 and 2.2) are normalized with respect to the limiting radius R_L and the total luminosity L_T . Using Eqn. 2.1 and 2.2 one can estimate the maximum distances d_1 , d_2 at which a galaxy can be and still is in agreement with the limiting parameter of the catalog. Considering the apparent luminosity $l = L/4\pi d^2$ ($d = \text{proper distance}$) and the apparent angular size $\theta = R/d$, the maximum distance is represented by the following equations (M represents the absolute magnitude):

$$d_1(\text{pc}) = \left(\frac{L_{\text{app}}}{L_T} \right)^{\frac{1}{2}} 10^{0.2(m_l - M + 5)} \quad (2.3)$$

$$d_2(\text{pc}) = \left(\frac{R_{\text{app}}}{R_L} \right) 10^{0.2(\mu_l - M + 5)/\pi^{1/2}\theta_l} \quad (2.4)$$

The visibility which is proportional to the volume over which a galaxy can be detected, is defined as follows (where d_M is the smaller of the two distances d_1 and d_2):

$$V_{\text{vis}} = \min [d_1(L_{\text{app}}), d_2(R_{\text{app}})]^3 = d_M^3 \quad (2.5)$$

This visibility shows a strong dependency of the central surface brightness μ_0 and reflects how selection effects could bias a sample of galaxies.

Another description of selection effects was published by McGaugh et al. (1995). The authors concentrated their studies mainly on disk dominated systems for which the surface brightness profiles could be described by an exponential law:

$$I(r) = I_0 e^{-\frac{r}{\alpha}} \quad (2.6)$$

$$\mu(r) = -2.5 \log[I(r)] = \mu_0 + 1.086 \frac{r}{\alpha} \quad (2.7)$$

where μ_0 represents the central surface brightness of the disk and α the angular scale length of the galaxy in arcsec. The scale length is the radius at which the surface brightness drops to e^{-1} . The angular scale length corresponds to the physical scale length h in units of pc at proper distance d . The majority of the population of LSB galaxies is represented by exponential surface brightness profiles. For a diameter limited sample we only have to specify two parameters, the limiting angular diameter θ_1 and the limiting surface brightness μ_1 at which θ_1 is measured. If now a galaxy is selected as member of a diameter limited catalog than its angular diameter has to match the selection criterium $\theta = 2r \geq \theta_1$. The maximum distances of galaxies detected in surveys applying certain surface brightness limits could be estimated using Eqn. 2.7:

$$\theta = 1.84 \alpha (\mu_1 - \mu_0) \propto \frac{h}{d} (\mu_1 - \mu_0) \quad (2.8)$$

$$d_{\max} \propto \frac{h}{\theta_1} (\mu_1 - \mu_0) \quad (2.9)$$

$$V(h, \mu_0) \propto d_{\max}^3 \propto h^3 (\mu_1 - \mu_0)^3 \quad (2.10)$$

For a flux limited sample the two specifying parameters are the limiting magnitude m_1 and the limiting surface brightness μ_1 above which the flux is measured. The visibility is again proportional to the volume sampled by the survey and could be described by:

$$V \propto [L_{\text{app}}(r < \theta/2)]^{\frac{3}{2}} \propto [I_0 h^2 (1 - (1 + 0.92 (\mu(r) - \mu_0)) e^{-0.92 (\mu(r) - \mu_0)})]^{\frac{3}{2}} \quad (2.11)$$

Using surface brightness μ in logarithmic units instead of surface brightness I in linear units and applying an arbitrary normalization μ_0^* the visibility can be expressed as:

$$V \propto h^3 10^{-0.6(\mu_0 - \mu_0^*)} (1 - (1 + 0.92 (\mu(r) - \mu_0)) e^{-0.92 (\mu(r) - \mu_0)})^{\frac{3}{2}} \quad (2.12)$$

The normalization is chosen to be the bright end cutoff comparable to L^* used as normalization for luminosity functions. The luminosity function describes the probability to find a certain galaxy with a certain luminosity within a certain survey. One parameterization of the luminosity function is the so called Schechter function (Schechter, 1976):

$$\phi(L)dL \sim L^\alpha e^{-L/L^*} dL \quad (2.13)$$

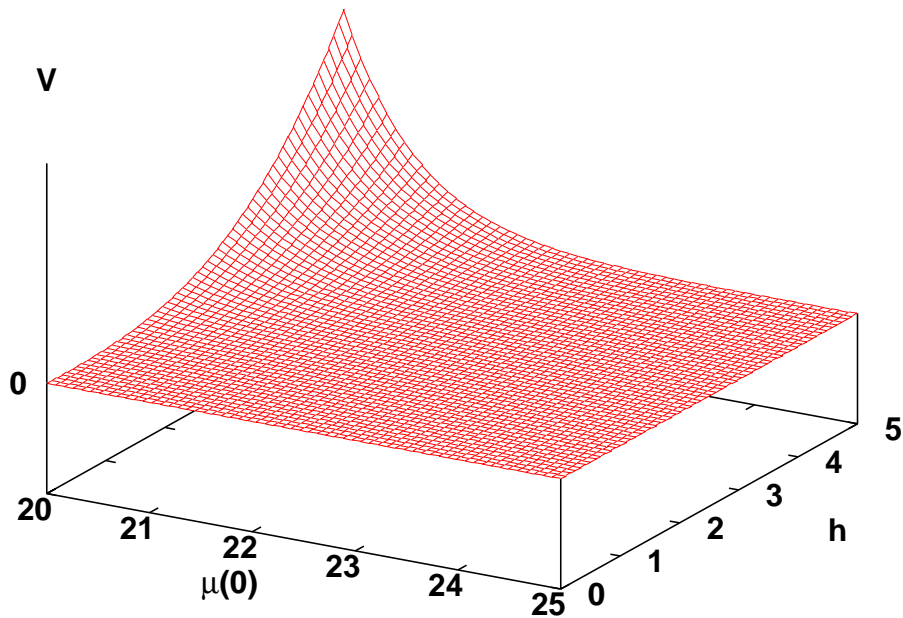
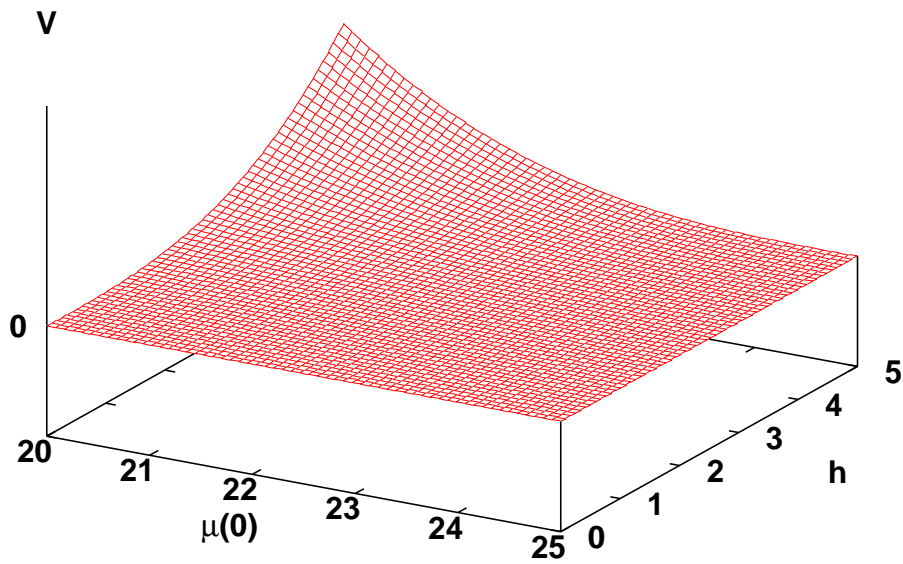


Figure 2.2: Three dimensional plot of the visibility function for diameter limited (upper panel) and magnitude limited (lower panel) surveys. As one can see the visibility is a strongly peaked function. For objects having large specific sizes h and high surface brightnesses μ , the visibility is high. Hence it follows that the volume sampled by a survey increases with increasing size and surface brightness.

The exponent α describes the rise at the faint end and L^* is the normalization of the function. Today a typical value for the rise of the galaxy luminosity function at the faint end is $\alpha = -1.21$ and results from a study of galaxies in the Sloan Digital Sky Survey (SDSS) by Norberg et al. (2002). For both diameter (Fig. 2.2, upper panel) and magnitude (Fig. 2.2, lower panel) limited surveys the visibility is a strongly peaked function. The visibility function shows a steeper increase for magnitude limited than for diameter limited samples. Magnitude limited surveys could identify more galaxies since they cover much larger volumes. Therefore the contamination with higher redshifted background galaxies is larger. In both, diameter and magnitude limited samples, the volume over which LSB galaxies could be detected is very small compared to the search volume for High Surface Brightness (HSB) galaxies. This smaller search volumes could explain the Gaussian surface brightness distribution of Freeman (1970) which did not take this effect into account.

Keeping in mind the existence of selection effects, in the following years more sensitive surveys showed that galaxies with much lower central surface brightnesses exist in large numbers. One of the first catalogs containing a significant amount of diffuse and faint galaxies was based on photographic plates. Most of the galaxies in the David Dominion Observatory (DDO) catalog (van den Bergh, 1959) were low mass galaxies and therefore not representative for the LSB galaxies as a whole. The following studies revealed a large number of these galaxies. Longmore et al. (1982) derived for example a sample of 151 LSB galaxies using optical and 21-cm data. The optical study of the HI selected LSB sample was done using data based on photographic plates observed with the UK Schmidt telescope. Also searches in the Uppsala General Catalog of Galaxies (Nilson, 1973) provided a large number of LSBs. In contrast to other catalogs the UGC catalog has only a pure diameter limit as selection criteria. There exist no formal limit in surface brightness – other than the one resulting from the used plate material – and therefore the UGC catalog contains more LSB galaxies than other catalogs so far. Romanishin et al. (1982) showed in a detailed study of LSB galaxies selected from the UGC catalog that these galaxies contain a relatively large amount of gas compared to their given luminosity.

LSB galaxies were not only found in the field they also exist in clusters. Large and sensitive surveys of the Virgo (Binggeli et al., 1985) and the Fornax cluster (Ferguson & Sandage, 1988; Ferguson, 1989) revealed a large number of LSB galaxies which are mostly dwarf galaxies. The development of amplification methods for photographic plates resulted in a progress for identifying LSB galaxies with lower central surface brightnesses. In the following years these amplification methods resulted in lower surface brightness limits down to limits around $\mu_{\text{lim}} \approx 27.5 \text{ B mag arcsec}^{-2}$ (Impey et al., 1988). As one result of this lower surface brightness limits Bothun et al. (1987) discovered a giant, HI rich LSB disk galaxy (Malin I). Malin I has a central surface brightness of about $\mu_{0,V} = 25.5 \text{ mag arcsec}^{-2}$, an optical diameter of $D \sim 150 \text{ kpc}$ and a HI mass of $M_{\text{HI}} \sim 10^{11} M_{\odot}$. This LSB galaxy is still one of the largest and HI richest objects known today. The existence of Malin-like LSB galaxies shows that low surface brightness is not only a property of gas poor dwarf galaxies (dE, dSph – galaxies). A large fraction of the LSB galaxies consists of large and gas rich disk galaxies.

The next step in sensitivity was gained by the procurement of the CCD detector. Due to high quantum efficiency, low noise and linear response of this digital detector it was possible to reach down to much lower surface brightness limits using shorter exposures times. One

of the first examples for this gain was the Texas survey (O'Neil et al., 1997a,b). This CCD based survey covered a field of $\sim 27 \text{ deg}^2$ and reached a limiting surface brightness of about $\mu_{\text{lim}} \approx 27.5 \text{ R mag arcsec}^{-2}$ in the R-band. The multi-color Texas survey was observed in U-, B-, V-, R-, I-filter and resulted in a sample of 119 newly discovered LSB galaxies. The derived sample consist of galaxies having central surface brightnesses fainter $\mu_{\text{B}}(0) \geq 22.0 \text{ mag arcsec}^{-2}$ and diameters $D \geq 13.5 \text{ arcsec}$. Another extensive search for LSB galaxies using CCD based data was performed by Dalcanton et al. (1997). The survey covered a field of 17.5 deg^2 and derived a number surface density for LSB galaxies of $4.1_{-2.1}^{+2.6} \text{ deg}^{-2}$. The derived LSB galaxies have central surface brightnesses between $23 \text{ mag arcsec}^{-2}$ and $25 \text{ mag arcsec}^{-2}$ in the V-band. The estimated number density was 4 times higher compared to surveys based on photographic data. The number density of LSB galaxies estimated by Dalcanton et al. (1997) is also similar to the volume density derived for "normal" HSB galaxies of comparable size.

Until a few years ago one disadvantage of the new generation of detectors was the small fields of only a few arcmin covered by the CCDs. Therefore searches for LSBs were done using relatively small survey fields or bad spatial resolution. This results in small and local object samples. Since a couple of years large sized mosaic imaging facilities are available (e.g. WFI@MPG/ESO 2.2m telescope, MOSAICII@Blanco 4m CTIO telescope). With these new multi CCD cameras it is now possible to cover much larger fields of up to 0.5 deg down to very low surface brightness limits and seeing limited resolution. In the following years large surveys based on CCD data like SDSS will make it possible to extract large samples of galaxies. With the next generation of Wide Field Imager (e.g. OmegaCam@VST) it will also be possible to reach very low surface brightness limits $\mu_{\text{lim}} \geq 27 \text{ mag arcsec}^{-2}$ just needing relatively short exposures times.

2.2 Properties of galaxies: LSB vs. HSB

Comparing images of HSB and LSB galaxies (see Fig. 2.3) a first and obvious property of LSBs can easily be seen. HSB galaxies often show bright and prominent features like strong bulges or bars. Features like spiral arms are clearly visible. In contrast to HSBs the LSB galaxies are mainly structureless and diffuse, only a small subset shows bulges (Beijersbergen et al., 1999). The spiral arms, if visible, mostly have low contrast. A more formal definition of LSB galaxies make use of the central surface brightness μ_0 . For this work a galaxy with a central surface brightness below $\mu_0 \geq 22.5 \text{ mag arcsec}^{-2}$ in the B-band will be classified as a LSB galaxy. The majority of the LSB galaxies can be classified morphologically as disk galaxies. They mostly do not show bright spheroidal features like bulges. Therefore in most cases a bulge to disk decomposition – where the bulge region shows an $r^{1/4}$ dependency – is not necessary. The surface brightness profiles of most LSB galaxies are measured to follow an exponential law (see Eqn. 2.7). This central surface brightness is more than 3σ fainter than the Freeman value of $\mu_0 = 21.65 \pm 0.3 \text{ mag arcsec}^{-2}$. Anyway the distribution in central surface brightnesses is not a discrete function. The distribution is continuously and there exists no sharp boundary between the HSB and the LSB regime.

Low Surface Brightness galaxies are not faded remnants of HSB galaxies. Otherwise one

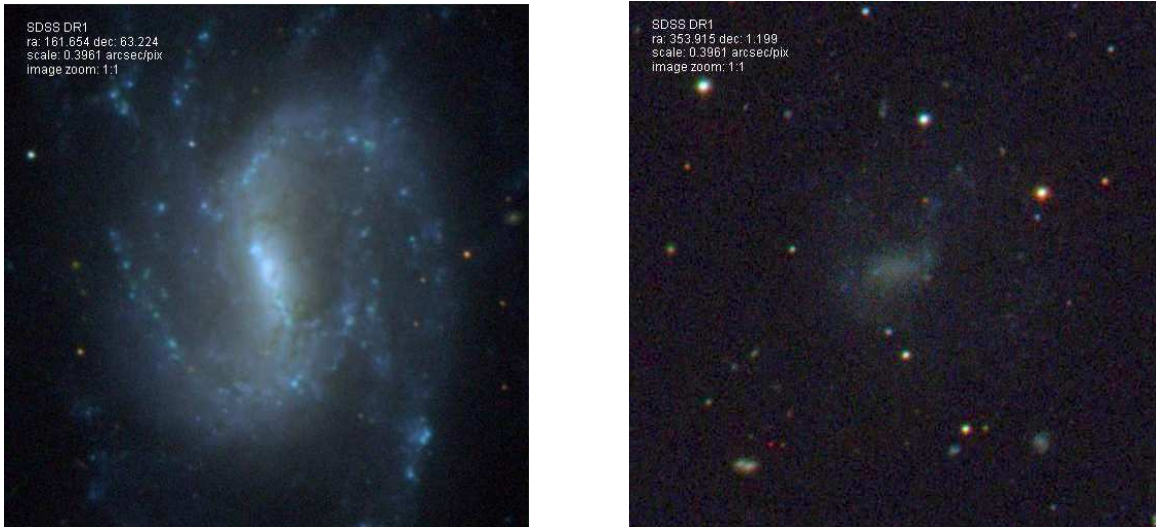


Figure 2.3: Example for a HSB galaxy (left, NGC 3359) and a LSB galaxy (right, UGC 12690). The images of both galaxies are taken from the Sloan Digital Sky Survey (SDSS). NGC 3359 shows bright and prominent features like a bar and spiral arms. In contrast to this the LSB galaxy UGC 12690 is only visible as diffuse structure. No bright features could be seen. The spiral arms are very faint.

would expect to find LSB galaxies showing mostly red colors. Although the LSBs are distributed over the whole color space covered by the HSB galaxies most of them show moderate or blue colors. In a study of a sample of 20 field LSB galaxies de Blok et al. (1995) showed that there exist no correlation of galaxy colors with decreasing central surface brightnesses. They also stated that their LSB sample tend to have bluer colors compared to the mean values estimated for HSB galaxies of the corresponding Hubble type. This effect is mainly seen in the $B - R$ color (HSB: $\overline{B - R} = 0.92$, LSB: $\overline{B - R} = 0.78$) and the $V - I$ color (HSB: $\overline{V - I} = 0.90$, LSB: $\overline{V - I} = 0.76$).

A study of a sample of LSB galaxies derived using modern photographic plates of the Second Palomar Sky Survey (PSS-II) demonstrated that there exists no dependency of LSB galaxies on the Hubble type (Schombert et al., 1992). The distribution on Hubble types for LSB galaxies is comparable to surveys governed by HSB galaxies, e.g. UGC catalog (Nilson, 1973). The LSB sample is well distributed over the whole Hubble sequence from elliptical (E/S0) to late type spirals (Sc/Sd) and irregulars (Irr). However the number of ellipticals is low ($\sim 14\%$). The sample is more dominated by late type disk galaxies.

Metallicities of the Interstellar Medium (ISM) of LSB galaxies are estimated to be lower compared to the ISM of HSB galaxies. De Blok & van der Hulst (1998a) found for the metallicity of 64 HII regions from 12 LSB galaxies values between $0.5 \cdot Z_{\odot}$ to $0.1 \cdot Z_{\odot}$. No HII region of the LSB sample was found to have solar metallicity. Other studies of blue LSB and LSB dwarf galaxies (e.g. Roennback & Bergvall, 1995; van Zee et al., 1997) derived low metallicities down to $0.05 \cdot Z_{\odot}$ comparable to metal poor HSB dwarf galaxies. The enrichment of α -elements (Ne,

S, Ar), which are products of the standard stellar nucleosynthesis, is found to be comparable to values of Blue Compact Dwarf (BCD) galaxies (van Zee et al., 1997). The N over O abundances for LSB galaxies is constant with decreasing O abundance (e.g. Roennback & Bergvall, 1995; van Zee et al., 1997). This result indicates that the major part of nitrogen in LSB galaxies is primary N produced by intermediated mass stars ($4 M_{\odot}$ to $8 M_{\odot}$). If the secondary nitrogen – produced in massive stars by incorporating O and C – is the major contribution of nitrogen the N over O abundances would increase with rising O abundance. This was also shown from a study of HII regions in the Pegasus dwarf galaxy by Skillman et al. (1997). The authors compared the results for the N/O and O/H abundances of the HII regions to the star formation history of the Pegasus dwarf galaxy derived by Aparicio & Gallart (1995).

Another important property of LSB galaxies is the deficiency of the CO molecule. A first search for CO in a sample of 19 LSB galaxies (Schombert et al., 1990) resulted in no detection reaching typical rms noise of 4–6 mK. The authors estimated an upper limit for a H_2 mass which was 0.1 times the HI mass. This is significantly lower compared to H_2 masses of HSB galaxies. The search of de Blok & van der Hulst (1998b) for the CO(2–1) emission line in a sample of 3 LSB galaxies only conducted in upper limits on levels of 6 mK rms. First detections of the CO(1–0) and CO(2–1) emission were obtained by O’Neil et al. (2000). The authors performed very sensitive observations of a sample of four LSB galaxies using the IRAM 30 m telescope. In one of the four LSB galaxies CO(1–0) as well as CO(2–1) emission could be detected on levels of 3.2 ± 0.6 mK (CO(1–0)) and 5.3 ± 1.1 mK (CO(2–1)). In the case of the other three LSBs only upper limits on levels of 0.5 mK to 1.3 mK could be estimated. Until now only few additional detections of CO in LSB galaxies are known (Matthews & Gao, 2001; O’Neil et al., 2003). This lack of CO could either mean no universal conversion between CO and H_2 mass exists, or the amount of molecular hydrogen is much lower for the LSB galaxies. In the first case one has to find a different conversion method for the LSB galaxies. From the standard conversion method ratios $M_{H_2}/M_{HI} = 0.1 - 0.01$ could be estimated. This is several times lower than found for HSB late type spirals. Until now there is not much known about the dust component in LSB galaxies. However the low CO content is also a hint for a low amount of dust in these galaxies. A general trend was derived for galaxies to show higher Far Infrared (FIR) to optical flux ratios with increasing surface brightness (Davies et al., 1989) using IRAS FIR data. Higher FIR fluxes also mean higher dust masses.

In contrast to the low CO and dust content LSB galaxies have in general a high quantity of unprocessed neutral hydrogen HI. Some of the giant LSB galaxies (e.g. Malin I) belong to the HI richest galaxies known today (Impey & Bothun, 1989). Although the HI content of LSB galaxies is comparable to HSB galaxies they are found to have a lower HI surface density Σ_{HI} (Pickering et al., 1997). The surface density in most cases is estimated to be below the critical surface density Σ_{crit} derived by Kennicutt (1989). The critical surface density Σ_{crit} is the limit below which a thin gas disk is gravitational stable against the growth of large-scale density perturbations. However if the gas density exceeds the critical density then density perturbations result in formation of giant molecular clouds (GMC) in which star formation could occur. Due to the low gas surface densities star formation in LSBs in general is suppressed. One possible scenario for star formation in LSB galaxies could be the formation of stars outside of GMCs in small molecular clouds. However the low gas surface densities also indicate a suppressed

formation of massive stars and possible differences in the initial mass function (IMF) compared to the IMF of HSB galaxies.

As well as the rotation curves of HSB galaxies also the rotation curves of LSB galaxies show a significant dark matter (DM) component (e.g. Pickering et al., 1997; Swaters et al., 2000; McGaugh et al., 2001). In contrast to HSB galaxies the rotation curve of LSB galaxies are dark matter dominated over the whole disk. Also in the inner part of the rotation curve—where the maximum disk model could explain the rotation curve for HSB galaxies with scaling the stellar component—a significant amount of dark matter is needed to explain the rotation curve of LSB galaxies (e.g. de Blok et al., 2001). The predicted dark matter halos of LSB galaxies are more extended compared to halos of HSB galaxies. Nevertheless the DM-halos of LSBs are less dense compared to their HSB counterparts. Therefore LSB galaxies conserve a large amount of angular momentum (e.g. Pickering et al., 1997).

Taking together the high amount of unprocessed HI in combination with the low gas surface densities, low metallicities as well as the low dust content indicates that the population of LSBs are relatively unevolved galaxies. Many of the properties are comparable to low metal dwarf galaxies, but these are often not LSB galaxies.

2.3 Formation and Evolution Scenarios

Today there exist two major models describing the formation and evolution of galaxies. The “Monolithic Collapse”-Model explains the formation of galaxies at high redshifts ($z > 2-3$) out of the collapse of a massive gas cloud followed by an extensive star formation event (Eggen et al., 1962; Tinsley, 1972b). After the formation out of the collapsing gas cloud the galaxies just show a pure luminosity evolution (PLE) until today. Some observational results support this formation scenario. From submm and mm surveys a population of high redshifted star burst galaxies is known, having large amount of dust (Blain et al., 2002). These dusty mm-submm galaxies could represent the progenitors of the massive elliptical galaxies known today. Consistent results came from the study of cluster elliptical galaxies. They seem to build a population of old systems formed at high redshifts (Cimatti, 2003, and references therein). Also in the field there exist old massive galaxies out to a redshift of $z \sim 1.5$. There is still a debate going on if these galaxies are the result of a pure luminosity evolution and formed due to the collapse scenarios at high redshifts (Cimatti, 2003, and references therein).

The most accepted model describing the formation of structure in the Universe is the so called “Hierarchical Clustering”-model (White & Rees, 1978; Kauffmann et al., 1993, 1996; Steinmetz, 2003). Following this model, structure in the Universe growth due to the merging of subunits to objects of higher mass (see Fig. 2.4). Today the most successful class of models in explaining structure formation due to Hierarchical Clustering is the so called “ Λ Cold Dark Matter”-Model (Λ CDM-Model). The Λ CDM-model provide the basics in order to describe galaxy formation and evolution using cosmological parameters (Ω_0 , Λ_0 , H_0 , Ω_b) know from other measurements, e.g. BOOMERANG, WMAP. The predictions of the Λ CDM-model are consistent with results from other fundamental observations.

- age of the Universe as measured from the oldest stars in the halo of the Milky Way

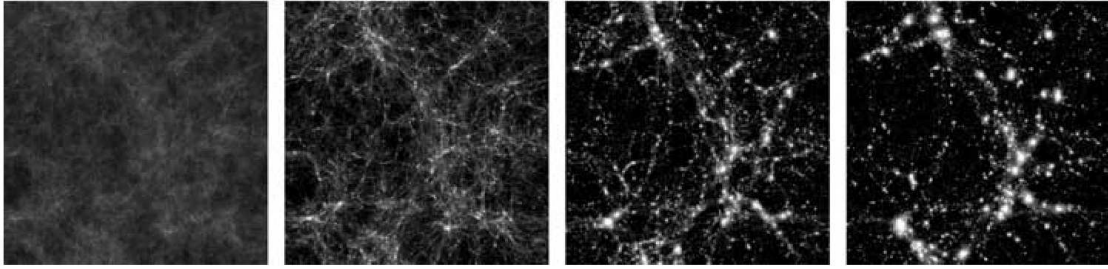


Figure 2.4: The four images show a time sequence of the structure formation due to “Hierarchical Clustering” adopted from Steinmetz (2003). The four images are snapshots at redshifts $z=9, 3.5, 1.0$. The simulation box has a comoving length of 50 Mpc.

- extragalactic distance scale measured by distant Cepheids
- primordial abundance of the light elements
- baryonic mass fraction of galaxy clusters
- amplitude of the CMB fluctuations measured by COBE, BOOMERANG, WMAP
- present day number density of massive galaxy clusters
- shape and amplitude of galaxy clustering pattern
- geometry of the Universe as obtained by observations of distant type Ia SNe

The hierarchical clustering model also gives an explanation for the morphological shape of individual galaxies (see Fig. 2.5). In the hierarchical scenario massive galaxies are formed due to merging processes of lower mass progenitor galaxies. Two disk galaxies of similar mass merge and the resulting object is converted into a higher mass elliptical galaxy. In the following gas is accreted and settles in a disk like structure. These new disk galaxies undergo again a merger event and form the massive elliptical galaxies known today. In the hierarchical clustering picture the Hubble–Sequence is the result of ongoing destruction of disks by merger events and therefore the formation of spheroids as well as the new formation of disks due to gas accretion.

2.4 Basic Physical Equations

The major aim of this section is to summarize the known cosmological basics which will be used in order to derive physical parameters of the observed galaxies. One basic assumption for constructing cosmological models is a isotropic, and at present epoch uniformly expanding Universe. Another important assumption is the so called “cosmological principle”. that

We are not located at any special location in the Universe.

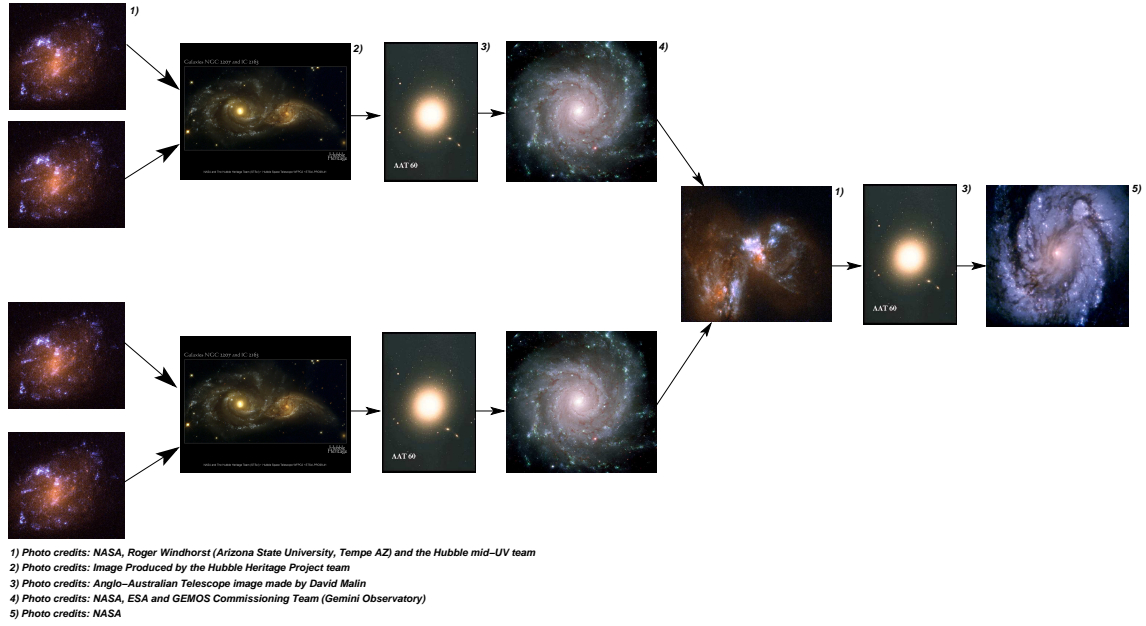


Figure 2.5: Schematical illustration of the “Hierarchical Clustering” scenarios adopted from Steinmetz (2003). In this model galaxies are formed due to merger events of lower mass objects. The merger also change the morphological shape of the galaxies.

This principle describes that any observer at any place in the Universe observes the same large scale structure (Longair, 1998). The first equation which is stated here is one of the fundamental equations. It is a description of a uniform and isotropic curved four dimensional space, and is called the *Robertson–Walker metric*:

$$ds^2 = dt^2 - \frac{R^2(t)}{c^2} \left[dr^2 + \mathfrak{R}^2 \sin^2 \left(\frac{r}{\mathfrak{R}} \right) (d\theta^2 + \sin^2 \theta d\phi^2) \right] \quad (2.14)$$

The metric defines the invariant interval ds^2 between events at any epoch or location in the expanding Universe. The time t used in the metric is the so called *cosmic time* and is a time measured with a clock of a *fundamental observer* which is an observer on a world line. The distance measure r is the *comoving radial distance coordinate* fixed for all times. It is the proper distance of a galaxy if the world line of this galaxy would be projected to the present time t_0 . The component $r_1 = \mathfrak{R} \sin(r/\mathfrak{R})$ is defined as the *comoving angular diameter distance*, with \mathfrak{R} describing the curvature of the space at present time t_0 . The redshift could also be seen as a result of the *Robertson–Walker metric*:

$$1 + z = \frac{1}{R(t_1)} \quad (2.15)$$

This equation represents the real meaning of redshift as *the measure of the scale factor (curvature of space) of the Universe at the time were the light was emitted*.

One simplification of Einstein's field equation describing the Universe as a four-dimensional space-time, is the so called "Friedmann equation". This equation sets the time evolution of the space curvature $R(t)$ in relation to matter and radiation:

$$\dot{R}^2 = \frac{8\pi G\rho}{3} R - \frac{c^2}{R^2} + \left[\frac{1}{3}\Lambda R\right] \quad (2.16)$$

$$\ddot{R} = -\frac{4\pi G}{3} R \left(\rho + \frac{3p}{c^2}\right) + \left[\frac{1}{3}\Lambda R\right] \quad (2.17)$$

In this equations the scale factor R describes the curvature of the space at any time t . The total initial mass density of the matter and radiation content of the Universe is represented by ρ . Whereas p describes the total pressure. Finally the constant Λ , the so called *cosmological constant* was originally introduced by Einstein in order to allow a static Universe. Today we know that we live in an always expanding and therefore dynamic Universe. A measure of this expansion is the so called *Hubble constant* H_0 :

$$H_0 = \frac{\dot{R}_0}{R_0} \quad (2.18)$$

New measurements of the Hubble constant from the WMAP experiment (Spergel et al., 2003) resulted in a very accurate value for the Hubble constant of $H_0 = (71_{-0.03}^{+0.04}) \text{ kms}^{-1}\text{Mpc}^{-1}$ which will be used throughout the following analysis. Using the Hubble constant H_0 the velocity-distance relation could be derived:

$$r \frac{dR(t)}{dt} = r R_0 H_0 \quad \Longleftrightarrow \quad v = r H_0 \quad (2.19)$$

With the knowledge of the Hubble constant H_0 and an estimation of the radial velocity of a galaxy it is possible to derive the distance in physical units. This relation is called the *Hubble Law*. Defining now the critical density:

$$\rho_c = \frac{3H_0^2}{8\pi G} \quad (2.20)$$

the density ρ_0 of the present epoch in terms of:

$$\Omega_0 = \frac{\rho_0}{\rho_c} = \frac{8\pi G\rho_0}{3H_0^2} \quad (2.21)$$

as well as the vacuum energy density Ω_Λ :

$$\Omega_\Lambda = \frac{\Lambda}{3H_0^2} \quad (2.22)$$

measured by WMAP as well, one can rewrite the first "Friedman equation" for the case of a Universe dominated by ordinary matter ($p=0$) as:

$$H^2(t) = H_0^2 \left(R^{-3}(t)\Omega_0 - R^{-2}(t)\frac{c^2}{R^2 H_0^2} + \Omega_\Lambda \right) \quad (2.23)$$

If one uses now the curvature of the space \mathfrak{R} at present time t_0 Eqn. 2.23 becomes:

$$K = \frac{1}{\mathfrak{R}^2} = \left(\frac{H_0}{c} \right)^2 (\Omega_0 + \Omega_\Lambda - 1) \quad (2.24)$$

Within this equation the sum of Ω_0 and Ω_Λ fixes the sign of the curvature of the Universe. Due to the fact that the Universe today is matter dominated the space curvature is defined by the fraction of matter density ρ and ρ_c as well as of the value of Λ :

$$\begin{aligned} \Omega &= \Omega_0 + \Omega_\Lambda > 1 &\implies & \text{closed Universe} \\ \Omega &= \Omega_0 + \Omega_\Lambda = 1 &\implies & \text{flat Universe} \\ \Omega &= \Omega_0 + \Omega_\Lambda < 1 &\implies & \text{open Universe} \end{aligned} \quad (2.25)$$

The next simplification one can make is the assumption of a “flat Universe” $\Omega_0 = 1$ with $\Lambda = 0$. This is the so called “Einstein–de Sitter” model. The “Einstein–de Sitter” case separates the open from the closed Universe and the collapsing from the Universe which is expanding for ever. The assumption $\Lambda = 0$ simplifies Eqn. 2.16 and 2.17 to:

$$\ddot{R} = -\frac{\Omega_0 H_0^2}{2R^2} \quad (2.26)$$

$$\dot{R}^2 = \frac{\Omega_0 H_0^2}{R} - \frac{c^2}{\mathfrak{R}^2} \quad (2.27)$$

Now insert Eqn. 2.24 and 2.15 into Eqn 2.27 results in:

$$\dot{R}^2 = H_0^2 (\Omega_0 z + 1) \quad (2.28)$$

Substituting dR with dz :

$$\frac{dz}{dt} = H_0^2 (1 + z)^2 (\Omega_0 z + 1)^{1/2} \quad (2.29)$$

and using the definition for the comoving coordinate distance r :

$$dr = \frac{c dt}{R(t)} = -c dt (1 + z) \quad (2.30)$$

it follows:

$$dr = \frac{c dz}{H_0 (1 + z) (\Omega_0 z + 1)^{1/2}} \quad (2.31)$$

Integrating now from redshift 0 to z , one can find a solution for the *distance measure* $D = \mathfrak{R} \sin(r/\mathfrak{R})$ also called the *proper distance*:

$$D = \frac{2c}{H_0 \Omega_0^2 (1 + z)} \left[\Omega_0 z + (\Omega_0 - 2) \left((\Omega_0 z + 1)^{1/2} - 1 \right) \right] \quad (2.32)$$

For the “Einstein–de Sitter” model this equation could be expressed as:

$$D = \frac{2c}{H_0(1+z)} \left[(z+1) - (z+1)^{1/2} \right] \quad (2.33)$$

the *proper length* of an object at redshift z follows than from the “Robertson–Walker Metric”:

$$d = R(t) \Re \sin\left(\frac{r}{\Re}\right) \Delta\theta = R(t) D \Delta\theta = \frac{D \Delta\theta}{(1+z)} \quad (2.34)$$

In the limit for small redshifts ($z \ll 1$) this reduces to the “Euclidian” relation $d = r \Delta\theta$. The part $D_A = D / (1+z)$ in this equation is defined as the so called *angular diameter distance* D_A . In a last step the redshift corrected surface brightness should be derived. For this we first define the specific flux $S(\nu_0)$ measured by an observer:

$$S(\nu_0) = \frac{L_{(1+z)}}{4\pi(1+z)D_L} \quad (2.35)$$

Were $D_L = D(1+z)$ is the *luminosity distance*. Rewriting the *luminosity distance* using the *angular diameter distance* D_A , $D_L = D(1+z) = D_A(1+z)^2$ results in the specific flux per solid angle $d\Omega$:

$$\frac{dS(\nu_0)}{d\Omega} = \frac{dL_{(1+z)}}{4\pi dA_S} \frac{1}{(1+z)^3} \quad (2.36)$$

which is also defined as the specific intensity I_{ν_0} . With this relation we have derived the relativistic version of the surface brightness conservation:

$$I(\nu_0) = \frac{I(\nu_1)}{(1+z)^3} \quad (2.37)$$

Were I_{ν_0} represents the specific intensity seen by the observer and I_{ν_1} the specific intensity radiated by the source.

The described Equations were derived using the simplifying assumption of $\Lambda = 0$. With a non zero cosmological constant Λ the Equations became more complicated and a solution has to be found by numerical approaches. The physical meaning of $\Lambda \neq 0$ could be described with a non zero vacuum energy density and lead to the definition of the “Dark Energy”.

LSB Galaxies in the HDF–S

In the following, the results of a spectroscopic study of a sample of LSB galaxy candidates will be presented. The candidate sample has been selected with a photometric search for LSBs in the Hubble Deep Field–South. For the LSB candidates, long–slit spectra were obtained, covering a spectral range from 3400 Å to 7500 Å. The observations have been done using the ESO 3.6 m telescope equipped with the EFOSC2 spectrograph. From the measured radial velocities, distances could be estimated. With this distance information, it was possible to differentiate between true LSB galaxies and higher redshifted HSB galaxies which may contaminate the sample. At higher redshifts, a correction for the surface brightnesses had to be applied, accounting for cosmological dimming effects (“Tolman Dimming”). After applying this surface brightness correction, many of the higher redshifted galaxies are no longer LSB galaxies. The surface brightness correction is not necessary for galaxies in the local Universe. With distance information, it could be shown that $\sim 75\%$ of the color–color selected candidates are indeed true LSB galaxies, having redshifts below $z = 0.1$. The derived sample consists of large LSBs with radii between 10 kpc and 32 kpc. The surface brightness corrected volume density for the HDF–S LSB galaxy sample stays flat down to very low surface brightnesses ($\sim 27 \text{ mag arcsec}^{-2}$).

3.1 Sample selection

The sample used in the following studies is a subsample of a galaxy sample obtained from data of the NOAO Deep Wide–Field Survey pilot field (Dell’Antonio et al., 1999). The observations were obtained by a team of the National Optical Astronomical Observatory (NOAO) and include the HDF–S as well as the flanking fields. The data are online¹ available. The whole field of view covered by the survey has a size of $56 \text{ arcmin} \times 56 \text{ arcmin}$ (0.87 deg^2). Due to the use of a mosaic CCD camera (see Fig 3.1, upper panel) and although observing a dither pattern for the single exposures, the final coadded data have some gaps so that the final effective area is only $\sim 0.76 \text{ deg}^2$. For this project, only the observations in the B_W filter were used for analysis. The B_W filter is broader than a typical Johnson B–band filter (see Fig. 3.1, lower panel). It also

¹For further information see <http://www.noao.edu/noao/noadeep/hdfsinfo.html>

shows extensions into the wavelength region of the Sloan u-band. The observations were done using the Blanco 4 m telescope at the Cerro Tololo Interamerican Observatory (CTIO, Chile) equipped with the Big Throughput Camera (BTC). The BTC is a mosaic camera consisting of four thinned CCDs. Each CCD has 2048×2048 pixel² with sizes of $24 \mu\text{m}$. This corresponds to a resolution of 0.43 arcsec at the prime focus of the Blanco 4 m telescope. The whole field of view covered by the BTC using this configuration is $34.8 \text{ arcmin} \times 34.8 \text{ arcmin}$ in size. The final coadded B_W image consists of 38 dithered exposures with an exposure time per frame of 840 s. This results in a total exposure time of nearly 32000 s. The typical seeing measured from stars in the image is about 1.7 arcsec. The photometric calibration was done using observations of spectrophotometric standards (AB magnitudes) and resulted in an accuracy of 0.05 mag. The magnitude zeropoint (flux zeropoint) was estimated to be 32.67 mag. The B_W -filter image has a detection limit (3σ) for point like sources of $m_{\text{lim}} \sim 27$ mag (see Fig. 3.4). The detection limit was derived for an aperture of 2 arcsec radius. The astrometric calibration was done using the USNO A-1 catalog. The astrometric solution could be derived with an accuracy of 0.28 arcsec.

The search for LSB galaxies within the NOAO pilot data was done using two different search methods (Haberzettl, 1999). For the LSB galaxies with higher surface brightnesses between $22.0 \text{ mag arcsec}^{-2}$ and $24.0 \text{ mag arcsec}^{-2}$, the source extraction program SExtractor (Bertin & Arnouts, 1996) was used in combination with a search filter optimized for faint and large objects. For the faintest LSBs in the NOAO pilot field—which were not detected by using SExtractor—a slightly modified method adopted from Armandroff et al. (1998) was preferred. First, a SExtractor search was performed for this method. This search yields an object image including all bright and small objects (e.g., stars). In a next step, this image has been subtracted from the original data, followed by adopting a median filter to the so cleaned image. The kernel size of the median filter has been chosen to be comparable to the diameter limit which was applied later in order to select the sample. The so obtained LSB galaxy sample has a lower diameter limit of 10.8 arcsec. Finally, all galaxies with central surface brightnesses below $\mu(0) = 22.0 \text{ mag arcsec}^{-2}$ and diameters larger than 10.8 arcsec have been selected. Accurate central surface brightnesses needed for the selection of the LSB candidates were derived using the IRAF task *ellipse*.

By applying the two search methods as well as the two selection criteria, it was possible to extract a sample of 37 LSB galaxy candidates. Since the surface brightness of an object is only in the local universe independent of the distance—out to a distance of $z \sim 0.1$ —no simple method exists to differentiate between the candidates which are genuine LSB galaxies or higher redshifted “normal” HSB galaxies. At distances $z > 0.1$, the dependency of the surface brightness μ from the redshift z starts to become important (see also Eqn. 2.37):

$$\mu_{\nu_0} = \frac{\mu_{\nu_1}}{2.5 \log(1 + z)^3} \quad (3.1)$$

This so called “Tolman–Dimming” (Hubble & Tolman, 1935) results in a decrease in surface brightness (see also Sect. 2.4). At a distance of e.g., $z = 0.5$, the surface brightness of a galaxy is reduced by $\sim 1.3 \text{ mag arcsec}^{-2}$. Without any distance information, it is not obvious whether a galaxy with $\mu = 23 \text{ mag arcsec}^{-2}$ is a low surface brightness galaxy or a cosmologically dimmed

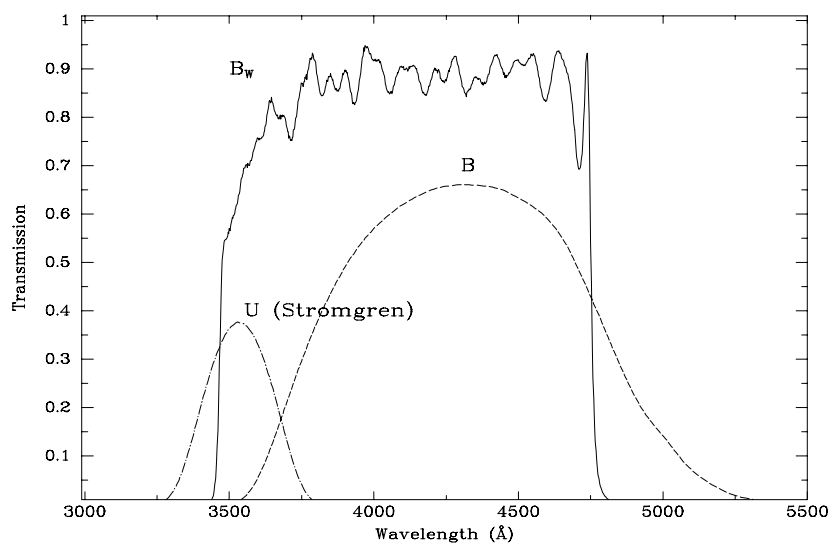
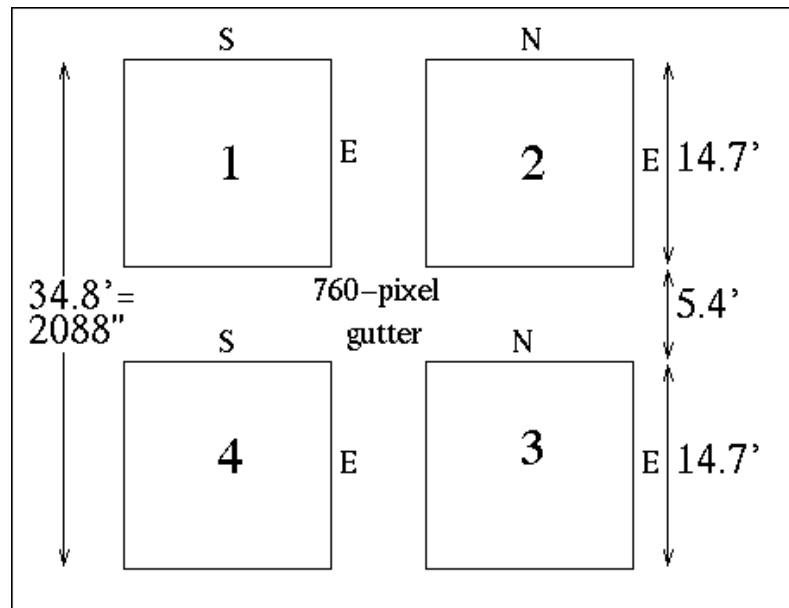


Figure 3.1: The geometry of the Big Throughput Camera (BTC) is shown (upper panel). The BTC is a mosaic camera consisting of 4 thinned CCDs (2048×2048 pixel²). The pixel size of the CCDs is $24 \mu\text{m}$, which is equivalent to 0.43 arcsec at the prime focus of the CTIO Blanco 4m telescope. The field of view covered by the BTC is $34.8 \text{ arcmin} \times 34.8 \text{ arcmin}$. For the NOAO Deep Wide-Field survey the B_W -filter was used. This filter is centered at 4135 \AA with a FWHM of 1360 \AA (lower panel). The B_W -filter is broader than a standard Johnson B-filter and shows an extension into the Stromgen u-filter.

Filter	Origin	Exp. Time/Frame	Total Exp. Time	Seeing FWHM
u	GSFC	1200 s	15600 s	1.90 arcsec
B	GSFC	600 s	7200 s	2.16 arcsec
V	GSFC	300 s	4500 s	1.85 arcsec
R	GSFC	300 s	4800 s	1.75 arcsec
I	GSFC	300 s	5100 s	1.55 arcsec

Table 3.1: Exposures times of the GSFC observations of the HDF-S for the different filters.

normal high surface brightness galaxy. Since LSB galaxies are present along the whole Hubble sequence (Schombert et al., 1992), a pure morphological selection can also be misleading.

Since no distance information for the LSB candidates were available at that time, a method was needed in order to differentiate LSB candidates from higher redshifted galaxies in the sample. A first selection was done using a relatively large lower diameter limit for the sample (10.8 arcsec). This selection criterion works due to the fact that galaxies show smaller angular diameters with increasing distances. However, there will be still a significant contamination by higher redshifted galaxies. Therefore, there is still a need for an additional selection criterion. A natural choice for further selection was the use of photometric redshifts (Koo, 1985; Loh & Spillar, 1986). This method is based on the fact that with a change in redshift, strong spectroscopic features—like the Balmer break and Lyman break—will be shifted into different filter bands (see Fig. 3.3). As a result of this shift, a typical spectral energy distribution (SED) of a galaxy moves along specific tracks in the color-color space (Liu & Green, 1998). The location and shape of the track in the color-color diagram depends on the shape of the SED and therefore on the stellar population mix of the galaxy. Since our knowledge of the Star Formation History of LSB galaxies is very limited until now, one cannot use the photometric redshift method to select LSB galaxies directly. Additionally, the photometric redshift method is not a good method in order to estimate the distances of nearby galaxies. For small redshift differences, the photometric error is in the range of the estimated color difference, which means that for low redshifts or small Δz the photometric errors become too large to estimate a useful distance. Still, it is known from deep pencil beam redshift surveys (e.g., Lilly et al., 1995) that the dominant contamination to the sample results from normal HSB disk galaxies at intermediate redshift ($z=0.1$ to 0.5). Subtracting this population of background galaxies should lead to a reasonably clean sample of genuine LSB galaxies. Therefore, a comparison of the location of the NOAO sample and the five standard galaxy types from E/S0 to Irr in the color-color diagrams has been performed (see Fig. 3.2). The colors of the five standard galaxy types were adopted from a work of Liu & Green (1998). The redshift tracks were plotted from $z=0$ to $z=0.5$ in steps of $\Delta z=0.025$, assuming no intrinsic evolution of the galaxies. This comparison was done using two different color-color diagrams (U-B vs. B-V and B-R vs. U-B), which makes multicolor information necessary. This information could be obtained from a second dataset produced by the Goddard Space Flight Center (GSFC) STIS team (Palunas

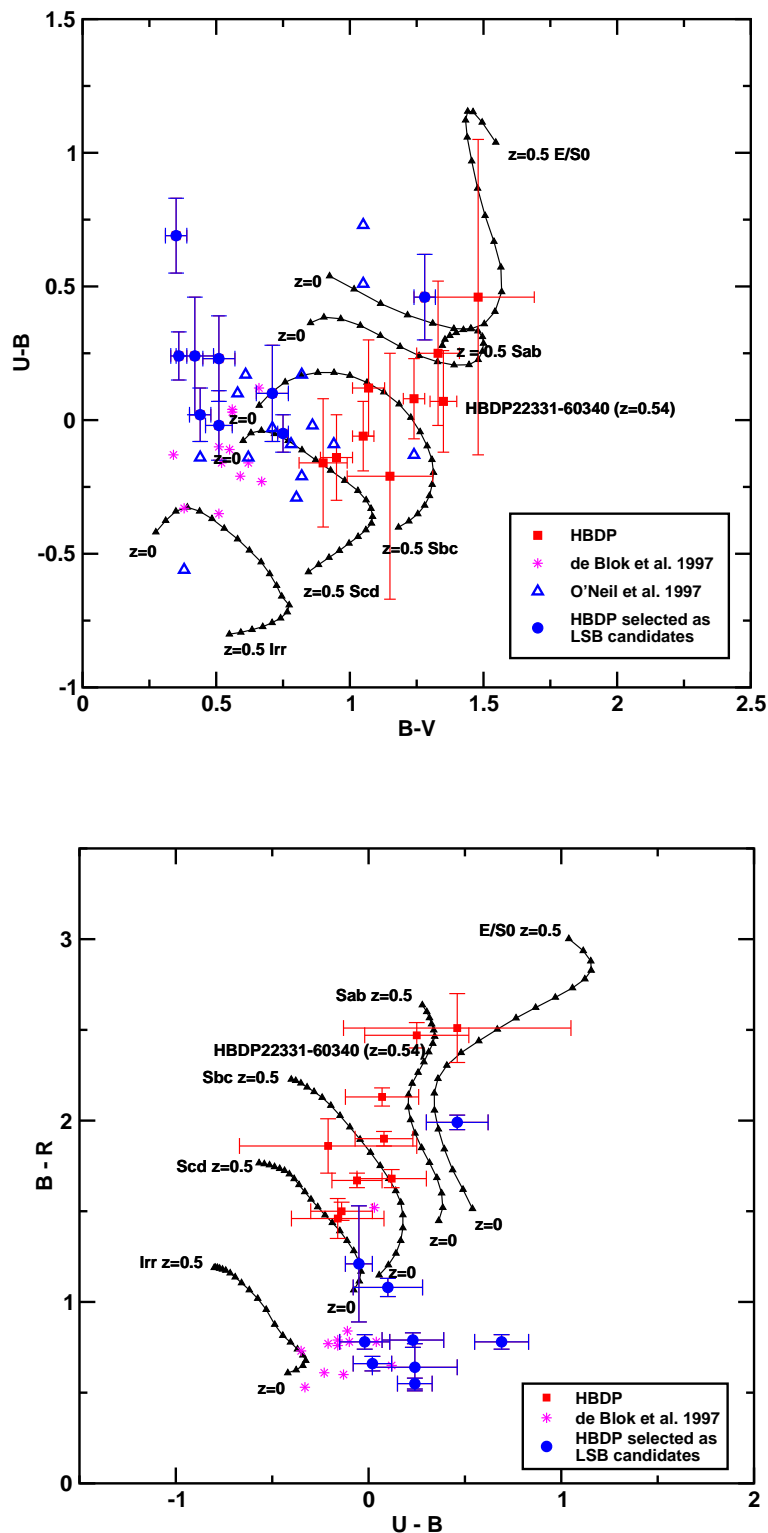


Figure 3.2: The two color-color diagrams (upper panel: $B-V$ vs. $U-B$, lower panel: $U-B$ vs. $B-R$) compare the location of the HDF-S sample (HBDP) to the redshift tracks (black lines + triangles) of five standard galaxy types (Irr, Scd, Sbc, Sab, E/S0). These tracks were adopted from a work of Liu & Green (1998). Plotted are also two samples of known LSB galaxies from O'Neil et al. (1997) (blue triangles) and de Blok et al. (1997) (purple stars). The diagrams show a clear separation between some galaxies of the HDF-S sample and the redshift tracks. These galaxies were selected as LSB galaxy candidates.

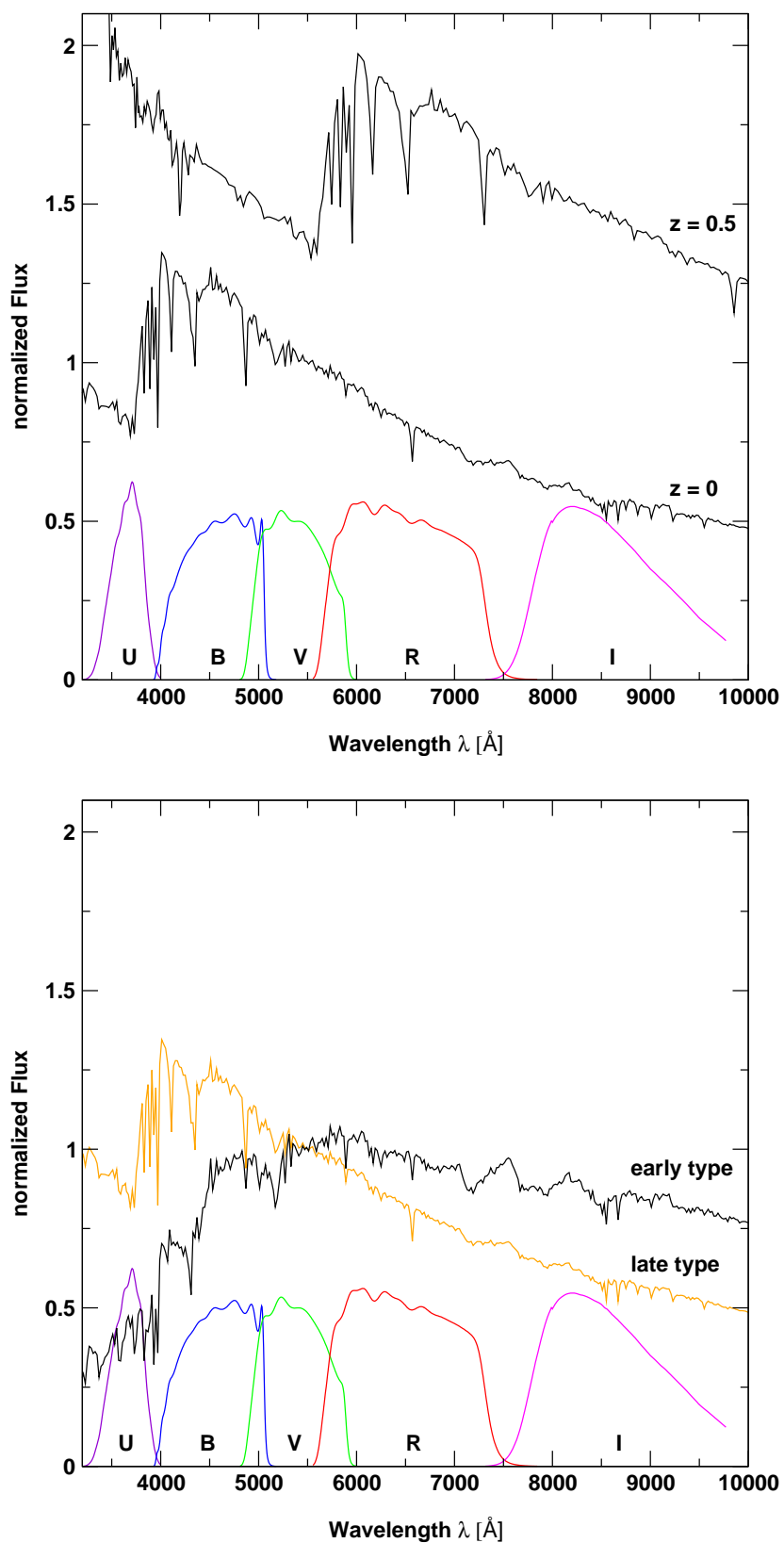


Figure 3.3: In the two diagrams, it is demonstrated how the change in redshift (upper panel) and the Star Formation History and therefore the Hubble type (lower panel) changes the color of galaxies. This change in color makes it possible to derive the distance of higher redshifted galaxies using only broad-band imaging data.

et al., 2000; Teplitz et al., 2001). The data are also online available². The data set includes observations in five filter bands (u, B, V, R, and I) and were obtained using also the CTIO Blanco 4m telescope equipped with the BTC mosaic-camera. The GSFC data are less sensitive

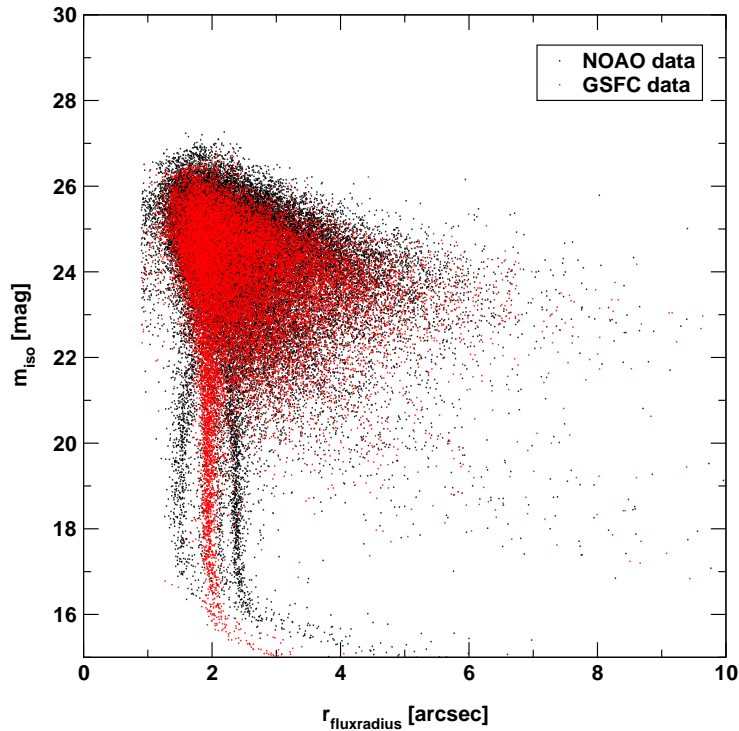


Figure 3.4: The diagram indicates the detection limits (3σ) for the B_W -filter of the NOAO data (black dots) and the B-filter of the Goddard Space Flight Center/STIS team data (red dots). From the plot, it can be seen that the GSFC data is slightly less sensitive compared to the NOAO data. The limit for detecting point like sources in an aperture of 2 arcsec radius has been estimated to be ~ 27 mag for the B_W -filter and ~ 26.5 mag for the B-filter.

(see Fig. 3.4) and provide a smaller field of view of $46 \text{ arcmin} \times 46 \text{ arcmin}$. The total exposures times range between 15600 s in the Sloan u-band filter and 4500 s in the Cousin R-band filter (see Tab. 3.1). The photometric calibration has been derived using spectrophotometric standard stars from the catalog of Landolt (1992). The calibration of the Stromgren u filter with respect to the Johnson U (used by Landolt, 1992) has been done applying a small color correction (Teplitz et al., 2001). The limit for detecting point like sources (aperture with 2 arcsec radius) has been derived to be ~ 26.5 mag and is therefore slightly lower compared to the B_W -filter of the NOAO data (see Fig. 3.4). The astrometric calibration was done with an accuracy for the astrometric solution of 0.07 arcsec. All images were observed under poor seeing conditions. The FWHM for stars has been estimated to range between 1.55 arcsec in the I-filter and 2.16 arcsec

²For more information about the GSFC data see: <http://hires.gsfc.nasa.gov/~research/hdfs-btc/>

in the B-filter (see Tab. 3.1). As a result of the smaller field of view, multicolor information for only half of the objects of the sample derived in the NOAO data (18 out of 37 galaxies, see Tab. 3.2) were available. In the following, if not stated otherwise, the description of the selection process is focused on the sample of the 18 galaxies for which multicolor information were available.

As next step, the HDF-S sample was plotted in the color-color diagrams. The location of the sample has been compared to the location of the redshift tracks of the five HSB standard galaxy types (see Fig. 3.2). Looking at the color-color diagrams, it could easily be seen that most of the sample galaxies follow the redshift tracks with redshifts $z > 0.1$. However, there exists a smaller subsample of seven galaxies which do not follow the redshift tracks of the standard Hubble types. The location of this subsample has an offset to the area defined by the redshift tracks (indicating redshifts below $z = 0$). As explained before (see right panel Fig. 3.3), the stellar population mix – and therefore the SFH – also has an effect on the change of colors of galaxies. Having this in mind, the different locations indicate that these galaxies show a different stellar population mix compared to the standard galaxy types. This may hint at a different SFH. The seven galaxies, together with two galaxies located at low redshifts ($z \leq 0.1$), were selected as LSB galaxy candidates. For spectroscopic follow up observations, two additional galaxies were randomly selected from the part of the sample for which no multi-color information is available. Finally, the spectroscopic observations were performed for a sample of 11 galaxies (for the spectra see App. A.).

3.2 Observations and Data Reduction

3.2.1 Observations

Observations were performed during the nights of October, 23.–25. 2000 at the ESO 3.6 m telescope on La Silla. The spectra were obtained using the ESO Faint Object Spectrograph 2 (EFOSC2) equipped with a Loral 2048² pixel CCD and a pixel size of $15 \mu\text{m}^2$ (0.157 arcsec^2). In order to derive long-slit spectra, a grating of 300 gr mm^{-1} (grism # 11) was used resulting in a spectral sampling of $2.12 \text{ \AA pixel}^{-1}$ and covering a spectral range from 3400 \AA to 7500 \AA . The CCD was binned by a factor of 2 in both directions, which results in a spectral resolution of $\sim 4 \text{ \AA pixel}^{-1}$. The spectrograph was equipped with a long-slit of slightly less than 5 arcmin size in the spatial direction. For the observation, a slit width of 1.2 arcsec has been chosen. With this setup, the derived spectra have a spectral resolution of $\sim 15.6 \text{ \AA}$ at 4000 \AA .

In order to minimize flux losses due to atmospheric differential refraction (Filippenko, 1982), the observations were carried out at low airmasses in the range between 1.1 and 1.8. This airmass range resulted in a refraction below 1.8 arcsec at 3500 \AA and above -0.9 arcsec at 7500 \AA . During the nights of the 23rd and 24th, the observing conditions were not photometric with a mean seeing of $\sim 2 \text{ arcsec}$. In the last night, the conditions were nearly photometric with a seeing below 1 arcsec . Bias frames, dome flats, twilight-sky flats, and He-Ne comparison lamp exposures were taken at the beginning and the end of each night. For flux calibration, spectroscopic standard stars were observed several times during each night (Hamuy et al.,

Name	U-B	$\Delta(U-B)$	B-V	$\Delta(B-V)$	V-I	$\Delta(V-I)$	B-R	$\Delta(B-R)$
HBDP22311-60503	-0.05	± 0.07	0.75	± 0.02	0.99	± 0.02	1.21	± 0.32
HBDP22315-60481	-0.21	± 0.46	1.15	± 0.16	1.30	± 0.13	1.86	± 0.15
HBDP22322-60142	0.46	± 0.59	1.48	± 0.21	1.57	± 0.12	2.51	± 0.19
HBDP22324-60520	0.46	± 0.16	1.28	± 0.04	1.27	± 0.02	1.99	± 0.04
HBDP22325-60155	0.02	± 0.10	0.44	± 0.04	0.64	± 0.03	0.66	± 0.04
HBDP22325-60211	-0.14	± 0.16	0.95	± 0.06	1.05	± 0.04	1.50	± 0.05
HBDP22330-60543	0.24	± 0.09	0.36	± 0.03	0.59	± 0.04	0.55	± 0.03
HBDP22331-60340	0.25	± 0.27	1.33	± 0.08	1.68	± 0.05	2.47	± 0.07
HBDP22341-60475	-0.06	± 0.13	1.05	± 0.04	1.20	± 0.02	1.67	± 0.04
HBDP22342-60505	-0.16	± 0.24	0.90	± 0.09	1.50	± 0.10	1.46	± 0.11
HBDP22343-60222	0.24	± 0.22	0.42	± 0.07	0.75	± 0.06	0.64	± 0.13
HBDP22345-60210	0.12	± 0.18	1.07	± 0.06	1.16	± 0.04	1.68	± 0.05
HBDP22352-60420	0.10	± 0.18	0.71	± 0.06	0.82	± 0.04	1.08	± 0.05
HBDP22353-60311	0.69	± 0.14	0.35	± 0.04	0.77	± 0.03	0.78	± 0.04
HBDP22354-60122	-0.02	± 0.13	0.51	± 0.05	0.73	± 0.04	0.78	± 0.04
HBDP22355-60183	0.23	± 0.16	0.51	± 0.06	0.70	± 0.04	0.79	± 0.04
HBDP22355-60390	0.07	± 0.19	1.35	± 0.05	1.36	± 0.03	2.13	± 0.05
HBDP22361-60223	0.08	± 0.15	1.24	± 0.04	1.23	± 0.02	1.90	± 0.04

Table 3.2: Color indices for the sample galaxies obtained in the Goddard Space Flight Center/STIS Field (Haberzettl, 1999).

1992). For the observations of the standard stars, the maximum slit width of 5 arcsec were used in order to increase the signal to noise ratio of the spectra as much as possible. Each science exposure was obtained with an exposures time of about 1800s. In most cases, two exposures per object were observed (see Tab. 3.3).

NAME	EXPOSURES TIME [s]	EXPOSURES
HBDP22300-60300	1800	1
HBDP22302-60352	1800	1
HBDP22311-60503	1800	2
HBDP22324-60520	1800	2
HBDP22325-60155	1800	2
HBDP22330-60543	1800	2
HBDP22343-60222	1800	2
HBDP22352-60420	1800	2
HBDP22353-60311	1800	1
HBDP22353-60122	1800	2
HBDP22355-60183	1800	2

Table 3.3: Exposure times and number of exposures for the HDF-S LSB candidate sample observed with ESO 3.6 m telescope.

3.2.2 Reduction and calibration

The data reduction and calibration were carried out based on the standard reduction procedures within IRAF (Massey, 1997; Massey et al., 1992). In a first step, an overscan correction and trimming were applied to the images. After bias subtraction in order to remove the readout-noise, the flatfield correction was done. With the flatfield correction, the pixel-to-pixel variations across the CCD chip could be removed. For this step, projector lamp flats produced by a quartz lamp which uniformly illuminate the spectrograph slit were used. In a next step, one has to remove wavelength-dependent variations along the slit. This was done combining a set of twilight-skyflats exposed during the sunset. From these combined twilight-skyflats, IRAF derives a slit illumination function. After that, the wavelength dependent variations along the slit were removed by dividing the object exposures by the illumination function. This procedure was applied to all science and standard star exposures.

After the pre-reduction of the data, a wavelength and flux calibration of the science spectra were done. For the wavelength calibration, the observed HeNe-calibration lamp spectra were used. The HeNe-calibration spectra were derived with the same setup as used for the science spectra. The exposure times were chosen to give high signal-to-noise ratios. With this wavelength calibration spectra, a dispersion solution was carried out. By fitting this dispersion solution to the science spectra, geometrical distortions along the dispersion axis could be removed. The wavelength calibration results in a spectral sampling of 4.04 Å per pixel with an accuracy between 0.3 Å and 1.0 Å per pixel. The accuracy depends on the wavelength region,

while the edges of the spectral region have lower accuracy. After the wavelength calibration, the single science exposures of every object were combined. This coaddition makes it also possible to remove cosmic rays from the exposures. The cosmic ray cleaning of the objects, for which only one science exposure was available, was done using the cosmic ray identification task L.A. cosmic (van Dokkum, 2001) which is based on Laplace filtering. The coadded and cosmic ray cleaned spectra were then flux calibrated using the standard star spectra. Finally, an extinction correction was applied to the science spectra. This correction is normally done by measuring the Balmer decrement ($I_{H\alpha}/I_{H\beta}$) and by comparing this to the theoretical ratio $I_{H\alpha_0}/I_{H\beta_0} = 2.76$ (e.g. Osterbrock, 1989). From the measured decrement $H\alpha$ over $H\beta$, one can calculate the logarithmic reddening parameter $c(H\beta)$:

$$c(H\beta) = -\frac{1}{f(\lambda) - f(H\beta)} \left[\log \frac{I_\lambda}{I_{H\beta}} - \log \frac{I_{\lambda_0}}{I_{H\beta_0}} \right] \quad (3.2)$$

This reddening parameter is used by the IRAF task *deredden* in order to correct the spectra for interstellar reddening.

Due to the low signal to noise ratios of the spectra, it was not possible in some cases to measure the $H\beta$ emission line or it was only possible to estimate an upper limit (see Tab. 3.4). For these cases, only the galactic extinction in the observed region of the sky was taken into account. At least for this correction, a value for the extinction of $E(B-V) = 0.028$, adopted from a work of Schlegel et al. (1998), was used. Applying only foreground extinction from the galaxy gives reasonable results for the LSB galaxies if one assumes low internal extinction for these galaxies, which is due to less dust. A hint for a negligible dust component in LSB galaxies results from the fact that there exist only a few detections on very low levels of LSB galaxies in the FIR and mm-wavelength range where dust radiates thermal emission (Hoepe et al., 1994). Therefore, one can make the assumption that no extinction exists in the LSB galaxies themselves. The final result of the reduction and calibration processes are 2D-spectra which will be used in the following analysis.

3.3 Results and Discussion

3.3.1 Physical Parameters of the LSB Sample

Most of the common internal parameters (see Tab. 3.5) of the studied galaxies (e.g., sizes in physical units, luminosities, absolute magnitudes) are distance-dependent parameters. In order to derive the distances, one has to estimate the shift of the restframe wavelength λ_0 to longer wavelengths, due to the expansion of Universe, the so called redshift z (see Eqn. 3.3). This was done by measuring the wavelength λ of the detectable, known emission lines and comparing these to their rest frame wavelength λ_0 . Using the simple approach in Eqn. 3.3, the redshifts of the sample galaxies were derived (see Tab. 3.4).

In order to maximize the signal-to-noise ratio in the science spectra, all columns along the spatial axis—where a significant signal could be detected—were summed up. In these integrated spectra (see App. A), it was now possible to detect the most important emission

lines e.g., [OII], H β , [OIII]–doublet, and H α . In some cases, also the [SII]–doublet could be detected and useful upper limits for the [NII] λ 6584 line could be derived.

Following Eqn. 3.3 for every clearly detectable emission line in a galaxy spectrum, a redshift was estimated. These redshifts were used in order to derive the mean redshifts \bar{z} of the single galaxies. The errors of this mean redshifts were determined using the standard deviation (see Eqn 3.4):

$$z = \frac{\lambda - \lambda_0}{\lambda_0} \quad (3.3)$$

$$\sigma_z = \sqrt{\frac{1}{N} \sum_{i=1}^N (z_i - \bar{z})^2} \quad (3.4)$$

For the determination of the mean redshift, only emission lines which were clearly detected and which were not influenced by nightsky emission lines were used. The lines which are only measured as upper limits or which were influenced by nightsky emission lines were not used and are marked with ^a (see Tab. 3.4). Due to the low resolution, it was not possible to resolve the [SII] $\lambda\lambda$ 6717,6731–doublet. Therefore, the [SII]–doublet was also not used for the estimation of the mean redshift and is also marked with ^a (see Tab. 3.4).

Following the formalism in Eqn. 3.5–3.10, from the estimated redshifts various parameter could be calculated for the selected LSB sample (see Tab. 3.5) e.g., radial velocities v_{rad} , proper distances D (see Eqn. 2.32), radii r in physical units (proper length), scalelength h in physical units (proper length), absolute B–band magnitudes M_B and luminosities L_B . In Eqn. 3.5 and 3.6, the equations on the right side were used for galaxies having distances $z \geq 0.1$:

$$v_{\text{rad}}[z < 0.1] = c \cdot z \quad v_{\text{rad}}[z \geq 0.1] = c \cdot \frac{(1+z)^2 - 1}{(1+z)^2 + 1} \quad (3.5)$$

$$D[z < 0.1] = \frac{v_{\text{rad}}}{H_0} \quad D[z \geq 0.1] = \frac{2c}{H_0} \frac{1}{1+z} [(1+z) - (1+z)^{1/2}] \quad (3.6)$$

The calculations were done assuming a Hubble constant $H_0 = 71 \text{ kms}^{-1} \text{Mpc}^{-3}$ (Spergel et al., 2003):

$$r[z < 0.1] = 2 \cdot D \cdot \tan \frac{r_{\text{arcsec}}}{2} \quad h[z < 0.1] = 2 \cdot D \cdot \tan \frac{\alpha_{B_W}}{2} \quad (3.7)$$

$$r[z \geq 0.1] = d = \frac{r[\text{rad}] \cdot D}{1+z} \quad h[z \geq 0.1] = d = \frac{\alpha_{B_W}[\text{rad}] \cdot D}{1+z} \quad (3.8)$$

The radius r (proper length d) in physical units as well as the scale length h (proper length) in physical units of objects lying at $z > 0.1$ were derived using Eqn. 3.8 (Longair, 1998). The absolute magnitudes result from the distance modulus (see Eqn. 3.9; Driver et al., 1994) using the proper distance D (see Eqn. 2.32). This absolute magnitudes were used to estimate the B_W–band luminosities in units of solar luminosities (see Eqn. 3.10):

$$M_\nu = m_\nu - 5 \cdot \log_{10} \left[\frac{2 \cdot c}{H_0} \cdot ((1+z) - (1+z)^{1/2}) \right] - 25 - 2.5 \cdot z \quad (3.9)$$

NAME	[OII] $\lambda 3727$ [Å]	H β $\lambda 4861$ [Å]	[OIII] $\lambda 4959$ [Å]	[OIII] $\lambda 5007$ [Å]	H α $\lambda 6563$ [Å]	[NII] $\lambda 6584$ [Å]	[SII] $\lambda\lambda 6717,6731$ [Å]	z	σ_z
HBDP22300-60300	4065	5303 ^a	5410	5463	7157 ^a	–	–	0.0908	0.0003
HBDP22302-60352	3877	5055	5158	5207	6824	6852 ^a	6986 ^a	0.0400	0.0002
HBDP22311-60503	4172	–	–	–	7351	–	–	0.1198	0.0004
HBDP22325-60155	3924	5118	5219	5270	6907	–	7077 ^a	0.0526	0.0002
HBDP22330-60543	3936	5133	5236	5287	6929	–	7096 ^a	0.0559	0.0001
HBDP22343-60222	3903	5089	5190	5242	6866	6888 ^a	7037 ^a	0.0467	0.0005
HBDP22352-60420	4170	5439	5550 ^a	5603 ^a	7347	–	–	0.1191	0.0003
HBDP22353-60311	3946	5146	5250	5297	6943	6968 ^a	–	0.0584	0.0004
HBDP22354-60122	4329	5647	5758	5816	–	–	–	0.1615	0.0002
HBDP22355-60183	4194	5468	5584 ^a	5632	7381	–	–	0.1249	0.0003
HBDP22324-60520	–	–	–	–	–	–	–	0.1723 ^b	–

Table 3.4: Position measurements of emission lines of the LSB galaxy sample used for the estimation of redshifts. All entries which are marked with ^a are not used for the estimation of the mean redshift z and therefore not for the estimation of the standard deviation σ_z either. All lines which were either influenced by nightsky emission lines or which had only upper limits were not used for the determination of the mean redshift. It was not possible to resolve the single component of the [SII]–doublet. Therefore, also [SII] was not used in order to estimate redshifts. The redshift of HBDP22324-60520 (marked with ^b) was estimated measuring the wavelength of the CaII–K absorption line.

$$M_{B_w} = 4.87 - 2.5 \cdot \log\left(\frac{L}{L_\odot}\right) \quad (3.10)$$

The described physical parameters were derived for the complete galaxy sample including also the higher redshifted HSB galaxies (HBDP22311-60503, HBDP22324-60520, HBDP22354-60122, and HBDP22355-60183). No emission line could be detected for HBDP22324-60520. This galaxy shows a spectrum of an elliptical galaxy with no ongoing star formation. Therefore, the estimation of the redshift has to be done by measuring the wavelength of the CaII-K absorption line and comparing this value to the rest wavelength of CaII-K ($\lambda_0 = 3933 \text{ \AA}$). The next sections will only be focused on the discussion of the spectroscopically verified LSB galaxies.

3.3.2 The HDF-S LSB Galaxies in the Color-Color Space

The selection of the possible LSB galaxy candidates was done using their locations in the color-color space (see Sect. 3.1). Thereby, the significant different locations of a part of the HDF-S sample in comparison to the location of the “normal” HSB galaxies (see Fig. 3.2) was used. The HSB galaxies in the color-color diagrams follow specific tracks (see black line+triangles), which depends on the Hubble type. The shape of the tracks results from changes of the color of the galaxies, due to different redshifts. Important spectroscopic features like e.g., the Balmer bump and the shape of the continuum are shifted into redder filter bands with increasing redshift (see Fig. 3.3). This shift in the color-color space is used in order to determine the redshifts based on photometric imaging data of large samples of galaxies. In contrast to the spectroscopic distance determination—which uses sharp emission lines in order to measure the redshift—the uncertainties are relatively large ($\Delta z \sim 0.1$). Therefore, this method is not adequate in order to measure the redshifts of nearby galaxies ($z \leq 0.1$) and it was not used to measure distances of the derived LSB candidates. The aim of the described selection method was the extraction of higher redshifted ($z > 0.1$) background HSB galaxies which contaminate the selected sample of LSB candidates. These background HSB galaxies show low surface brightnesses due to “Tolman-Dimming” (see Eqn. 3.1).

After plotting the sample galaxies into the color-color diagrams (see Fig. 3.2), it could be shown that the majority of the HDF-S sample galaxies follow these so called redshift tracks and could be identified as higher redshifted background galaxies. Now, it was possible to remove these galaxies from the selected LSB sample. However, a smaller subsample did not follow the redshift tracks of “normal” HSB galaxies. This subsample (see Tab. 3.6 blue and green squares) has a location in the color-color diagrams where one would not expect any galaxy. The location indicates a redshift $z < 0$. The galaxies have a redder U-B color ($U-B \geq -0.05 \text{ mag}$). In the B-R and B-V color, the subsample is shifted into the blue color range ($B-R \leq 1.08 \text{ mag}$, $B-V \leq 0.71 \text{ mag}$). For the so derived LSB candidate sample, distances were derived using spectroscopic follow up observations (see Sect. 3.2). It turned out that the majority of the selected LSB candidates (5 out of 9) have redshifts $z \leq 0.1$ (blue squares in Fig 3.5). These galaxies are local galaxies and therefore real LSB galaxies. One of these candidates

NAME	RA [hh:mm:ss.s]	DEC [dd:mm:ss]	v_{rad} [km s ⁻¹]	d [Mpc]	r [arcsec]	r [kpc]	h [kpc]	M_{B} [mag]	L_{B} [10 ⁹ · L _⊙]
HBDP22300-60300	22:30:09.8	-60:30:07	27240±75	381.8±19.0	17.5	32.4±1.6	6.1±0.3	-19.06±0.09	3.73
HBDP22302-60352	22:30:23.0	-60:35:29	12000±45	168.2±8.4	12.9	10.5±0.5	3.6±0.2	-18.01±0.06	1.42
HBDP22311-60503	22:31:13.0	-60:50:34	33854±78	503.7±25.1	12.9	31.5±1.6	6.2±0.3	-20.36±0.07	12.36
HBDP22324-60520	22:32:41.8	-60:52:07	46717	638.0	8.5	7.15	1.25	-20.17	10.38
HBDP22325-60155	22:32:52.2	-60:15:58	15780±69	221.2±11.0	17.2	18.4±0.9	4.6±0.2	-16.90±0.09	0.51
HBDP22330-60543	22:33:03.2	-60:54:38	16770±33	235.0±11.7	15.1	17.1±0.9	2.5±0.1	-18.31±0.08	1.87
HBDP22343-60222	22:34:32.3	-60:22:21	14010±159	196.4±10.0	13.8	13.1±0.7	4.3±0.1	-17.43±0.09	0.83
HBDP22352-60420	22:35:22.5	-60:42:09	33615±62	500.8±24.9	10.8	23.4±1.2	6.6±0.3	-18.67±0.15	2.61
HBDP22353-60311	22:35:34.4	-60:31:12	17520±120	245.6±12.3	10.8	12.9±0.6	7.3±0.4	-17.77±0.11	1.14
HBDP22354-60122	22:35:46.1	-60:12:20	44581±44	679.0±33.8	7.6	21.5±1.1	6.2±0.3	-19.82±0.13	7.52
HBDP22355-60183	22:35:58.3	-60:18:40	35149±57	525.2±26.1	7.8	17.7±0.9	5.3±0.3	-19.15±0.13	4.06

Table 3.5: Derived physical parameters of the observed galaxy sample.

Name	U-B [mag]	B-V [mag]	B-R [mag]	μ_0 $B_W \text{mag arcsec}^{-2}$	$\mu_0(\text{corr})$ $B_W \text{mag arcsec}^{-2}$	LSB galaxy
HBDP22311-60503	-0.05	0.75	1.21	22.4	21.9	no
HBDP22324-60520	0.46	1.28	1.99	22.2	–	no
HBDP22325-60155	0.02	0.44	0.66	23.3	23.3	yes
HBDP22330-60543	0.24	0.36	0.55	22.3	22.3	yes
HBDP22343-60222	0.24	0.42	0.64	23.3	23.3	yes
HBDP22352-60420	0.10	0.71	1.08	23.1	22.6	yes
HBDP22353-60311	0.69	0.35	0.77	23.4	23.4	yes
HBDP22354-60122	-0.02	0.51	0.78	22.5	21.8	no
HBDP22355-60183	0.23	0.51	0.79	22.5	22.0	no

Table 3.6: List of the galaxies which were selected as LSB candidates using color–color diagrams. The last column marks whether the candidate, after analyzing the spectroscopic information, is a true LSB galaxy or not. The central surface brightness in column 6 is corrected against fading due to “Tolman Dimming”.

(HBDP22352-60420) has a slightly larger redshift of $z = 0.12$. However, after correcting the central surface brightness for “Tolman–Dimming”, this galaxy still remains as a LSB galaxy, showing a central surface brightness below $\mu_0 > 22.0 \text{ mag arcsec}^{-2}$ (see Tab. 3.6). The other 4 selected candidates (green squares) show redshifts $z \geq 0.1$. After correcting these candidates against the “Tolman–Dimming” effect, the central surface brightnesses came out to have values $\mu_0 \leq 22 \text{ mag arcsec}^{-2}$. Therefore, these galaxies are higher redshifted “normal” HSB galaxies. After a first inspection, it turned out that by using the color–color selection criterion, 56 % of the selected galaxies are genuine LSB galaxies. However, the color–color selection criterion also resulted in nearly the same amount (44 %) of higher redshifted “normal” HSB background galaxies. This result looks not very impressive. On a first look, there seems to be nearly a 50 % probability to select a LSB galaxy due to their location in the color–color diagram. Therefore, this would not be a very reliable method in order to select a LSB subsample from a large sample of galaxies. A more careful analysis of the color–color selection method (see Fig. 3.5) shows that two of the higher redshifted HSB galaxies (HBDP22311-60503, HBDP22324-60520) which were also selected as LSB candidates do follow the redshift tracks with redshifts around $z \sim 0.1$. After correcting the surface brightnesses against “Tolman–Dimming”, these galaxies appear to be higher redshifted “normal” HSB galaxies. Their classification as LSB candidates was too optimistic, due to the relatively large uncertainties in the photometric redshifts. Two additional galaxies (HBDP22354-60122, HBDP22355-60183) which are clearly separated from the redshift tracks turned out to also be located at redshifts $z \geq 0.1$. After again correcting the surface brightness against “Tolman–Dimming”, these galaxies also turned out to be HSB galaxies. However, these two galaxies do not behave like “normal” HSBs. They must have extreme colors in order to be moved to this location in the color–color space. Excluding now the two higher redshifted galaxies located along the redshift tracks, the method yields 5 LSB galaxies (71 %) out of a sample of 7 selected galaxies. Only 2 out of 7 galaxies (29 %) are

higher redshifted HSB galaxies.

3.3.3 Volume densities of the HDF–S LSB galaxies

One result of the search for LSB galaxies in the HDF-S is a surface number density of 8.5 LSB galaxies per deg^2 . This is more than two times higher than found in previous surveys (e.g., O’Neil et al., 1997a,b, 4 LSB galaxies deg^{-2}). This number density is not very significant if one has in mind that, due to the use of much more sensitive data ($\mu_{\text{lim}} \approx 29 \text{ mag arcsec}^{-2}$), a much larger search volume is covered.

In order to also include the covered volume V , it is more convenient to calculate the volume density n for the derived sample. This was done by following a method from McGaugh (1996). With this method, surface brightness corrected and normalized volume densities Φ could be estimated. The volume density was derived from a relation between the number density N and the volume V :

$$n = \Omega \frac{N}{V} \quad (3.11)$$

In this relation, Ω represents the solid angle. Assuming now that the light distribution of a LSB galaxy is described by an exponential profile (see Eqn. 2.7), one can estimate the maximum distance d at which a galaxy can be found and is still in agreement with the selection limits of the survey, using $\theta = 2r = 1.84 \alpha (\mu_1 - \mu_0)$ and $\alpha = \frac{h}{d}$:

$$d = 1.84 \frac{h}{\theta_1} (\mu_1 - \mu_0) \quad (3.12)$$

The maximum distance d is now related to the characteristic central surface brightness μ_0 of each sample and the isophotal level μ_1 at which the diameter θ is measured and is still consistent with the limits of the survey ($\theta \geq \theta_1$). The volume V covered by the survey is described by Eqn. 3.13, where Ω represents the solid angle scanned by the survey:

$$V = \frac{4\pi}{3} \Omega d^3 \quad (3.13)$$

Now the relative volume density of LSB galaxies n_{LSB} in relation to the number density of a well known sample of HSB galaxies n_{HSB} is estimated:

$$\frac{n_{\text{LSB}}}{n_{\text{HSB}}} = \frac{N_{\text{LSB}}}{N_{\text{HSB}}} \left(\frac{(V/\Omega)_{\text{HSB}}}{(V/\Omega)_{\text{LSB}}} \right) \quad (3.14)$$

$$\Phi_{\text{norm}} = \frac{n_{\text{LSB}}}{n_{\text{HSB}}} = \frac{N_{\text{L}}}{N_{\text{H}}} \left(\frac{\theta_{\text{L}}^{\text{L}}}{\theta_{\text{H}}^{\text{H}}} \right)^3 \left(\frac{h_{\text{H}}}{h_{\text{L}}} \right)^3 \frac{(\mu_{\text{L}}^{\text{H}} - \mu_0)^3}{(\mu_{\text{L}}^{\text{L}} - \mu_0^{\text{L}})^3} \quad (3.15)$$

Most of the parameters in Eqn. 3.15 can be derived without having distance information for the sample galaxies. The only exception is the scale length h in physical units. For the calculation

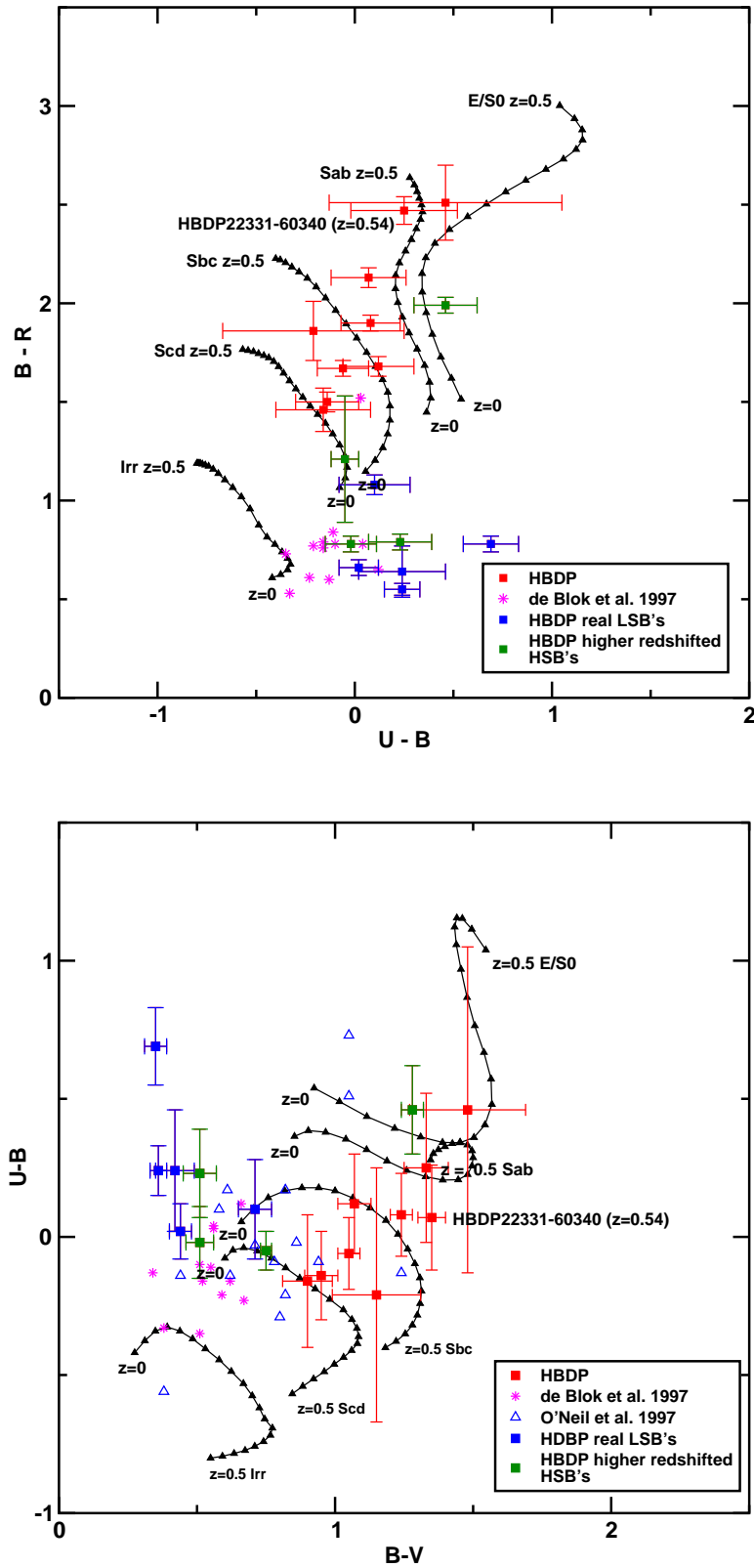


Figure 3.5: Color-color diagrams $U-B$ vs. $B-R$ and $B-V$ vs. $U-B$ accounting for the spectroscopically derived distance information. From the selected LSB candidates (blue + green squares), 56% of the galaxies are found to be true LSB's (blue squares) and 44% are higher redshifted HSB galaxies (green squares). Two of the higher redshifted HSBs are located at $z \sim 0.1$. They follow the redshift tracks of the “normal” HSB galaxies and therefore should not be selected as LSB candidates.

of the volume density, the assumption is made that the scale length h_L of the derived LSB galaxy sample is comparable to the scale length h_H of the sample of HSB galaxies to which the sample will be normalized ($h_H/h_L = 1$). If, on average, HSB galaxies had a larger scale length, the value of $n_{\text{LSB}}/n_{\text{HSB}}$ would increase. Using this assumption, lower limits for the normalized volume densities of LSB galaxies will be calculated.

For the derived HDF–S LSB galaxy sample, a number density of $N_L = 8.5 \text{ deg}^{-2}$ as well as a surface brightness limit of $\mu_l = 29.0 \text{ mag arcsec}^{-2}$ were estimated. The diameter limit was chosen to be $\theta_l \geq 10.8 \text{ arcsec}$. Due to the small number of objects, the volume densities were derived using a central surface brightness bin size of $1 \text{ mag arcsec}^{-2}$. The sample was normalized with respect to the well known galaxy sample of de Jong (1996). This is a statistically complete sample of 86 galaxies. The sample was selected from the UGC catalog including galaxies with diameters θ larger than 2 arcmin and a minor to major axis ratio larger than 0.625. The survey covered an area of $1.57 \text{ srad} \equiv 5154.3 \text{ deg}^{-2}$. The surface brightness limit of the catalog is about $\mu_l = 26.5 \text{ mag arcsec}^{-2}$. The errors for the surface brightness corrected volume densities were calculated using Poisson statistics and Gaussian errors:

$$\sigma_L = \sqrt{\frac{1}{N_L}} \quad (3.16)$$

$$\Delta\Phi_{\text{norm}} = \pm \sqrt{\left(\frac{\partial\Phi_{\text{norm}}}{\partial N_L} \sigma_L\right)^2 + \left(\frac{\partial\Phi}{\partial\mu_0^H} \Delta\mu_0^H\right)^2} \quad (3.17)$$

For a comparison, the surface brightness corrected volume densities for two additional, well known LSB samples of O’Neil et al. (1997a, Texas survey) and Impey et al. (1996) were estimated. The Texas survey covered an area of 27 deg^2 on the sky. In this area, a sample of 127 LSB galaxies with diameters larger than 13.5 arcsec was derived. The survey reached a surface brightness limit of $\mu_l = 27 \text{ mag arcsec}^{-2}$. The search area of the survey of Impey et al. (1996) covers about 768 deg^2 of the sky. The field is located around the equatorial strip over a declination range of $\pm 2^\circ$. The survey reached a surface brightness limit of $\mu_l = 26 \text{ mag arcsec}^{-2}$. The derived sample consists of 693 galaxies larger than 30 arcsec. For the comparison samples, the estimations of the volume densities were done using surface brightness bins of $0.5 \text{ mag arcsec}^{-2}$.

The volume density vs. the central surface brightness is plotted in Fig. 3.6. In the diagram, one can see that the central surface brightness distribution for the HDF–S sample (HBDP, blue triangles) follows the flat distribution of the other LSB surveys. At lower central surface brightnesses (more than 3σ below the Freeman value of $\mu_0 = 21.65 \pm 0.3 \text{ mag arcsec}^{-2}$), there exists much more LSB galaxies than expected from the Freeman Law (purple line). This law is described by a Gaussian distribution of the following form:

$$\Phi(\mu_0) = \frac{1}{\sqrt{2 \cdot \pi \cdot 0.35}} \cdot \exp\left(-0.5 \cdot \frac{(\mu_0 - 21.65 \text{ mag arcsec}^{-2})^2}{(0.35 \text{ mag arcsec}^{-2})^2}\right) \quad (3.18)$$

The distribution was normalized to be 1 at a central surface brightness of $21.65 \text{ mag arcsec}^{-2}$. The volume density of the HDF–S LSB galaxy sample derived for the $\mu = 22.5 \text{ mag arcsec}^{-2}$

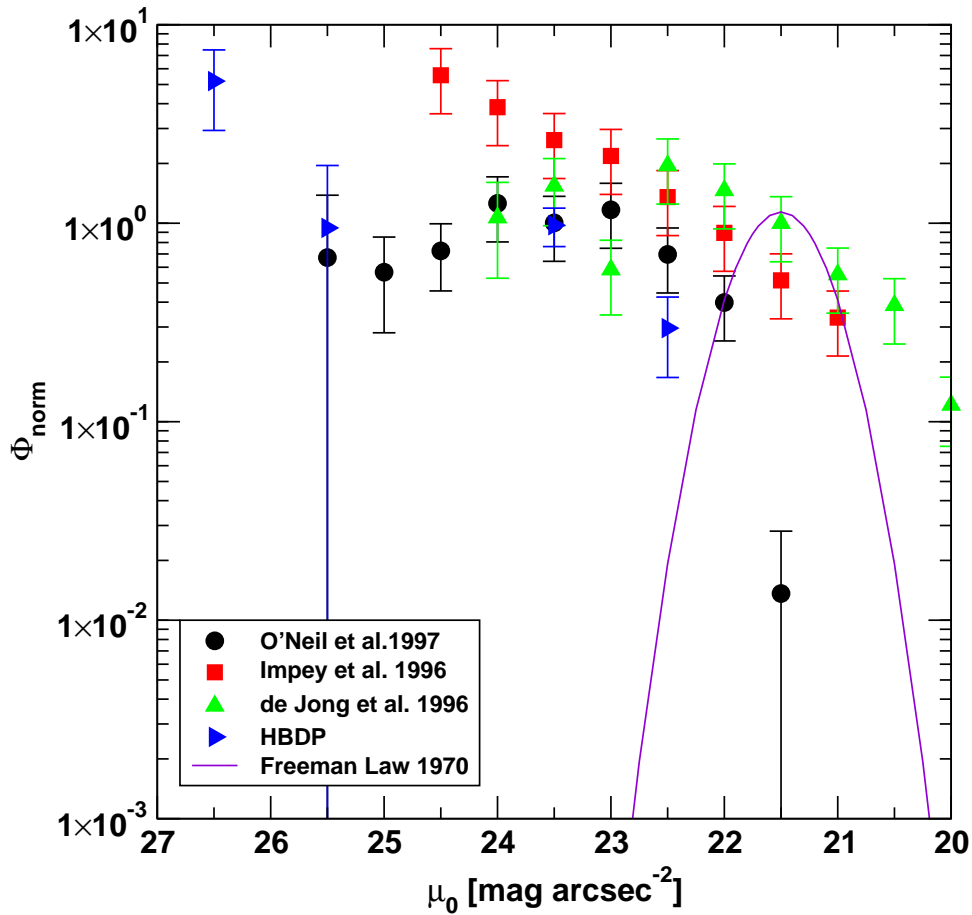


Figure 3.6: Surface brightness corrected volume densities for several samples of LSB galaxies and the HSB galaxy sample of de Jong (1996, green triangle). The LSB galaxy sample derived in the HDF-S is represented by the blue triangles. For a comparison, the distribution of the galaxies expected from the Freeman Law (Freeman, 1970, purple line) is plotted. The diagram shows that in contrast to the expected distribution of the Freeman Law, the distribution for the LSB galaxies stays flat down to very low central surface brightnesses.

surface brightness bin is slightly lower compared to the values of O'Neil et al. (1997a); Impey et al. (1996) and de Jong (1996). This is maybe the result of incompleteness at the upper surface brightness limit of the HDF-S sample ($\mu = 22.0 \text{ mag arcsec}^{-2}$). The Texas survey also shows an incompleteness around the Freeman value ($\mu = 21.5 \text{ mag arcsec}^{-2}$). The large error bar at $\mu = 25.5 \text{ mag arcsec}^{-2}$ results from low number statistic for this bin (1 LSB galaxy). However, the one object at this value and the two objects at the next bin ($\mu = 26.5 \text{ mag arcsec}^{-2}$) still have a big implication for the volume density, due to the low volume over which such very Low Surface Brightness galaxies could be found. This means that finding one of these extrem LSB galaxies in such a small field has a very low probability.

3.4 Conclusions and Summary

The results of spectroscopic follow up observations of a sample of LSB galaxy candidates, derived in a field around the HDF-S were presented. The spectroscopic data was obtained using the ESO 3.6 m telescope. By analyzing the observed spectra, distances could be estimated in the redshift range of $z \sim 0.05$ to $z \sim 0.16$. The majority of the observed HDF-S sample galaxies is located at redshifts below $z \leq 0.1$, which makes them real LSB galaxies. Using color-color diagrams, it could be shown that 71 % of the selected galaxies are genuine LSB galaxies. This indicates that using the location in the color-color diagrams is an efficient method in order to select the LSB galaxy content against higher redshifted background galaxies. In the color-color diagrams, the LSB galaxies are shifted to the blue region for the B-R and B-V color and to the red region for the U-B color. This different location in the color-color diagrams seems to be a hint for a different stellar population mix and therefore a different Star Formation History (SFH, see Sect. 4) of the selected LSB galaxies. The shifts could be caused by a stronger Balmer bump indicating a relatively young stellar population. The shift into the red region of the U-B color could result from a low UV flux due to a low formation rate of O, B, and A stars which produce a strong UV radiation. The blue shift of the B-R, and B-V color seems to indicate that there exists no strong underlying old stellar population which causes the red shift in the U-B color. To produce this blue shift, we need a more steep decline of the red part of the stellar continuum emission. Therefore, the red U-B color could also not be the result of a higher metallicity. In this case, the decline in the red part of the continuum emission must be shallower, caused by a stronger underlying old stellar population. Depletion of the U-flux due to a large amount of dust could also be excluded. Until now, there exist only a few detections of LSB galaxies in the FIR wavelength region on very low levels (Hoeppe et al., 1994).

The derived LSB sample consists of galaxies with radii between 10.5–32.4 kpc and absolute B-band magnitudes between $M_B = -16.90 \text{ mag}$ and $M_B = -19.06 \text{ mag}$ (see Tab. 3.5). From the absolute magnitudes, luminosities were derived in the range of $0.51 - 3.73 \cdot 10^9 L_\odot$. Therefore, the sample does not include dwarf galaxies, which is often expected for LSB galaxy samples. All galaxies have distances larger than $z = 0.05$. No nearby LSB galaxy could be found.

In the recent years, more sensitive surveys have shown that the Freeman Law (Freeman, 1970) was the result of selection effects (see Fig. 3.6). From these surveys, volume densi-

ties which stay flat down to central surface brightnesses of about $25.5 \text{ mag arcsec}^{-2}$ could be obtained. An estimation of the volume density for the HDF-S LSB sample indicate that the derived result is consistent with results found for these surveys (O'Neil et al., 1997a,b; Impey et al., 1996; de Jong, 1996). Additionally, the distribution could be expanded down to very low surface brightnesses of $\mu_0 = 27 \text{ mag arcsec}^{-2}$. It could be shown that the distribution stays flat also for these very low central surface brightnesses. From the results of the HDF-S LSB sample, it can be assumed that LSB galaxies represent a major contribution to the local galaxy population. O'Neil (2000) stated that if the distribution stays flat down to a central surface brightness around $30 \text{ mag arcsec}^{-2}$, up to 50% of the local galaxy population could consist of LSB galaxies. Therefore, the LSB galaxies play an important role for the understanding of the formation and evolution processes of galaxies in general.

Chapter 4

SFH of LSB galaxies in the HDF–S

In this section, results from a study of the Star Formation History of the LSB galaxy sample in the HDF–S will be presented. In order to derive the SFH, medium resolved spectra were used. The spectra were observed in the optical wavelength range from 3400 Å to 7500 Å. The SFHs for the sample will be obtained comparing these spectra to a library of nearly 3000 synthetic Spectral Energy Distributions (SED), created using the synthesis evolution model PÉGASE (Fioc & Rocca-Volmerange, 1997). The results will then be compared to the SFHs derived for the sample of HSB galaxies by Kennicutt (1992a). It will be shown that there exists a significant difference in the SFH between these two populations of galaxies. The LSB galaxies tend to have younger dominant stellar populations (< 5 Gyr). Therefore, they must undergo their major star formation event at much later stages ($z \sim 0.2$ to 0.4). This result is an indication that the LSB nature of the LSB galaxies could be the result of being relatively unevolved. Setting the results for the SFHs of LSBs in context to results of other studies, an evolutionary scenario, where the LSB galaxies are formed in the minimum phases of the large scale density fluctuation, will be presented.

4.1 Data and sample selection

In order to study the SFHs of LSB galaxies, spectroscopic data, derived from follow up observations of the HDF–S LSB galaxy sample, were used. For the galaxies, integrated spectra were obtained covering a spectral range from 3400 Å to 7500 Å. The aim of this spectroscopic observations was to derive distances of the HDF–S sample. In order to observe as many galaxies as possible, relatively short exposures times resulting in relatively low signal-to-noise ratios were used. You will find a more detailed description of the observation and the data reduction, as well as the flux calibration in Sect. 3.2. After the estimation of the redshifts for the photometrically selected sample, the central surface brightnesses were corrected for cosmological dimming effects (“Tolman Dimming”, see Sect. 3.1). This correction resulted in a sample of 7 true LSB galaxies. The sample consists of 5 LSB galaxies which were selected using the color-color method (see. Sect. 3.1) and two additional galaxies, randomly selected from the subsample of the HDF–S galaxies for which no multi-color information were available. For this two galaxies,

spectroscopic observations were also obtained. After the distance estimation ($z < 0.1$), they turned out to be also true LSB galaxies. The following discussion will be concentrated on the spectroscopically confirmed sample of 7 LSB galaxies.

In contrast to many other spectroscopic studies of LSB galaxies –which are focussed on the properties of the bright HII regions (e.g., McGaugh, 1991; de Blok & van der Hulst, 1998a)–, the aim of this project is the extraction of global properties of the sample galaxies. Therefore, integrated spectra were taken, summing up all information along the spatial axis of the slit which was positioned along the major axis of each galaxy (see figures in App. A). Due to the integration along the spatial axis, additionally the signal-to-noise ratios will be increased. In a next step, the spectra were smoothed along the dispersion axis by a factor of 4, resulting in a spectral resolution of $\sim 16 \text{ \AA}$ per pixel. With this spectral resolution, the integrated spectra match the spectral resolution of the synthetic spectra ($\Delta\lambda = 20 \text{ \AA}$ in the optical wavelength range) obtained from the synthesis evolution model PÉGASE (Fioc & Rocca-Volmerange, 1997). After summing up the spectra along the spatial and smoothing them along the dispersion axis, the signal-to-noise ratios are high enough to detect in most cases the important absorption lines, e.g., Balmer lines, CaII doublet, CN-band. Due to the fact that the synthetic SEDs provided by PÉGASE are calculated for a redshift $z = 0$, a Doppler correction according to the redshift of the individual LSB galaxies was applied.

4.2 PÉGASE

4.2.1 Stellar Population Synthesis

The discussion about the basics of synthesis evolution modeling is mainly based on the paper of Fioc & Rocca-Volmerange (1997) and the manual of PÉGASE itself. First attempts in order to describe the spectrophotometric evolution of galaxies were made comparing linear combinations of stellar spectra of different stellar types to spectra of galaxies (e.g., Spinrad & Taylor, 1971; Faber, 1972). First simple synthesis models (e.g., Tinsley, 1972a; Searle et al., 1973) were then developed in order to explain the broad band colors of galaxies and derive their ages. Over the last decade, stellar population synthesis has become a standard method for studying the evolution of galaxies (e.g., Charlot & Bruzual, 1991; Bruzual & Charlot, 2003; Fioc & Rocca-Volmerange, 1997). In contrast to direct isochrone fitting methods applied to resolved stellar populations, synthesis evolution models derive evolutionary stages of stellar populations by using just integrated spectrophotometric measurements. With the direct isochrone fitting method, one compares evolutionary tracks of stars in the mass range $[m_l, m_u]$ with a certain metallicity and a certain age θ_i to measure the positions of stars in Color–Magnitude Diagrams (CMDs):

$$F_\lambda = \int_{m_l}^{m_u} \Phi(m) f_\lambda(m, \theta_i) dm \quad (4.1)$$

The distribution of stellar masses in the range between the lower mass limit m_l and the upper mass limit m_u is described by the Initial Mass Function (IMF). The direct comparison of

isochrones to the positions of stars in the CMD could only be used for objects which could be resolved into single stars (star clusters in the Milky Way, nearby galaxies). For galaxies, this method only works out to a distance of ~ 6 Mpc. At this distance, galaxies could be resolved into single stars using high resolution space based observations, e.g., from the Hubble Space Telescope (HST). The synthesis evolution models are rather aimed at the extraction of information from integrated spectrophotometric observations of ensembles of stars of various masses and metallicities in the theoretical CMD. Once the position of every star in the CMD is known, integrated spectra are produced by adding up spectra of the individual stars. For synthesis models, the monochromatic flux at wavelength λ of a galaxy with age t can then be calculated by:

$$F_{\lambda} = \int_0^t \int_{m_l}^{m_u} \tau(t - \theta) \Phi(m) f_{\lambda}(m, \theta) dm d\theta \quad (4.2)$$

In Eqn. 4.2, $\tau(t - \theta)$ –the Star Formation Rate (SFR)– describes the mass in units of solar masses M_{\odot} formed at the time $t - \theta$. How many stars in the range between lower and upper mass limit $[m_l, m_u]$ are formed is described by the IMF $\Phi(m)$. The monochromatic flux of a star at wavelength λ , with an initial mass m and at the age since the Zero Age Main Sequence (ZAMS) θ is represented by $f_{\lambda}(m, \theta)$. A discretization of both integrals leads to an oscillation of the emitted light (Charlot & Bruzual, 1991; Fioc & Rocca-Volmerange, 1997) due to fast evolutionary phases (e.g. TP-AGB, massive red supergiants). The most common way to solve this double integral is the discretization of the integral on time:

$$F_{\lambda} = \sum_{i=1}^{p-1} \tau(t - \theta_i) (\theta_{i+1} - \theta_i) \int_{m_l}^{m_u} \Phi(m) f_{\lambda}(m, \theta_i) dm \quad (4.3)$$

This so called isochrone method keeps the time fixed and integrates the monochromatic stellar flux $f_{\lambda}(m, \theta_i)$ at wavelength λ over all stellar masses between lower mass limit m_l and upper mass limit m_u . Again, the distribution of stellar masses in the range $[m_l, m_u]$ is described by the IFM $\Phi(m)$. The isochrone method has the benefit that isochrones are directly comparable to CMDs measured for stellar populations (e.g., globular clusters).

4.2.2 Parameter Study

For the study of the SFHs of the HDF–S LSB galaxy sample, the synthesis evolution model PÉGASE (Fioc & Rocca-Volmerange, 1997) was used. As a first step, a detailed parameter study was carried out in order to understand the influence of the individual parameters of PÉGASE on the resulting synthetic SEDs. The parameter study will be described in more detail in the following paragraphs. The synthetic spectra, resulting from the parameter study, will then build up a library which will be used in order to estimate the ages of the galaxy samples. The library only consists of synthetic SEDs where the variation of a certain parameter shows a significant effect on the computed SED in comparison to the measured spectra of the HDF–S LSB galaxy sample. Due to the fact that all masses used within the PÉGASE model are normalized to $1 M_{\odot}$, it is not possible to directly compare the fluxes of the measured spectra of the galaxies

to the modeled SEDs. In order to make this comparison, the flux of the measured spectra and the synthetic SEDs are normalized to the flux at 5500 Å rest frame wavelength. At this wavelength, the spectra of galaxies only show continuum emission and no absorption or emission line features. The normalization does not depend on the strength of the spectral features, which could be different for different types of galaxies. In the following, the parameters which are used to build up the synthetic library are described in detail. The description is based on the manual of PÉGASE as well as on Fioc & Rocca-Volmerange (1997). Synthetic SEDs which illustrate the change in the spectra for certain varied parameters are shown in App. B.

Initial Mass Function (IMF): The Initial Mass Function is a quantity describing the distribution in the numbers of stellar masses in the range $[M, M + dM]$ formed in a star formation event. A common description of the IMF is a parameterization as a power law.

The PÉGASE model provides the user with a broad range of parameterizations of the IMF. Some of these parameterizations are included in the PÉGASE model in an analytical form (e.g., Miller & Scalo, 1979; Rana & Basu, 1992; Ferrini et al., 1990, see Fig 4.2 lower panel).

log-normal IMF (Miller & Scalo, 1979):

$$dn = dn \cdot 10^{\left(-\frac{m^2}{2} - m\right)} \quad (4.4)$$

Ferrini (1991):

$$dn = dn \cdot 10^{\left(-0.52m - \sqrt{2.07m^2 + 1.92m + 0.73}\right)} \quad (4.5)$$

Rana & Basu (1992):

$$dn = dn \cdot 10^{\left(1.548 - 1.513m - 0.395m^2 + 0.502m^3 - 0.169m^4\right)} \quad (4.6)$$

Other parameterizations of the IMF are included in a numerical form (e.g., Kennicutt, 1983; Kroupa et al., 1993; Miller & Scalo, 1979; Salpeter, 1955, see Fig 4.1, upper panel).

Salpeter (1955):

$$\Psi \sim m^{-2.35} \quad (4.7)$$

Miller & Scalo (1979):

$$\begin{aligned} \Psi &\sim m^{-1.4} && (0.1 M_{\odot} < m < 1 M_{\odot}) \\ &\sim m^{-2.5} && (1 M_{\odot} < m < 10 M_{\odot}) \\ &\sim m^{-3.3} && (10 M_{\odot} < m < 100 M_{\odot}) \end{aligned} \quad (4.8)$$

Kennicutt (1983):

$$\begin{aligned} \Psi &\sim m^{-1.4} && (0.1 M_{\odot} \leq m \leq 1 M_{\odot}) \\ &\sim m^{-2.5} && (1 M_{\odot} \leq m \leq 100 M_{\odot}) \end{aligned} \quad (4.9)$$

Scalo (1986):

$$\Psi \sim m^x \quad (4.10)$$

M/M_{\odot}	x
0.1	3.200
0.11	2.455
0.14	2.000
0.18	0.300
0.22	0.000
0.29	0.000
0.36	-0.556
0.45	-1.625
0.54	-1.833
0.62	-1.286
0.72	1.500
0.83	-1.857
0.98	0.000
1.17	-2.333
1.45	-3.455
1.86	-1.692
2.51	-2.571
3.47	-1.722
5.25	-1.611
7.94	-1.667
12.02	-2.333
18.20	-1.353
26.92	-0.947
41.69	-1.778
120.00	-1.778

Kroupa (1993):

$$\Psi \sim m^{-1.2} \quad (0.1 M_{\odot} \leq m \leq 0.5 M_{\odot}) \quad (4.11)$$

$$\begin{aligned} &\sim m^{-2.2} && (0.5 M_{\odot} \leq m \leq 1 M_{\odot}) \\ &\sim m^{-3.3} && (1 M_{\odot} \leq m \leq 120 M_{\odot}) \end{aligned}$$

Scalo (1998):

$$\begin{aligned} \Psi &\sim m^{-1.2} && (0.1 M_{\odot} \leq m \leq 1 M_{\odot}) && (4.12) \\ &\sim m^{-2.7} && (1 M_{\odot} \leq m \leq 10 M_{\odot}) \\ &\sim m^{-3.3} && (10 M_{\odot} \leq m \leq 120 M_{\odot}) \end{aligned}$$

In order to figure out how the changes of the parameterization of the IMF influence the final

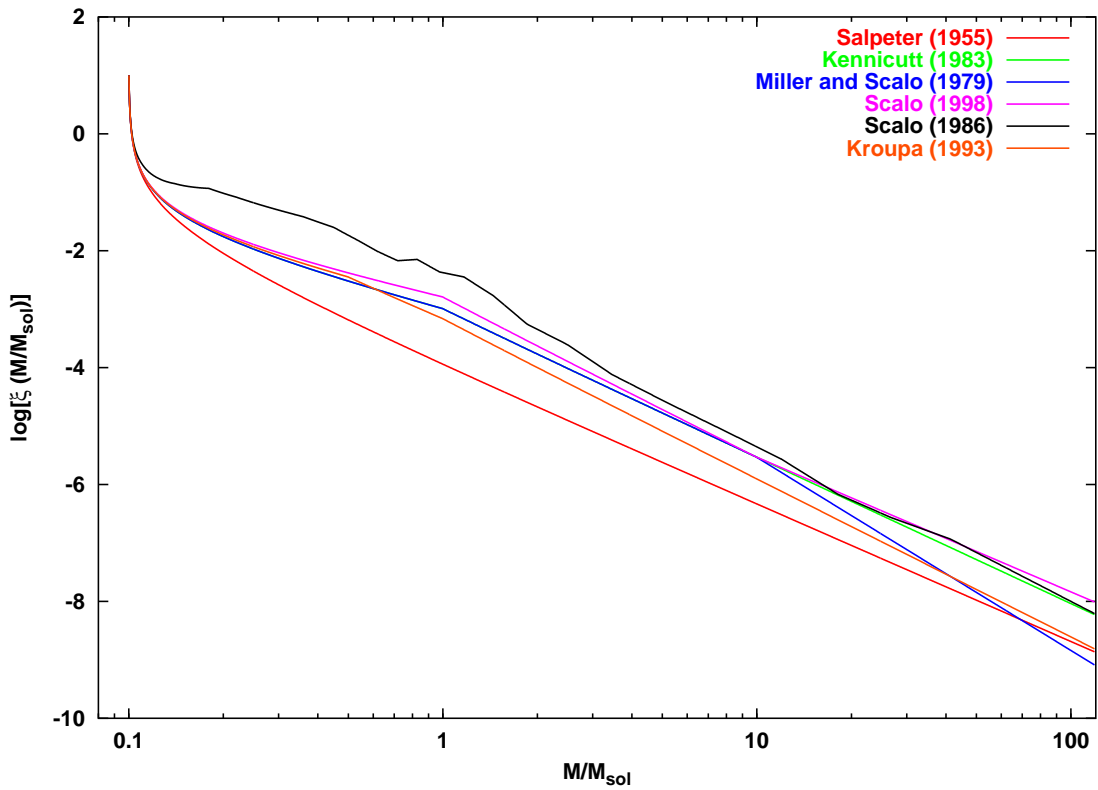


Figure 4.1: Different IMFs which are used with numerical solutions within the PÉGASE synthesis evolution model.

spectra, a comparison of spectra computed for different IMFs, different SFLaws and different ages was made (see App. B.1 to B.4). The most common IMF used for calculations of galaxy spectra is the parameterization of Salpeter (1955, see Fig 4.2, upper panel red line). Compared to the Salpeter IMF, all other parameterizations included in the PÉGASE model produce a higher number of low mass stars and a smaller number of high mass stars. However, this different weighting results in only slight variations in the optical wavelength range (3400 Å–7400 Å), taking place in the bluest parts of the spectra (~ 3400 Å). In this wavelength range, the

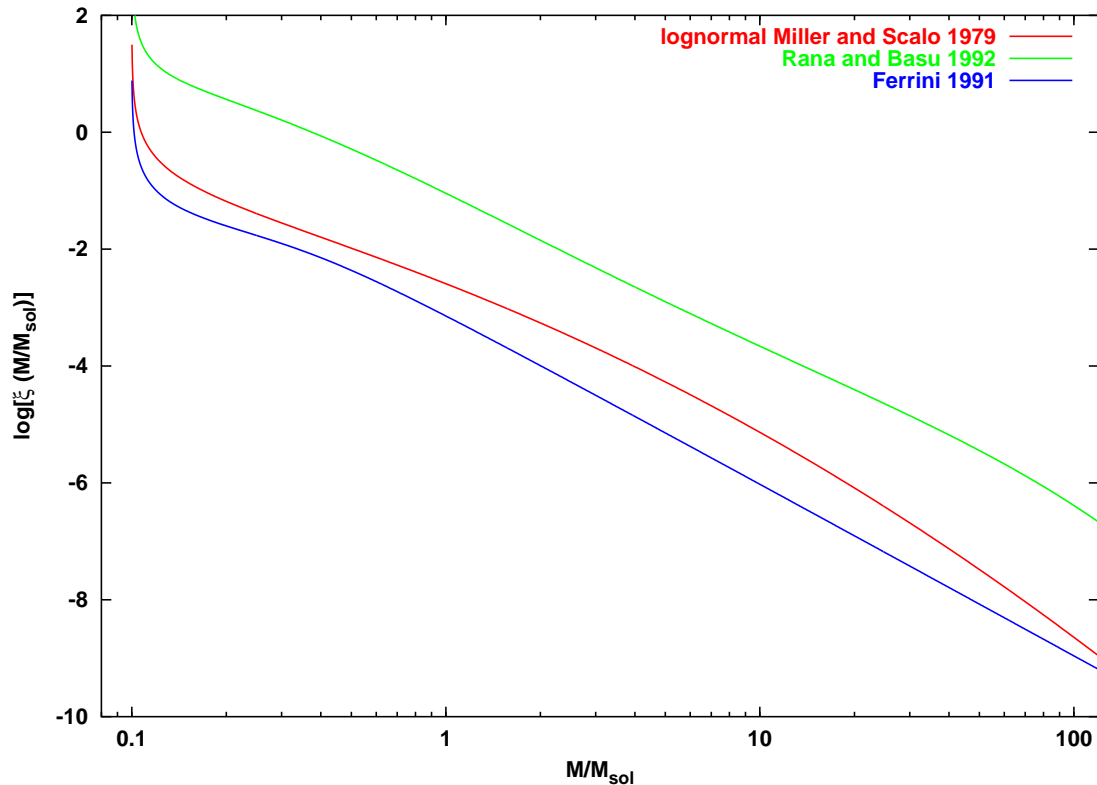


Figure 4.2: Different IMFs for which analytical solutions are used within the PÉGASE model.

spectra which were computed by using the Salpeter IMF show the highest flux values. Using an exponential SFLaw, no variation is visible at all (see App. B.3). In the young spectra where the high mass stars dominate the UV part, the variations are strongest. They become smaller for the older ones where the older, lower mass stars dominate the spectra. From the comparison, it became clear that the variations due to the use of different IMFs are small with respect to the noise pattern of the measured LSB galaxy spectra (see Fig. 4.3). This parameter will be kept fixed. Therefore, the parameterization of the IMF of Salpeter (1955) will be used in the following studies.

Lower and Upper Mass Limit: The range of stellar masses formed in the star formation processes in galaxies is an important parameter influencing the shape of the spectra of the galaxies. High mass stars ($\geq 10 M_{\odot}$) are observed to have high temperatures and a large energy release in the UV and blue wavelength range. Their life times are relatively short (several Myrs) compared to cooler low mass stars which release a large fraction of their energy in the red wavelength range. Therefore, spectra of young or star bursting galaxies are dominated by hot high mass stars which e.g., produce a prominent Balmer bump. The spectra of evolved galaxies are mostly dominated by cooler low mass stars. In these spectra, metal absorption lines as well

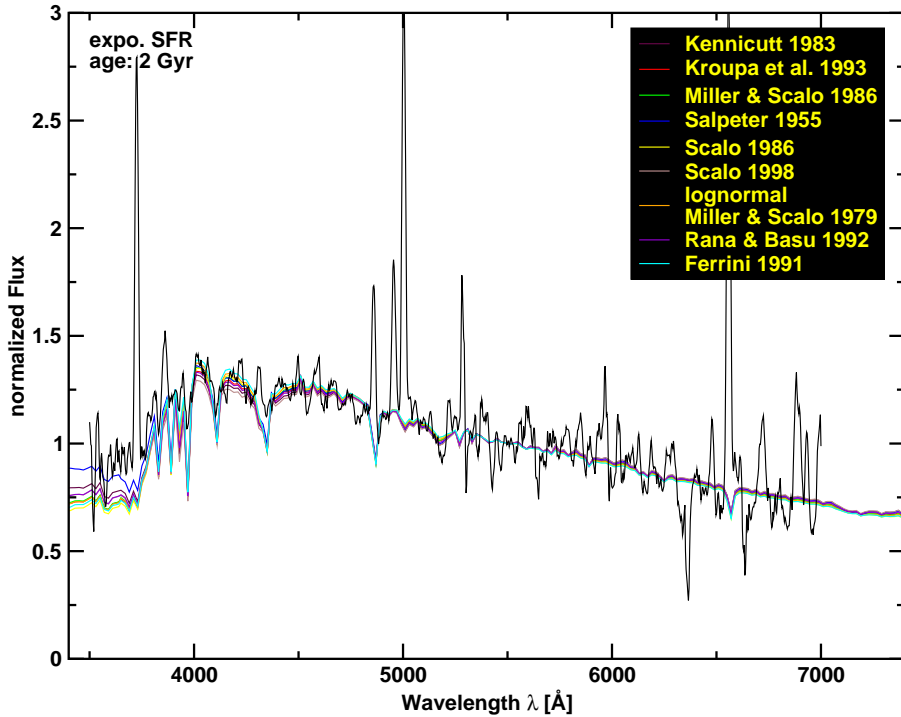


Figure 4.3: SEDs modeled by using different IMFs and overlaid to a typical spectrum of a HDF-S LSB galaxy (HBDP22325-60155). In comparison to the noise pattern of the measured spectrum, no significant differences are visible in the optical wavelength range between the SEDs modeled by using different IMFs. The used SEDs have ages of 2 Gyr and were modeled for an exponential decreasing SFR with a decay time $\tau = 1400$ Myr.

as a strong red continuum emission are visible. In order to test the influence of the stellar mass on the spectra, a comparison of different synthetic SEDs using different upper ($7 M_{\odot}$, $10 M_{\odot}$, $30 M_{\odot}$, $50 M_{\odot}$, and $80 M_{\odot}$) and lower mass limits ($0.08 M_{\odot}$ and $1 M_{\odot}$) was performed. The synthetic spectra were computed for different SFLaws (constant SFR, star burst, exponential SFR and power law) and plotted for different ages (500 Myr, 1 Gyr, 10 Gyr). As for the IMF, the use of different upper and lower mass limits results in only slight variations between most of the different synthetic SEDs. The variations are again strongest in the blue part of the spectra. The variations also become smaller with increasing ages of the SEDs (see App. B.5 to B.8). Using the star burst scenario, no variation for most of the mass ranges is visible (see App. B.7). The use of the mass range $1 M_{\odot}$ to $120 M_{\odot}$ in combination with the star burst scenario results in a different shape for the 10 Gyr old SED. For this SED, only continuum emission and no spectral features (Balmer bump, absorption lines) are visible in the optical wavelength range (see App. B.7 lower panel). This different shape results from the fact that after 10 Gyr all stars above $1 M_{\odot}$ reach the final phase of their evolution. Therefore, only the continuum emission of stellar remnants contributes to the galaxy spectrum. On the first look, it seems

that the variations in the blue part of the optical spectrum are large enough to discriminate between the different scenarios using different mass limits (see Fig. B.5 – B.8). However, the largest variations are visible for the models using upper mass limits of $10 M_{\odot}$ (magenta line) and $7 M_{\odot}$ (dark green line). Forming a galaxy with these mass limits is not very realistic. No O and B stars would be formed and therefore, not enough energy will be released in order to ionize the ISM. Observations of the ionized hydrogen show the existence of ionized regions (so called HII–Regions) in HSB as well as in LSB galaxies. Another special case is the model using a lower mass limit for stars to be formed of $1 M_{\odot}$. In this case, no stars older than 10 Gyr exit. Depending on the star formation law (const. SFR, star burst, expon. SFR, power law), there is much more emission in the blue or the red part of the spectrum of the 10 Gyr old SEDs (see Fig. B.5 – B.8). One extreme case is the star burst scenario (see Fig. B.6, lower panel) where all stars are formed in a single event at the beginning of the evolution of the galaxy. After 10 Gyr, all stars reach their final evolutionary stages (SNe, White Dwarf, etc.), and only the continuum emission of the stellar remnants is detectable. The model of a galaxy only forming stars with masses above $1 M_{\odot}$ is again relatively unrealistic, especially for LSB galaxies where we assume that star formation processes occur in small molecular clouds, due to low gas surface densities. Due to the small variations for the other model SEDs resulting from changes of the lower and upper mass limit (see Fig. 4.4), the mass limit will also be kept fixed. For the following analysis, a lower limit of $0.08 M_{\odot}$ and an upper limit of $80 M_{\odot}$ will be used.

Star Formation Law and Star Formation Rates: The Star Formation Law is one of the important parameters defining the shape of the modeled SEDs. Using the PÉGASE model, one can choose between four different implemented star formation laws (see Fig. 4.5).

First of all a continuous star formation rate is given by:

$$\begin{aligned} \text{SFR}(t) &= p_1 & \text{if } t \leq p_2 \\ &= 0 & \text{if } t > p_2 \end{aligned} \quad (4.13)$$

$$[p_1] = M_{\odot} \text{Myr}^{-1}; \quad [p_2] = \text{Myr}$$

In this case, the galaxies form the same amount of stars p_1 at every time until the end of the given time interval for star formation p_2 (see Fig. 4.6). This leads to a relatively prominent Balmer bump, also in the late stages of the evolution of galaxies (see Fig B.9 lower panel). The strength of spectral features like the Balmer bump depends on the Star Formation Rate in the late stages of the galaxy evolution. The features are strongest for low star formation rates. Thereby, the formation of several O and B stars have a strong effect on the spectrum which is mainly dominated by old evolved low mass stars. In the star burst scenario, all stars are formed in the beginning of the evolution of the galaxies in one single event. After this event, no other stars are formed:

$$\text{SFR}(t) = \delta(t) \quad (4.14)$$

The shape of the synthetic spectrum only changes due to the evolution of the formed stars. With increasing age, spectral features in the blue part of the SED become less prominent.

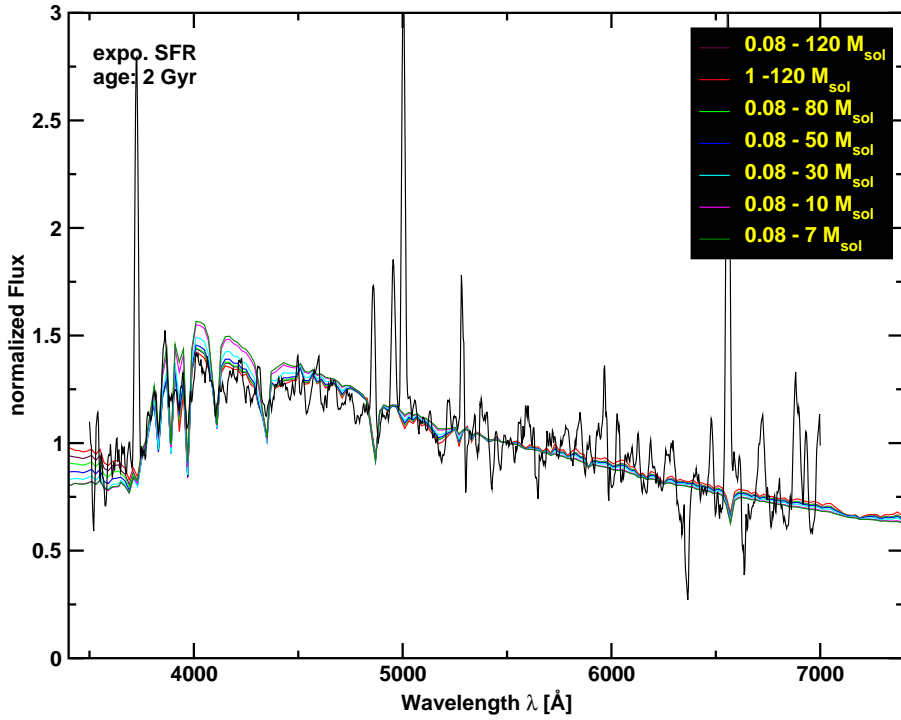


Figure 4.4: Comparison between a typical measured spectrum of the HDF-S LSB galaxies (HBDP22325-60155) and SEDs modeled using different lower and upper mass limits. No significant differences are visible compared to the typical noise pattern of the measured spectra for most of the used mass limits. The used SEDs have ages of 2 Gyr and were modeled for an exponential decreasing SFR with a decay time $\tau = 1400$ Myr.

The hydrogen absorption lines fade away and the metal absorption lines become visible. In the red part of the spectrum, the continuum emission becomes stronger. For an exponential decreasing star formation rate, the galaxy forms stars over the whole life time of the galaxy. The star formation rate is highest in the beginning of the evolution of the galaxy and decreases exponentially with increasing age:

$$\text{SFR}(t) = p_2 \cdot \frac{\exp\left(-\frac{t}{p_1}\right)}{p_1} \quad (4.15)$$

$$[p_1] = \text{Myr}; \quad [p_2] = M_\odot$$

The strength of the star formation is defined by the decay time p_1 and the mass p_2 which is available for star formation in the beginning of the evolution of the galaxy (see Fig. 4.7). In the early evolution stages of the galaxy, the synthetic SEDs show a strong Balmer bump in the blue part of the spectrum as well as strong hydrogen absorption lines. At late evolutionary stages, the Balmer bump becomes less prominent. The hydrogen absorption lines fade away and again

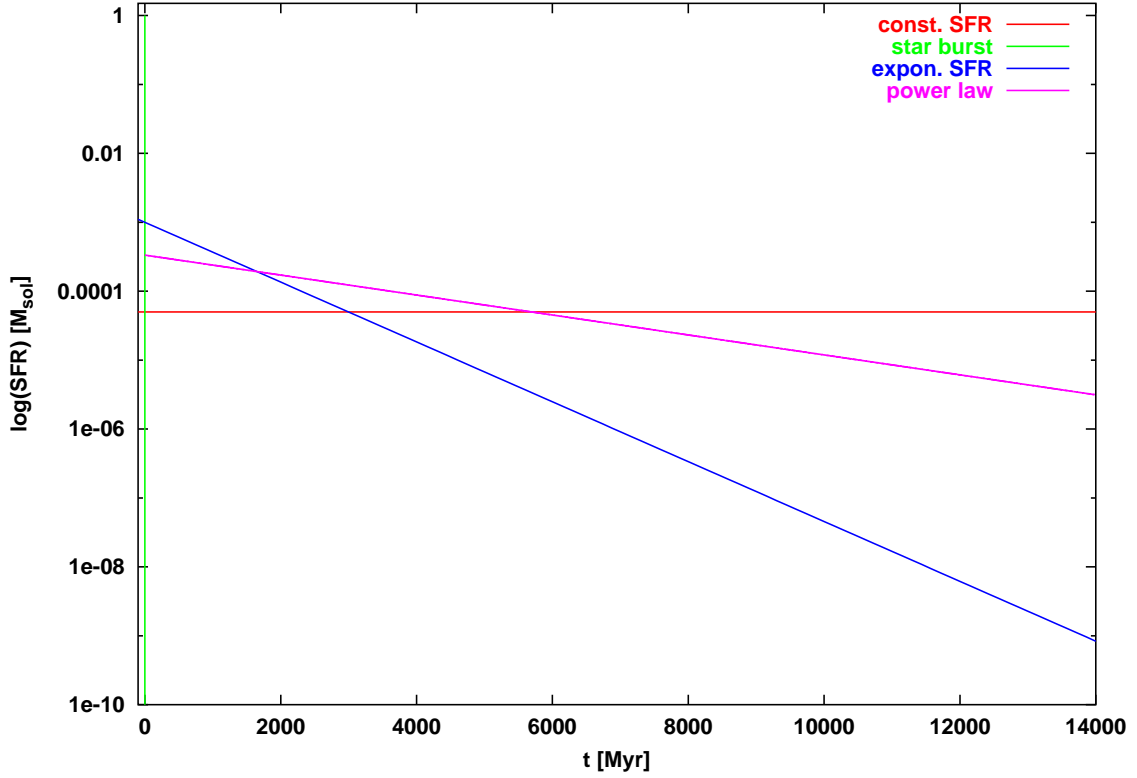


Figure 4.5: Examples for the 4 different star formation laws (SFLaw) used within PÉGASE.

the metal absorption lines become visible (see Fig. B.9). The strength of the star formation is defined by the decay time (see Fig. 4.7). For short decay times (several hundred Myrs), the star formation is very high in the beginning of the evolution, and shows a steep decrease after several Gyr. In the end of the evolution of the galaxy, the SFR becomes very low. For long decay times (several Gyr), the star formation is relatively low in the beginning and shows a very low decrease with increasing age. For very long decay times ($t \geq 5$ Gyr), the star formation is nearly constant. In the early evolutionary stages of the galaxy, differences between the SEDs, resulting from the use of different decay times, became only visible in the very blue part of the spectra (below $\sim 3700 \text{ \AA}$). In the late stages of the galaxy evolution, clear differences between the SEDs exist, calculated by using different decay times.

A similar behavior can be seen for a synthetic SED calculated by using a star formation rate following a power law (see Fig B.12). The SFR depends strongly on the time p_2 needed to transform one solar mass of gas into stars and the exponent p_1 with which the available amount of gas is decreasing (see Fig. 4.8 to 4.10):

$$\text{SFR}(t) = \frac{M_{\text{gas}}^{p_1}(t)}{p_2} \quad (4.16)$$

$$[p_1] = 1; \quad [p_2] = \text{Myr } M_{\odot}^{-1}$$

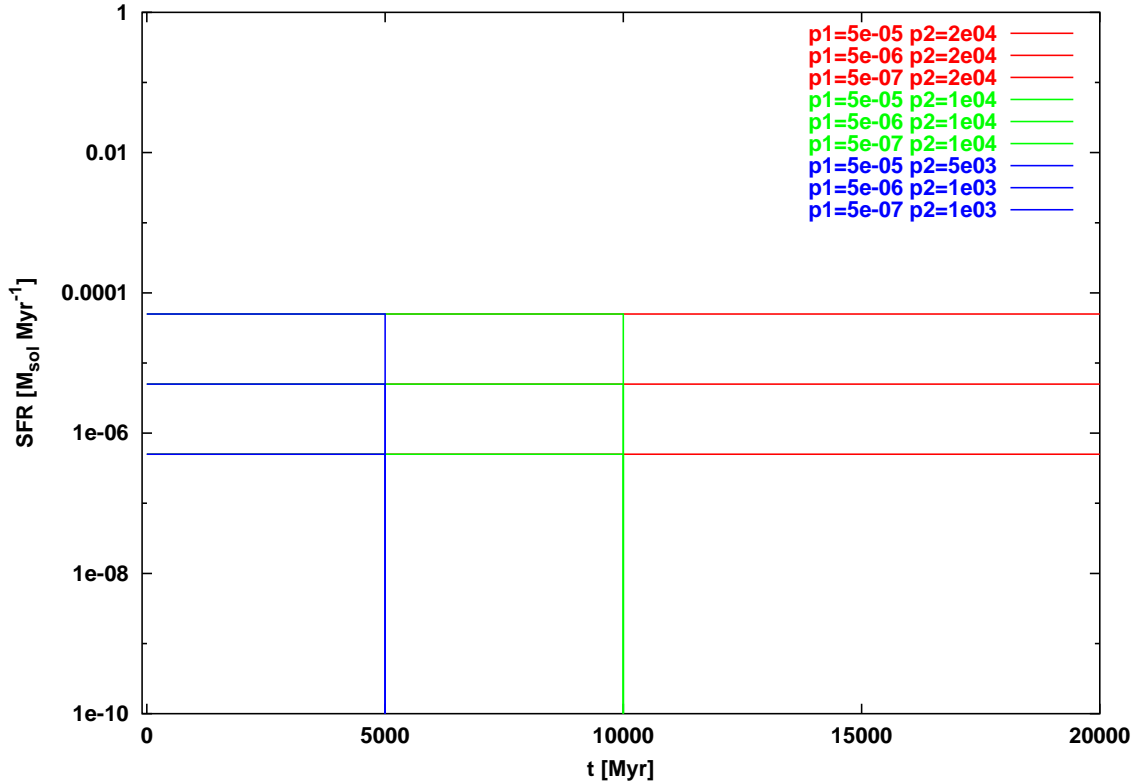


Figure 4.6: Constant SFR modeled using different values for the strength of SFR p_1 ($M_{\odot}\text{Myr}^{-1}$) and the duration p_2 (Myr) of the star formation.

Compared to an exponential decreasing SFR in the earlier evolution stages of the galaxy (until ~ 1 Gyr), the power law produces a more prominent Balmer bump as well a lower continuum emission in the red part of the spectrum. The effect of using different parameter for the power law is very small in the beginning of the evolution of the galaxy (see Fig. B.12, upper panel) and is visible after several Gyrs of evolution (see Fig. B.12, lower panel).

Extinction: The final parameter which will be discussed here is the extinction. The effect of the extinction on the shape of the SEDs strongly depends on the geometry of the distribution of dust. Within PÉGASE, one can choose between three different dust geometries included in the model (spheroidal distribution, disk geometry with an averaged inclination or for a specific inclination angle i). Additionally to the geometry of the dust, the distribution of stars and their composition which depends on the metallicity Z influence the dust properties. The evolution of metallicities Z is modeled from the SNII ejecta models of Woosley & Weaver (1995). The effect of SNIa, intermediated and low mass stars on the metallicity is neglected. The following parameterization for the net yields m_Z , based on the Woosley & Weaver (1995)

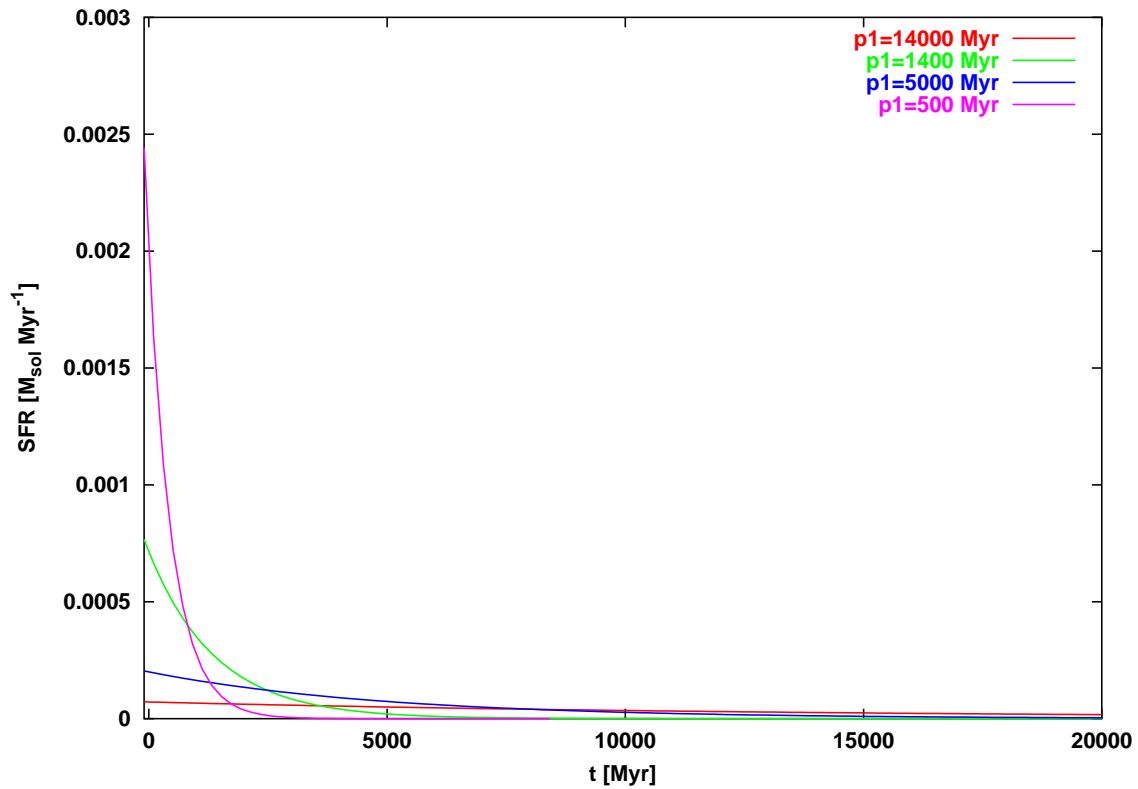


Figure 4.7: Exponential SFR modeled by using different decay times τ (parameter p1).

models ($Z = 0.001$ and $Z = 0.02$) is used:

$$\begin{aligned}
 m_Z &= 0 & \text{if } m &\leq 10.2 M_{\odot} & (4.17) \\
 m_Z &= 0.223 m - 2.27 & \text{if } 10.2 M_{\odot} &\leq m \leq 18.8 M_{\odot} \\
 m_Z &= 0.401 m - 5.62 & \text{if } 18.8 M_{\odot} &\leq m \leq 30.9 M_{\odot} \\
 m_Z &= 0.00896 m - 4 & \text{if } 30.9 M_{\odot} &\leq m
 \end{aligned}$$

The dust effects for a disk geometry are modeled following the scattering model by Calzetti et al. (1994). This model is a combination of isotropic and forward-only scattering accounting for anisotropy. For the PÉGASE synthesis model, the extinction is computed for a model where dust and ionizing sources are mixed (see Fig. 4.11). The radiative transfer in a plane-parallel slab is described by:

$$\cos \theta \frac{dI_{\lambda}}{dz} = -\kappa_{\lambda} I_{\lambda} + \epsilon_{\lambda} + \kappa_{\lambda} \frac{\omega_{\lambda}}{4\pi} \int I_{\lambda} \Phi(\cos \Theta) d\Omega \quad (4.18)$$

θ is the angle perpendicular to the plane and the line of sight, I_{λ} is the radiated intensity, κ_{λ} is the extinction coefficient of the dust combined of the absorption and the scattering coefficients, ϵ_{λ} is the emissivity of the source, ω_{λ} is the albedo of the dust particles, $\Phi(\cos \Theta)$ is their phase

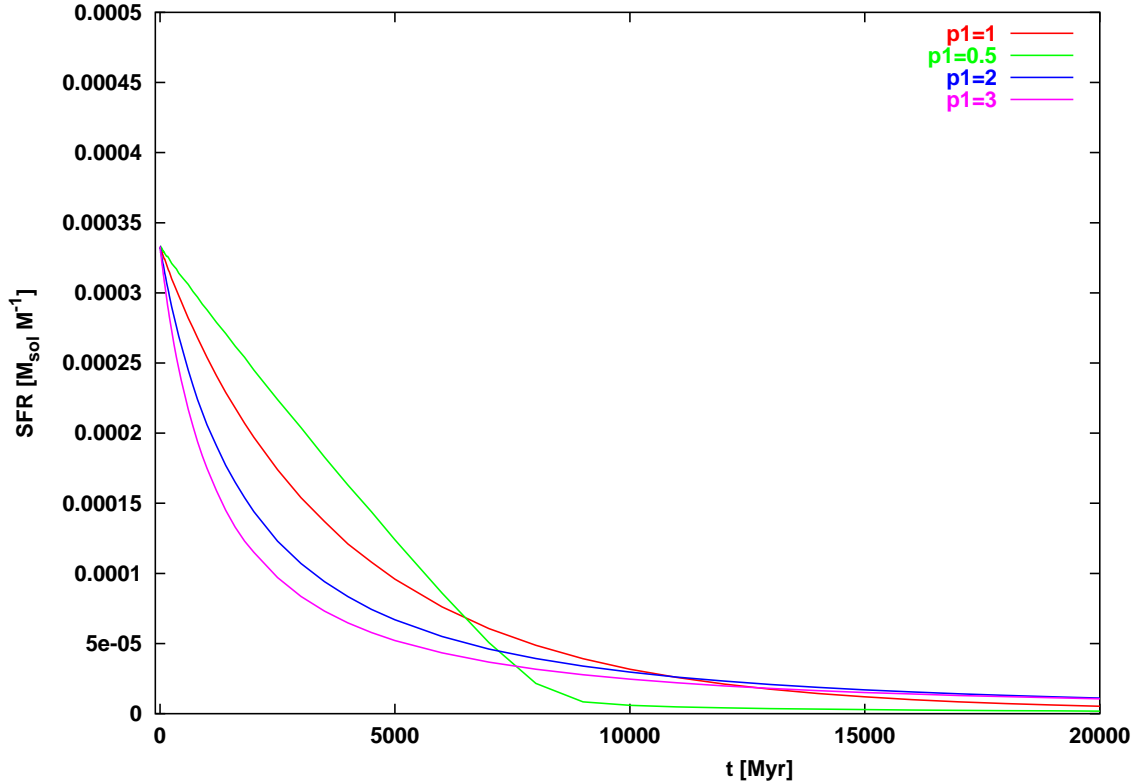


Figure 4.8: SFR following power law modeled by using different values for the parameter $p1$. The parameter $p2$ is fixed to $p2 = 3 \cdot 10^3 \text{ Myr } M_{\odot}$.

function, and $d\Omega = d \cos \theta d\phi$ is the solid angle as seen from the dust particle. The albedo is defined as the ratio of scattering coefficient to the extinction coefficient. The phase function describes the probability of a photon to be scattered in a certain direction. For the case that radiating sources and dust are mixed ($\epsilon(\lambda) = \text{constant}$), scattering is effective by removing photons along the line of sight. The solution of equation 4.18 is:

$$I_{\lambda} = I_{\lambda}^0 \frac{1 - \exp(-\tau_{\text{sc}}(\lambda))}{\tau_{\text{sc}}(\lambda)} = I_{\lambda}^0 \gamma(\lambda) \quad (4.19)$$

For more details see Calzetti et al. (1994). In order to include dust effects for disks, the extinction is modeled by a plan-parallel slab with inclination i (Guiderdoni & Rocca-Volmerange, 1987):

$$A_{i\lambda} = -2.5 \log \left(\frac{1 - \exp(-\tau_{\text{sc}} \sec(i))}{\tau_{\text{sc}} \sec(i)} \right), \quad (4.20)$$

where τ_{sc} is derived from the phase function $\Phi(\cos \Theta)$ (see Calzetti et al., 1994):

$$\tau_{\text{sc}} = (h_{\lambda} (1 - \omega_{\lambda})^{1/2} + (1 - h_{\lambda}) (1 - \omega_{\lambda})) \tau_{\lambda} \quad (4.21)$$

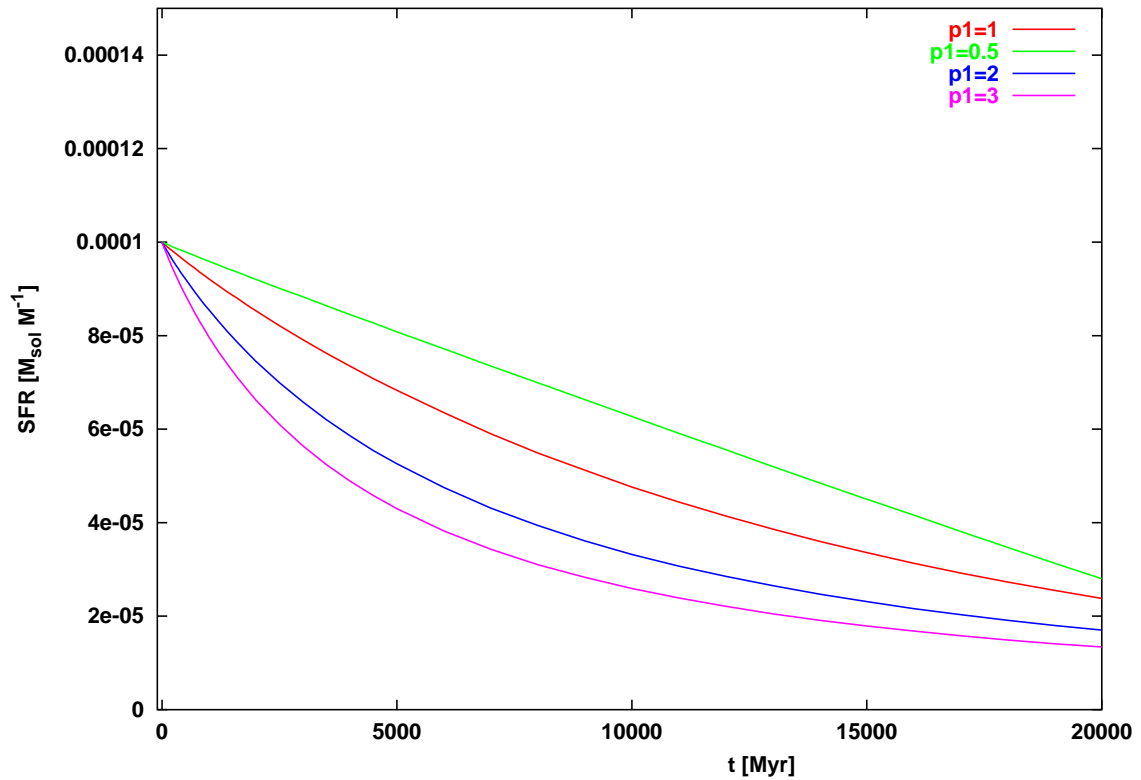


Figure 4.9: SFR following a power law modeled by using different values for the parameter p_1 . The parameter p_2 is fixed to $p_2 = 1 \cdot 10^4 \text{ Myr } M_\odot$.

The modeling of extinction in spheroids is much more complicated. First, one had to specify the distribution of stars and dust. Due to the fact that the inner regions of ellipticals (spheroidal geometry) are more effected by dust, Fioc & Rocca-Volmerange (1997) use a King model in order to describe the distribution of stars (King, 1962):

$$\rho_* \left(\frac{r}{r_c} \right) = \rho_{*,0} \left(1 + \left(\frac{r}{r_c} \right)^2 \right)^{-3/2} \quad \text{if } r < r_t \quad (4.22)$$

$$0 \quad \text{if } r > r_t$$

r_t is the distance from the center to which the tidal force of the system is effective. The distribution of gas in spheroidal shaped galaxies is described by a density proportional to the density of the stars with a power of n :

$$\rho_{\text{dust}} \sim \rho_{\text{stars}}^n \quad (4.23)$$

Fioc & Rocca-Volmerange (1997) found the exponent n to be $n \sim 1/2$ assuming a constant dust-to-gas ratio. The flux reduced due to the dust is described by Eqn. 4.24. In Eqn. 4.24, the reduced flux F is expressed in cylindrical coordinates, $z_t = (r_t^2 - R^2)^{1/2}$, $r = (R^2 + z^2)^{1/2}$,

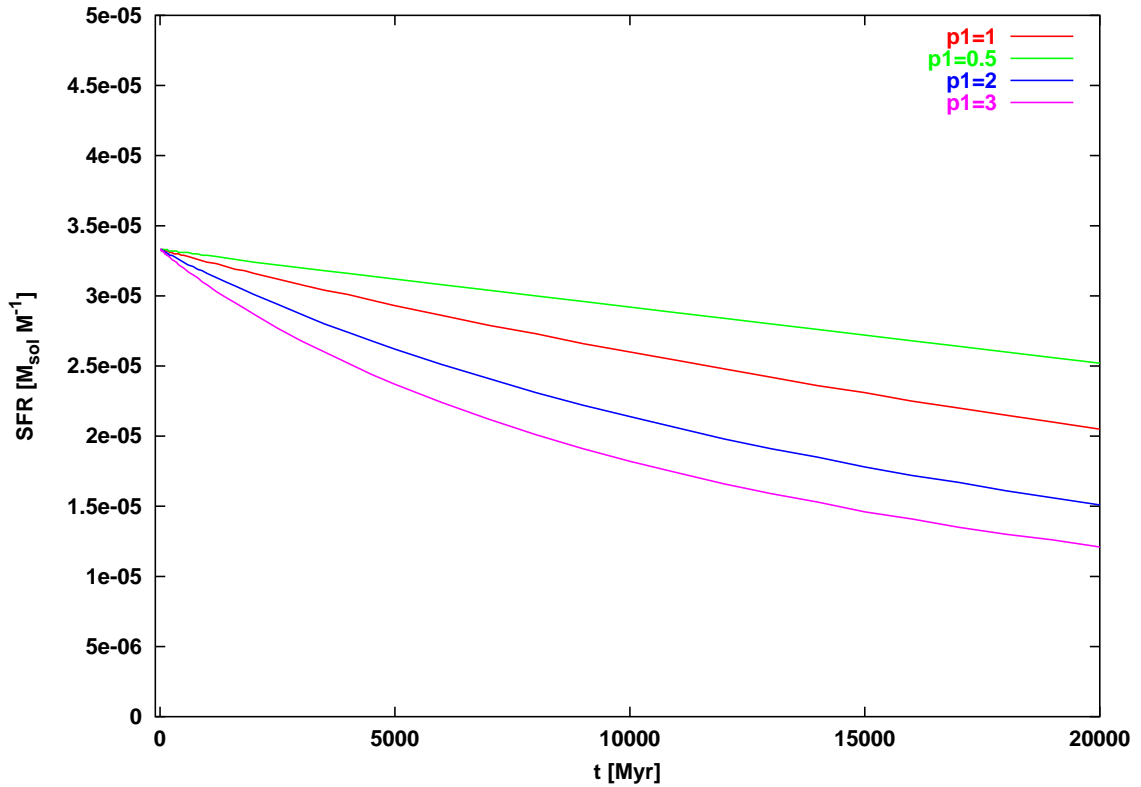


Figure 4.10: SFR following a power law modeled by using different values for the parameter p_1 . The parameter p_2 is fixed to $p_2 = 3 \cdot 10^4 \text{ Myr } M_\odot$.

and the optical depth $\tau(R, z) = \int_z^{z_t} k (1 + (R^2 + \zeta)/r_c^2)^{-3n/2} d\zeta$:

$$F = F_0 \frac{\int_0^{r_t} 2 \pi R \left(\int_{-z_t}^{z_t} \rho_*(r) \exp(-\tau(R, z)) dz \right) dR}{\int_0^{r_t} 2 \pi R \left(\int_{-z_t}^{z_t} \rho_*(r) dz \right) dR} \quad (4.24)$$

For more details see Fiac & Rocca-Volmerange (1997) and the included references.

For this parameter study, the effect of extinction for different geometries (spheroidal geometry, disk geometry with an averaged inclination, and disk geometry for inclination $i = 0^\circ$, $i = 45^\circ$, and $i = 89^\circ$) was modeled. The modeled SEDs for the different geometries were then compared to each other at different ages of the SEDs (100 Myr, 1 Gyr, 10 Gyr). This comparison is done for the four different SFLaws included in this parameter study (see Fig. B.13–B.16). In the following, the results of this comparison will be discussed in detail.

Burst (see Fig. B.13): For the one burst model, large differences between the SED computed without extinction and the SEDs effected by dust are visible at all ages (100 Myr, 1 Gyr, and 10 Gyr). The reduction of the flux due to dust is largest at the Balmer Bump around 4000 \AA . The differences between the used dust models are neglectable. The reduction of the flux due to dust is strongest for the dust model with an edge-on-disk geometry.



Figure 4.11: Dust model used in order to compute extinction within the PÉGASE synthesis model.

constant SFR (see Fig. B.14): Using an constant SFR (relatively young SED, age 100 Myr), the models computed without extinction show no significant difference to the SEDs calculated with a certain dust model. One exception is the SED resulting from the dust model computed for an edge on disk geometry. However, this difference is neglectable in our case due to the low S/N ratios in the measured spectra. After 1 Gyr, the SED for the edge-on-disk geometry dust model shows significantly reduced flux compared to the no extinction case. The difference between the SEDs is largest at the Balmer bump around 4000 \AA . The other dust models show no significantly reduced flux compared to the case of no extinction. For the 10 Gyr SEDs a significant reduced flux is visible for all dust models. Again, the reduction of the flux due to dust is strongest for the edge-on-case.

expon. SFR (Fig. B.15): In the case of an exponential SFR for the 100 Myr old SEDs, there is a large reduction of the flux visible using the edge-on-disk dust model. For all other dust models, no significant change in flux could be seen. After 1 Gyr—in contrast to the constant SFR—, there is already a significant reduction of flux due to dust for all used models. The dilution of the flux is largest for the edge-on-dust model. All other dust models show no significant difference to each other. At an age of 10 Gyr, the flux dilution due to dust becomes smaller in the blue part of the SEDs ($\sim 4000 \text{ \AA}$) and larger in the red part ($> 6000 \text{ \AA}$). Again, the dilution is strongest for the edge on dust model.

power law SFR (Fig. B.16): The synthetic SEDs, calculated for SFRs following a power law, show similar behavior at an age of 100 Myr than the 100 Myr SEDs for exponential SFRs, except for the SED of the edge-on-disk dust model. Compared to the exponential SFR, the dilution of the flux for the edge-on-disk is lower. The SEDs of all other dust models show no significant dilution in comparison to the SED calculated for no extinction. After 1 Gyr, most of the dust models used for the power law SFR show no significant dilution compared to the SED calculated without extinction, except for the edge-on-dust model which shows significant dilution to the no extinction SED. This dilution is comparable to the dilution of the 1 Gyr SED of the exponential SFR. The behavior of the 10 Gyr SED for the power law SFR is similar to the one for the exponential SFR. However, the dilution of the flux for most of the dust models

compared to the SED computed without extinction is lower than the dilution for the exponential SFR. Only the edge-on-dust model shows a higher dilution of the flux.

Parameter	Value
Initial Mass Function (IMF)	Salpeter IMF
Upper Mass Limit	$80 M_{\odot}$
Lower Mass Limit	$0.08 M_{\odot}$
Type of SNII ejecta	Woosley & Weaver (1995) model C
Stellar Winds	yes
Fraction of Close Binary Systems	0.05
Initial Metallicity of the ISM	0
Infall	no
Galactic Winds (Outflow)	no
Fraction of Substellar Objects	0
Nebular Emission Lines	yes

Table 4.1: The table shows the values of the parameters used within PÉGASE, for which variations have no influence on the modeled SEDs in the optical wavelength range.

In this section, the variation of the most important parameters (IMF, Mass limits, SFL, SFR, Extinction) of the modeled SEDs were presented. Another parameter which has strong influence on the shape of the modeled SEDs is the metallicity. PÉGASE gives the user the possibility to choose a certain metallicity between $Z = 0.0001$ ($Z = 1/20 Z_{\odot}$) and $Z = 0.1$ ($Z = 5 Z_{\odot}$). Using one fixed metallicity is not a realistic scenario in order to describe the evolution of a galaxy. Galaxies are complex systems built out of different stellar populations formed at different times in different surroundings and resulting in different metallicities. Accounting for this effect, a chemical consistent evolution was chosen in order to build up the synthetic spectral library. Using this consistent chemical evolution, the metallicity is no free parameter any more. The galaxy model which was used in order to calculate synthetic SEDs is comparable to a so-called “closed box” model. This means that no gas infall and no gas outflow was included. The calculation of the synthetic SEDs starts with a still constituted galaxy. The initial metallicity of the ISM was chosen to be zero. However, some other parameters which could be influenced by the user (SNII model, fraction of binary systems, mass fraction of substellar objects) have no significant influence on the shape of the modeled spectra in the optical wavelength range (see Fig. B.17 – B.28). For all these parameters, the typical or the default ones are used (see Tab. 4.1).

4.3 Results

As mentioned before, the parameter study described in section 4.2.2 results in a library of several thousand synthetic SEDs. The parameters which are finally selected in order to build up the library and which will now be used to derive SFHs of galaxy samples are the SFR, SFLaw, and extinction. All other parameters do not have strong influences on the shape of the SEDs in the optical wavelength range (3400 Å to 7400 Å). In the following two subsections (Sect. 4.3.1 and 4.3.2), the procedure of deriving SFHs of samples of galaxies as well as the results of this method will be described. Therefore, the library was compared to the measured galaxy spectra. From this comparison, the SFLaw and the mean age of the dominant stellar population of the galaxies was obtained. The comparison was done by eye. Therefore, the synthetic SEDs were overplotted to the measured spectra. The comparison was started with SEDs calculated without any extinction, searching for the best matching SED for every type of star formation scenario (star burst scenario, constant SFR, exponential SFR, and the SFR following a power law). To find the best matching synthetic SEDs, several criteria were applied. First, the continuum of the synthetic SED must match the shape of the continuum of the measured spectra as good as possible. Important features are here the strength of the Balmer bump indicating a younger (strong Balmer bump) or older (no Balmer bump) stellar population. The next important feature which has to be matched by the synthetic SEDs is the strength of the absorption lines. Especially the hydrogen absorption lines around 4000 Å (Balmer lines) are important. These lines are produced in stars during the hydrogen burning phase. These stars could be found on the Main Sequence in the Hertzsprung–Russel Diagram and indicate a relatively young stellar population (strong Balmer absorption in A stars). In later phases of the stellar evolution, the effective temperature of the stars t_{eff} decreases and the hydrogen absorption lines become weaker. Due to lower stellar temperatures, metall absorption lines (e.g., CaII, Mg) start to become stronger. Therefore, a relatively old stellar population is indicated by metall absorption lines and no prominent Balmer bump. The described effects always depend on the metall content of the stars. A higher metallicity results in stronger metall absorption lines and therefore, the SEDs look older. A lower metallicity result in a younger looking SED. This effect is the so called age–metallicity degeneracy. In order to break this degeneracy, a comparison of Balmer and metall absorption lines could be made. In the following analysis, the use of consistent chemical evolution makes it not necessary to account for this effect. For a comparison of metall and Balmer absorption lines, spectra with higher S/N ratios and higher spectral resolution are needed. Following this, a list of synthetic spectra delivering a reasonable description of the measured spectra was extracted. In a next step, the synthetic SEDs calculated for different dust models were compared to the measured galaxy spectra. Again, this comparison results in a list of synthetic SEDs which give a reasonable description of the measured galaxy spectra. From this list, the best matching synthetic SED was chosen in order to describe the SFH of the studied galaxy. However, not every star formation scenario (with or without extinction) results in a synthetic SED giving a reasonable description of the studied galaxy spectra. In these cases, the correlation with the synthetic SEDs is much easier.

In order to reduce bias effects, scenarios which are in contrast to the selected SEDs are also compared to the galaxy spectra. The spectra of the LSB sample show relatively low S/N ratios,

which results in a restricted accuracy of the comparison of ~ 500 Myr to ~ 1000 Myr.

4.3.1 SFH of LSB Galaxies

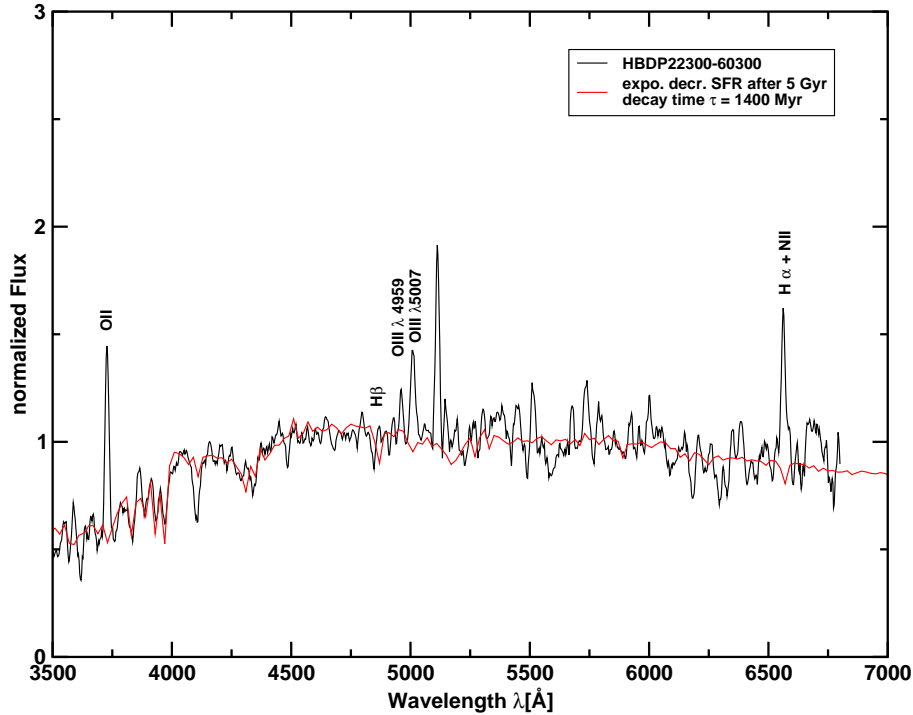


Figure 4.12: The diagram shows the comparison of the measured spectra of the LSB galaxy HBDP22300-60300 to a synthetic SED following an exponential decreasing SFR by using a decay time $\tau = 1400$ Myr. The spectra fit well to a stellar population of a mean age of 5 Gyr.

HBDP22300-60300: The LSB galaxy HBDP22300-60300 is one of the two randomly selected sample galaxies (see Sect. 3.1). It shows a clear disk like structure with two arm like features in the southern part of the galaxy. A central surface brightness of $\mu_0 = 22.87$ mag arcsec $^{-2}$ was derived for this galaxy. It is located in a distance of 382 Mpc ($z = 0.09$) and has a size of ~ 60 kpc. HBDP22300-60300 shows two large star formation regions in the northern part (see Fig. 4.19). The two regions have sizes of ~ 4.5 kpc, which corresponds to the size of spiral arm fragments. The slit was positioned with a rotator angle of ~ 190 deg., avoiding the two star forming regions in the northern part. This has the advantage that the spectra are not dominated by the bright HII regions and the summed spectra are more representative of the mean properties of the galaxy. The spatial axis of the slit covers ~ 10 arcsec of the galaxy. The S/N ratio is high enough to also get information from the outer part of the disk. Therefore the finally integrated 1D spectrum includes spectral information from the center to the lower surface brightness areas of the outer disk region. Due to the low S/N ratios, some problems in

the background subtraction occur (see Fig. 4.12), especially in the range between 5500 Å and 7000 Å. Some night sky lines are over- or under-subtracted. This results in residuals of this emission lines or artificial absorption like features which had to be excluded from the comparison to the synthetic SEDs. In order to produce the integrated spectra used for the comparison to the modeled SEDs, 32 rows in spatial direction were summed up (~ 10 arcsec). The measured spectrum is well represented by a synthetic SED modeled following an exponential decreasing SFR with a decay time $\tau = 1400$ Myr. The best matching SED has a mean age of the dominant stellar population of about 5 Gyr.

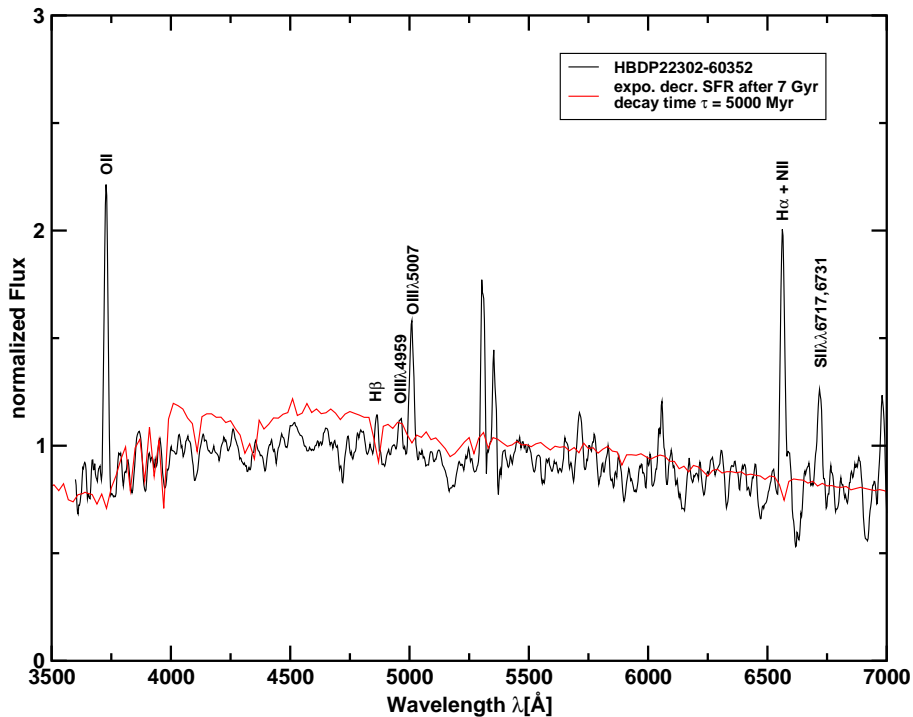


Figure 4.13: The comparison of the measured spectra of HBDP22302-60352 and the modeled SED shows that the LSB galaxy is well represented by an exponential decreasing SFR with a decay time $\tau = 5000$ Myr. The mean age of the dominant stellar population is about 7 Gyr.

HBDP22302-60352: HBDP22302-60352 is the second randomly selected LSB galaxy. It is a relatively round, nearly face-on spiral galaxy. In the disk of HBDP22302-60352, three arm-like features are clearly visible. Again, there are two spiral arm fragments visible in the northern and western part of the galaxy's disk (see Fig. 4.19). The two fragments have sizes of ~ 2.5 kpc (northern fragment) and ~ 1.9 kpc (western fragment). For this LSB galaxy, a central surface brightness $\mu_0 = 22.7$ mag arcsec $^{-2}$ was measured. HBDP22302-60352 is located in a distance of 168 Mpc ($z = 0.04$) and has a physical size of ~ 20 kpc. The slit was positioned

with a rotator angle of ~ 340 deg. The slit is slightly off-centered and also cuts the western edge of the northern arm fragment. Although due to the bright central part of the galaxy, the emission of this HII region does not dominate the integrated spectrum to much. In spatial direction, the slit covers nearly 15 arcsec of the galaxy. In the spectrum, one can measure emission with sufficiently high S/N ratios over an area of ~ 14 arcsec. This means that the integrated spectrum is composed out of information detected over nearly the whole galaxy. Again, there exist some problems in removing the night sky emission lines. Therefore, the spectrum include some residuals of these emission lines. There are still two strong residuals visible around 5300 \AA and two smaller around 5700 \AA and 6000 \AA . Also redwards of the $H\alpha$ emission line, an artificial absorption and some residuals of night sky emission lines are visible. These residuals were not considered for the comparison to the modeled SEDs. To construct the integrated spectra, 45 rows (~ 14 arcsec) were summed up. In Fig. 4.14, the comparison to the best matching modeled SED is shown. One can see that the two spectra do not match very good. The modeled SED overpredict the flux in the blue part of the spectrum near the Balmer bump. Anyway, the absorption lines around 4000 \AA are reasonable well represented by the modeled SED. The differences in this wavelength region could be caused due to problems during the extinction correction, although this model SED was chosen to be the best matching SED in the library. Therefore, this galaxy will be described by an exponential decreasing SFR with a decay time $\tau = 5000$ Myr. The mean age of the dominant stellar population is around 7 Gyr.

HBDP22325-60155: The galaxy HBDP22325-60155 is one of the LSB galaxies selected via the color-color selection method (see Sect. 3.1). This galaxy has a more complicated structure (see Fig. 4.19). In the center of the galaxy, a bright elongated feature is visible. This structure has a size of ~ 9 kpc and looks like a bar. In the outer regions, a very weak and diffuse underlying disk is clearly visible. The disk shows two arm like features in the northern and western part of the galaxy. The overall shape of HBDP22325-60155 is similar to the one of the Large Magellanic Cloud (LMC), our neighbor irregular dwarf galaxy. In the southern part of the disk, two bright HII regions are located. The HII regions have sizes of ~ 3 kpc (right HII region) and ~ 2 kpc (left HII region). The slit was positioned along the major axis of the galaxy using a rotator angle of 323 deg. Slightly off-centered, the slit covers the east edge of the bar like structure in the center as well as the right HII region. In spatial direction, the slit covers ~ 24 arcsec. However, the disk region in the northern part of the galaxy has too low surface brightnesses to make a significant signal in the 2D spectrum. Therefore, the integrated spectrum just contains information of ~ 14 arcsec in the southern part of the galaxy including the bar like feature and the bright HII region. The central surface brightness of HBDP22325-60155 is $\mu_0 = 23.30 \text{ mag arcsec}^{-2}$. The estimated distance of this LSB galaxy is 221 Mpc ($z = 0.05$). The S/N ratio of the measured spectra in this case is much higher so that it was not so problematic to remove the night sky emission lines. No influencing features are visible except for two smaller residuals around 5300 \AA and 6000 \AA as well as two artificial absorption features (around the $H\alpha + [\text{NII}]$ emission line) which are strengthened due to the smoothing of the spectra. However, these residuals do not have an effect on the comparison

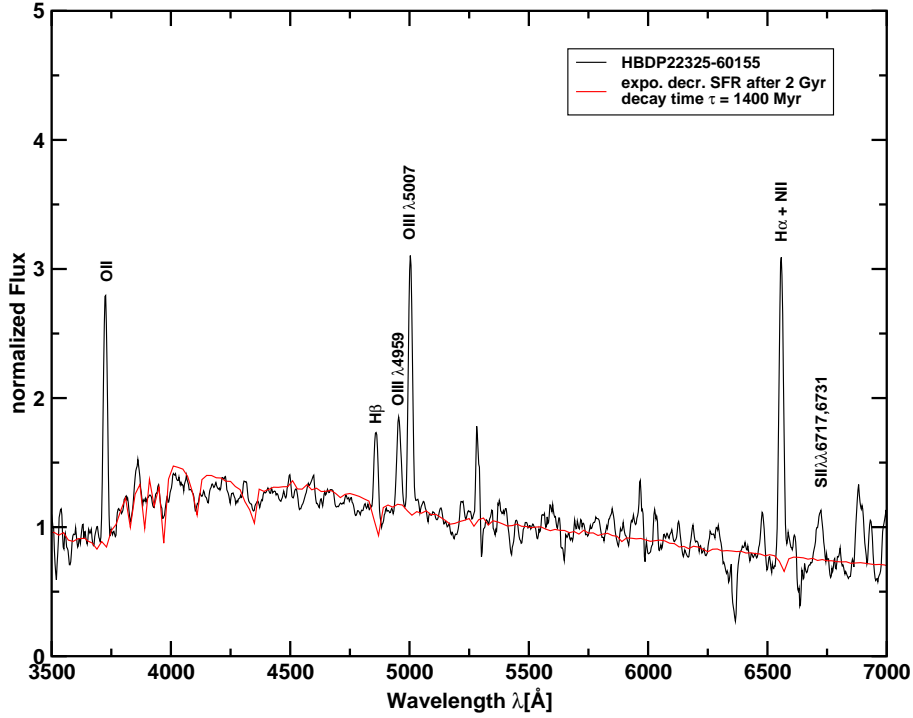


Figure 4.14: The diagram show that the LSB galaxy HBDP22325-60155 is well represented by a synthetic SED modeled for an exponential decreasing SFR by using a decay time $\tau = 1400$ Myr. The mean age of the dominant stellar population is about 2 Gyr.

to the modeled SEDs. Again, this comparison results in an exponential decreasing SFR for HBDP22325-60155 by using a decay time $\tau = 1400$ Myr for the best matching model SED. The mean age of the dominant stellar population is around 2 Gyr.

HBDP22330-60543: The galaxy HBDP22330-60543 is one of the LSBs which have a relatively high central surface brightness of $\mu_0 = 22.3$ mag arcsec $^{-2}$. They represent the overlapping region in the central surface brightness space of the sample. Anyway, the central surface brightness is still 2σ lower than the Freeman value (see Sect. 2.1). HBDP22330-60543 was selected as LSB candidate using the two color selection method. The galaxy has a nearly face-on, disk-like structure showing two arm-like features in the east and south part of the galaxy. The estimated distance of HBDP22330-60543 is around 235 Mpc ($z = 0.06$). The slit was positioned slightly off-centered with a rotator angle of ~ 210 deg (see Fig. 4.19). The slit covers ~ 14 arcsec in spatial direction including the edge of the bright central region. The outer region of the disk has too low surface brightnesses to contribute a significant signal to the 2D spectrum. Therefore, the integrated spectrum only contains information from the inner ~ 8 arcsec which corresponds to an area of ~ 9 kpc size. Due to the relatively high S/N ratio, it was more easy to remove the night sky emission lines from the 2D spectrum. Therefore, just

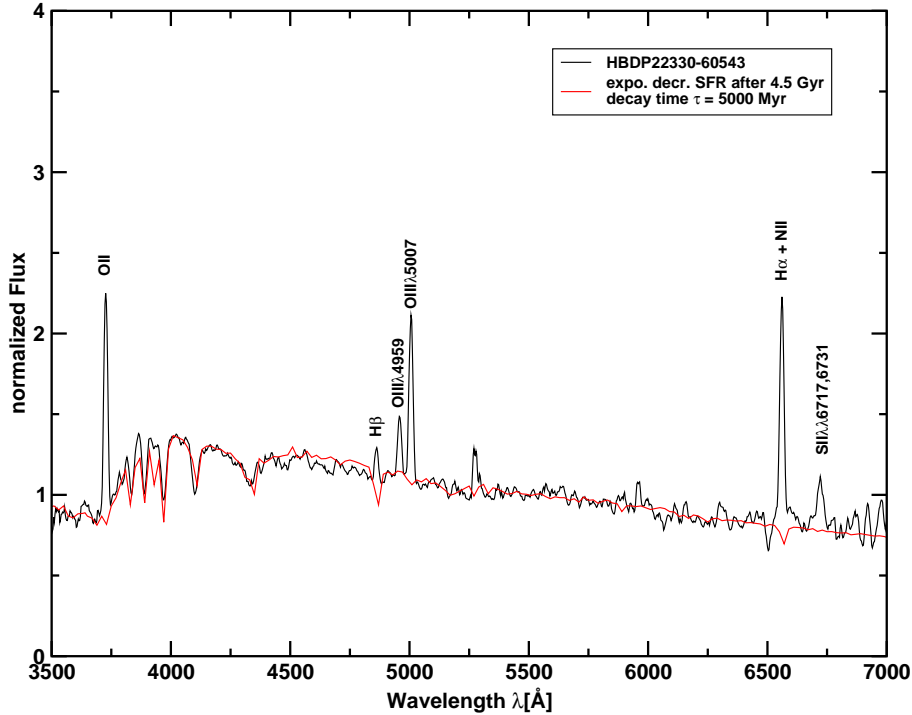


Figure 4.15: The LSB galaxy HBDP22330-60543 is well represented by an exponential decreasing SFR using a decay time $\tau = 5000$ Myr. The mean age of the dominant stellar population is around 4.5 Gyr.

two stronger residuals around 5260 \AA and 5960 \AA retained in the final spectrum. Additionally, one artificial absorption like feature at 6460 \AA (bluewards of the $H\alpha + [NII]$ emission line) is visible. Anyway, these residuals do not influence the comparison to the modeled SEDs. The comparison to the modeled library of synthetic SEDs results in a SFH following an exponential SFR with a decay time $\tau = 5000$ Myr (see Fig. 4.15). The estimated mean age of the dominant stellar population is around 4.5 Gyr.

HBDP22343-60222: The LSB galaxy HBDP22343-60222 was selected as a candidate for the HDF-S LSB galaxy sample using the two color method. The central surface brightness of HBDP22343-60222 is about $\mu_0 = 23.3 \text{ mag arcsec}^{-2}$. The estimated distance is around 196 Mpc ($z = 0.05$). The galaxy has an overall disk-like structure with a central bulge-like feature of $\sim 3.8 \text{ kpc}$ size and a faint diffuse disk. In the south-east and the north-west part of the galaxy, two arm like structures are visible. Near the eastern arm-like structure, two star forming fragments are visible with sizes of $\sim 3.2 \text{ kpc}$ and $\sim 2.8 \text{ kpc}$. The slit was positioned along the major axis of the galaxy with a rotation angle of $\sim 286 \text{ deg}$. The position of the slit on the galaxy is slightly off-centered avoiding the bulge-like structure in the center (see Fig. 4.19). The slit covers $\sim 18 \text{ arcsec}$ in spatial direction. Due to the low S/N ratio, the outer areas of

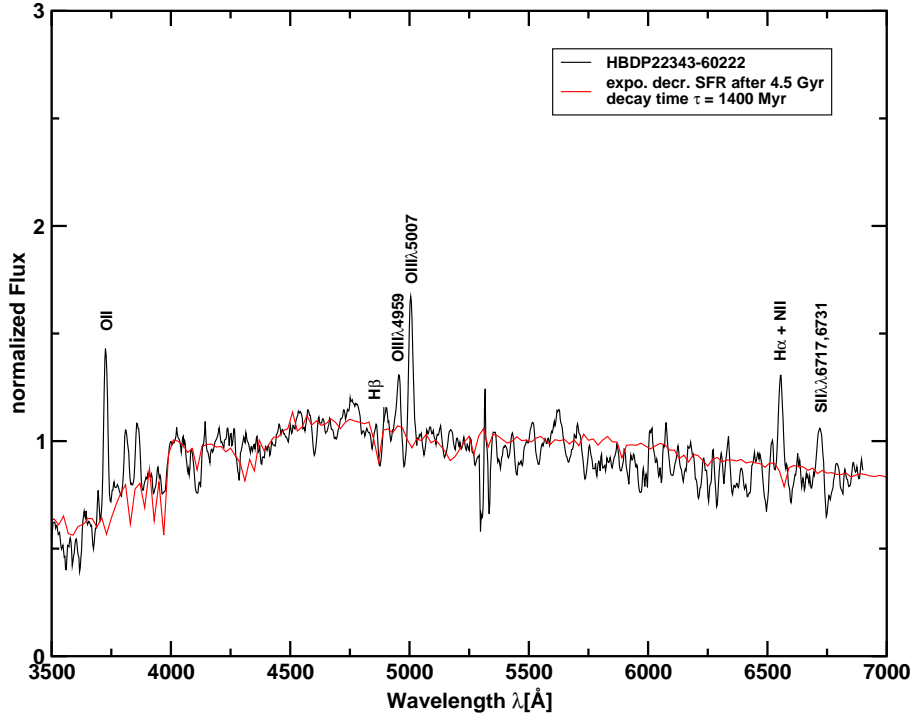


Figure 4.16: The SFH of HBDP22343-60222 is well represented by an exponential decreasing SFR with a decay $\tau = 1400$ Myr. The mean age of the dominant stellar population is around 4.5 Gyr.

the disk contain no significant signal in the 2D spectrum. Therefore, the integrated spectra were produced by just including information from the inner ~ 9 arcsec of HBDP22343-60222. Due to the slightly off-centered position of the slit, the integrated spectra contain information just from the disk of the galaxy. Some problems occurred during the reduction of the data. For HBDP22343-60222, just one 1800 s exposure was available. This makes it difficult to remove cosmic rays from the spectrum. For the cosmic ray reduction, the IRAF task *L.A.-cosmic* was used (see Sect. 3.2.2). In several cases, this cosmic ray reduction results in an over-subtraction of the cosemics, which leads to residuals in the 2D spectra. The final integrated 1D spectrum was produced summing up 30 rows. It was not possible to avoid all of the residuals to get a clean spectrum. One example for this is the residual of a night sky emission line combined with an artificial absorption due to over-subtraction of a cosmic ray around 5300 \AA . Therefore, the noise in the red part of the spectrum is higher than in the blue part of the spectrum. The comparison to the synthetic SEDs resulted in an exponential decreasing SFR using a decay time $\tau = 1400$ Myr. The estimated mean age of the dominant stellar population is about 4.5 Gyr. The two Balmer absorption lines around 3900 \AA are slightly stronger in the model SED than in the measured spectrum. Therefore, the age of the dominant stellar population could be slightly underestimated. Furthermore, the two night sky emission line residuals at this wavelength

could reduce the strength of the Balmer bump. Thus, the age could be slightly overestimated. Nevertheless, the chosen model SED is the best matching SED in the library.

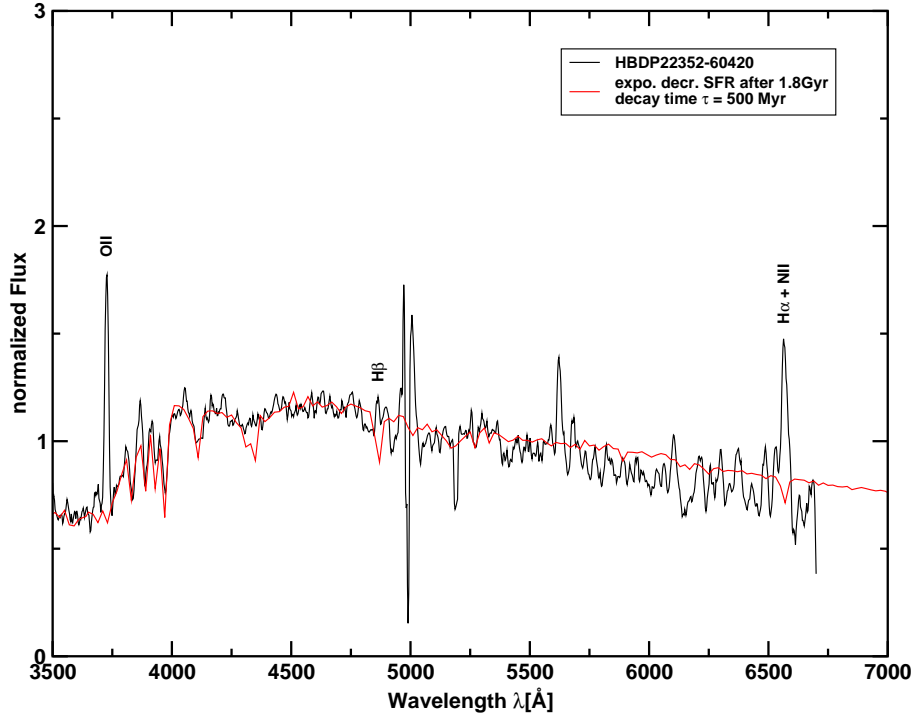


Figure 4.17: The galaxy HBDP22352-60420 is well represented by an exponential decreasing SFR with a decay time $\tau = 500$ Myr. The estimated mean age of the dominant stellar population is about 1.8 Gyr.

HBDP22352-60420: HBDP22352-60420 is the only higher redshifted LSB galaxy in the HDF-S sample. The estimated distance is about $z = 0.12$ ($d \sim 500$ Mpc). It belongs to the LSB galaxies which were selected for the LSB candidate sample using the two color method. In the color-color diagrams, this LSB galaxy is located near the redshift tracks of the “normal” HSB galaxies (see Fig. 3.5). Nevertheless, the location of HBDP22352-60420 still satisfies the selection criteria of the LSB candidate sample. HBDP22352-60420 has a central surface brightness of about $\mu_0 = 23.0$ mag arcsec $^{-2}$ and after correcting for cosmological dimming effects, it still remains as a LSB galaxy ($\mu_0 = 22.5$ mag arcsec $^{-2}$). The optical size is about ~ 13 arcsec (~ 31 kpc). HBDP22352-60420 is highly inclined (inclination angle $i \sim 60$ deg, resulting from photometric studies), which results in a large correction of the surface brightness ($\mu_{0_{corr}} = 23.8$ mag arcsec $^{-2}$). The overall structure of HBDP22352-60420 is a disk-like shape (see Fig. 4.19). For the spectroscopic observations, the slit was positioned along the major axis with a rotator angle of about ~ 200 deg. Due to the low S/N ratio in the outer regions of the disk, no significant signal accounts for the 2D spectrum from this areas. Therefore, the

integrated spectrum just contains information of the inner ~ 7 arcsec (22 rows). Again, some problems occurred removing the night sky emission lines from the 2D spectrum. Due to the redshift, one very strong night sky line is aligned with the O[III] emission line at $\lambda = 5008 \text{ \AA}$. The subtraction of this night sky line resulted in an artificial absorption in the spectrum. Two other strong residuals are visible at $\lambda \sim 5200 \text{ \AA}$ and $\lambda \sim 6600 \text{ \AA}$. However, the residuals do not effect the comparison to the synthetic SEDs. For the LSB galaxy HBDP22352-60420, an exponential decreasing SFR with a decay time $\tau = 500 \text{ Myr}$ was derived. The estimated mean age of the dominant stellar population is about 1.8 Gyr.

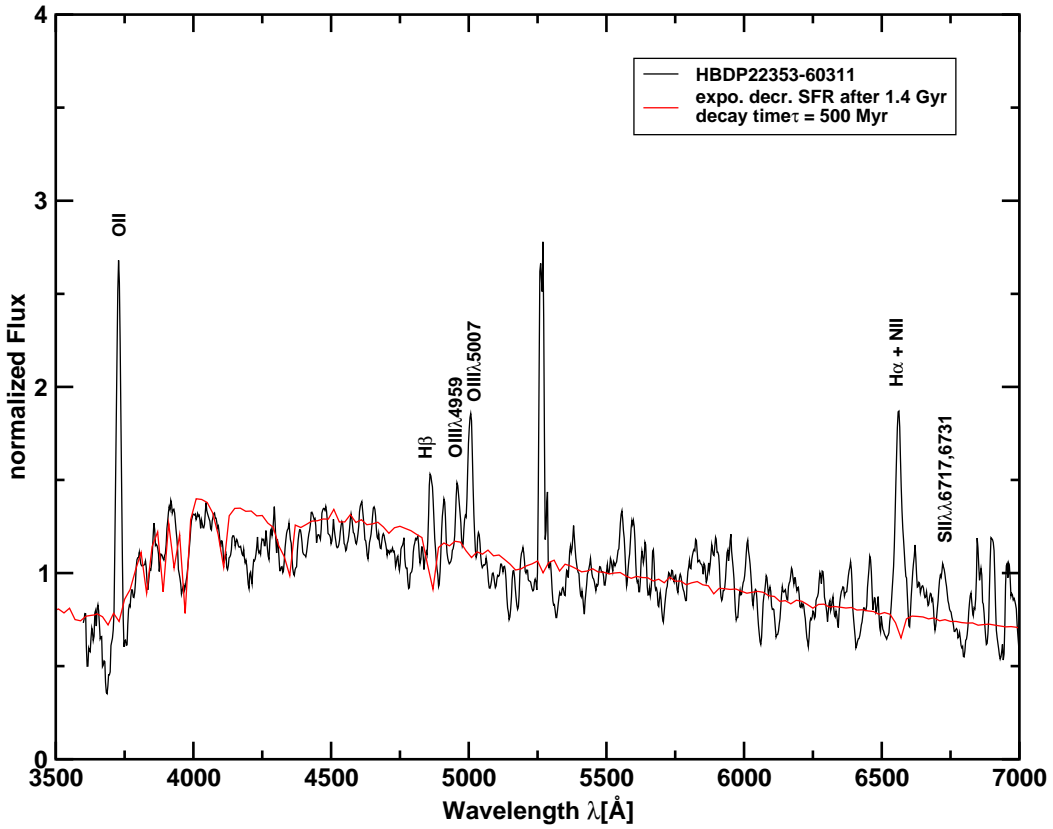


Figure 4.18: The spectrum of the LSB galaxy HBDP22353-60311 is well represented by an exponential decreasing SFR using a decay time $\tau = 500 \text{ Myr}$. The estimated mean age of the dominant stellar population is about 1.4 Gyr.

HBDP22353-60311: HBDP22353-60311 is a nearly face-on, spiral-shaped LSB galaxy (see Fig. 4.19). The central surface brightness is about $\mu_0 = 23.4 \text{ mag arcsec}^{-2}$. This galaxy is located at a redshift $z \sim 0.06$ ($\sim 246 \text{ Mpc}$). The optical size of HBDP22353-60311 is about $\sim 13 \text{ arcsec}$ ($\sim 16 \text{ kpc}$). Two spiral arm-like features are clearly visible in the north and south part of the galaxy. In the north and western part, two star forming arm fragments with sizes of

~ 2.9 kpc (west) and ~ 3.3 kpc (north) could be detected. The slit of the EFOSC spectrograph was positioned crossing the center of HBDP22353-60311 as well as the northern star forming fragment. For the orientation of the slit, a rotation angle of ~ 340 deg was used. In spatial direction, the slit covers ~ 13 arcsec of the galaxy. Due to the low S/N ratio, no significant signal of the outer regions of the disk could be used for the integrated spectrum. In order to produce the integrated spectrum, the inner 34 rows (~ 11 arcsec) were summed up. Nevertheless, the slit covers a large fraction of HBDP22353-60311, and therefore the integrated spectrum represents a good average of the whole galaxy. During the reduction process, it was not possible to remove all night sky emission lines completely from the 2D spectrum. For this reason, some residuals are still visible in the spectrum. For example, a very strong residual is visible at ~ 5250 Å. This residual is as strong as the O[II] emission line which is the strongest emission line of the galaxy. The artificial absorption at 4200 Å is also the result of the over-subtraction of a night sky emission line. Anyway, this artificial feature did not influence the comparison to the synthetic SEDs. No absorption line is located at 4200 Å. The noise between 5500 Å and 7000 Å is also slightly enhanced due to residuals of night sky emission lines. HBDP22353-60311 belongs to the three galaxies for which only one 1800s exposure is available. This means that again, the cosmic rays had to be removed from the 2D spectrum using the *L.A.-cosmic* tool. This removing process also results in residuals (e.g., peak at 4293 Å) and an enhanced noise pattern. From the comparison to the synthetic SEDs, an exponential decreasing SFR with a decay time $\tau = 500$ Myr was derived for HBDP22353-60311. The estimated mean age of the dominant stellar population is about 1.4 Gyr.

Name	SFLaw	decay time τ [Myr]	age t [Gyr]
HBDP22300-60300	expon. decreasing	1400	5.0
HBDP22302-60352	expon. decreasing	5000	7.0
HBDP22325-60155	expon. decreasing	1400	2.0
HBDP22330-60543	expon. decreasing	5000	4.5
HBDP22343-60222	expon. decreasing	1400	4.5
HBDP22352-60420	expon. decreasing	500	1.8
HBDP22353-60311	expon. decreasing	500	1.4

Table 4.2: The table summarizes the results of the SFH study of the LSB galaxy sample.

4.3.2 SFH of HSB Galaxies

In order to compare the results for the SFHs of LSB galaxies, the same analysis were done for a sample of HSB galaxies. To do so, the *spectrophotometric atlas of galaxies* by Kennicutt (1992a) was used. This catalog consists of a sample of 55 integrated spectra of nearby normal and peculiar HSB galaxies. The spectra are online available as ASCII-catalog via the CDS

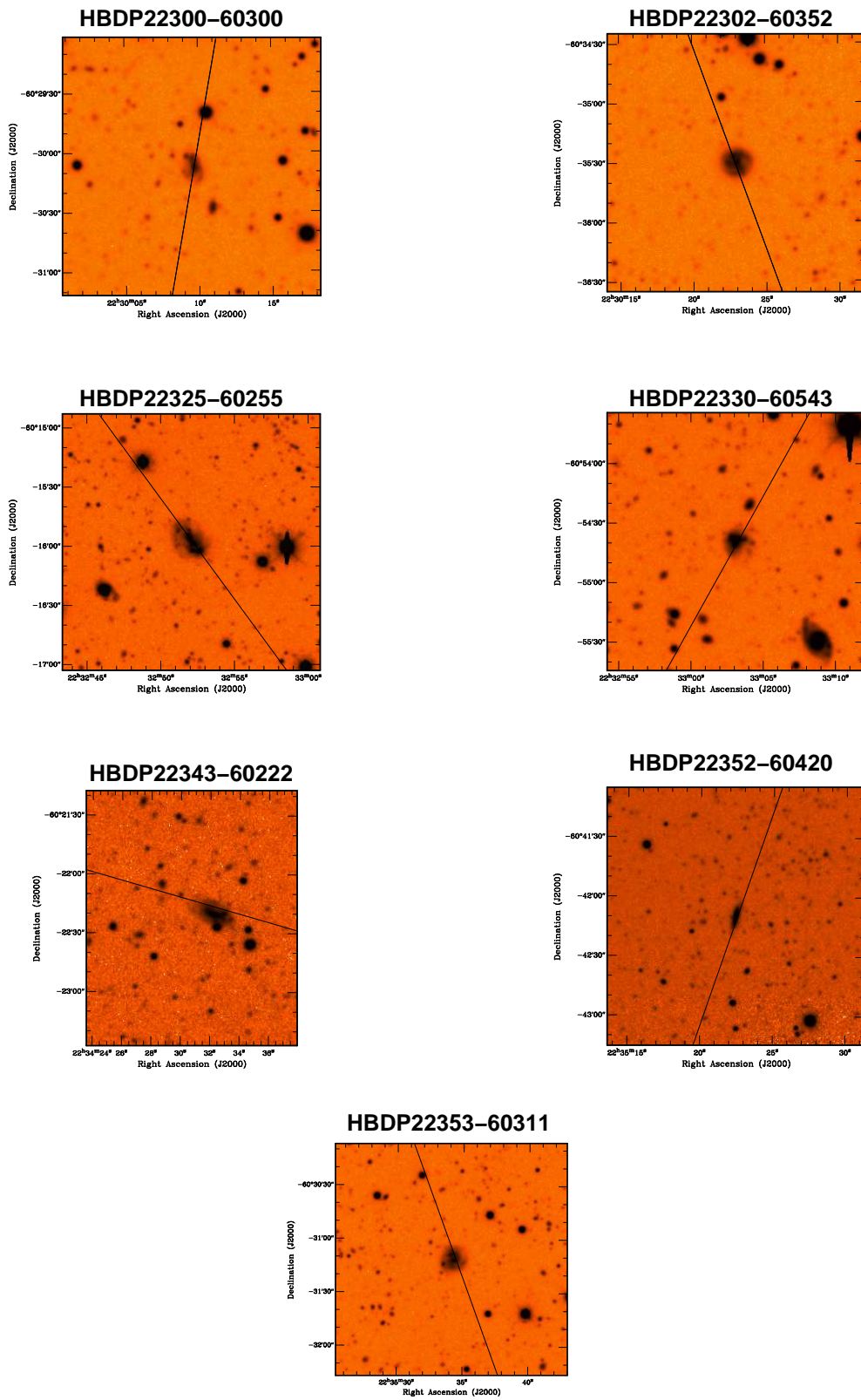


Figure 4.19: Collection of B_W images of the LSB galaxies in the HDF-S. The image size is about $2 \text{ arcmin} \times 2 \text{ arcmin}$. The black line represent the position and orientation of the EFOSC2 slit.

pages (Centre de Données astronomiques de Strasbourg)¹. The spectroscopic observations of the sample were performed by using two different telescopes. For the majority of the sample (41 galaxies), high-resolution data is available obtained with the Steward Observatory 2.3 m telescope at Kitt Peak. These spectral energy distributions cover a spectral range between 3650 Å and 7100 Å with a spectral resolution of about 5–7 Å. In order to produce integrated spectral energy distributions, the galaxies were observed in drift scanning mode. The scan length range between 44 arcsec and 800 arcsec. The drift scan exposures were repeated at least four times. For the rest of the sample (14 galaxies), the data were derived using the 0.9 m telescope at the Kitt Peak Observatory. With this setup, a spectral coverage of 3650 Å–6900 Å and a spectral resolution of 10–25 Å could be reached. For the galaxies observed with lower spectral resolution, integrated spectra were constructed combining spectra which were taken at three fixed positions. For more details about the observations see Kennicutt (1992a). The photometric accuracy is about a few percent or less. For the galaxies observed with larger apertures, the photometry is less precise. Several tests have shown that typical instrumental uncertainties over the whole wavelength range are about $\pm 10\%$. In some cases, peak errors of up to $\pm 15\%$ could be found. These errors are the dominant uncertainties in the spectra (for more details see Kennicutt, 1992a).

In order to minimize bias effects, all galaxies which are marked as strong interacting ones as well as all galaxies which are members of galaxy clusters were excluded from the analysis. Furthermore, all galaxies which are marked as peculiar galaxies were not analyzed. For these types of galaxies, star formation due to external triggering (e.g., merging processes, gravitational interaction in high dense environments) could play a major role and could result in extremely young or extremely old (e.g., gas stripping in the cluster environment) dominant stellar populations. In order to be comparable to the HDF-S LSB sample, only isolated field galaxies are chosen for the analysis. With this selection criteria, a subsample of 27 HSB galaxies was selected from the *spectrophotometric atlas of galaxies* by Kennicutt (1992a). The subsample covers the whole Hubble sequence. Therefore, the results from the SFH analysis should also not being biased by any special galaxy type. The analysis was done in the same way as described for the HDF-S LSB sample (see Sect. 4.3.1). The library of synthetic SEDs was compared to the measured spectra by eye. The best matching SED then describes the SFLaw and gives an estimation for the mean age of the dominant stellar population (see Tab.4.3). Two examples for this comparison are shown in Fig. 4.20. The upper panel of Fig. 4.20 shows the result for NGC2903 as an example for a relatively young dominant stellar population described by an exponential decreasing SFR with a decay time $\tau = 1000$ Myr. The spectrum of NGC3627 (lower panel) is an example for a relatively old stellar population. For this galaxy, the comparison results in an exponential decreasing SFR with a decay time $\tau = 5000$ Myr. The mean age of the dominant stellar population of NGC3627 is about 12 Gyr. The spectra of the complete sample could be found in App. C. Due to the relatively low S/N ratios of the HSB spectra, the accuracy of the estimated ages is around ~ 500 Myr. The accuracy of the age estimation for the HSB galaxies is therefore comparable to the accuracy of the estimated ages for the LSB galaxies. In contrast to the LSB sample, the spectra of the HSB galaxies were not smoothed to

¹<http://vizier.u-strasbg.fr/viz-bin/VizieR?-source=VII/141/>

Name	SFLaw	SFR [$M_{\odot} \text{ Myr}^{-1}$]	decay time τ [Myr]	Dust model	Inclination [deg]	age t [Gyr]	type	Instrument [m]
NGC1357	expon. decreasing	–	1000	spheroidal geometry		4.0	Sa	2.3
NGC1832	expon. decreasing	–	5000	disk geometry	45	6.0	SBb	2.3
NGC2775	expon. decreasing	–	1400	no dust	–	14.0	Sa	2.3
NGC2903	expon. decreasing	–	1000	disk geometry	45	3.0	Sc	2.3
NGC3034	expon. decreasing	–	1000	disk geometry	89	4.0	I0	2.3
NGC3077	expon. decreasing	–	1000	disk geometry	0	3.0	I0	2.3
NGC3147	expon. decreasing	–	5000	no dust	–	14.0	Sb	2.3
NGC3245	expon. decreasing	–	1400	no dust	–	14.0	S0	2.3
NGC3368	expon. decreasing	–	1400	no dust	–	14.0	Sab	2.3
NGC3379	expon. decreasing	–	1000	disk geometry	45	10.0	E0	2.3
NGC3471	expon. decreasing	–	5000	no dust	–	14.0	Sa	0.9
NGC3516	expon. decreasing	–	5000	no dust	–	14.0	S0	2.3
NGC3623	expon. decreasing	–	1400	no dust	–	14.0	Sa	2.3
NGC3627	expon. decreasing	–	5000	no dust	–	12.0	Sb	2.3
NGC3941	expon. decreasing	–	1400	no dust	–	10.0	SB0/a	2.3
NGC4449	constant	$5 \cdot 10^{-5}$ (a)	–	no dust	–	3.0	Sm/lm	2.3
NGC4631	expon. decreasing	–	500	no dust	–	1.2	Sc	2.3
NGC4648	expon. decreasing	–	1400	no dust	–	14.0	E3	0.9
NGC4775	constant	$5 \cdot 10^{-6}$ (a)	–	no dust	–	7.0	Sc	2.3
NGC5248	expon. decreasing	–	1400	no dust	–	5.0	Sbc	2.3
NGC5548	expon. decreasing	–	5000	no dust	–	9.0	Sa	2.3
NGC5866	constant	$5 \cdot 10^{-5}$ (b)	–	disk geometry	0	14.0	S0	0.9
NGC5996	constant	$5 \cdot 10^{-5}$ (a)	–	spheroidal geometry	–	7.0	SBd	0.9
NGC6181	expon. decreasing	–	5000	disk geometry	45	5.0	Sc	2.3
NGC6217	expon. decreasing	–	1400	no dust	–	3.0	SBbc	2.3
NGC6643	expon. decreasing	–	1000	disk geometry	45	2.0	Sc	2.3
NGC6764	expon. decreasing	–	1000	disk geometry	0	3.5	SBb	0.9

Table 4.3: Results for the SFH of the HSB galaxy sample. Column 1: Galaxy name, Column 2: SFLaw, Column 3: SFR if the spectrum is represented by a constant SFR, Column 4: in the case of an expon. decreasing SFR, the decay time τ is given in Myr, Column 5: used dust model, Column 6: in the case of a disk geometry, the inclination angle is given in deg, Column 7: mean ages of the dominant stellar populations in Gyr, Column 8: Hubble type, Column 9: telescope used for the observations

the resolution of the PÉGASE spectra. Therefore, the absorption features in the measured HSB spectra could be deeper and sharper than their counterparts detected in the synthetic SEDs. Anyway, it was possible to find a solution for the star formation scenario of the Kennicutt HSBs by comparing synthetic SEDs to the integrated spectra. The major part of the Kennicutt subsample is well represented by an exponential decreasing SFR. The decay times τ range between $\tau = 500$ Myr and $\tau = 5000$ Myr. Four HSB galaxies are better represented by a constant SFR. For this scenarios, a SFR of $5 \cdot 10^{-5} M_{\odot} \text{ Myr}^{-1}$ and $5 \cdot 10^{-6} M_{\odot} \text{ Myr}^{-1}$ was used (masses within PÉGASE are normalized with respect to $1 M_{\odot}$). For $\sim 1/3$ of the sample, one has to include a dust model in order to derive a star formation scenario for these galaxies. Most of these cases use a dust model for a disk geometry. In two cases, a spheroidal geometry matches well the shape of the measured spectra. The estimated ages of the HSB sample range between 1.2 Gyr and 14 Gyr. For the majority of the 27 HSB galaxies, the estimated mean ages of the dominant stellar population are higher than 5 Gyr. For the Hubble type Sc/Sd, a clear drop in the age is visible. For the late type galaxies (Sc/Sd, I/Sm), mean ages of the dominant stellar populations below 5 Gyr could be estimated. For one of the HSB galaxies in the Kennicutt sample, there also exists an age estimation from a work of Terlevich & Forbes (2002). For NGC3379, the authors derived a age of ~ 9.3 Gyr which is in good agreement to the age of 10 Gyr derived in this thesis. This result is a hint that the method described here works well.

4.4 Discussion

Using the synthesis model PÉGASE, mean ages for the dominant stellar populations of the HDF-S LSB galaxy sample as well as for the sample of nearby HSB galaxies from Kennicutt (1992a) were derived. An extensive parameter study resulted in a library of several thousand synthetic SEDs. The library consists of SEDs modeled by using different star formation laws, different SFRs and different extinction laws. Mean ages of the dominant stellar populations were obtained comparing the synthetic SEDs of the library to the measured spectra by eye. For the HDF-S LSB galaxy sample, this comparison resulted in mean ages for the dominant stellar population between 1.4 Gyr and 7 Gyr. For $\sim 60\%$ of the HSB galaxy sample, the mean ages of the dominant stellar population range between 5 Gyr to 14 Gyr. Only 40% of the HSBs show ages below 5 Gyr (see Fig. 4.21). The data indicate that the LSB galaxies are significantly younger than the majority of the HSB galaxies. From this result, one can assume that the LSB galaxies underwent their major star formation event at much later stages.

$$\int_0^t dt = \int_0^r \frac{R(t)}{c} dr \quad (4.25)$$

Solving Eqn. 4.25, one can calculate the distance corresponding to the derived age². The mean ages of the dominant stellar populations of the HDF-S LSB galaxy sample indicate that the major star formation event for these galaxies happens at redshifts around $0.1 \leq z \leq 0.5$ ($1.4 \text{ Gyr} \leq t_0 \leq 5 \text{ Gyr}$). Only for one LSB galaxy (HBDP22302-60352), the major star formation

²The values used for this thesis were calculated using the Javascript calculator of Edward L. Wright "<http://www.astro.ucla.edu/wright/CosmoCalc.html>"

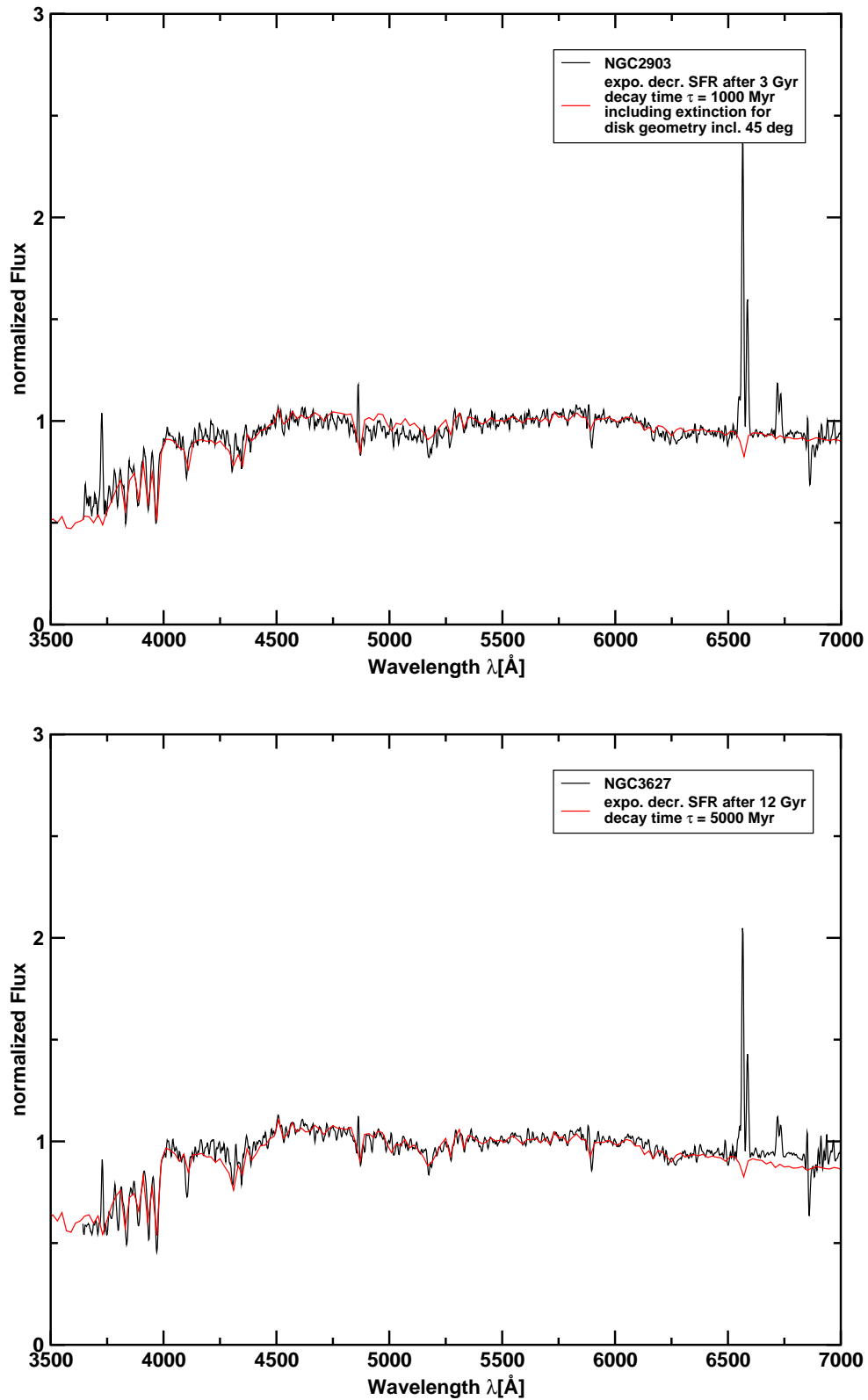


Figure 4.20: Example for a relatively young (NGC 2903) and a relatively old (NGC3627) stellar population from the HSB galaxy sample. Both galaxies are represented by exponential decreasing SFRs using decay times $\tau = 1000$ Myr (NGC2903) and $\tau = 5000$ Myr (NGC3627). Obtaining the SFH for NGC2903, it was necessary to include dust for disk geometry with an inclination angle of 45 deg.

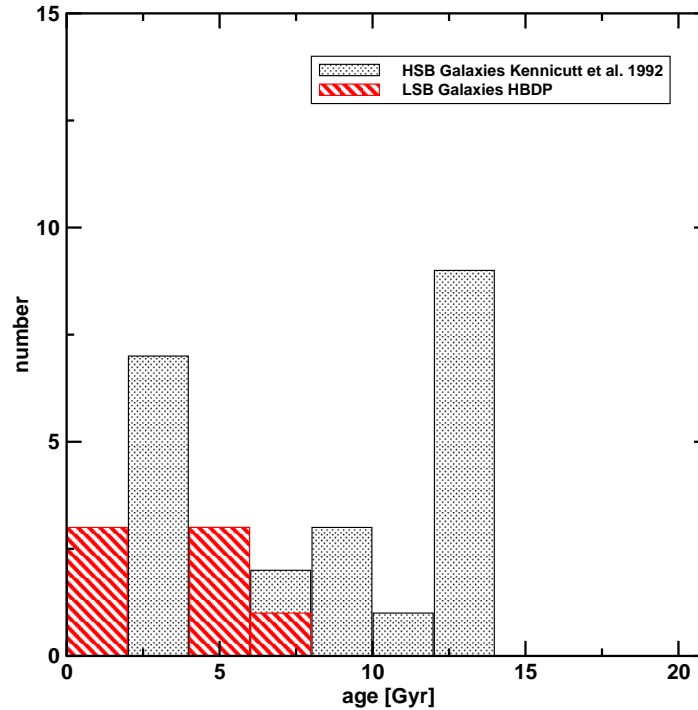


Figure 4.21: The diagram shows the distribution of mean ages of the dominant stellar population for the LSB (red bars) and HSB galaxies (black bars). For the LSB galaxies only relatively young ages between 1 Gyr and 7 Gyr could be derived, whereas the majority of the HSB sample has an old dominant stellar population above 5 Gyr.

event happened at a redshift $z \approx 0.85$ (7 Gyr). Consistent results for the young dominant stellar populations of LSB galaxies came from a study of the SFH of the local group LSB dwarf galaxy IC1613 (Skillman et al., 2003). In this study, the SFH was obtained by analyzing the Color-Magnitude Diagram (CMD) of two pointings observed with the WFPC2@HST (see Fig. 4.22, left panel). From the CMD, the authors could show that IC1613 had an enhanced SFR between 3 Gyr and 6 Gyr ago (see Fig. 4.22, right panel). This means that IC1613 underwent his major star formation event in the redshift interval $0.25 \geq z \geq 0.65$. This is in good agreement to the result obtained here for the HDF-S LSB galaxies. Due to the fact that IC1613 is a more isolated and non interacting dwarf LSB in our local group, external triggered star formation does not play a major role. Therefore, one can compare the result for the SFH of IC1613 to the SFHs of the HDF-S LSB galaxies which are all isolated field galaxies. Zackrisson et al. (2005) also studied the SFH of a sample of blue LSB galaxies. However, from the used broad band photometric data it was not possible to determine definite ages for the sample galaxies. As the authors assert, information from only four broad band filters are not sufficient in order to make constraints on the ages of galaxies. From their data they found that the ages of the single galaxies range between 2 Gyr and 15 Gyr. However, for some of the galaxies one could favor young ages. Bell et al. (2000) also used broad band photometric data (B,V,R,K') in order

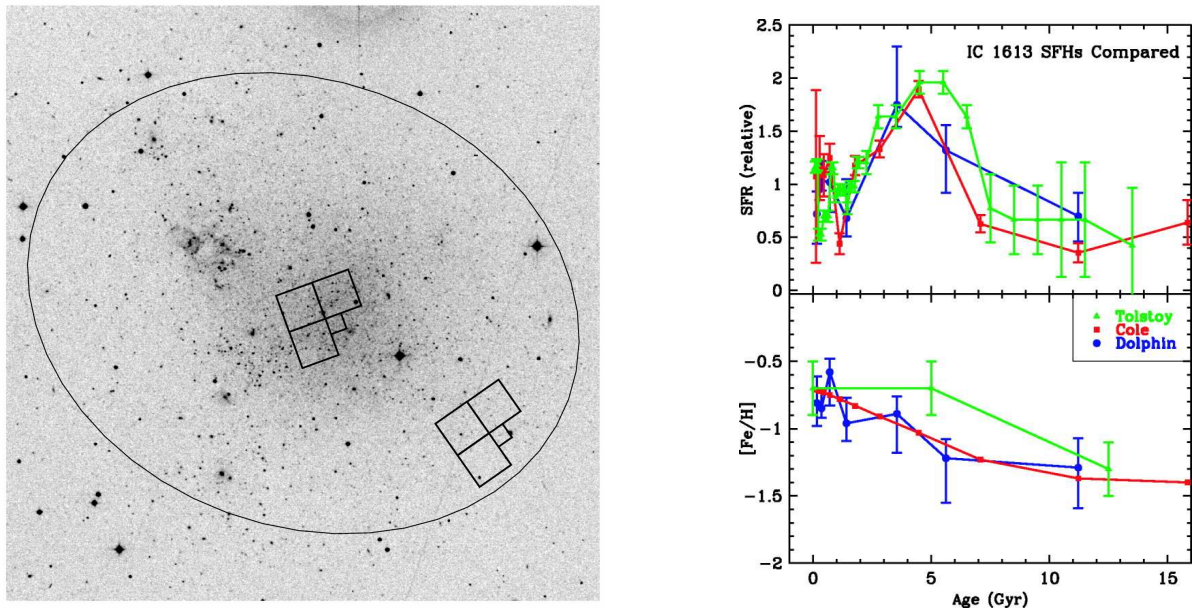


Figure 4.22: Results for the SFH of the local group dwarf LSB galaxy IC1613 obtained by Skillman et al. (2003). Analyzing CMDs of two HST/WFPC2 pointings (left panel), the authors derived an enhanced SFR between 3 Gyr and 6 Gyr (right panel).

to study the SFHs of a sample of LSB galaxies. The studied sample consists of blue as well as red LSB galaxies. In this study the authors also found a trend for LSB galaxies to have younger stellar populations. However, the limitations of the described studies are mainly the use of photometric broad band color data. Describing the shape of a galaxy spectra, by measuring only at four points along the SED, higher uncertainties are introduced. The description of the SFH by just using simple stellar populations (SSPs, meaning one fixed metallicity) is not very realistic. This also gives some uncertainties on the derived ages of the studied galaxies. In contrast to this, the use of chemically evolving stellar populations –as done in this thesis– would give a more realistic description of the SFH of galaxies.

As described earlier, in contrast to the LSB galaxies it could be shown that the majority of the HSB sample has relatively old stellar populations with mean ages above 5 Gyr. The HSB galaxies therefore underwent their major star formation event at redshifts between $2 \geq z \geq 4$. Terlevich & Forbes (2002) presented consistent results for a sample of 161 HSB galaxies. The sample was selected from the literature and consists of mainly early-type galaxies. For the sample, the ages were derived analyzing central absorption line indices which were calibrated to the Lick/IDS system of Worthey et al. (1994). In their work, it could be shown that $\sim 61\%$ of the HSB galaxies have mean ages of above 5 Gyr, only considering the field galaxies which were not classified as peculiar. This matches well the result for the HSB sample derived in this thesis (60%).

In Fig. 4.23, one can see a clear tendency of the Hubble type with the averaged mean age of the dominant stellar population. For the early type galaxies (E/S0, Sa/ab) the averaged

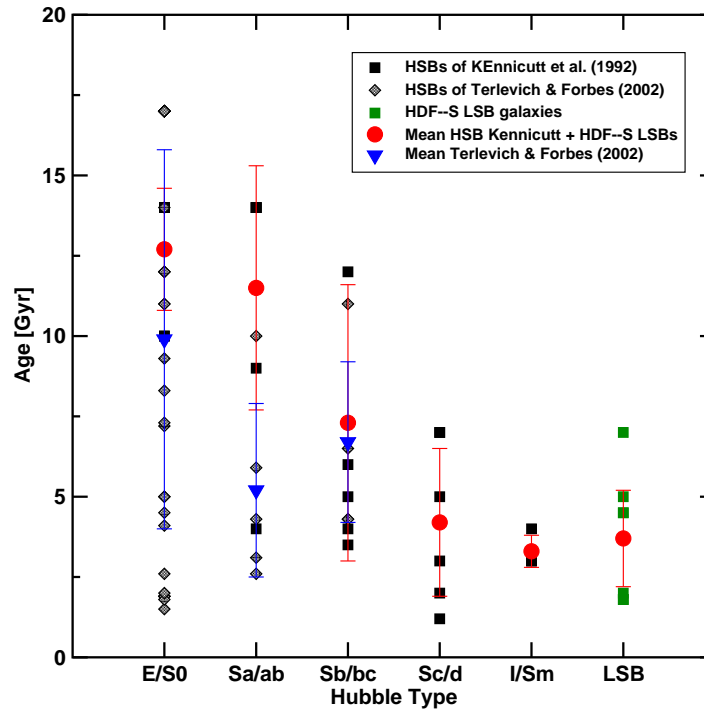


Figure 4.23: The diagram indicates a relation between the Hubble-type and the age of the dominant stellar population. The early type galaxies show older dominant stellar population than the late type galaxies. The red circles represent a mean age calculated from all galaxies in this Hubble type bin (black squares). The error bars are derived calculating standard deviation.

age is higher than for the late type galaxies (Sc/d, I/Sm).

4.5 Conclusion

As described in Sect. 4.4, the results for the SFH of the HDF-S LSB galaxies indicate a significant younger mean age of the dominant stellar population compared to those of HSB galaxies. This does not naturally mean that these galaxies do not have an old stellar population. From the relatively young stellar population, one can conclude that the majority of the stellar mass which dominates the integrated spectrum was formed at later stages as in most HSB galaxies. Anyway, this relatively young stellar population is an explanation for the different location in the color-color diagrams (see Sect. 3.3.2). In the spectra of the LSB galaxies, the Balmer bump is much more prominent. Due to this, the B-band is stronger in relation to the other filter bands. A more prominent Balmer bump explains the blue shift in the B-V and B-R color as well as the shift to redder colors for the U-B index. Therefore, one can conclude from the young mean ages of the dominant stellar population that the low surface brightness

nature of the LSB galaxies is the result of being relatively unevolved. This is also consistent with their generally low metallicities and large HI content.

From a study of the environment it is known that LSB galaxies are preferentially found in low density regions. Using data of the SDSS, Rosenbaum & Bomans (2004) could show that the LSBs are located at the rims of the filaments of the Large Scale Structure (LSS). Some LSB galaxies are also found in the extreme low density environment of the voids (see Fig. 4.24, left panel). With this study, the authors could show that the LSB galaxies in comparison to the HSBs are more isolated on intermediated scales ($2 \text{ Mpc} \leq r \leq 5 \text{ Mpc}$). From this result, it can be expected that external triggered star formation does not play a major role for LSB galaxies. The analysis of the rotation curves showed that LSB galaxies tend to have a larger spin parameter than their HSB counterparts. These studies revealed that the LSBs are less concentrated. LSB galaxies consist of more extended halos than HSB galaxies of comparable mass. They conserve more angular momentum. However, these halos are more extended and

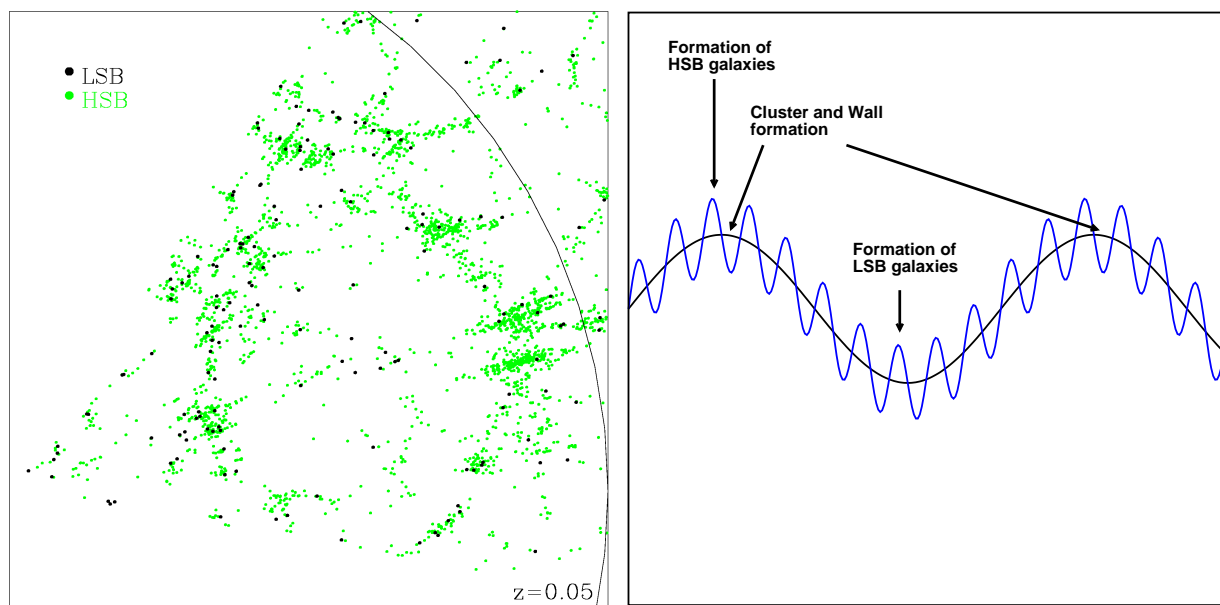


Figure 4.24: Pie-slice diagram (left panel) showing the environment of LSB galaxies (Rosenbaum & Bomans, 2004). The LSB galaxies (black dots) are mostly found in a low density environment at the rims of the filaments which are formed by the HSBs (green dots) or in the very low density environment of the voids. The right panel illustrates how the scheme of the large scale density fluctuations is connected to galaxy formation.

less dense, which also results in low gas surface densities. Therefore, it can be assumed that internal star formation will be suppressed. Taking this together, one can conclude that either the evolution of LSB galaxies happened much slower or they are formed later than the HSBs. Rosenbaum & Bomans (2004) propose a scenario where the LSB galaxies are formed later in the minimum phases of the large scale density fluctuations (see Fig. 4.24, right panel). In this scenario, galaxy clusters and walls of the LSS are formed during the maximum phases of

the large scale density fluctuation (black line). Galaxies are now formed at the maxima of the overlaid small scale density fluctuation (blue line).

How can the evolution of the LSB galaxies in context to the two galaxy evolution models described in Sect. 2.3, be understood ? As shown above, the LSB galaxies underwent an evolution path where external triggered star formation does not play a major role. Therefore, one can assume that interaction or merging processes are not important for the evolution of LSB galaxies. With this assumption, the LSB galaxies match well the “Monolithic Collapse” scenarios where the galaxies are formed in an earlier epoch and, after formation, just follow a pure luminosity evolution. However, this does not mean that the LSBs do not fit the “Hierarchical Clustering” model. Also in this scenario, it is possible that galaxies are formed and evolve without any merging process, which is especially due to the low density environment favored by the LSB galaxies. The evolutionary scenario for the LSB galaxies derived from the results of this thesis in combination with results of other projects does not prefer any of the galaxy evolution models. It is obvious that the explanation of the evolution of LSB galaxies is one of the critical tests for these models and should be further investigated in the future.

Chapter 5

Summary

I presented the first study of the SFH of LSB galaxies by using integrated spectra. The analyzed sample was derived during a search for LSBs in the HDF–S. The selection was done using a new method based on the locations of the galaxies in the color–color diagrams. As shown by Habertzettl (1999), the LSB galaxies in the color–color diagrams do not follow the redshift tracks built by the HSB galaxies. In the color–color diagrams, these tracks represent the five standard Hubble types. The different locations of the selected LSB galaxies are a first hint for their different stellar population mix. With additional selection criteria ($\mu_0 \geq 22.0 \text{ mag arcsec}^{-2}$ and diameter $D \geq 10.8 \text{ arcsec}$), a sample of 11 LSB galaxy candidates could be derived. In the first part of this thesis, it could be shown from spectroscopic observations that the majority of the selected sample (7 candidates) is located at low redshifts ($z \lesssim 0.1$). Due to the low redshifts, only a small surface brightness correction had to be applied to the estimated central surface brightnesses, and these galaxies are proven to be true LSB galaxies. The derived distances for the LSB galaxy sample range between 170 Mpc and 500 Mpc. Using these distances, physical parameters could be calculated. The calculated sizes of the sample range between 10 kpc and 32 kpc. Therefore, the sample only consists of large LSB galaxies (comparable to the Milky Way) and no dwarf–like objects. For the absolute magnitudes of the sample, values between -17 mag and -20 mag were calculated which corresponds to luminosities of $0.5 \cdot 10^9$ to $3.7 \cdot 10^9$ solar luminosities. These values also show that the sample members are large and relatively luminous galaxies. Following the method of McGaugh (1996), volume densities for the LSB sample were estimated. These volume densities include a correction for the surface brightness dependent volume over which a galaxy could be detected. From other galaxy surveys (e.g., O’Neil et al., 1997a; Impey et al., 1996) it was known that the central surface brightness distribution does not follow a Gaussian distribution with a maximum at $\mu_0 = 21.65 \pm 0.3 \text{ mag arcsec}^{-2}$ as originally stated by Freeman (1970, Freeman Law). The distribution stays flat down to central surface brightnesses lower than $22.5 \text{ mag arcsec}^{-2}$, which is more than 3σ below the maximum of the assumed Gaussian distribution (Freeman value). The volume densities estimated for the HDF–S LSB galaxy sample also recover this flat distribution. In addition to this, it was possible to extend the distribution to much lower central surface brightnesses. It could be shown that at this very low central surface brightnesses of $\mu_0 \approx 27 \text{ mag arcsec}^{-2}$, the volume density

distribution still stays flat. This result indicates that LSB galaxies are a common product of galaxy evolution processes. Therefore, the LSBs are an important factor for the understanding of galaxy formation and evolution models.

In the second subproject of this thesis, it should therefore be tried to derive information about the SFHs of the HDF-S LSB galaxy sample. In order to do so, the flux calibrated LSB galaxy spectra were compared to a library of several thousand synthetic SEDs calculated with the synthesis evolution model PÉGASE. The library was built up from an extensive parameter study which was done in order to restrict the parameter space to those parameters influencing the shape of the SEDs significantly in the optical wavelength region. From a comparison by eye, it was then possible to estimate the star formation laws and the mean ages of the dominant stellar population of the studied galaxy sample. For the HDF-S sample, mean ages of the dominant stellar population ranging between 1.4 Gyr and 7 Gyr could be estimated. This relative young mean ages were then compared to the mean ages of a sample of HSB galaxies. The HSB sample was analyzed using the same method as used for the LSBs. For the majority of the HSBs ($\sim 60\%$) mean ages larger than 5 Gyr were estimated. This result indicates that the LSB galaxies have significant younger dominant stellar populations compared to those of the HSBs. Therefore, the LSBs underwent their major star formation event at much later stages. The majority of the stellar masses of LSB galaxies should be formed in a redshift interval of $0.2 \leq z \leq 0.5$, whereas the HSB galaxies appear to have their major star formation event in a redshift interval of $2 \leq z \leq 4$, which is consistent with expectations of the “Hierarchical Clustering” model (Springel & Hernquist, 2003). The results derived in this thesis are consistent with other published results for the SFH obtained by using different methods. The HSB galaxies are found to follow a trend where the mean ages of the dominant stellar populations decreases when going to later Hubble type. The results for the SFH of the LSB galaxies also offer an explanation for the different location of the LSBs in the color-color diagrams. Due to relatively young mean ages, the spectra of the LSB galaxies show a more prominent Balmer bump. Therefore, the flux in the B-band in relation to the other filter bands is higher compared to SEDs of HSB galaxies. This higher B-band flux causes the shift in the color-color space. Bringing together the results of this thesis with results of other studies of LSB galaxies (e.g., environment studies), an evolutionary scenario could be proposed where the LSB galaxies are formed in a low density environment (e.g., voids or rims of the filaments of the LSS) during the minimum phases of the large scale density fluctuation. Due to suppressed internal (low gas densities) and external triggered star formation, the evolution of the LSBs after formation is slower compared to the evolution of the HSB galaxies. The evolutionary scenarios proposed here neither prefer the “Monolithic Collapse” model, where galaxies formed at high redshifts and then just follow a pure luminosity evolution, nor the “Hierarchical Clustering” model, where the galaxies are build due to ongoing merging processes of smaller progenitor galaxies. Finally, it should be mentioned that the explanation of the formation and evolution of LSB galaxies is the critical test for the existing galaxy evolution models.

Chapter 6

Outlook

The HDF–S LSB galaxy sample – for which SFHs were obtained in this thesis – has not yet a large statistical significance. With the analysis of the SFH of the HDF–S LSB galaxy sample, only a first step was made, and this directly leads to an obvious future project. In order to prove the assumption about the evolution of LSB galaxies which was made in this thesis, it is planned to expand the described analysis to a larger sample of LSB galaxies. In order to do so, observations were carried out in the last observing season (data arrived just in April 2005) using the 8.2 m ESO Very Large Telescope (VLT) equipped with the FOcal Reducer/low dispersion Spectrograph 2 (FORS2). With these observations, spectra were obtained having higher spectral resolution as well as higher S/N ratios. The observed sample was selected as a subsample from the catalog of extremely late-type spiral galaxies of Matthews & Gallagher (1997) which consists of 49 morphologically selected moderate-to-low surface brightness late type galaxies within the Local Supercluster. In order to get a statistically significant sample of LSB disk galaxies, all objects were selected which show diffuse distributed stellar light and no bright features indicating regions with enhanced ongoing star formation. This selection results in a sample of 19 moderate-to-low surface brightness late type galaxies. The fact that most of the galaxies are detected in HI surveys gives information about their radial velocities and HI masses (Fouque et al., 1990; Gallagher et al., 1995; Kraan-Korteweg & Huchtmeier, 1992). From the photometric studies (Matthews & Gallagher, 1997), information about the broad band colors of the selected subsample is available. For the selected subsample, it is planned to compare the measured spectra with the library of synthetic SEDs in the same way as described in this thesis. With the new and higher quality spectra, it will also be possible to compare the metal absorption lines to the Lick/IDS system (Worthey et al., 1994), which could not be done for the HDF–S LSB sample in this thesis. With this comparison, information about stellar metallicities will be obtained. This metallicity information makes it more easy to find a solution for the stellar population mix. Due to the higher quality data, it will also be possible to apply the described analysis at different positions along the spatial axis of the observed galaxies. Therefore, the results will be radial dependent and it could be looked for radial gradients.

Further on, it is planned to study the chemical properties of LSB galaxies by analyzing the emission lines of the extracted spectra. Abundances of the main elements found in HII regions

(e.g., Oxygen, Nitrogen) will be derived using the empirically strong line method (McGaugh, 1991, 1994). The oxygen abundance is an indicator for the metallicity of the ISM and offers information about the physical parameters of the ISM like electron temperatures, densities, and averaged ionization states $\langle U \rangle$. For this method, it is only necessary to measure the abundance indicating line ratio $([\text{OII}]\lambda 3727 + [\text{OIII}]\lambda\lambda 4959, 5007)/\text{H}\beta$ and the ionization sensitive line ratio $[\text{OIII}]\lambda\lambda 4959, 5007/[\text{OII}]\lambda 3727$. For the calibration of this empirical method, it is planned to follow the calibration of McGaugh (1991, 1994). This empirical function is a twofold degenerate function. The degeneracy can be resolved by obtaining $[\text{NII}]/[\text{OII}]$ line ratios. This line ratio varies monotonically with oxygen abundance, but is less sensitive to $\langle U \rangle$ so we can distinguish between the upper and the lower branch of this degenerated distribution. The analysis will be done using the integrated spectra and therefore giving information about the global chemical composition of the LSB galaxies. This is in contrast to most former studies of LSB galaxies which are targeted at bright HII regions. With this analysis, an additional assumption about the evolution of the LSB galaxies can be made.

However, until now it is not really understood how star formation processes occur in the low density environment of the LSB galaxies. One way to investigate this question is the study of the molecular content of these galaxies. In HSB galaxies, star formation occurs in giant molecular clouds. These giant molecular clouds can be formed in the case that the surface density reaches a critical density as proposed by Kennicutt (1989). One possibility to obtain information about the molecular content of galaxies is the observation of the CO emission. The amount of CO in galaxies can be converted into the amount of H_2 . The nature of the CO and how it is related to the amount of molecular hydrogen in LSB galaxies is still an open question. Only a few detections of CO in small samples of LSB galaxies were published up to now (O'Neil et al., 2000; Matthews & Gao, 2001; O'Neil et al., 2003; Matthews et al., 2005). The idea which now should be followed in a future project is based on the assumption star formation happens in small molecular clouds diffusely distributed over the whole galaxy disk. Therefore, the observations were designed to cover as much of the galaxy as possible (the limit is caused by the beam size) in order to integrate over the whole CO in the observed galaxy. First observations for this project were made using different mm and submm telescopes (SEST@ESO, Heinrich Hertz Telescope, Five College Radio Astronomy Observatory), and first results will be published soon. Anyway, the sensitivities of the used telescopes are not high enough in order to detect CO on such low levels within useful integration times. The next step in telescope development will be the construction of the Atacama Large Millimeter Array (ALMA). This array will be built out of 64 telescopes each with a dish size of about 14 m. With the much lower noise level reached by ALMA, it will now be possible to investigate the question for the molecular content in LSB galaxies further on.

Until now, all knowledge about LSBs is based on the analysis of a sample of low redshift ($z < 0.1$) LSB galaxies. The results for the SFHs presented here in this thesis indicate that the LSB galaxies undergo their major star formation event at much later stages corresponding to redshifts between $0.1 \leq z \leq 0.4$. As mentioned before, this could be the result of being formed later and/or following a slower evolution due to reduced external triggered star formation. In order to prove the evolutionary scenario – proposed for the LSB galaxies – in more detail, it is planned to study these galaxies at higher redshifts ($z > 0.1$). Therefore, the first sample of

LSB galaxies at higher redshifts ($0.1 \leq z \leq 0.5$) will be derived using the 6.5 m Baade Magellan Telescope equipped with the Inamori Magellan Areal Camera and Spectrograph (IMACS), the new wide field imaging and multi-object spectrograph (proposal submitted). LSB candidates were selected using very sensitive multi-color imaging data from the Chandra Deep Field-South (CDF-S). For the CDF-S data, observed in five filters (U,B,V,R,I), are available (Erben et al., 2005). Selecting LSB candidates from samples of galaxies always has the problem of contamination with galaxies showing low surface brightnesses, due to cosmological dimming effects (“Tolman Dimming” Hubble & Tolman, 1935). Therefore, one could easily select a

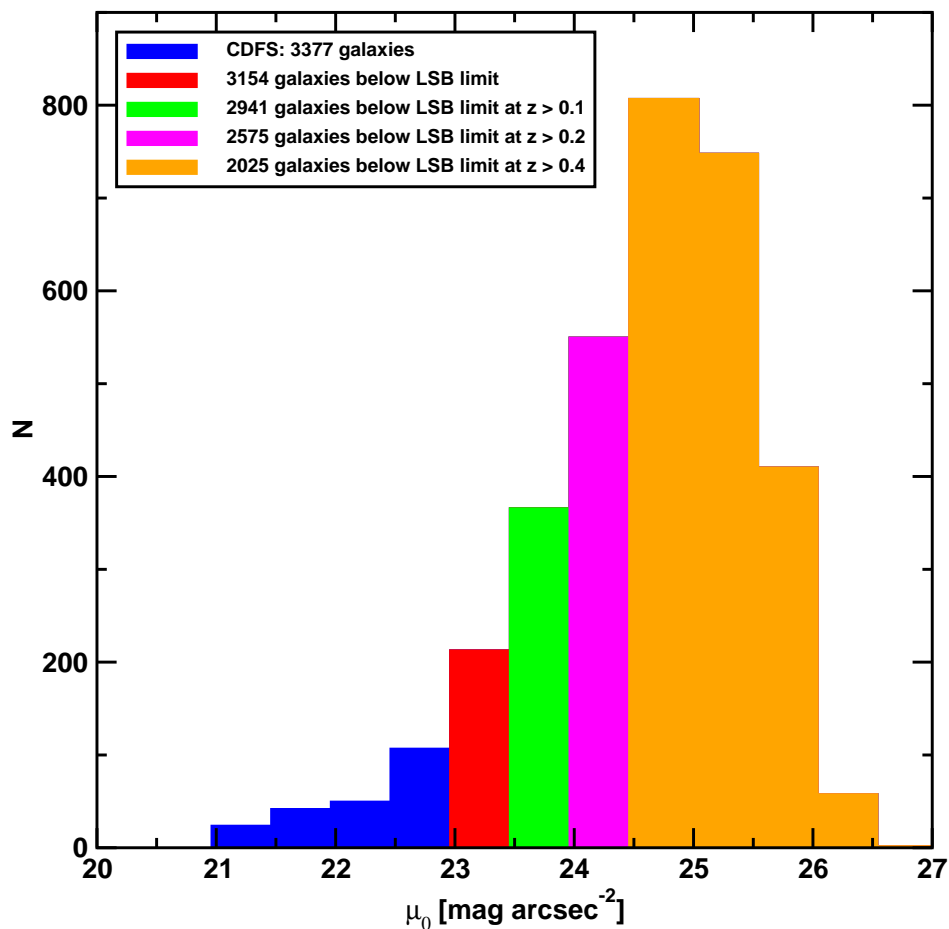


Figure 6.1: Central surface brightness distribution of the LSB galaxy candidate sample in the CDF-S. Color coded are the surface brightness bins showing the limiting surface brightness for being a LSB galaxies at different redshifts. With the selected sample, it should be possible to find LSB galaxies out to a redshift of $z \sim 0.5$.

higher redshifted galaxy which appears at low surface brightness mimicking a LSB galaxy. Also in this case, where the goal is to search for higher redshifted LSBs, the “Tolman Dimming”

causes problems. Additionally, the limiting central surface brightness for being a LSB galaxy is shifted with increasing redshift to much lower surface brightnesses (see Fig. 6.1). As no distance information is available upto now, one can not select the real LSB galaxies against the cosmological dimmed ones. Distance estimation using photometric redshifts does also not work for the LSB galaxies. As presented in this thesis, in color–color diagrams the LSB galaxies do not follow the classical redshift tracks of the HSB galaxies (Haberzettl et al., 2003). Therefore, it is necessary to obtain spectroscopic distance measurements. With this project, several questions, helping to understand the evolution and formation of LSB galaxies in more detail, will be addressed. First of all, the question will be answered whether it is possible to find any LSB galaxies at higher redshifts and which number densities they have at these redshifts. From the results of this study, information can be obtained about how common LSB galaxies are at different redshifts. For the confirmed higher redshifted LSB sample, the SFRs will be measured giving information about the evolutionary stage of the LSBs at different redshifts. The derived LSB sample will be grouped into different redshift bins for which mean SFRs will be calculated. Following the redshift paths, information about the evolution of the SFR of the LSB galaxies can be obtained. Based on the proposed evolutionary models for the local LSBs, one can expect a peak in the SFR at redshifts around $z \sim 0.4$ and a decrease towards lower redshifts. In order to derive SFRs for the LSB sample, it is planned to follow the formalism of Kennicutt (1983, 1992b) who derived SFRs using $H\alpha$ and $[OII]$ emission line fluxes. It can be assumed to extract global SFRs for the LSB sample without large corrections as necessary for the SDSS (Hopkins et al., 2003), due to the fact that the observed galaxies are comparable in size to the sizes of the used slits. The detected emission line fluxes represent a lower limit which will be close to the total emission of the galaxies. As described before, for the local LSB sample the chemical composition of the derived higher redshifted LSBs will also be analyzed. The analysis will again be performed for different redshift bins for which it is planned to estimate mean oxygen abundances. With this mean abundances, it will be possible to follow the evolution of the chemical composition with redshift. Finally, the flux calibrated spectra of the LSB galaxies will be compared to the library of synthetic SEDs (described in Sect. 4) in order to derive SFHs, star formation laws as well as mean ages of the dominant stellar population for the observed sample. From all these results, we will get information about the evolutionary stages of the LSB galaxies at different redshifts. This will also be a critical test for the evolution scenario sketched in this thesis.

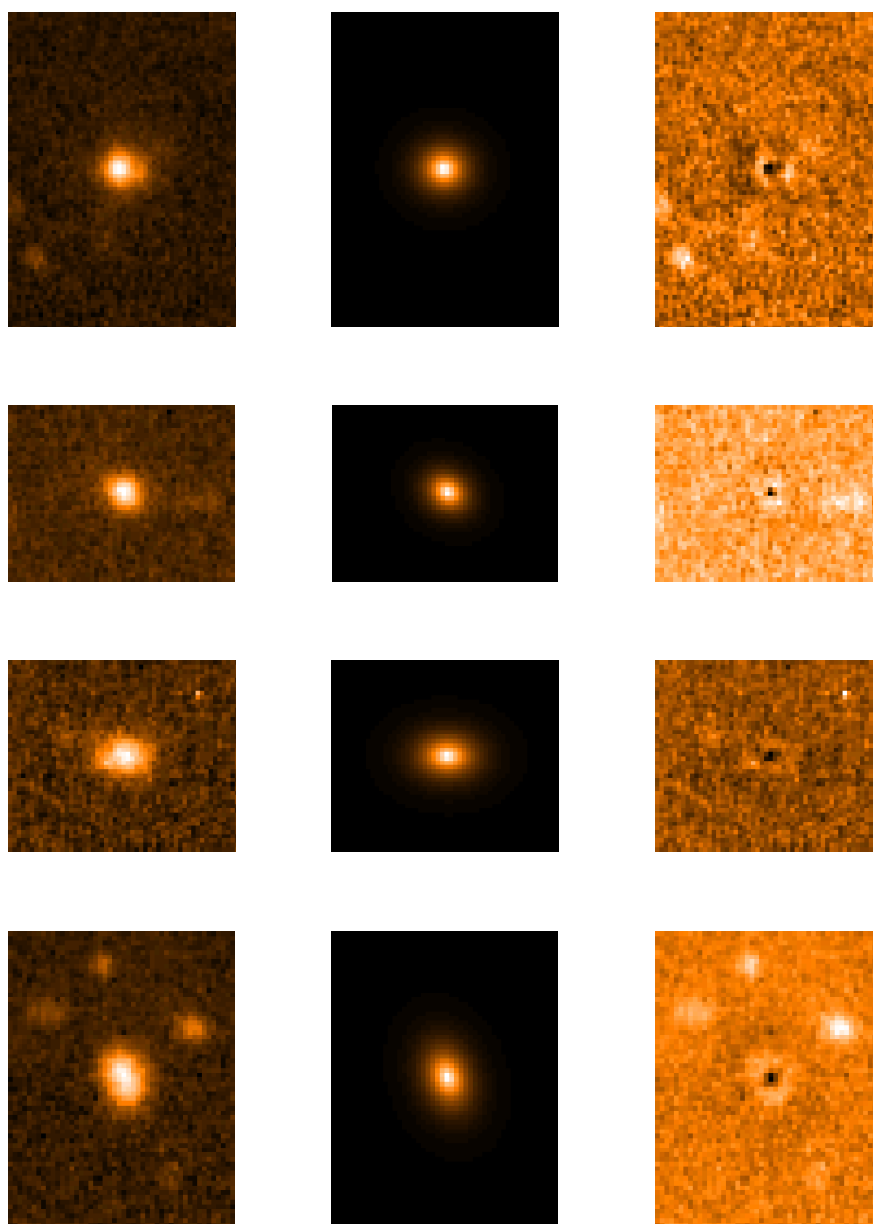


Figure 6.2: Four examples of typical, selected LSB candidates. In the left row, the real images of the galaxies are shown. The middle row presents the models resulting from the photometric analysis using Galfit (Peng et al., 2002). The right row shows the residual image after subtracting the model from the real galaxy image.

Appendix A

HDF-S Sample

In this Appendix, the data used for the analysis will be presented. For every spectroscopically observed galaxy of the HDF-S sample (11 galaxy), the optical image as well as the 1D and 2D spectra are shown. The optical images origin from the B_W data of the NOAO survey and cover $2\text{ arcmin} \times 2\text{ arcmin}$ in size. The B_W data of the HDF-S were observed as a test field for the NOAO Deep wide-field survey. For the observation, the CTIO Blanco 4 m telescope, equipped with the Big Throughput Camera—a four CCD mosaic iager—, was used. The final image was combined out of 38 dithered 840 s exposures resulting in a total exposure time of 32000 s. Although performing the observation with a dither pattern, the final data still consist of gabs as well as a varying sensitivity. The observation of the spectroscopic data was obtained with the EFOSC2 spectrograph at the ESO 3.6 m telescope. For 8 galaxies of the sample, two 1800 s exposures were derived. For the rest of the sample (3 galaxies), only one 1800 s exposure was obtained. The black lines overlaid to the images represent the position and orientation of the slit used with the EFOSC2 spectrograph. The slit length of the slit used with the EFOSC2 spectrograph is about $\sim 5\text{ arcmin}$. The spectra cover the wavelength range from 3400 \AA to 7400 \AA . Along the spatial axis, the presented 2D spectra just show the emission of the observed galaxy. In addition, on the bottom of the 2D spectra, the intensity is indicated due to color coding. The 1D spectra were extracted summing up all light along the spatial axis shown in the 2D spectra. The integration along the spatial axis results in the signal-to-noise ratios needed in order to obtain SFHs from the spectra.

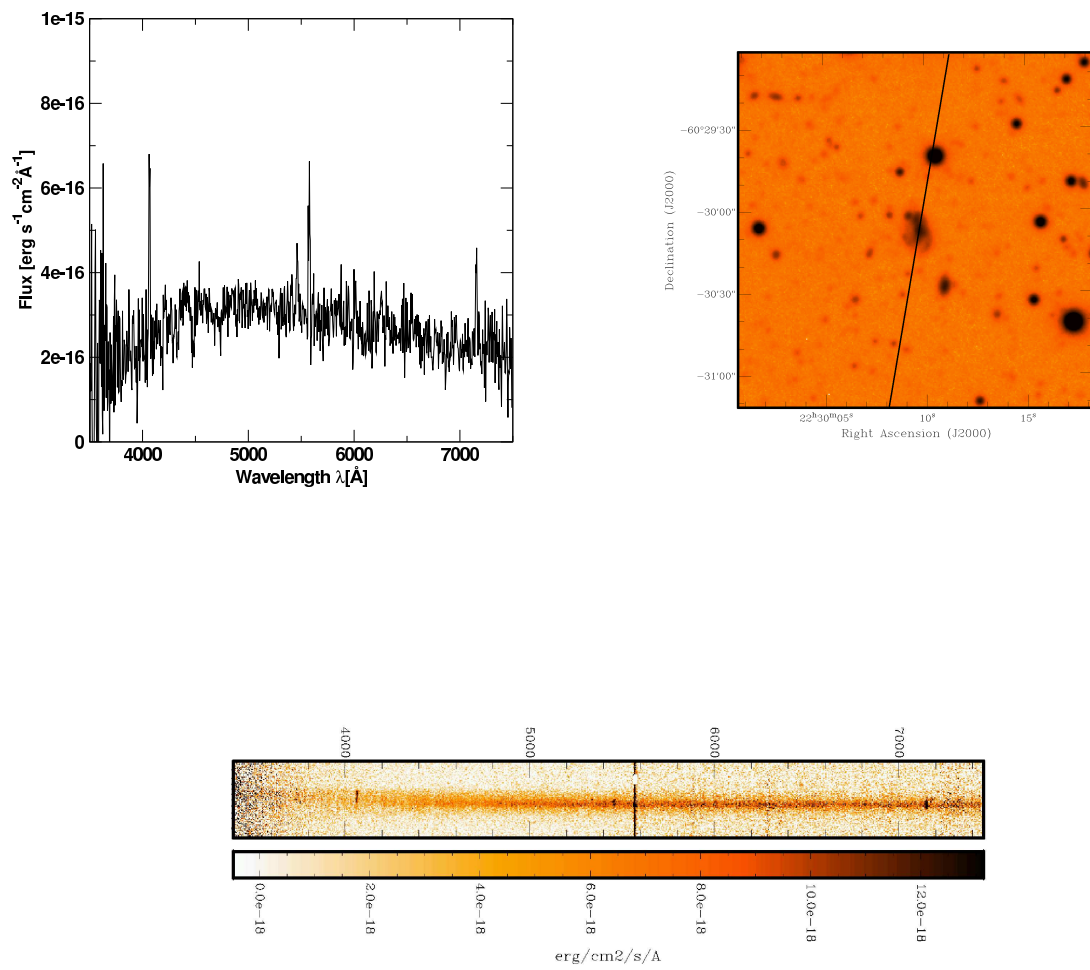


Figure A.1: HBDP22300-60300

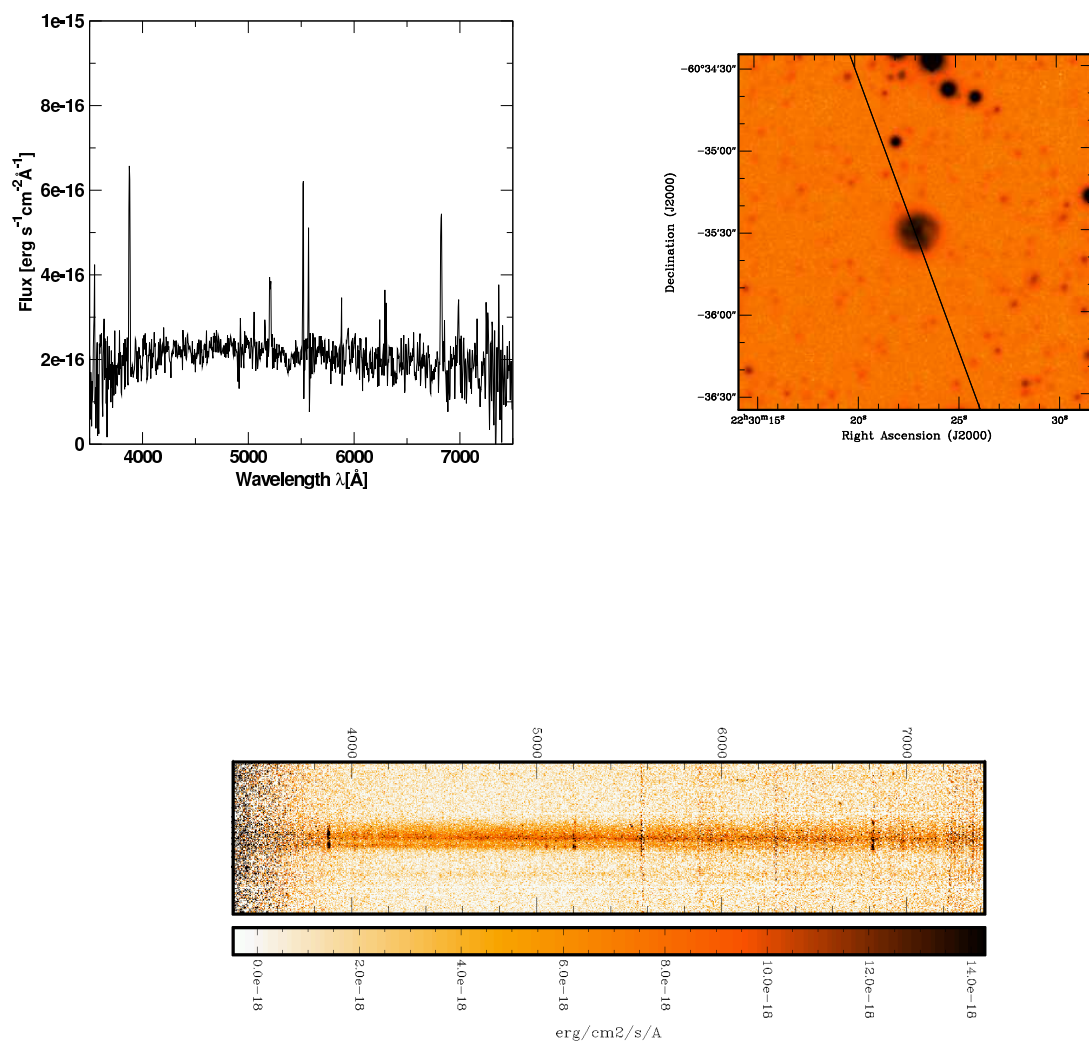


Figure A.2: HBDP22302-60352

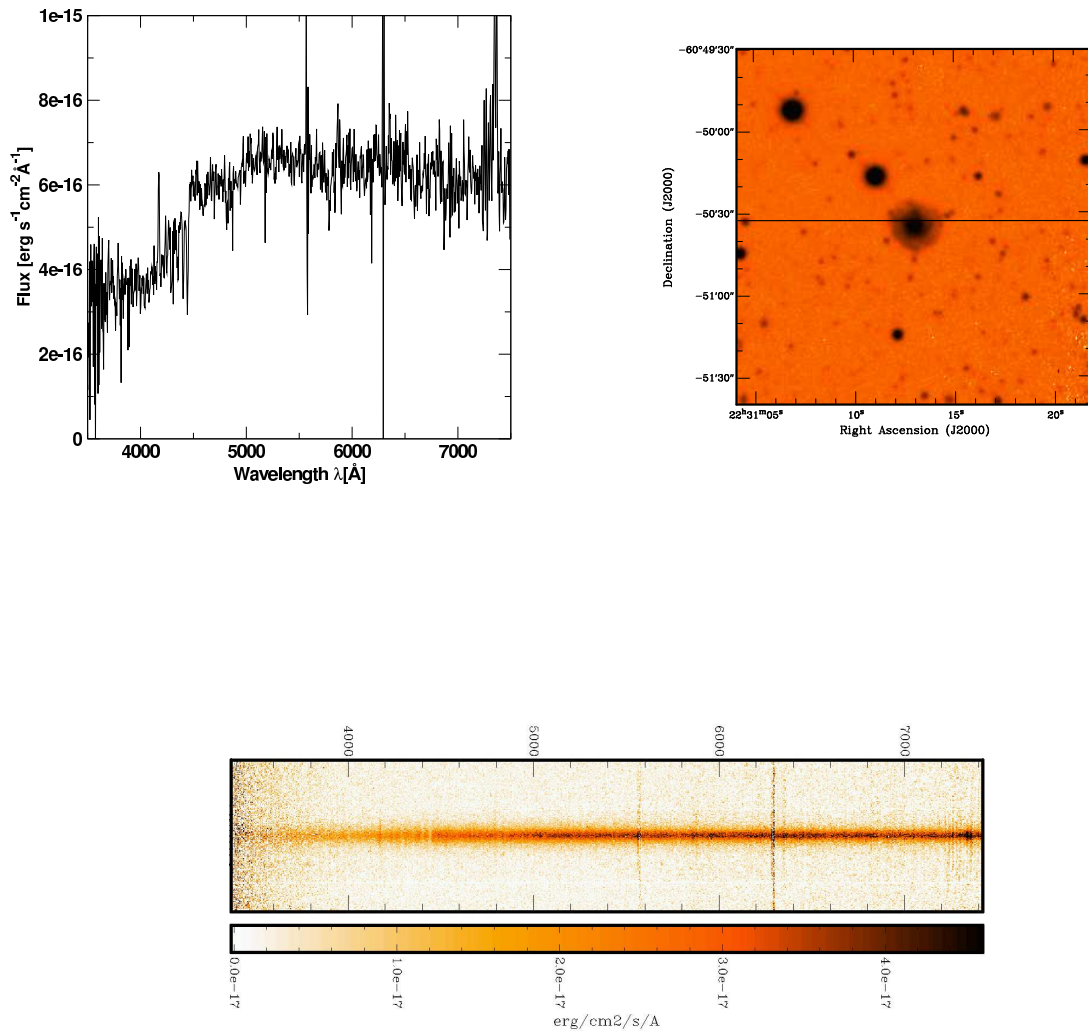


Figure A.3: HBDP22311-60503

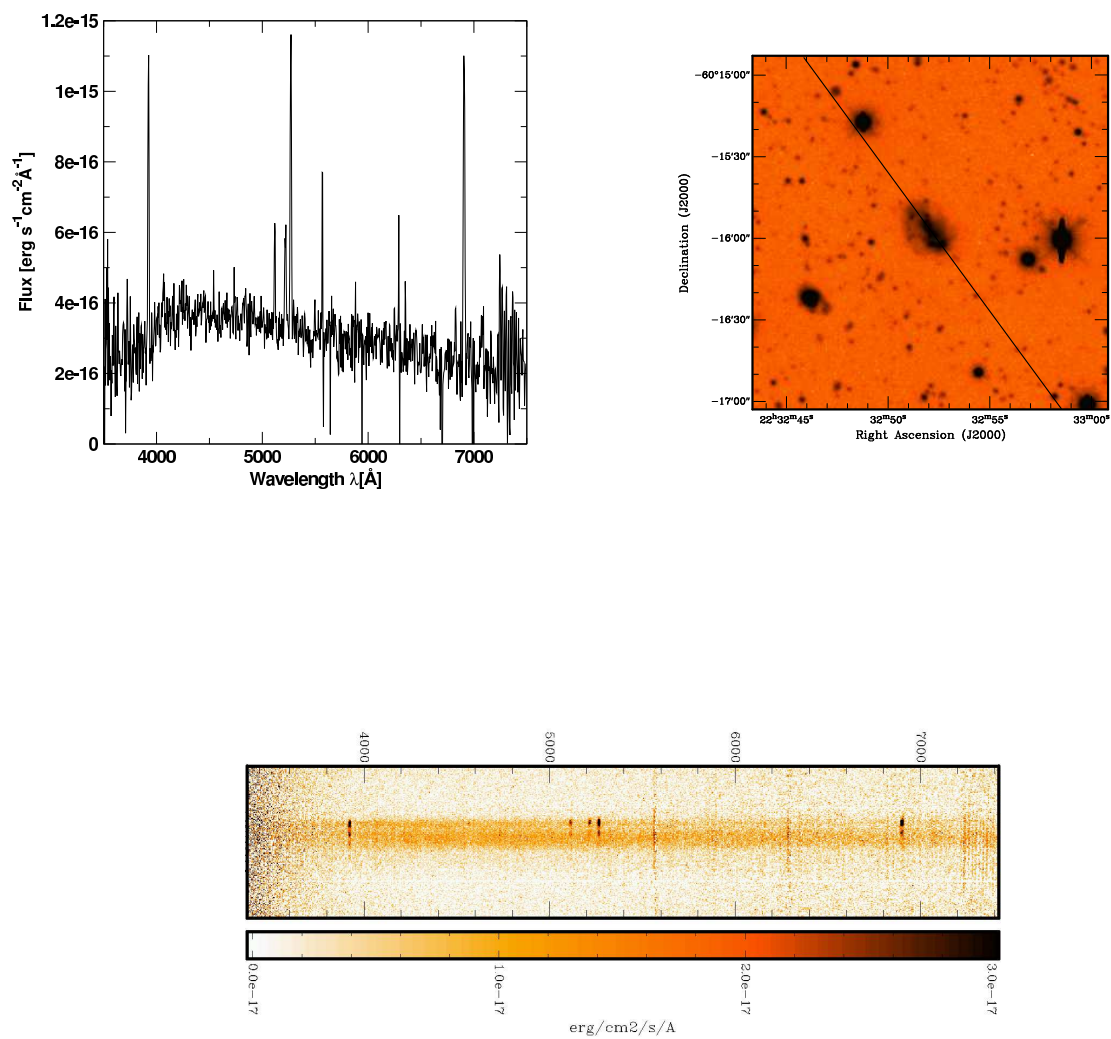


Figure A.4: HBDP22325-60155

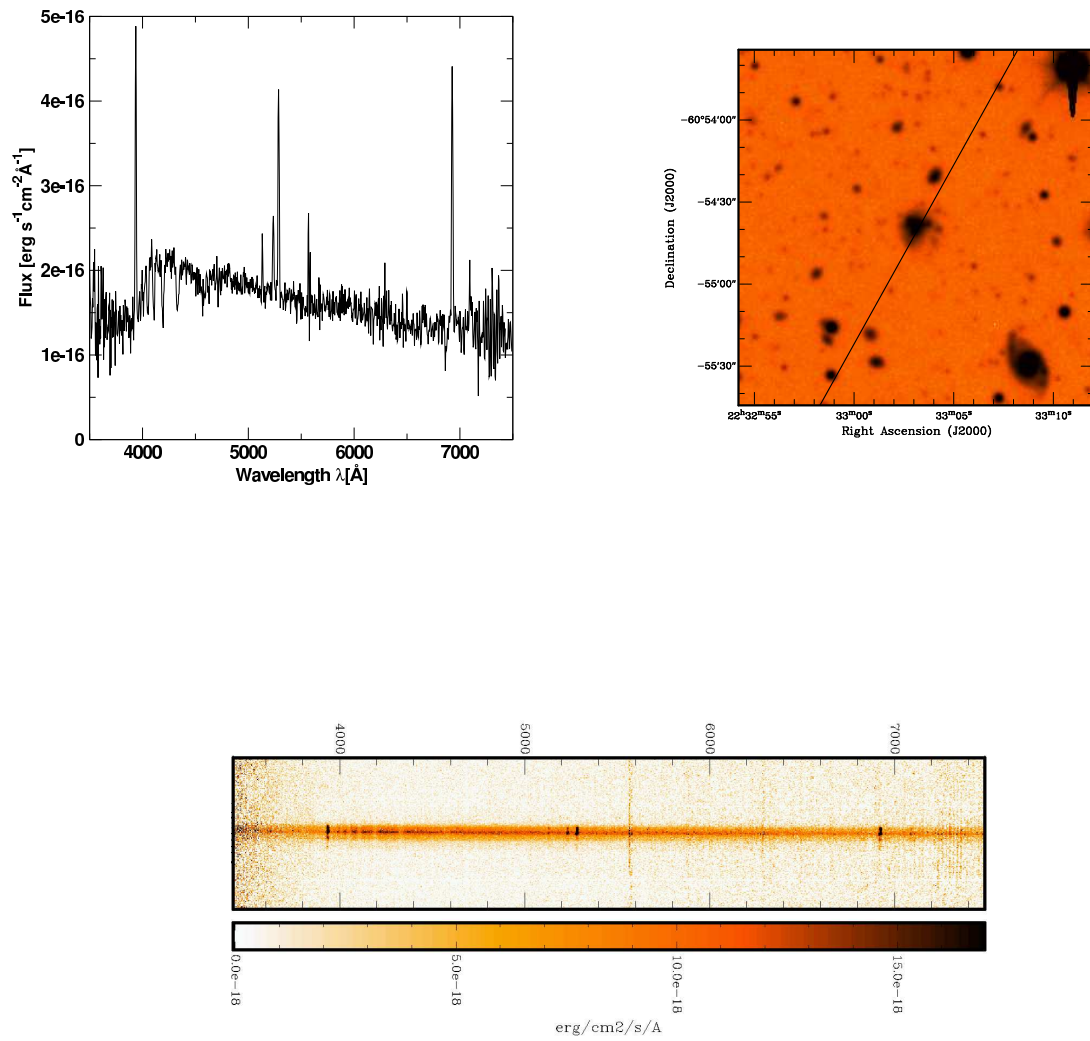


Figure A.5: HBDP22330-60543

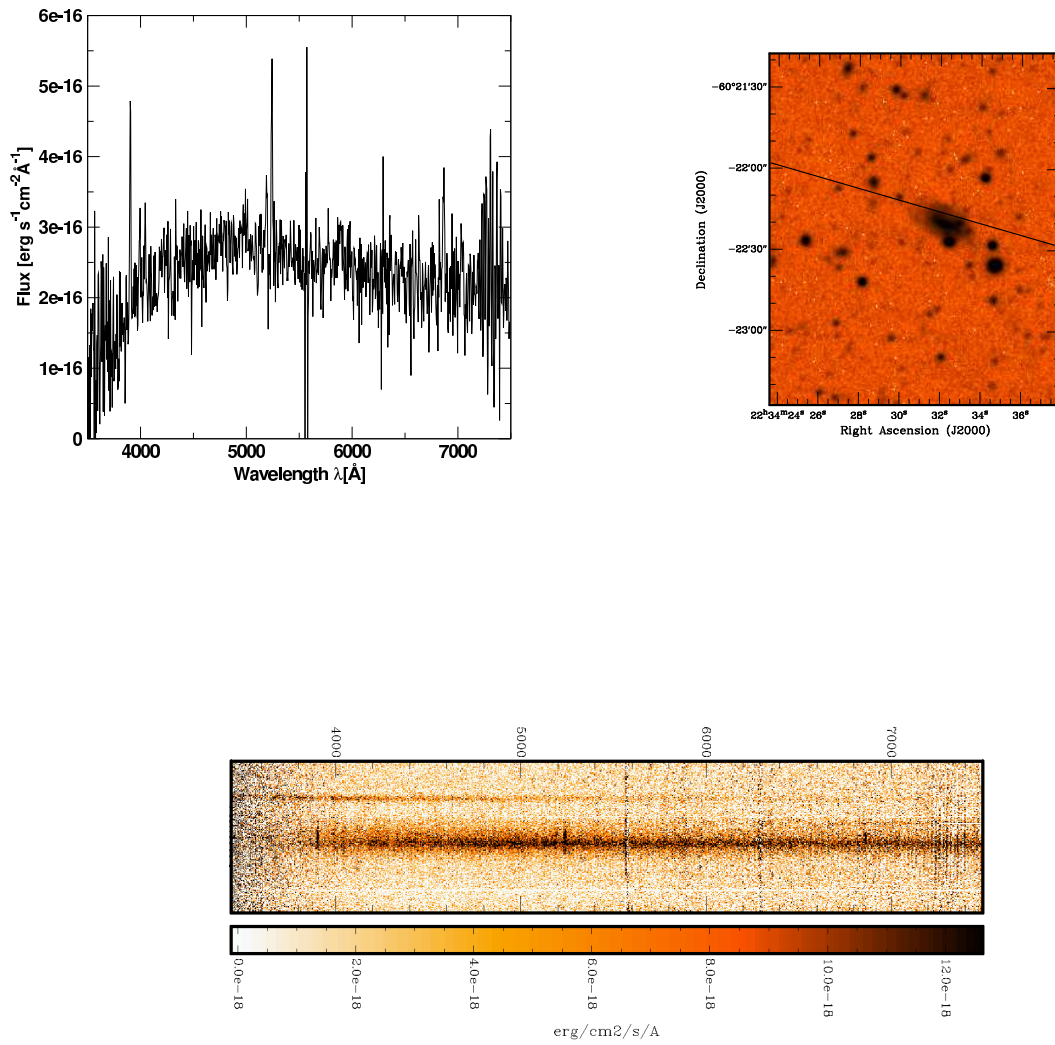


Figure A.6: HBDP22343-6022

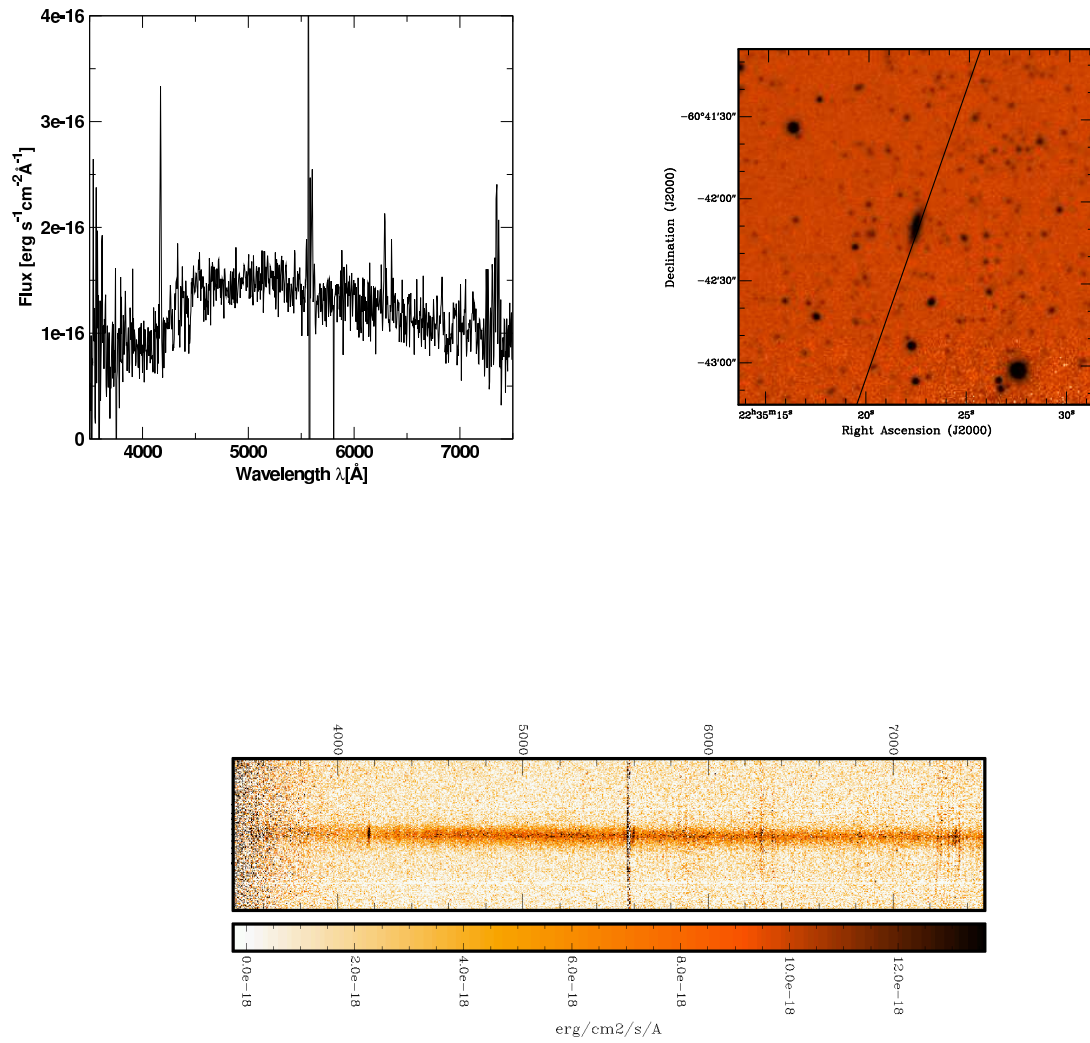


Figure A.7: HBDP22352-60420

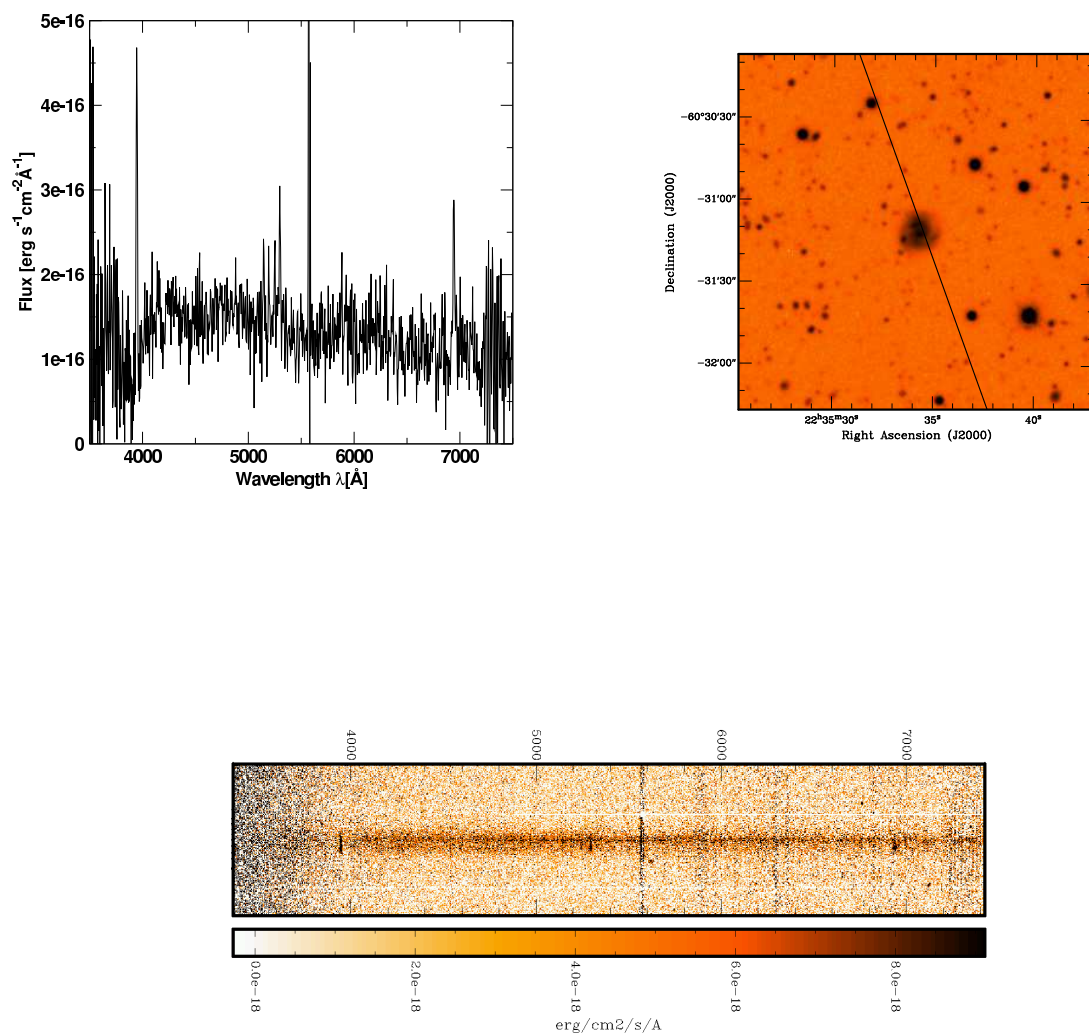


Figure A.8: HBDP22353-60311

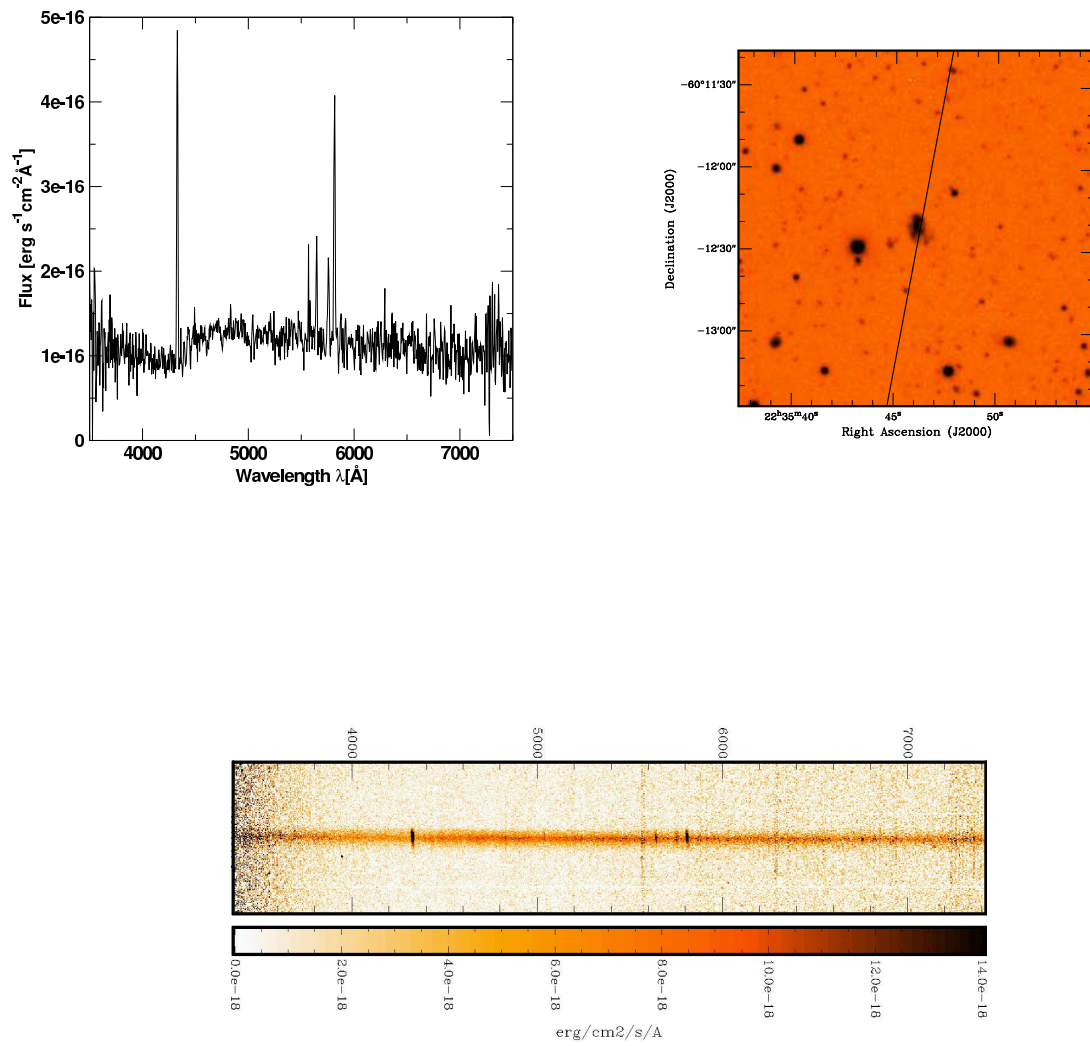


Figure A.9: HBDP22354-60122

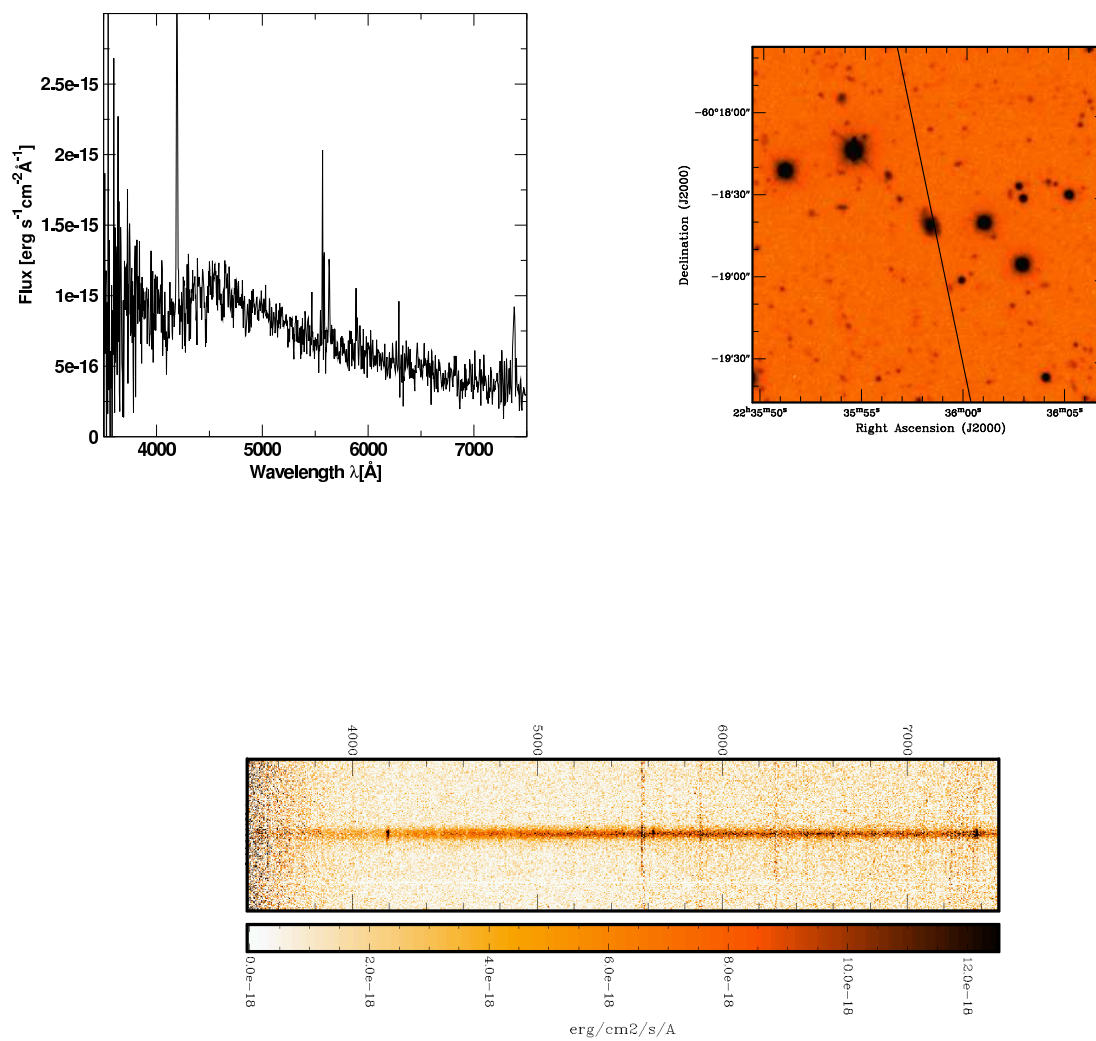


Figure A.10: HBDP22355-60183

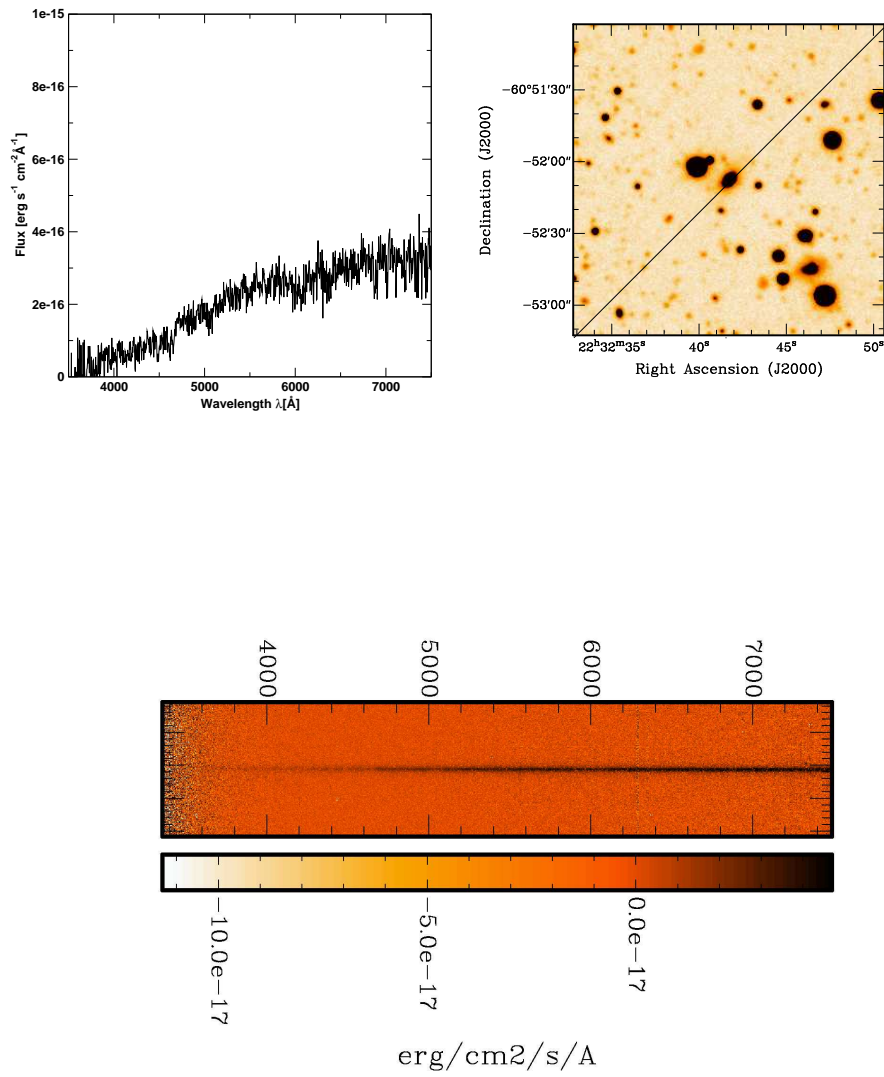


Figure A.11: HBDP22324-60520

Appendix B

PÉGASE parameter study

In order to obtain SFHs for the studied galaxy samples, the synthesis evolution model PÉGASE was used. In the beginning, an extensive parameter study was done verifying between parameters significantly influencing the shape of the modeled SEDs in the optical wavelength range and those which have no influence on the SED (see Sect. 4.2.2). The following diagrams show the results of this parameter study. For this analysis, eight parameters were varied.

- Initial Mass Function (IMF)
- upper and lower mass limit
- Star Formation Law (SFLaw)
- Star Formation Rate (SFR)
- extinction
- SNII model
- fraction of binary stars
- fraction of substellar objects

The SFHs should be derived from measured optical spectra of galaxies. Therefore, the parameter study is limited to the wavelength range from 3400 Å to 7400 Å. In order to be comparable to the measured spectra, all modeled SEDs were normalized to the flux at 5500 Å. From the parameters (SFLaw, SFR, extinction), which show a significant influence on the modeled SEDs, a library was built. This library was then used in order to obtain SFHs of the observed galaxy samples.

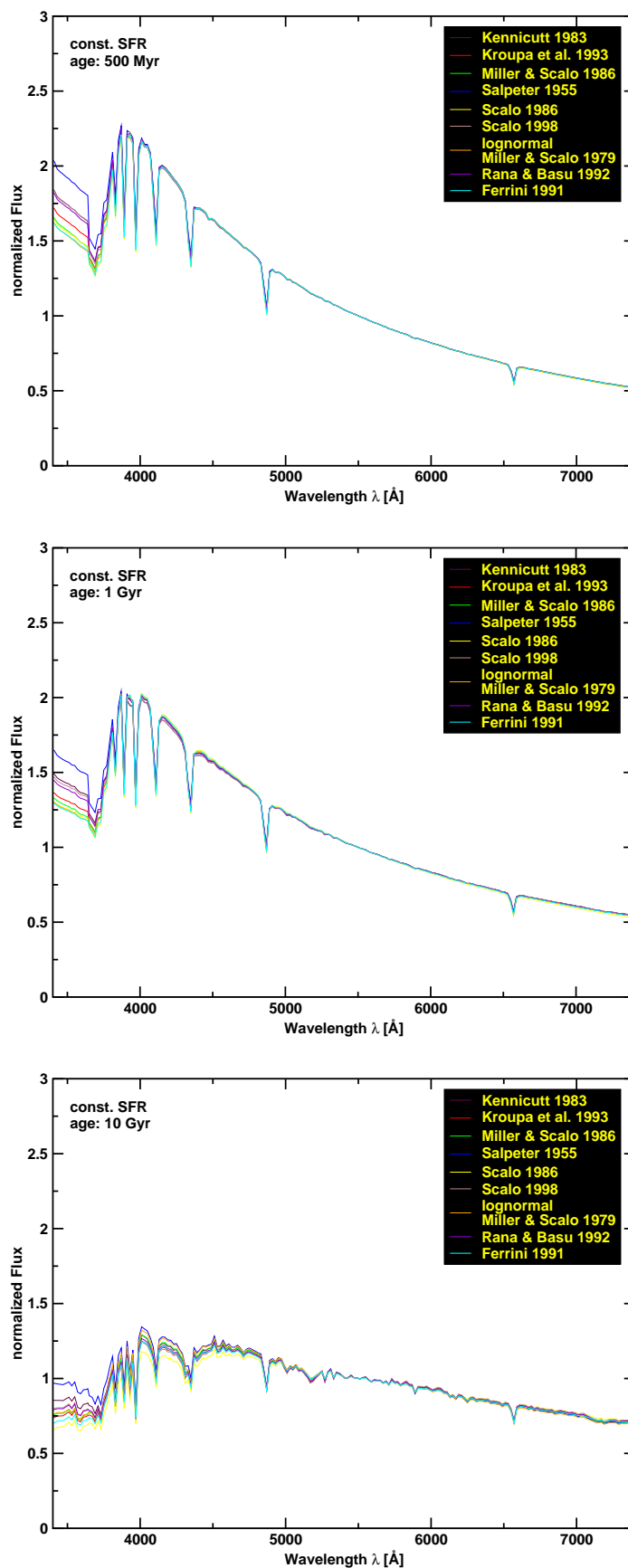


Figure B.1: SEDs modeled using different IMFs for a constant SFR. Three diagrams are shown for three different ages of the SEDs (500 Myr, 1 Gyr, 10 Gyr).

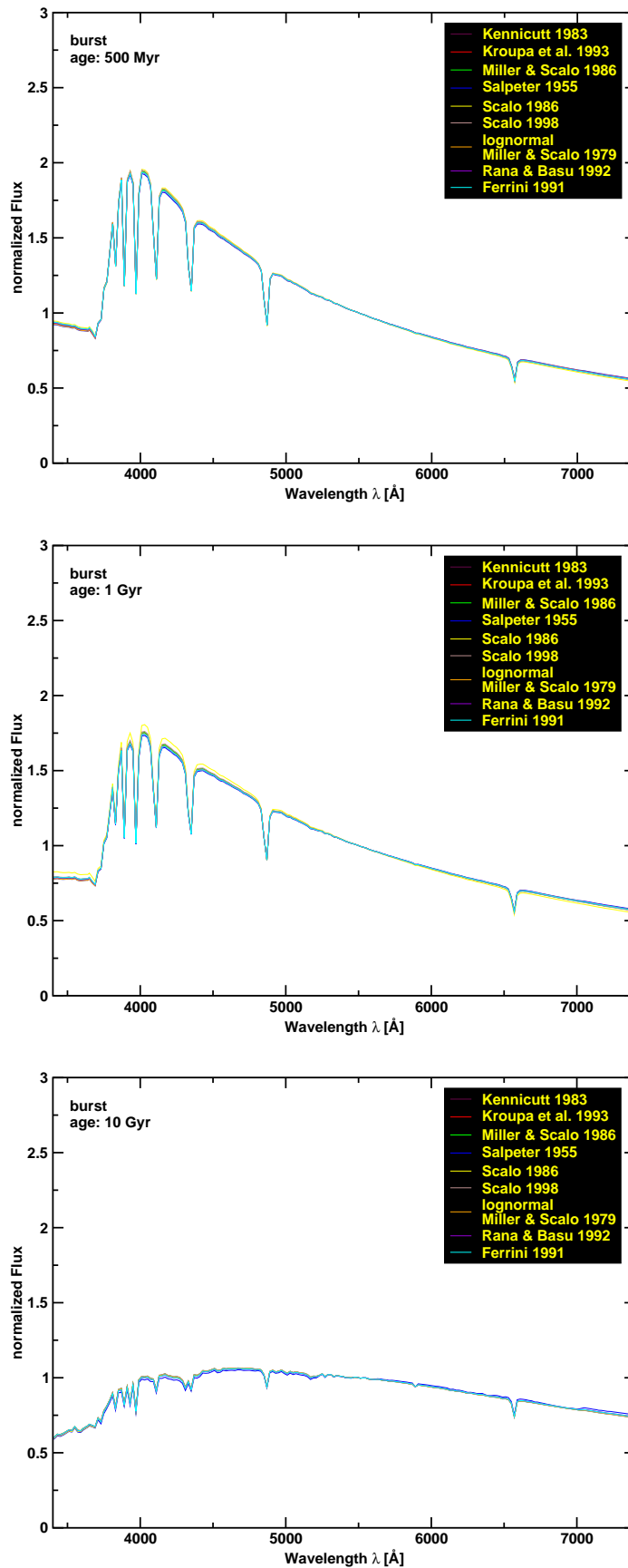


Figure B.2: SEDs modeled using different IMFs and an one star burst scenario. Three diagrams are shown for three different ages of the SEDs (500 Myr, 1 Gyr, 10 Gyr).

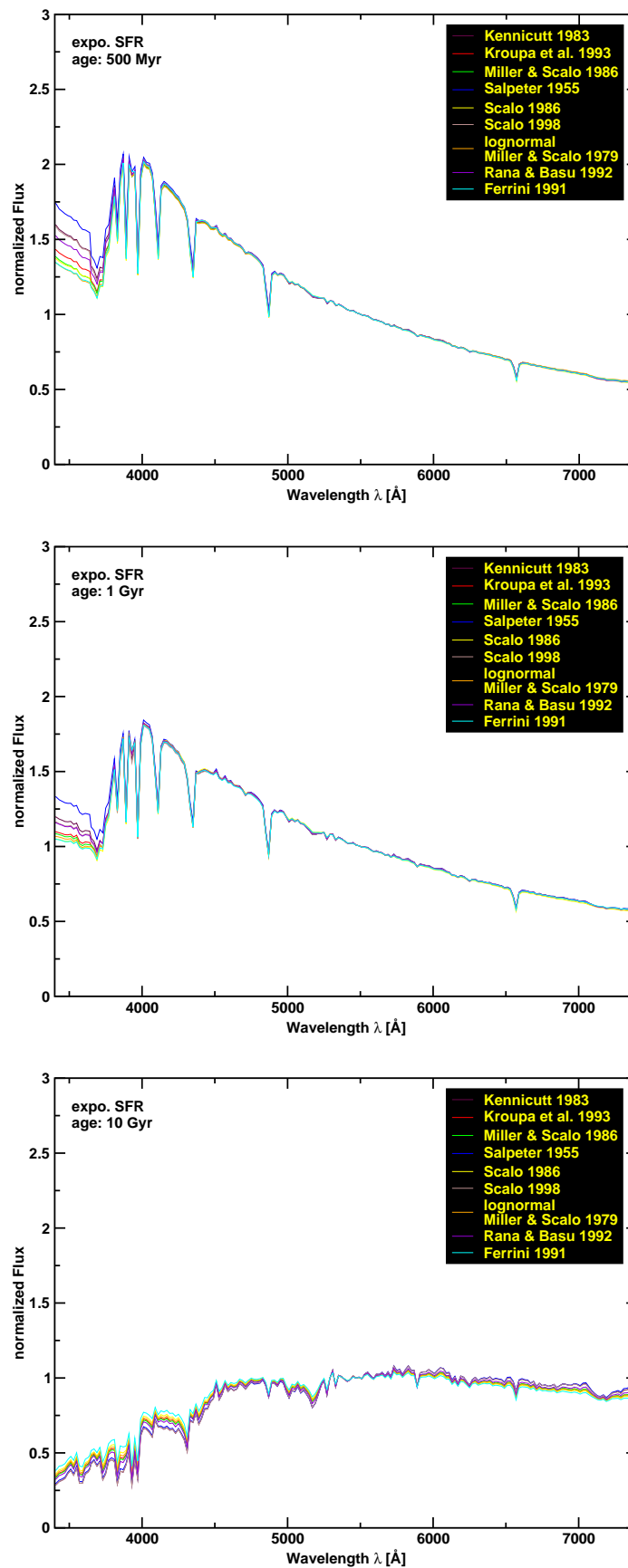


Figure B.3: SEDs modeled using different IMFs and an exponential SFR. Three diagrams are shown for three different ages of SEDs (500 Myr, 1 Gyr, 10 Gyr).

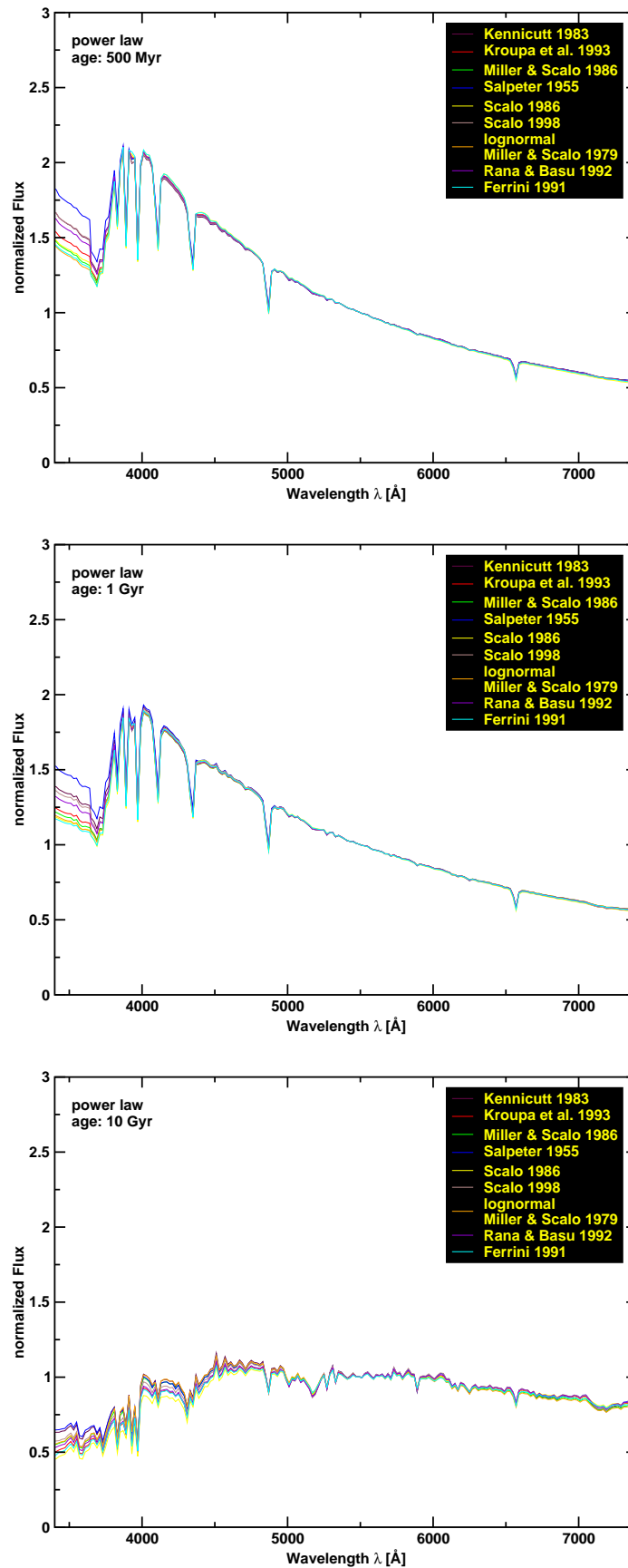


Figure B.4: SEDs modeled using different IMFs and a SFR following a power law. Three diagrams are shown for three different ages of the SEDs (500 Myr, 1 Gyr, 10 Gyr).

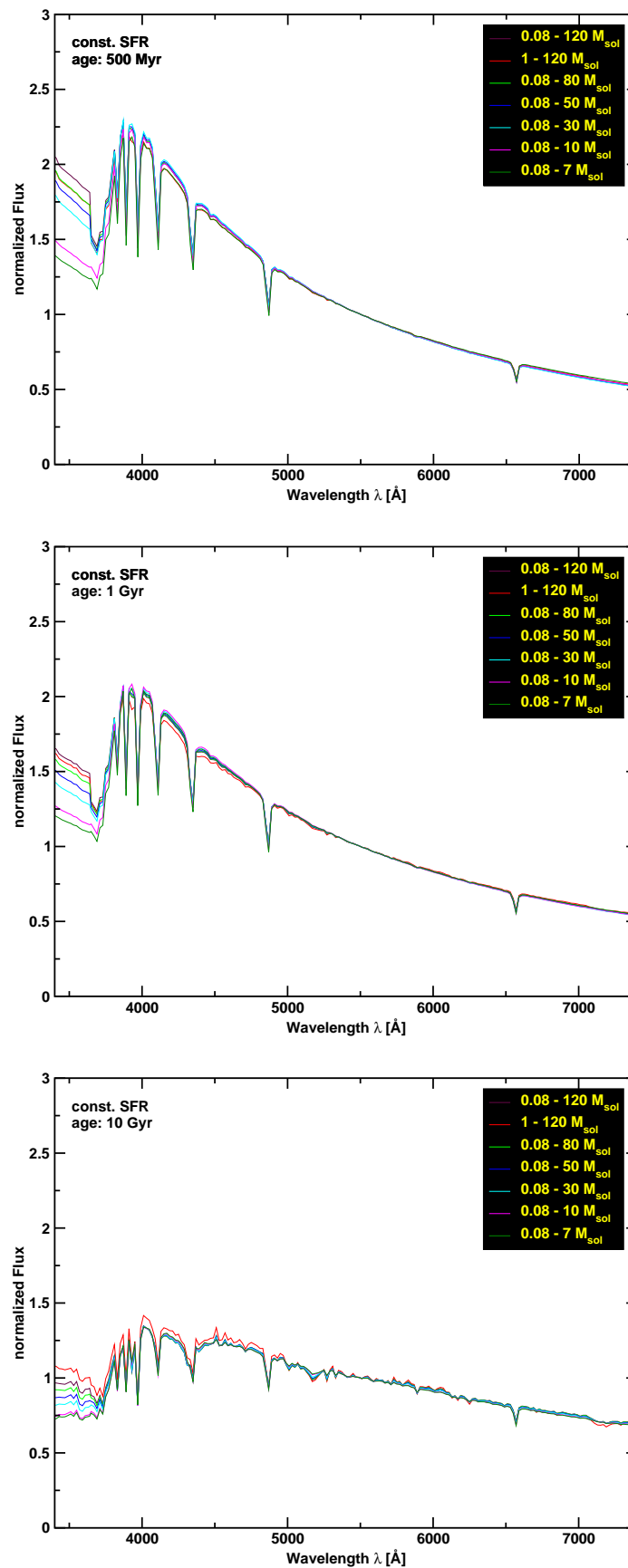


Figure B.5: SEDs modeled using different upper and lower mass limit and a constant SFR. Three diagrams are shown for three different ages of the SEDs (500 Myr, 1 Gyr, 10 Gyr).

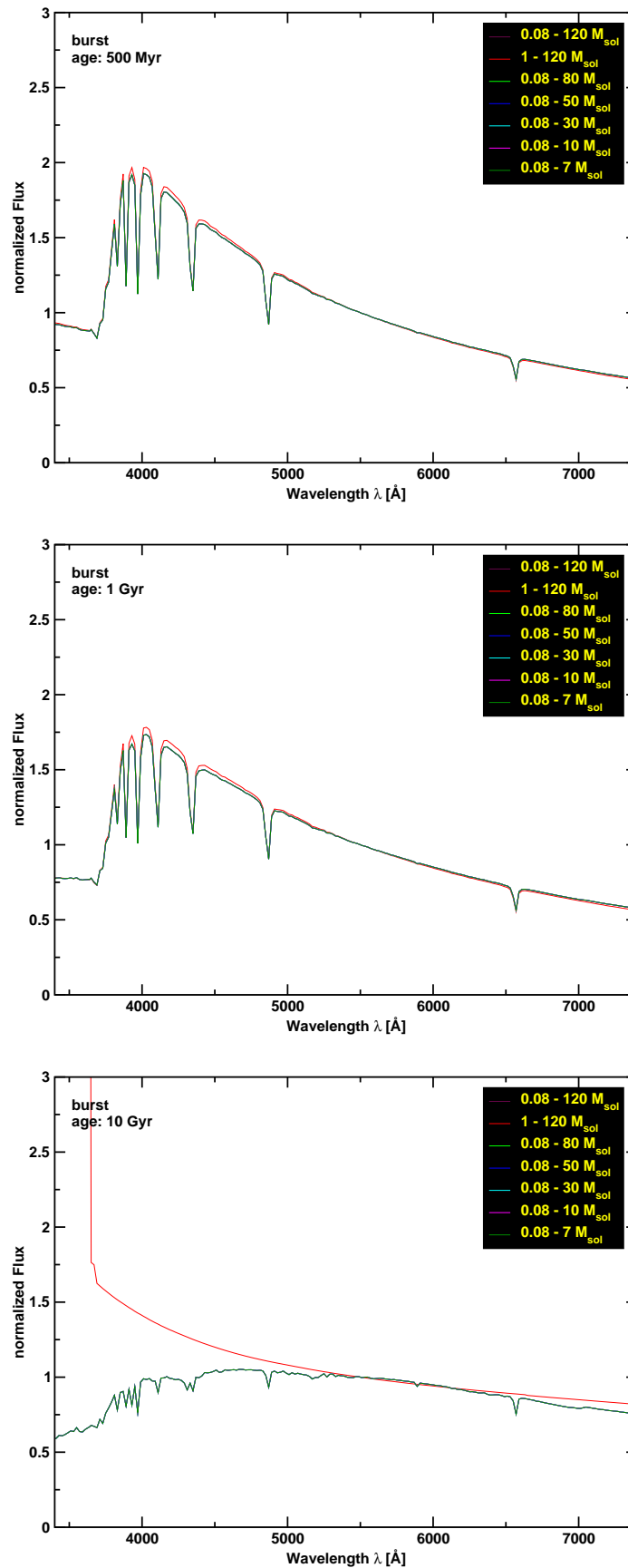


Figure B.6: SEDs modeled using different upper and lower mass limits and an one star burst scenario. Three diagrams are shown three for different ages of the SEDs (500 Myr, 1 Gyr, 10 Gyr).

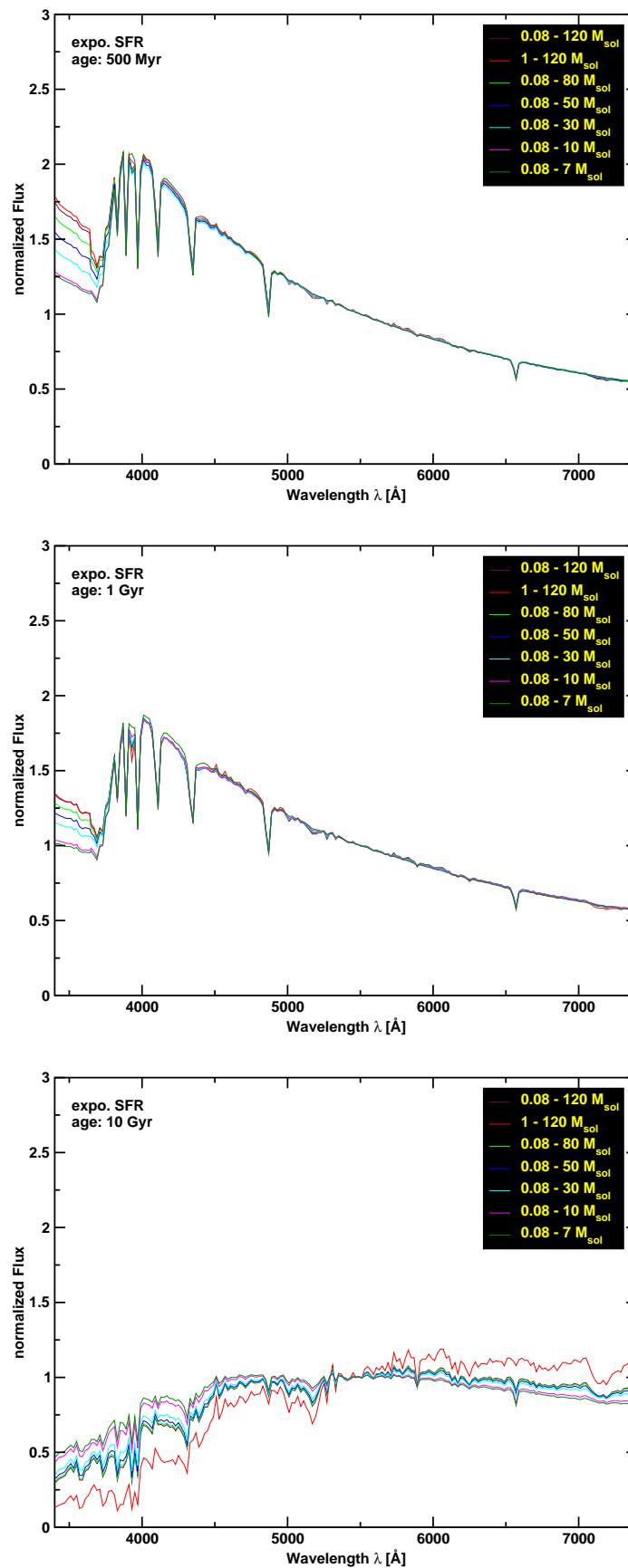


Figure B.7: SEDs modeled using different upper and lower mass limits and an exponential SFR. Three diagrams are shown for three different ages of the SEDs (500 Myr, 1 Gyr, 10 Gyr).

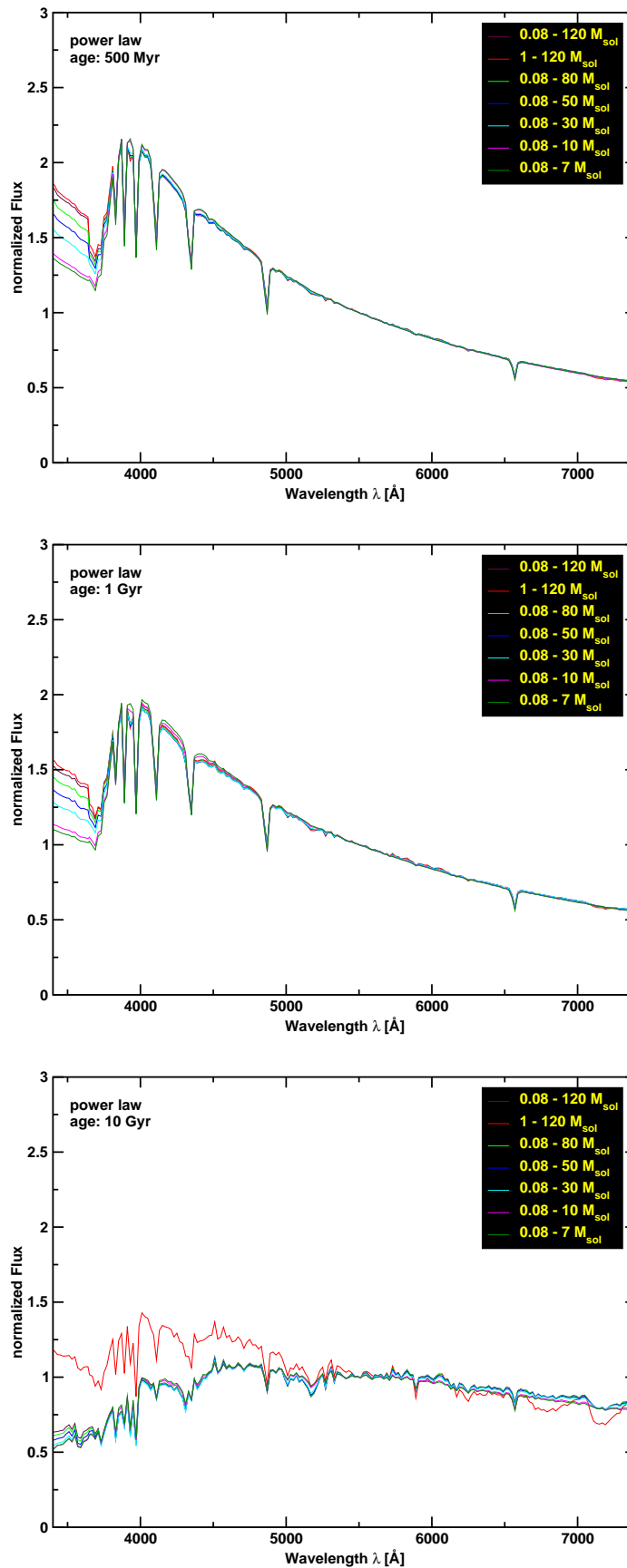


Figure B.8: SEDs modeled using different upper and lower mass limits and a SFR following a power law. Three diagrams are shown for three different ages of the SEDs (500 Myr, 1 Gyr, 10 Gyr).

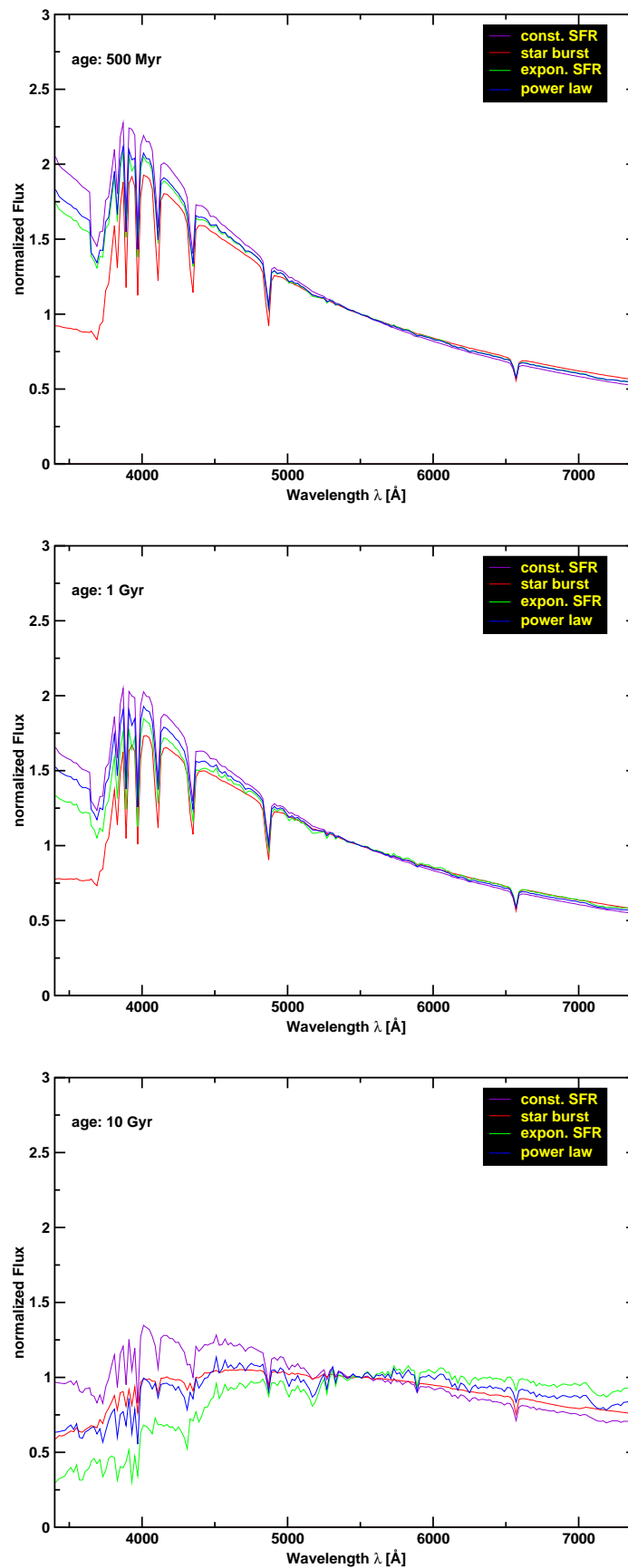


Figure B.9: SEDs modeled using different Star Formation Laws. Three diagrams are shown for three different ages of the SEDs (500 Myr, 1 Gyr, 10 Gyr).

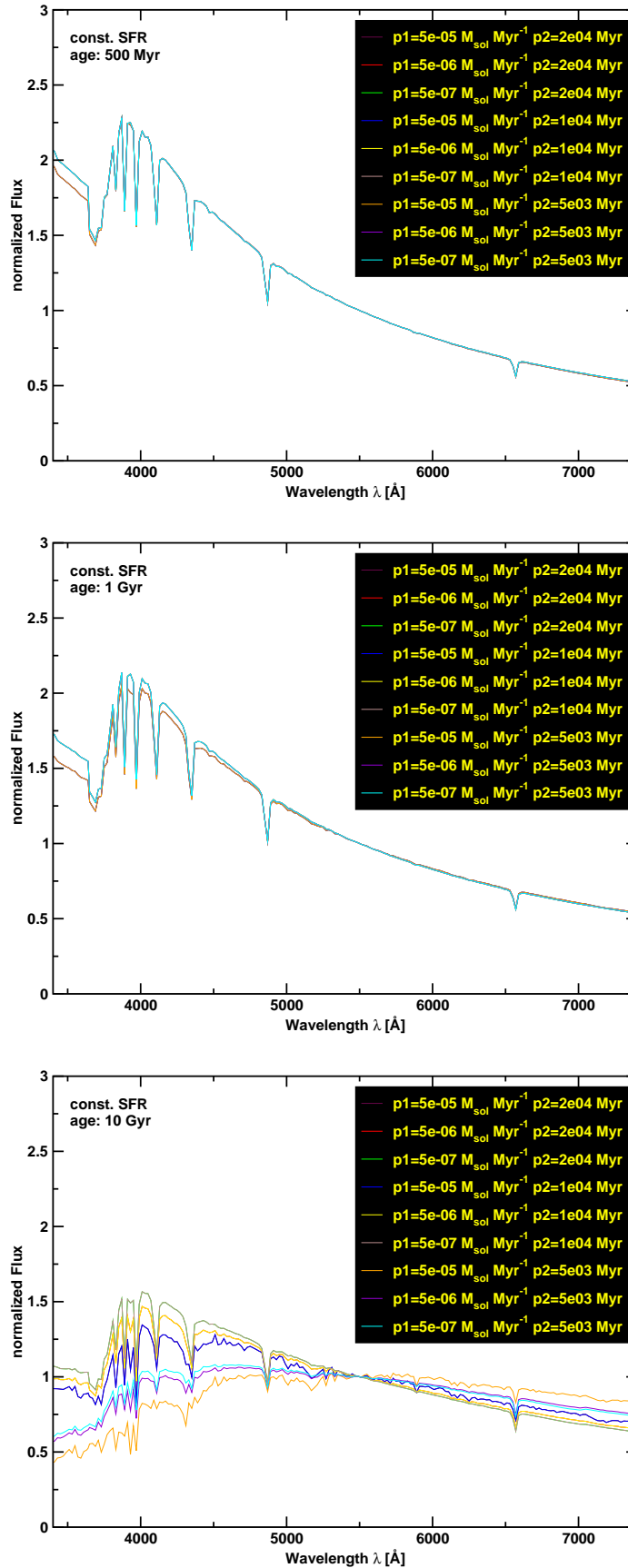


Figure B.10: SEDs modeled using different SFRs and a constant SFR. Three diagrams are shown for three different ages of the SEDs (500 Myr, 1 Gyr, 10 Gyr).

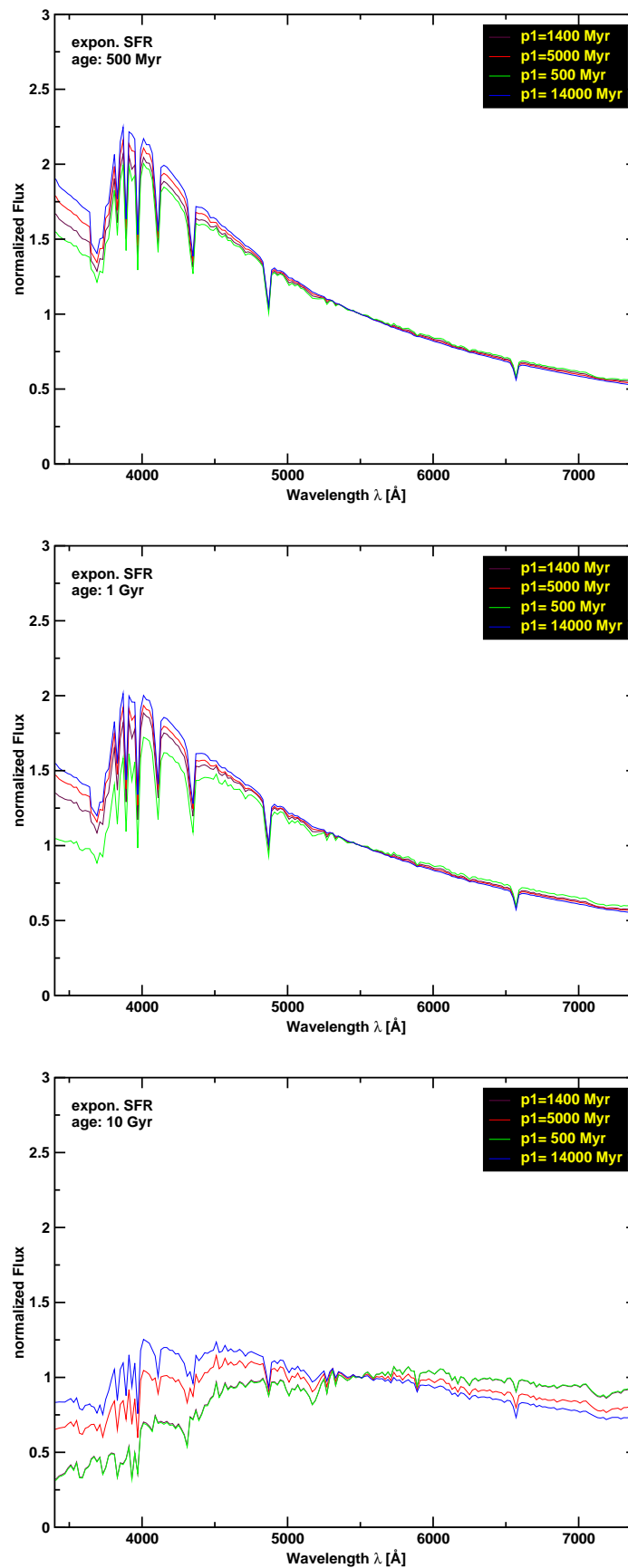


Figure B.11: SEDs modeled using different SFR and an exponential SFR. The SFR is varied modeling SEDs with different decay times τ (500 Myr, 1400 Myr, 5000 Myr, 14000 Myr). Three diagrams are shown for three different ages of the SEDs (500 Myr, 1 Gyr, 10 Gyr).

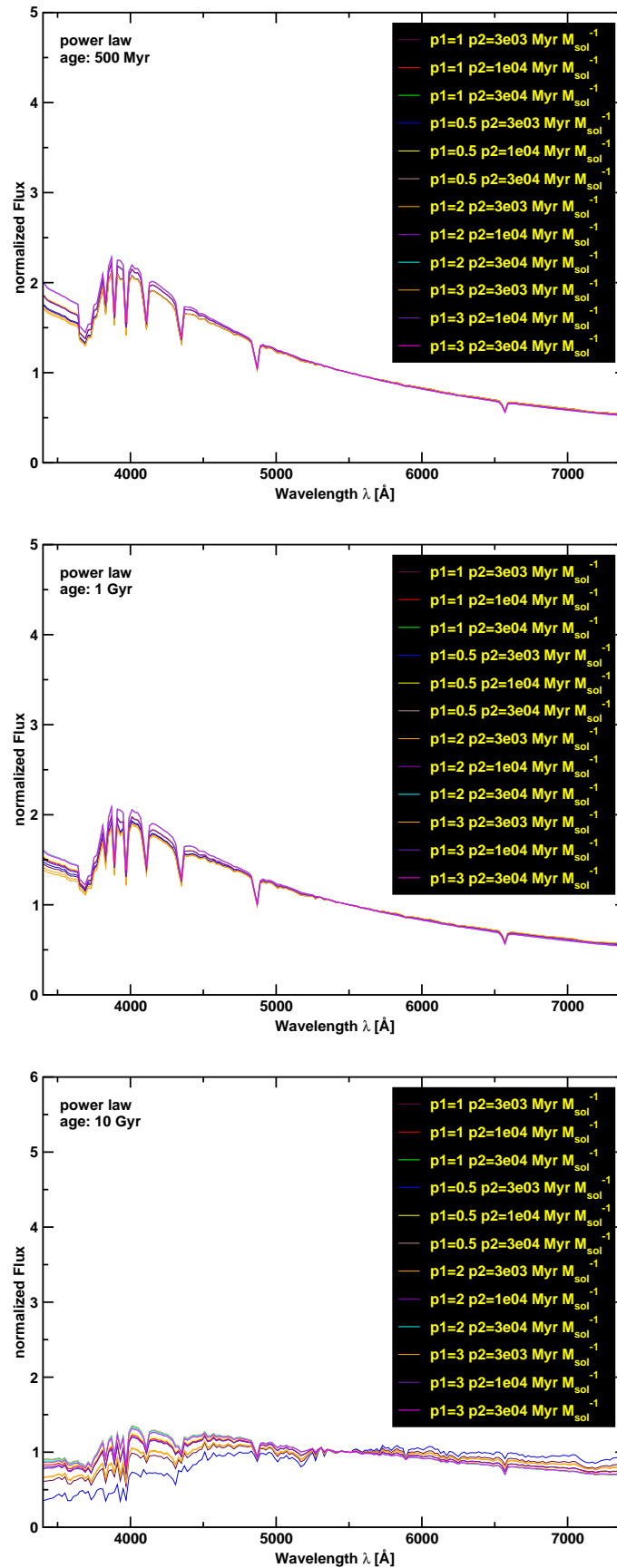


Figure B.12: SEDs modeled using different SFRs. The SFRs following a power law. Three diagrams are shown for three different ages of the SEDs (500 Myr, 1 Gyr, 10 Gyr).

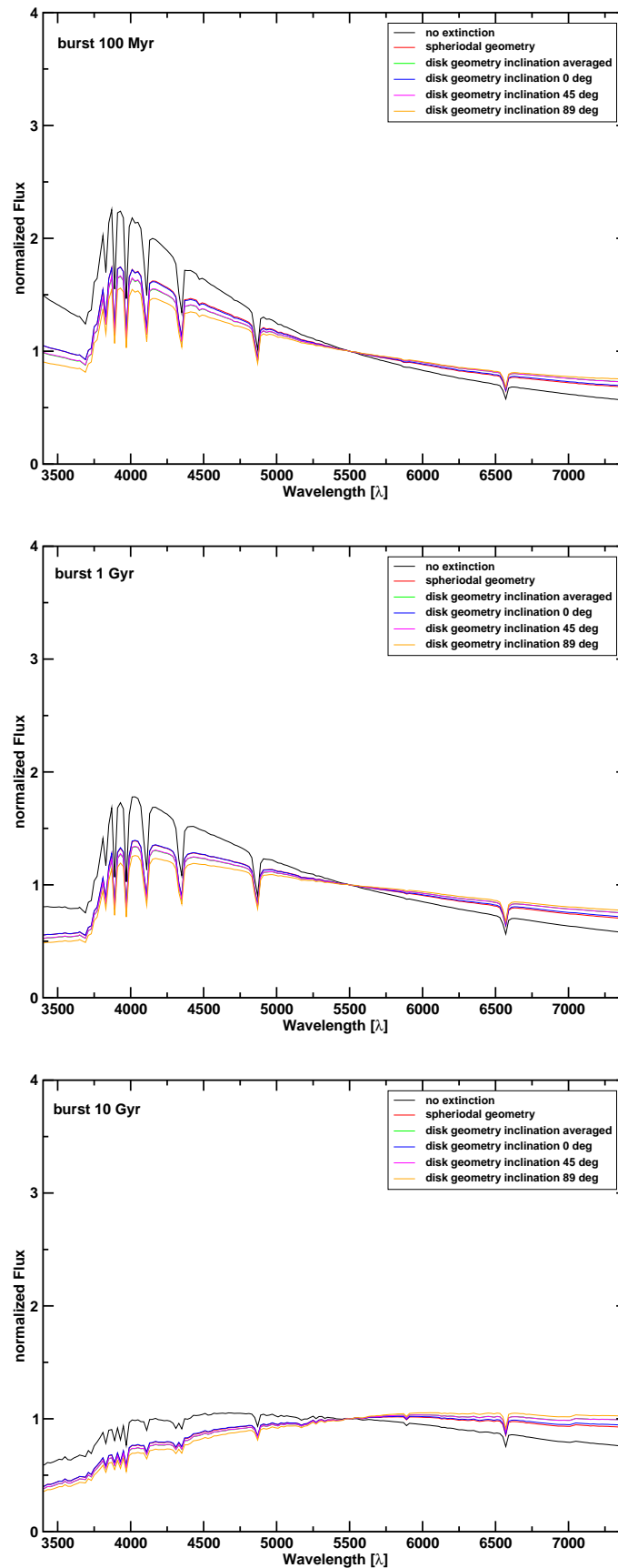


Figure B.13: SEDs modeled using different extinction laws and an one star burst scenarios. Three diagrams are shown for three different ages of the SEDs (500 Myr, 1 Gyr, 10 Gyr).

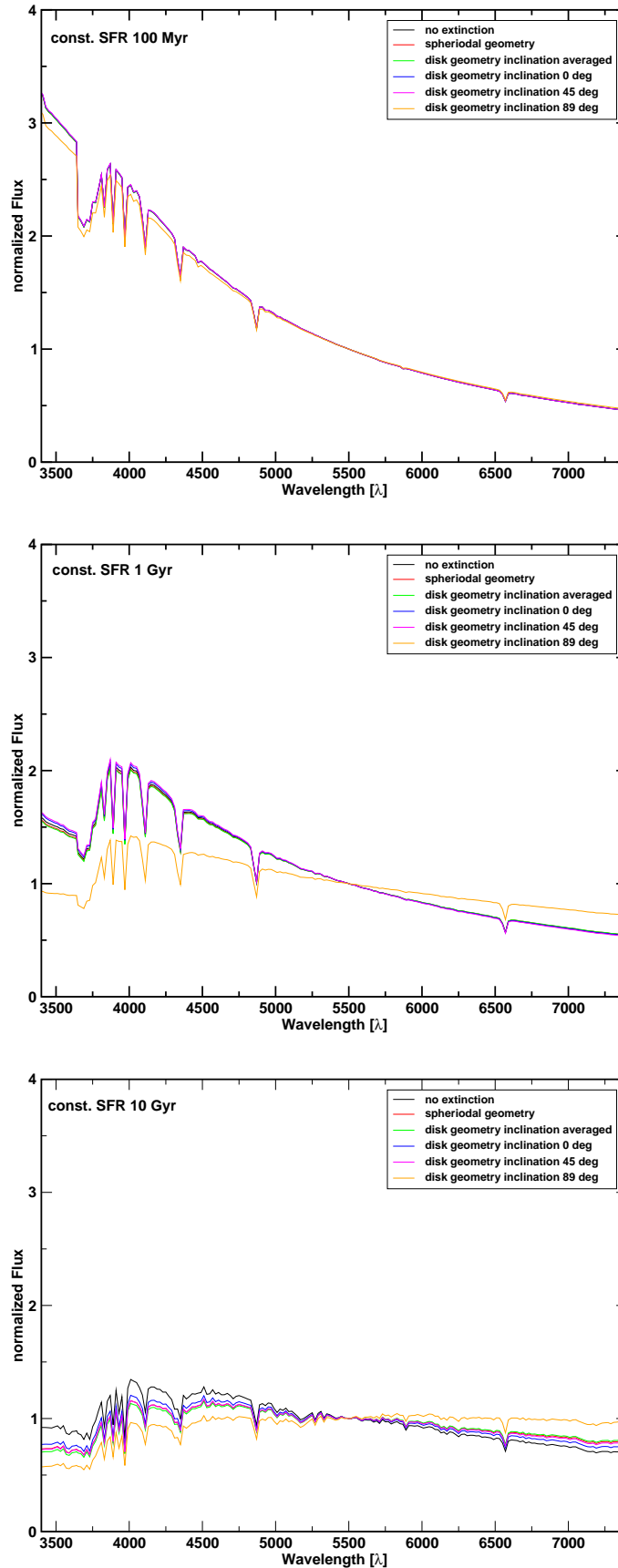


Figure B.14: SEDs modeled using different extinction laws and a constant SFR. Three diagrams are shown for three different ages of the SEDs (500 Myr, 1 Gyr, 10 Gyr).

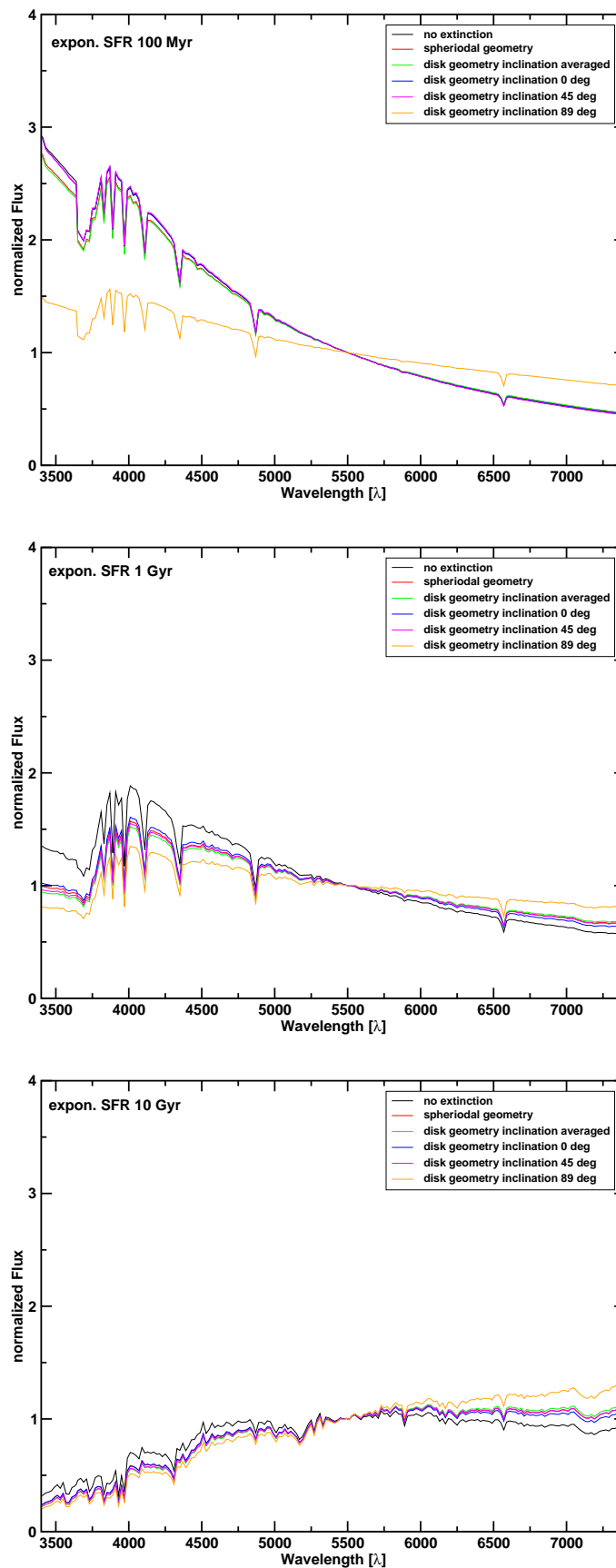


Figure B.15: SEDs modeled using different extinction laws and a exponential SFR. Three diagrams are shown for three different ages of the SEDs (500 Myr, 1 Gyr, 10 Gyr).

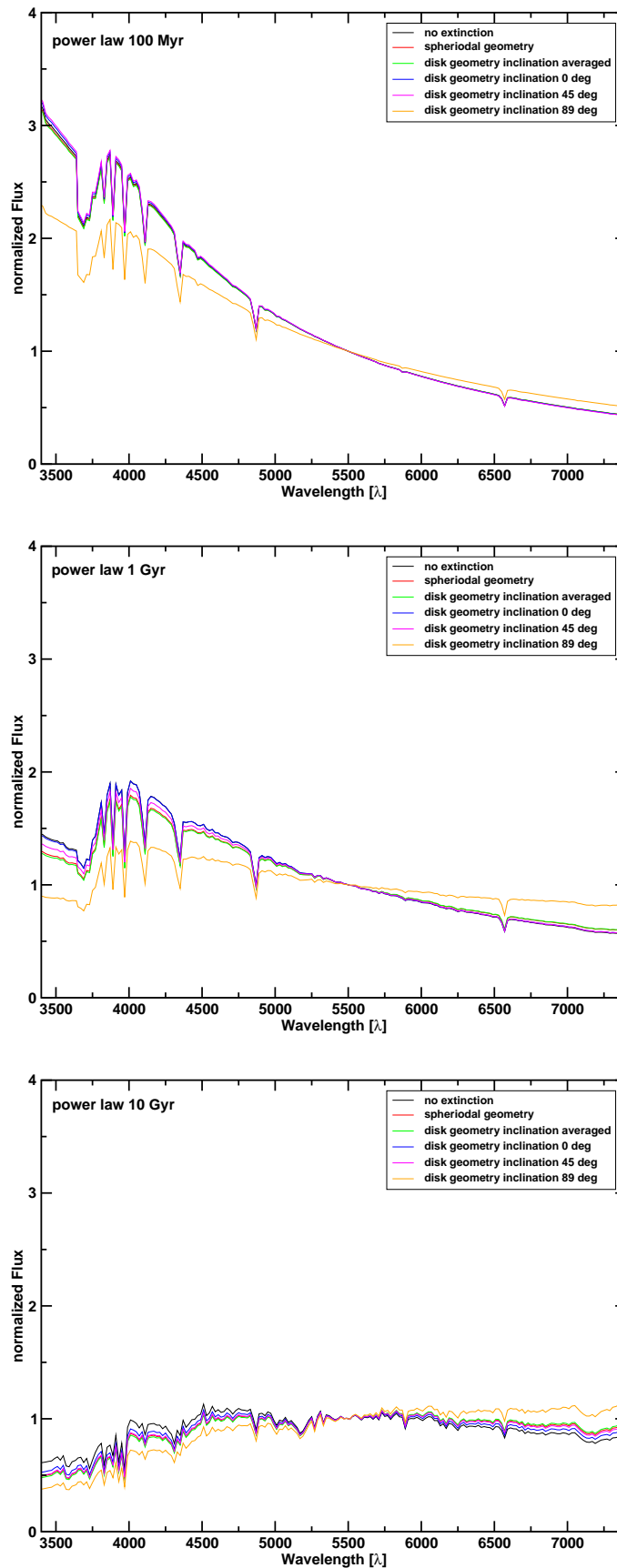


Figure B.16: SEDs modeled using different extinction laws and a SFR following a power law. Three diagrams are shown for three different ages of the SEDs (500 Myr, 1 Gyr, 10 Gyr).

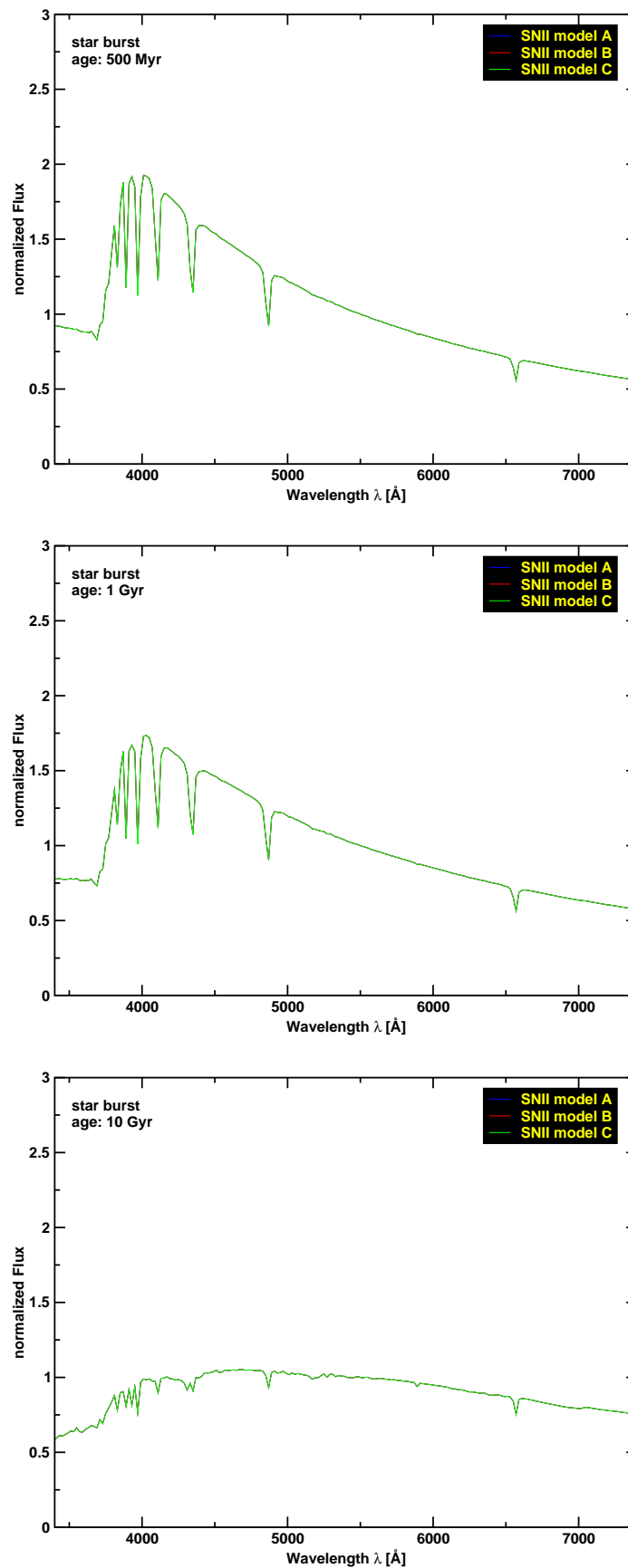


Figure B.17: SEDs modeled using different SNII energy ejection models and an one star burst scenario. Three diagrams are shown for three different ages of the SEDs(500 Myr, 1 Gyr, 10 Gyr).

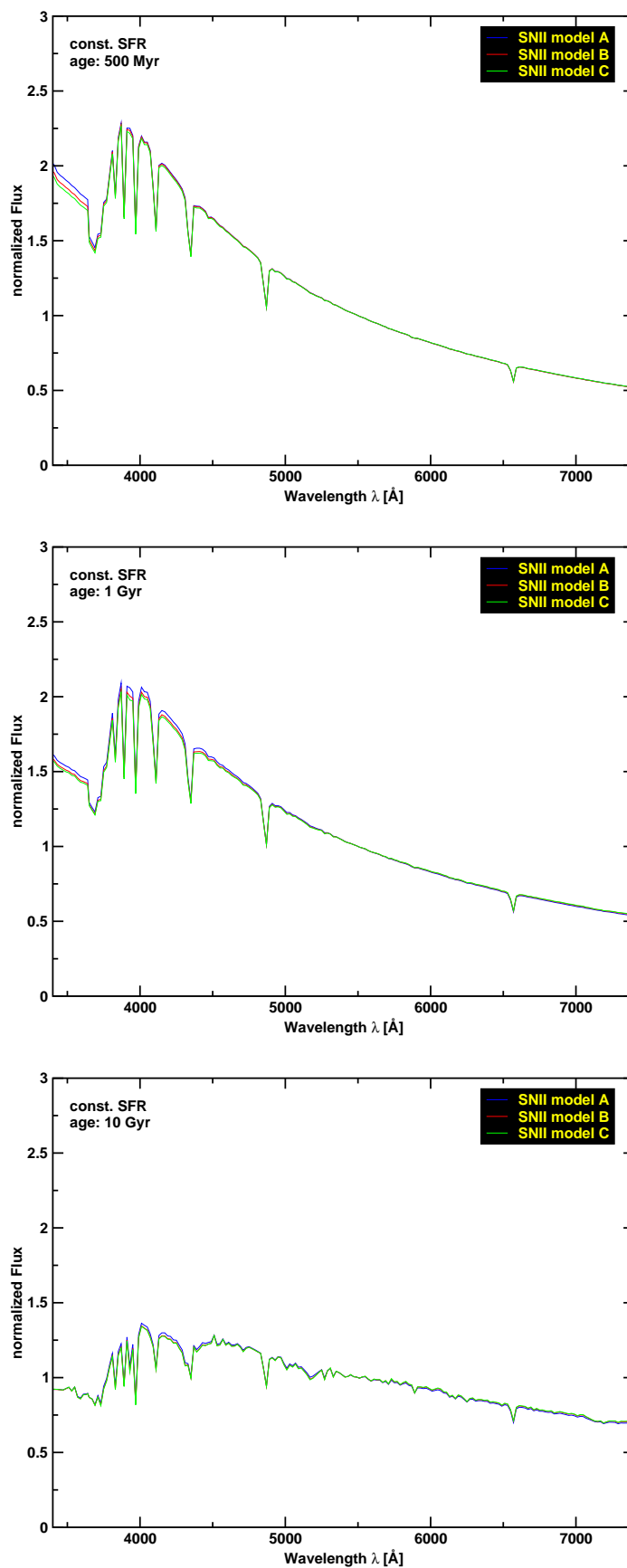


Figure B.18: SEDs modeled using different SNII energy ejection models and a constant SFR. Three diagrams are shown for three different ages of the SEDs (500 Myr, 1 Gyr, 10 Gyr).

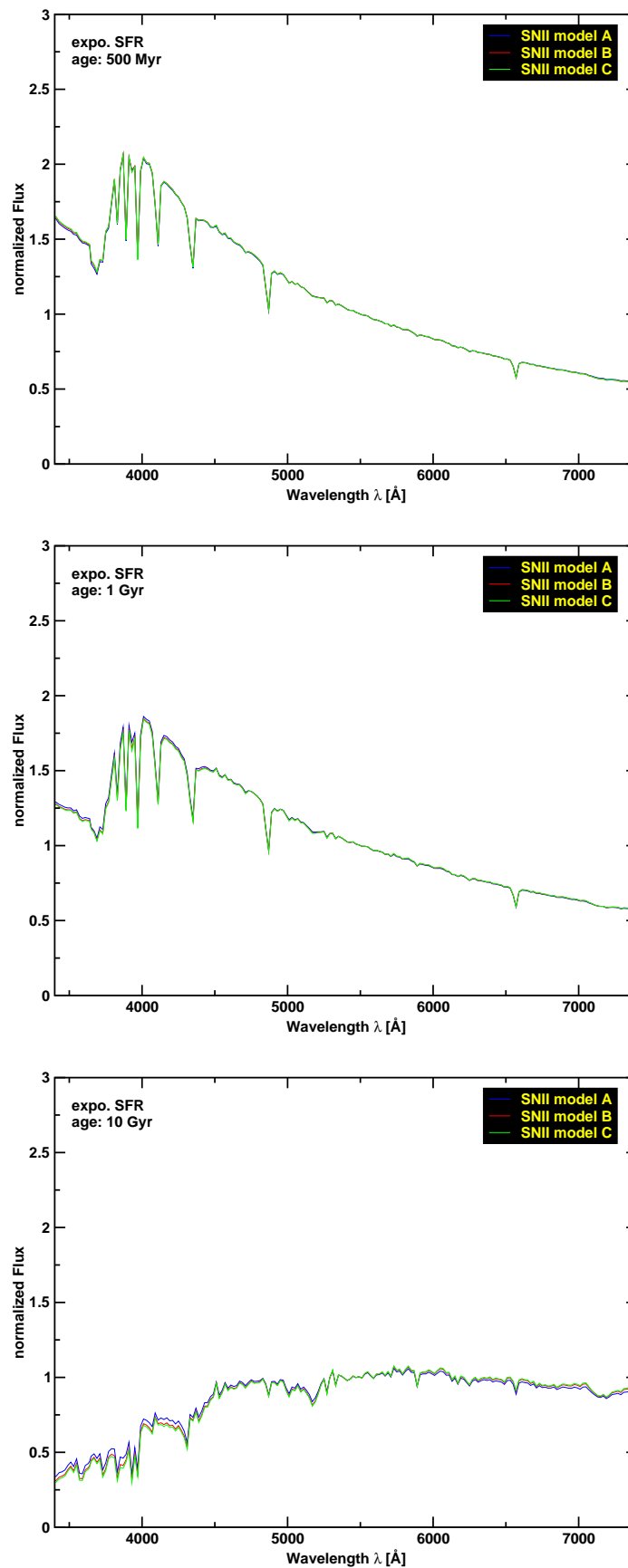


Figure B.19: SEDs modeled using different SNII energy ejection models and an exponential SFR. Three diagrams are shown for three different ages of the SEDs (500 Myr, 1 Gyr, 10 Gyr).

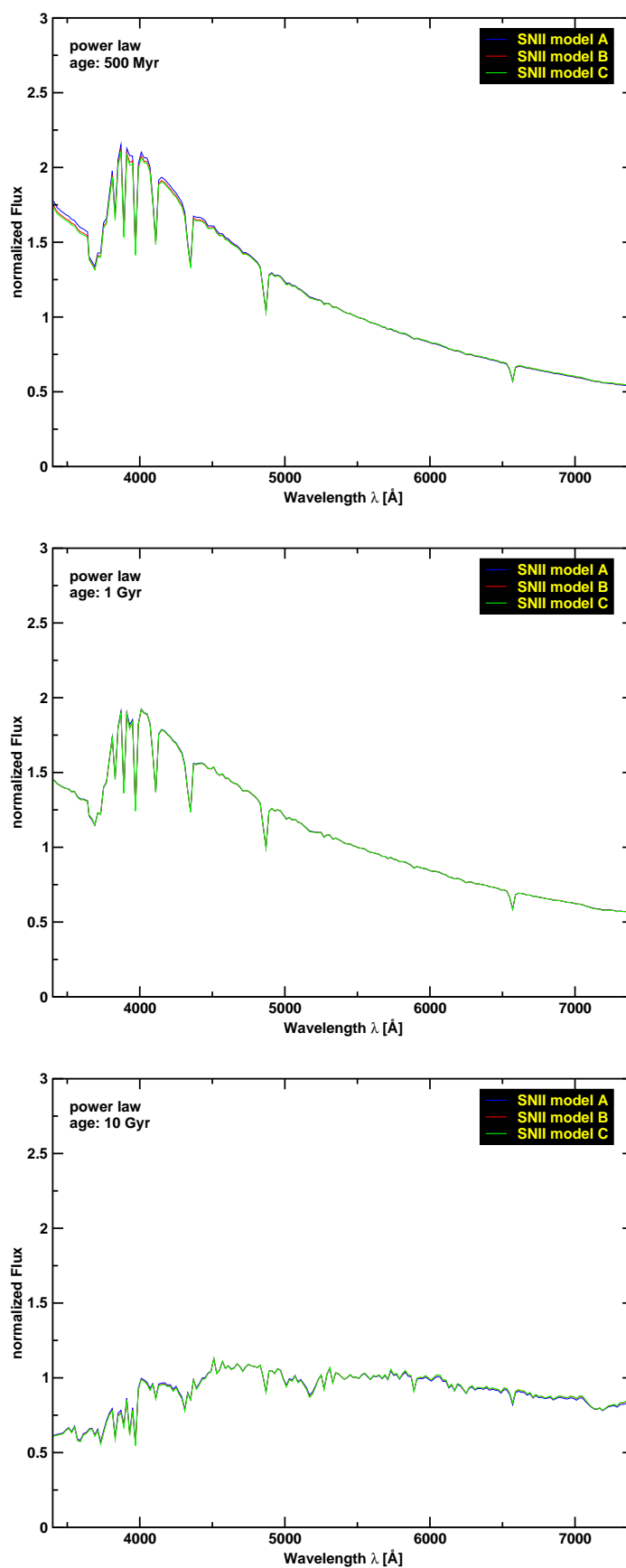


Figure B.20: Change of the shape of the SEDs using different SNII energy ejection models for an SFR following an power law and plotted for different ages (500 Myr, 1 Gyr, 10 Gyr).

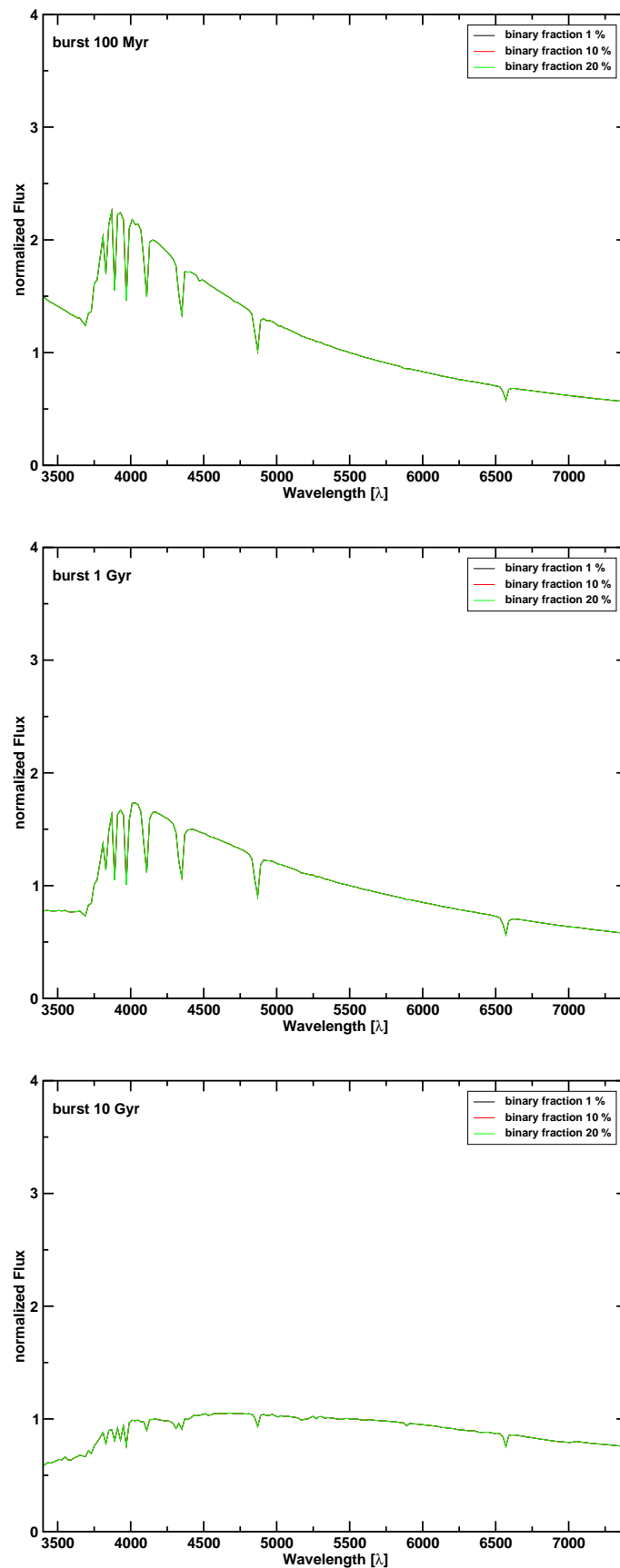


Figure B.21: SEDs modeled using different fractions of binary stars and an one star burst scenarios. Three diagrams are shown for three different ages of the SEDs (100 Myr, 1 Gyr, 10 Gyr).

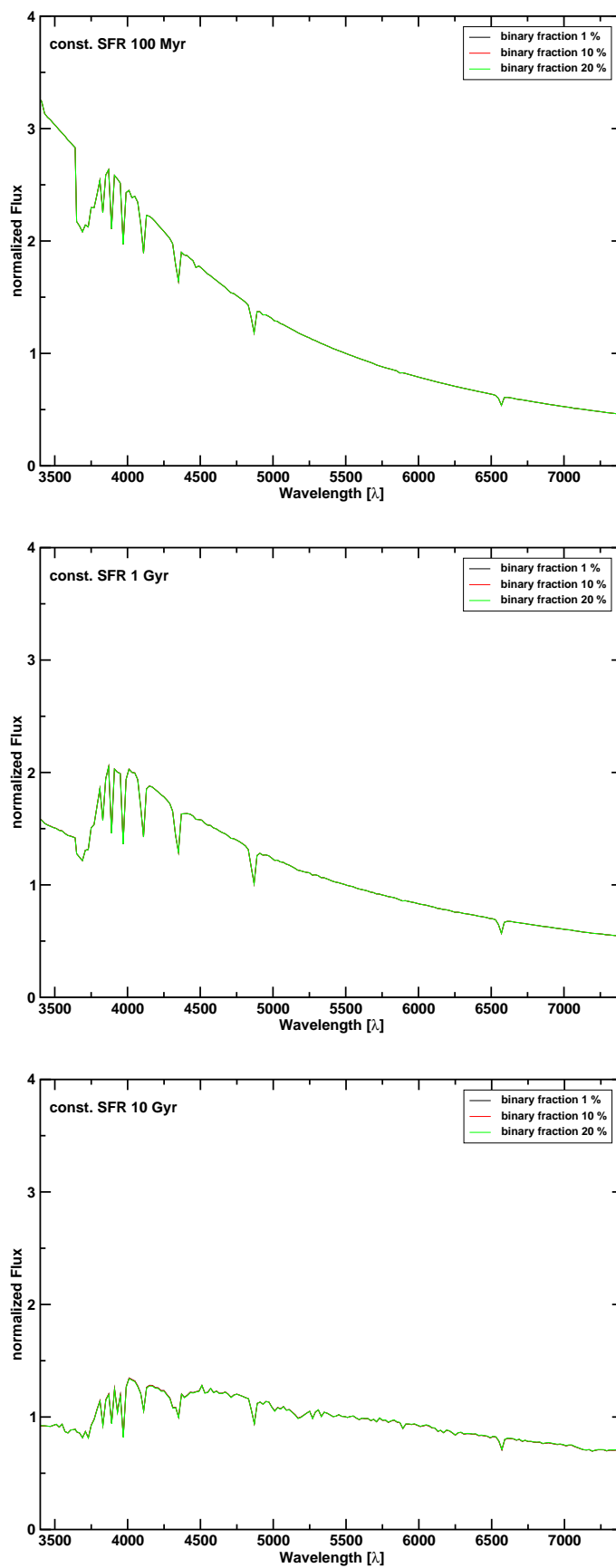


Figure B.22: SEDs modeled using different fractions of binary stars and constant SFR. Three diagrams are shown for three different ages of the SEDs (100 Myr, 1 Gyr, 10 Gyr).

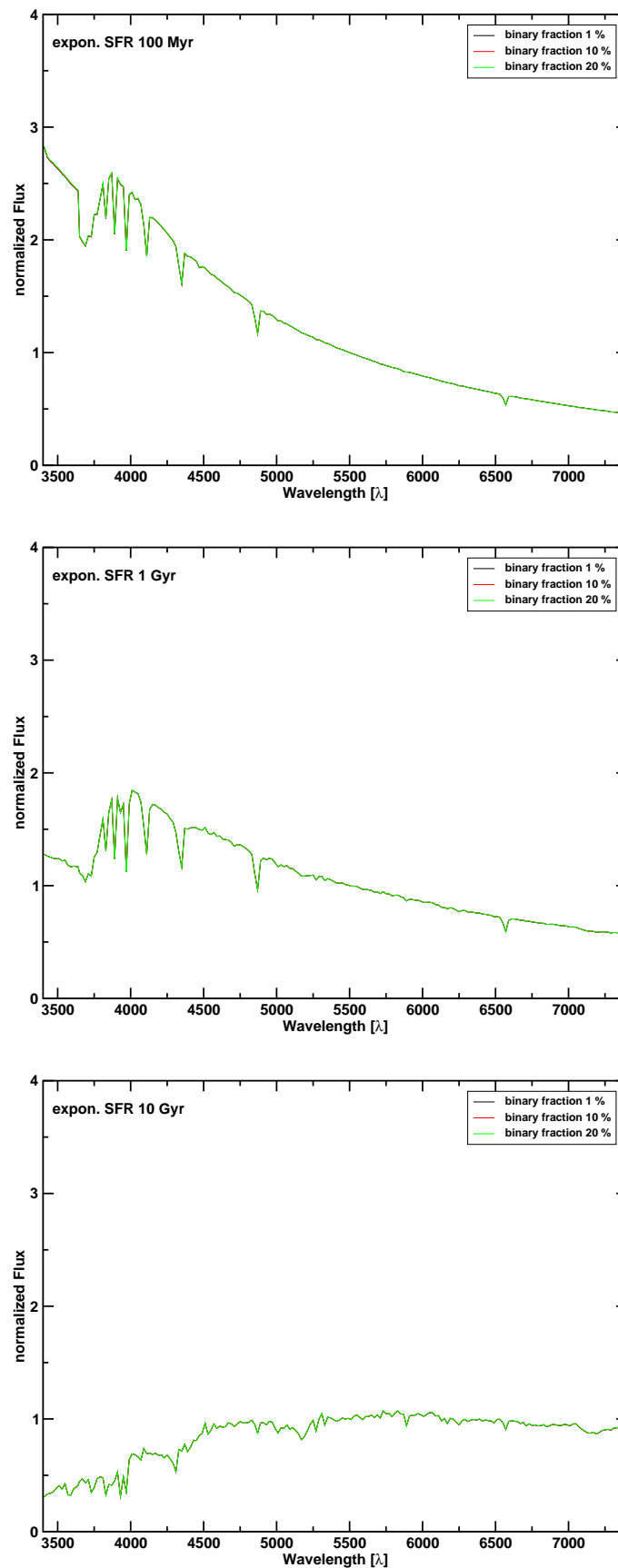


Figure B.23: SEDs modeled using different fractions of binary stars and an exponential decreasing SFR. Three diagrams are shown for three different ages of the SEDs (100 Myr, 1 Gyr, 10 Gyr).

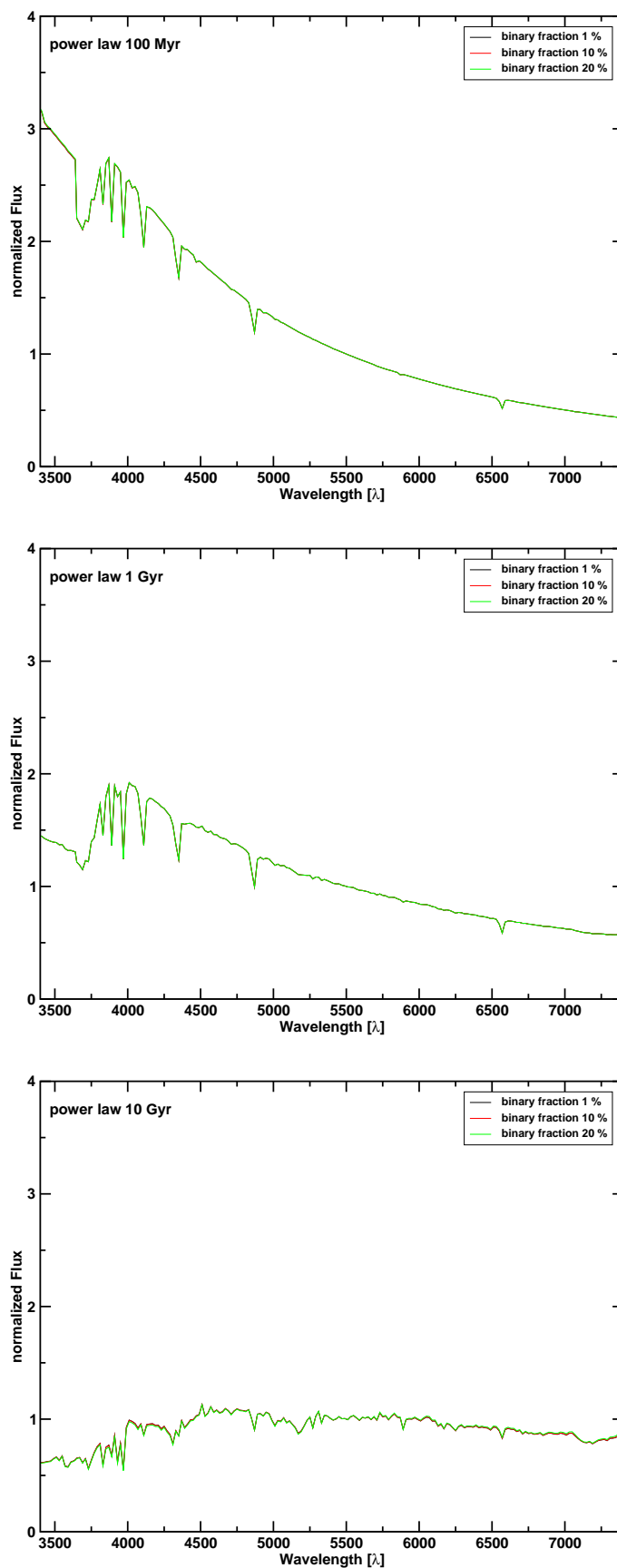


Figure B.24: SEDs modeled using different fractions of binary stars and a SFR following a power law. Three diagrams are shown for three different ages of the SEDs (100 Myr, 1 Gyr, 10 Gyr).

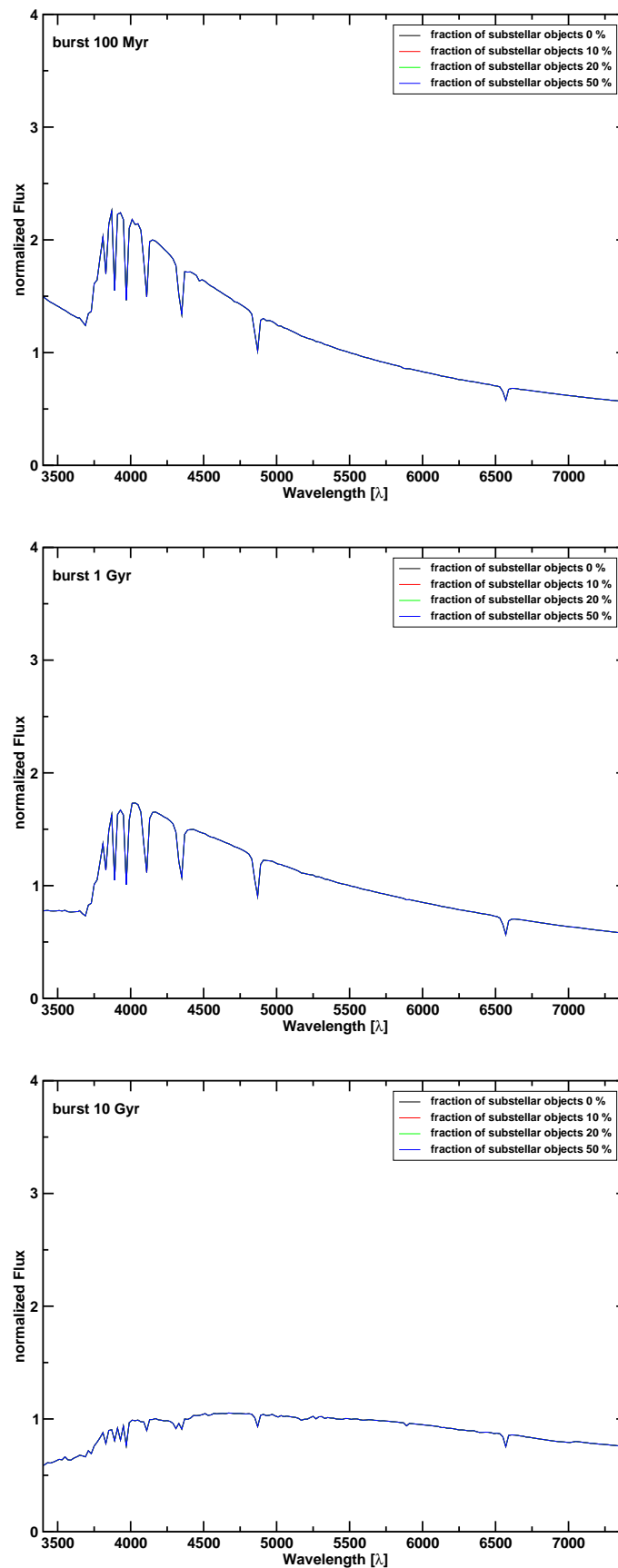


Figure B.25: SEDs modeled using different fractions of substellar objects and an one star burst scenarios. Three diagrams are shown for three different ages of the SEDs (100 Myr, 1 Gyr, 10 Gyr).

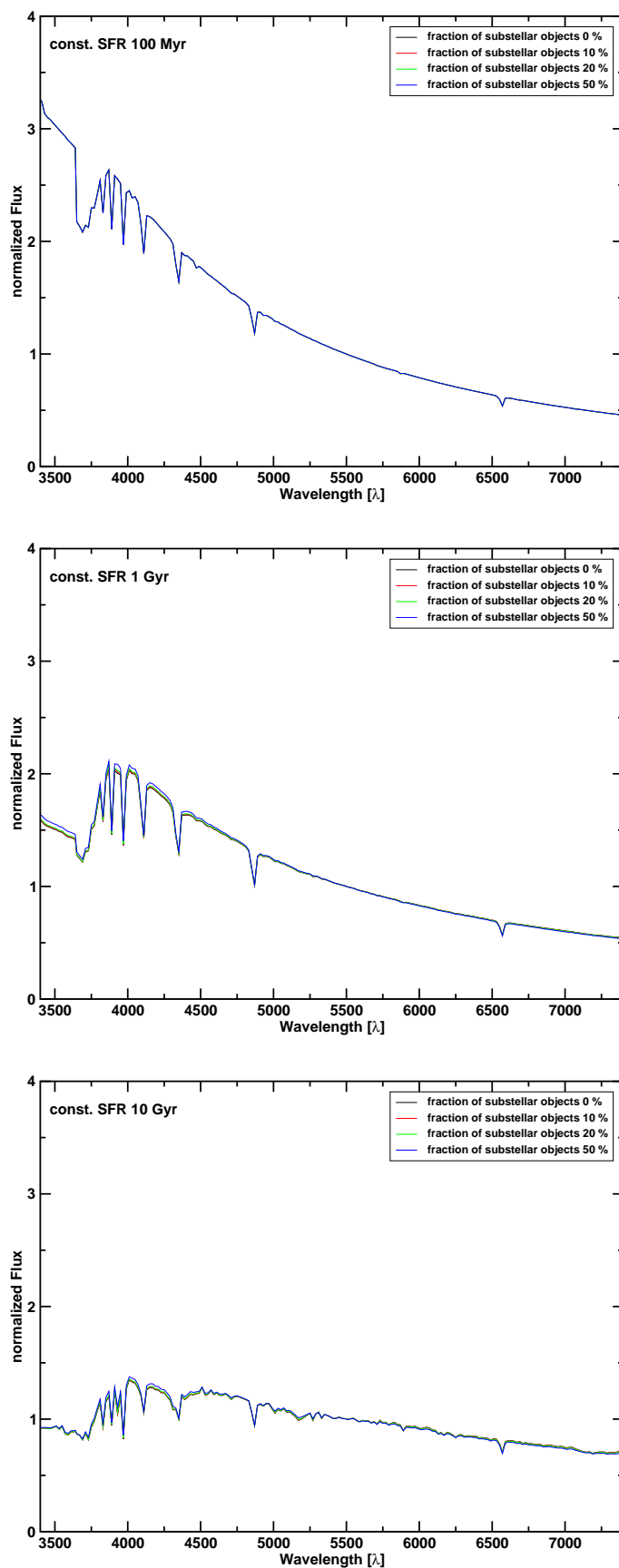


Figure B.26: SEDs modeled using different fractions of substellar objects and a constant SFR. Three diagrams are shown for three different ages of the SEDs (100 Myr, 1 Gyr, 10 Gyr).

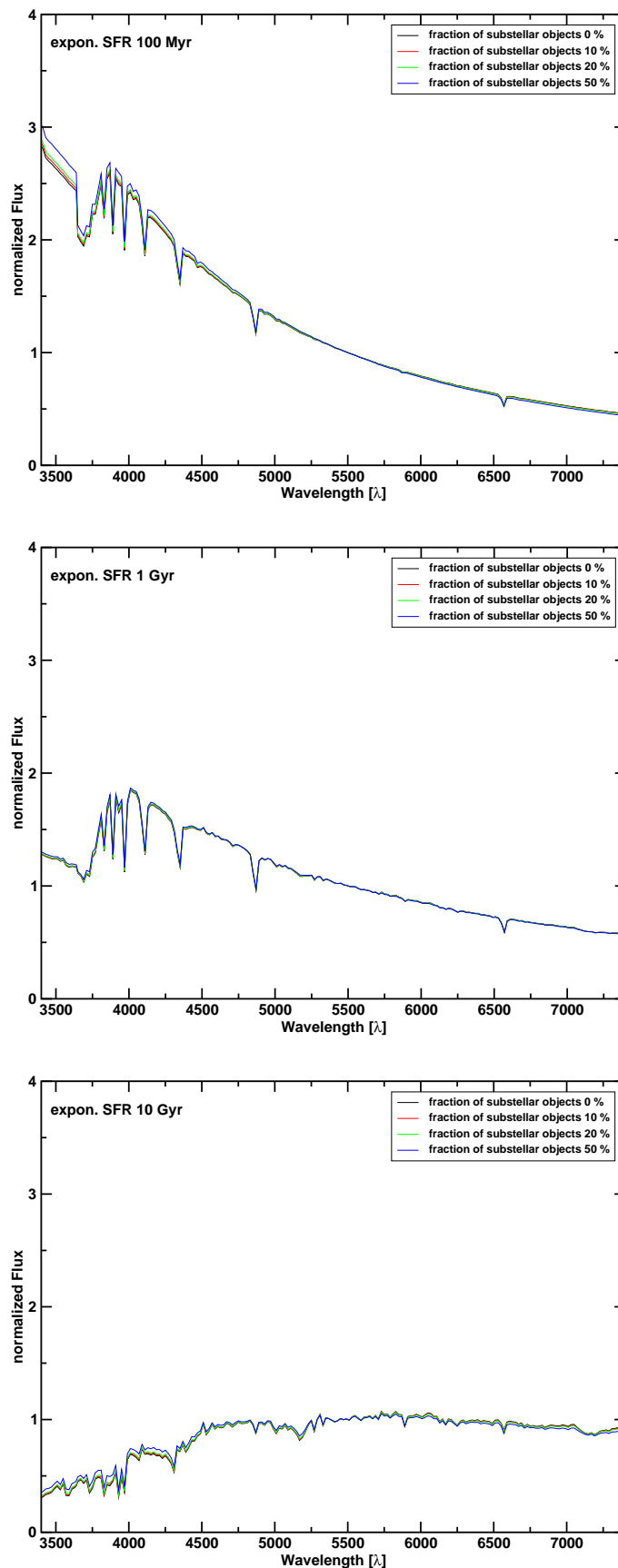


Figure B.27: SEDs modeled using different fractions of substellar objects and an exponential decreasing SFR. Three diagrams are shown for three different ages of the SEDs (100 Myr, 1 Gyr, 10 Gyr).

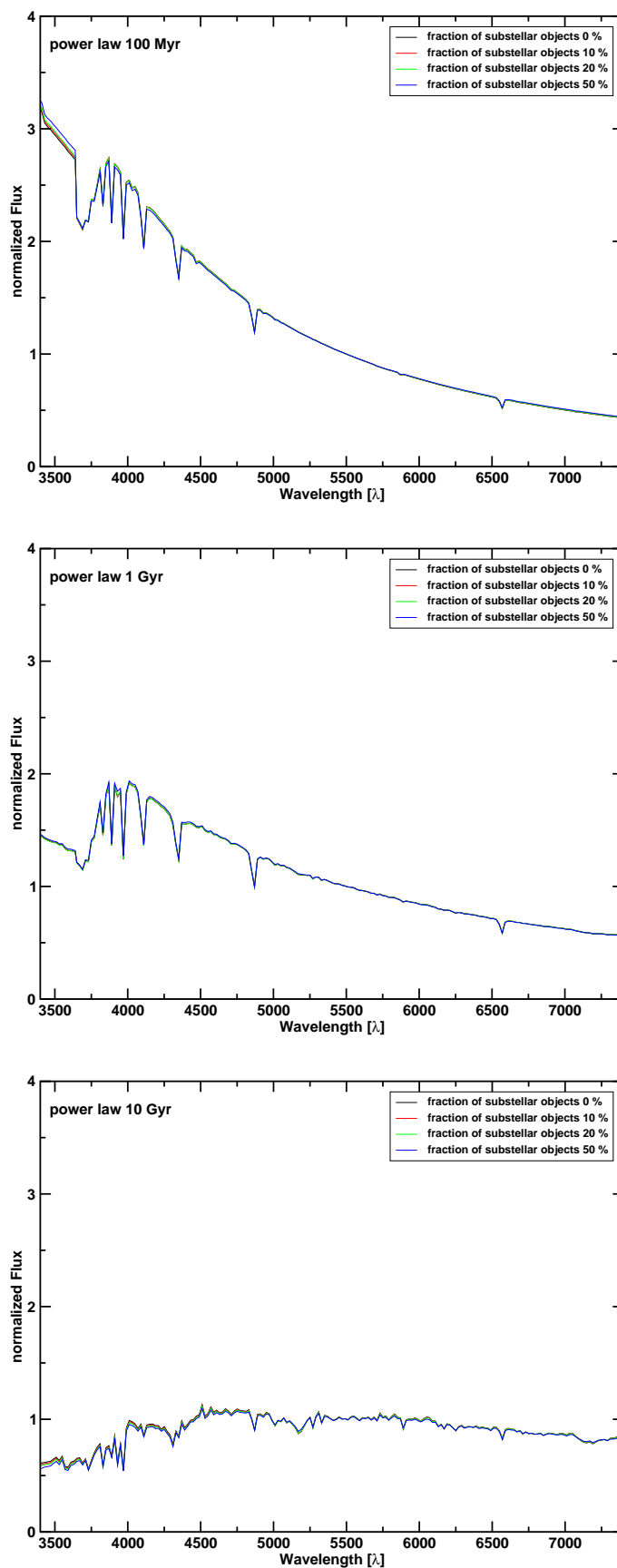


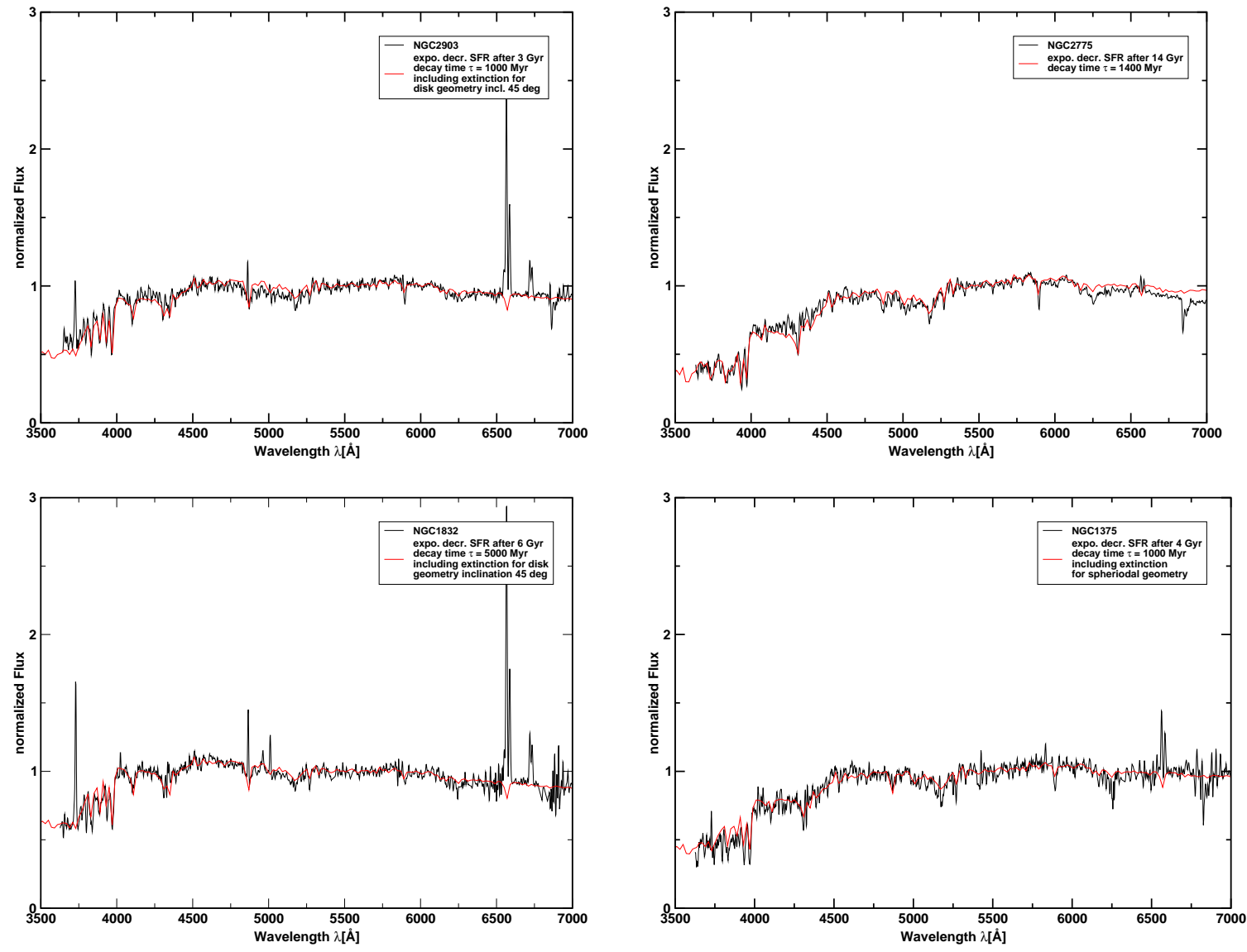
Figure B.28: SEDs modeled using different fractions of substellar objects and a SFR following a power law. Three diagrams are shown for three different ages of the SEDs (100 Myr, 1 Gyr, 10 Gyr).

Appendix C

HSB galaxy sample

In this Appendix, the spectra of the HSB galaxies in comparison to the best matching model SEDs are shown. The HSB galaxy sample consists of spectra from the *spectrophotometric atlas of nearby galaxies* of Kennicutt (1992a). The studied sample consists of 27 field HSB galaxies. In order to derive the SFHs of the HSB galaxies, the measured spectra are also normalized to the flux at 5500 Å.

Figure C.1: NGC1375, NGC1832, NGC2775, NGC2903



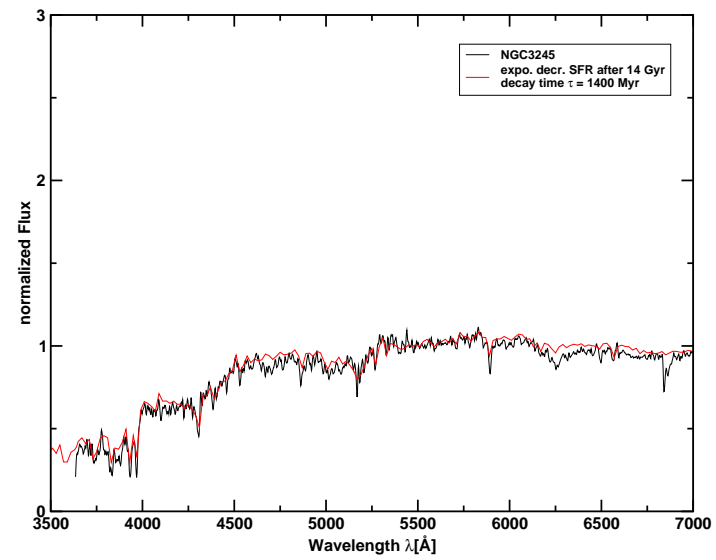
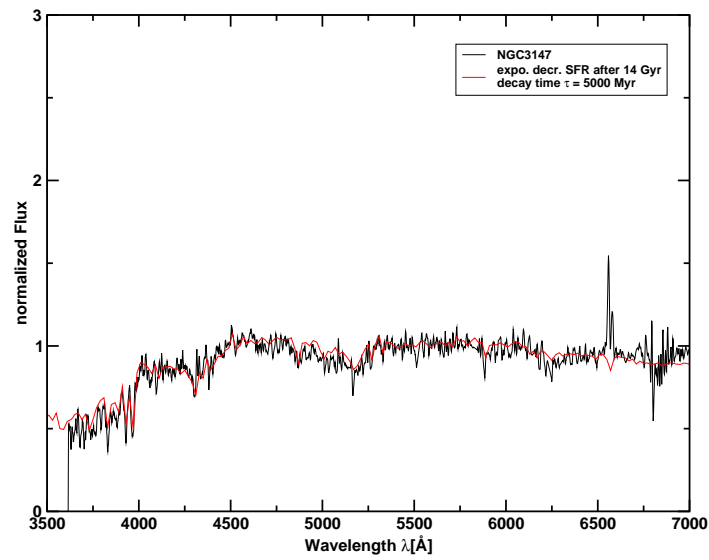
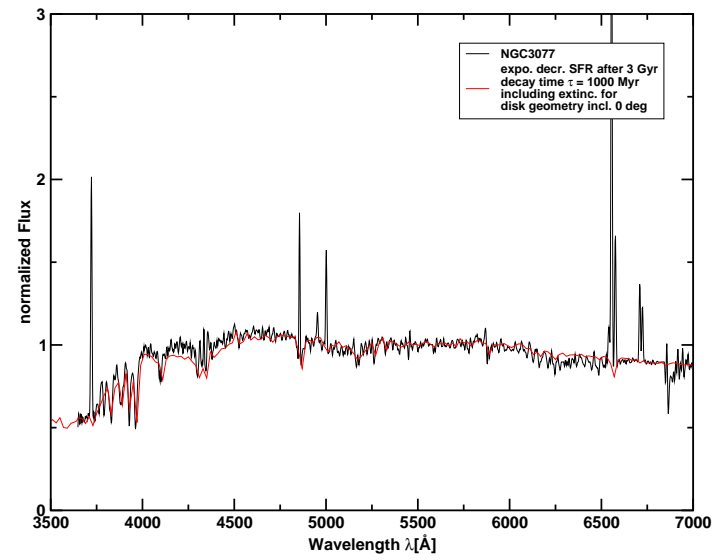
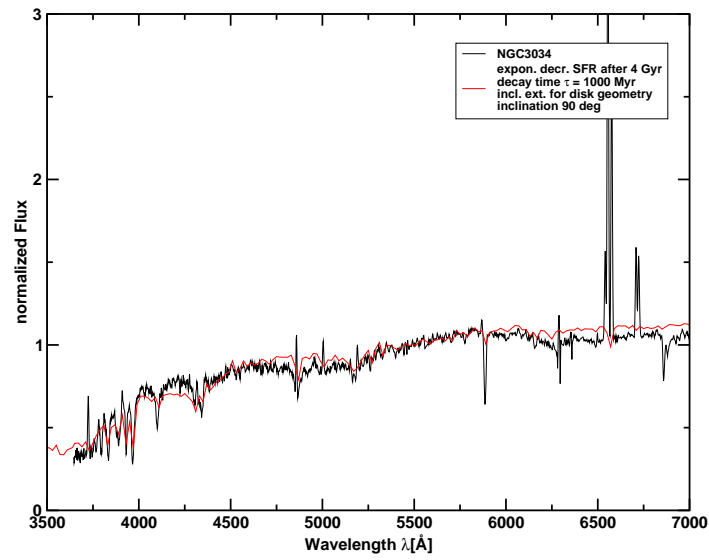
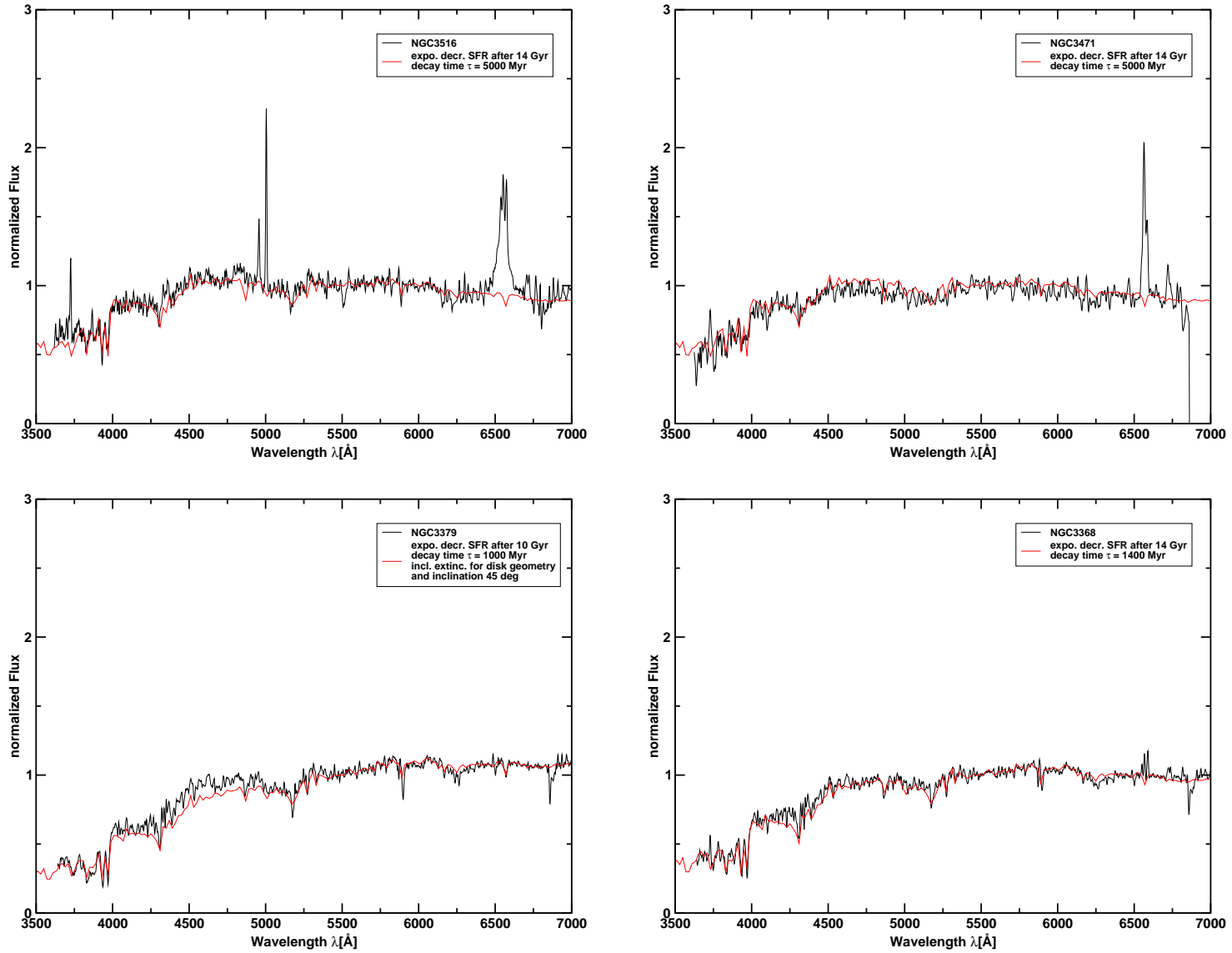


Figure C.2: NGC3034, NGC3077, NGC3147, NGC3245

Figure C.3: NGC3368, NGC3379, NGC3471, NGC3516



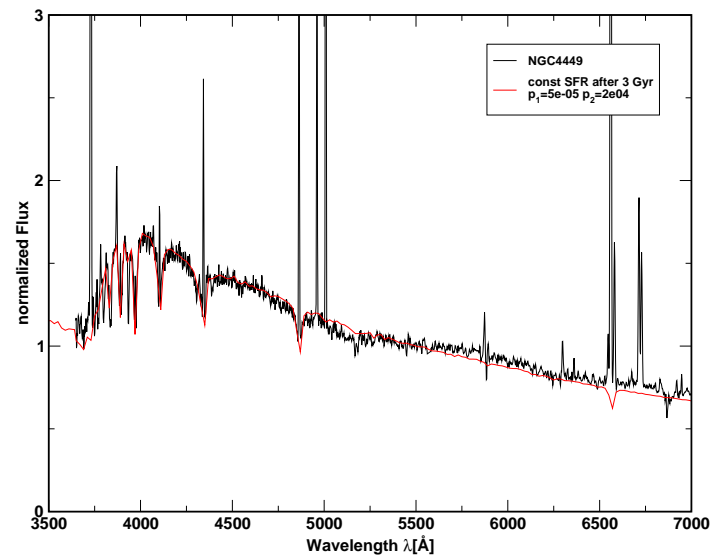
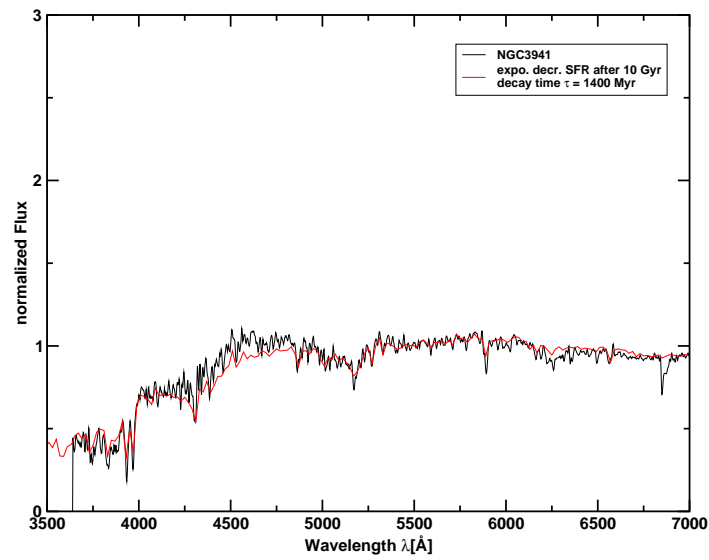
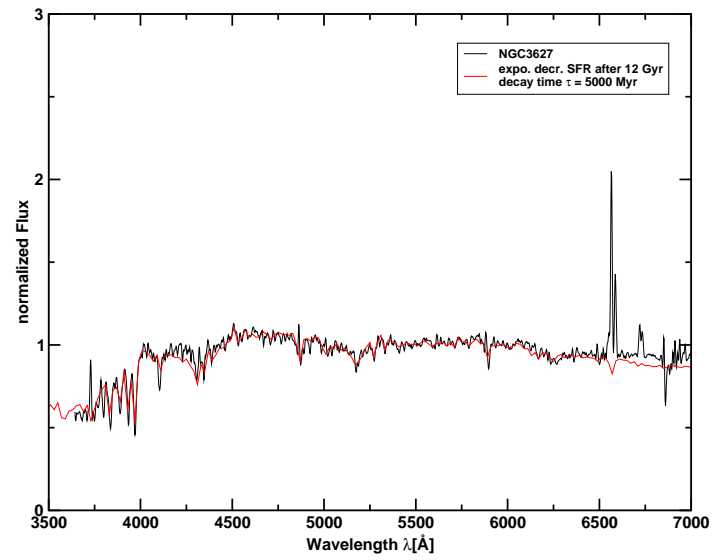
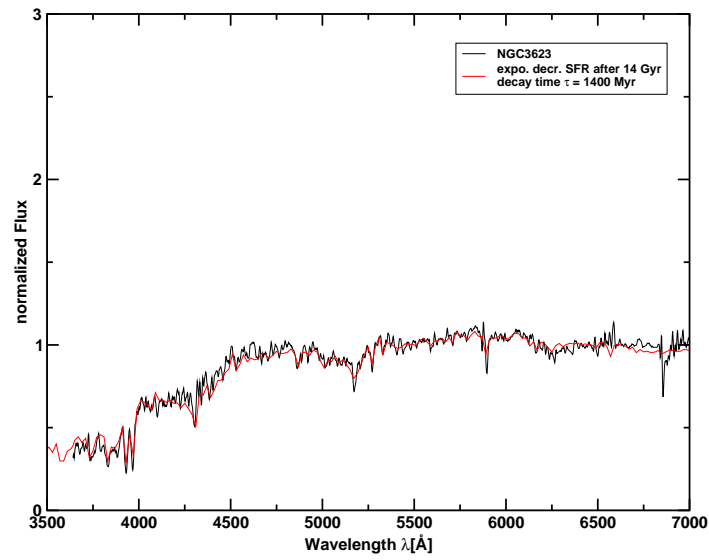
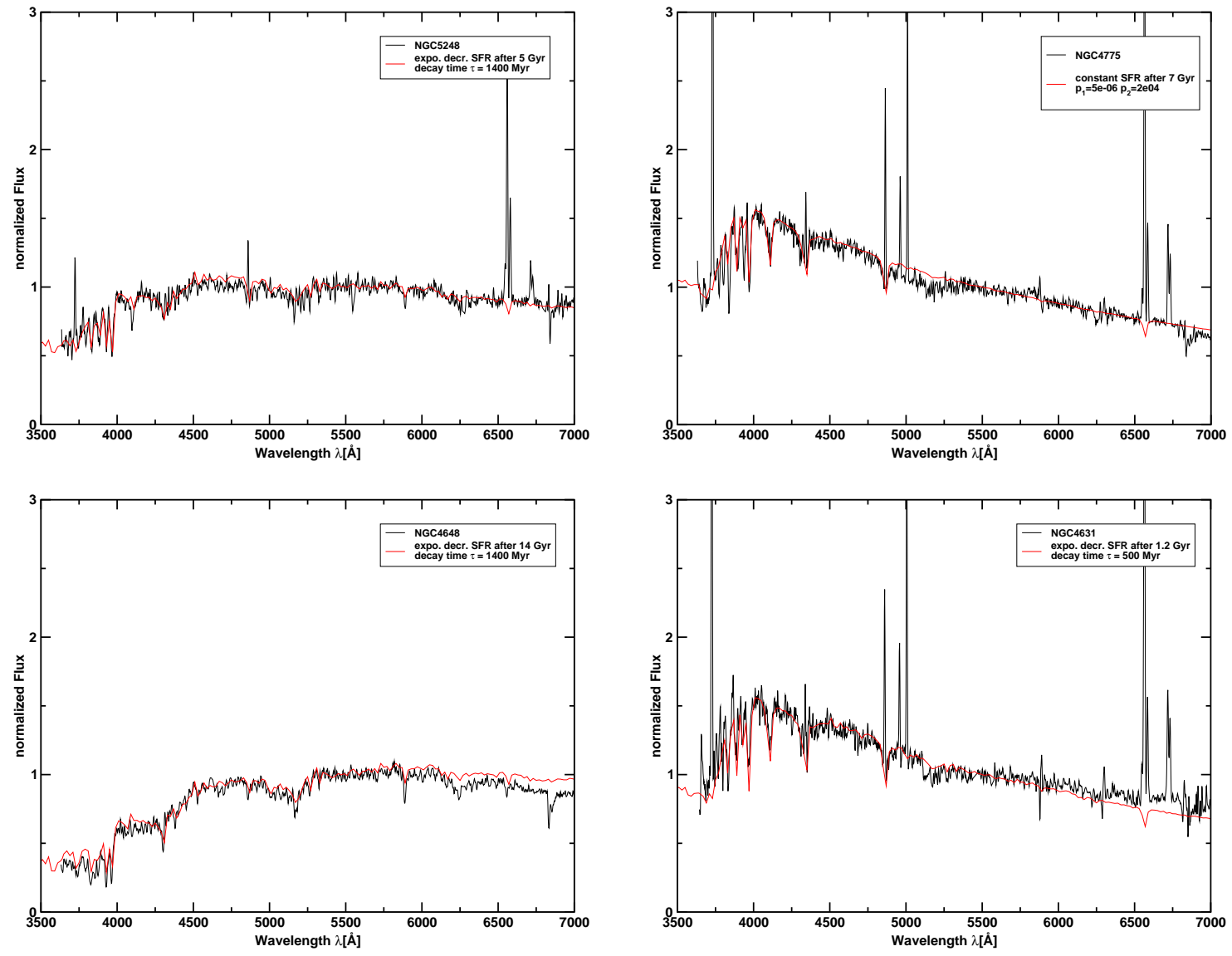


Figure C.4: NGC3623, NGC3627, NGC3941, NGC4449

Figure C.5: NGC4631, NGC4648, NGC4775, NGC5248



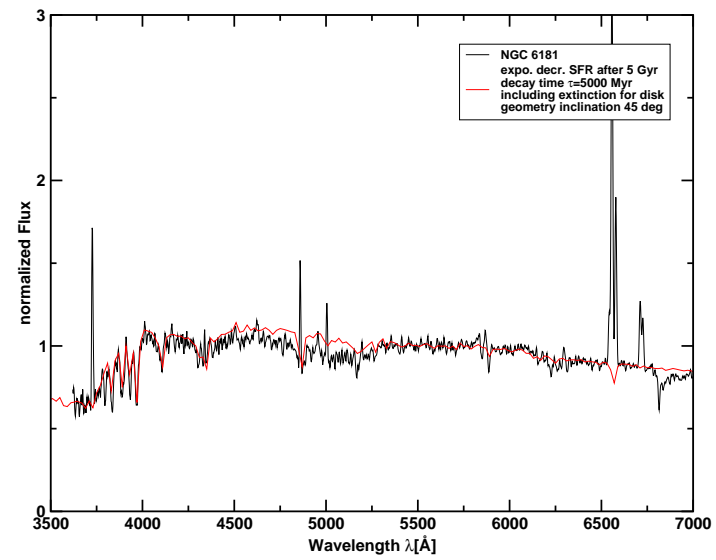
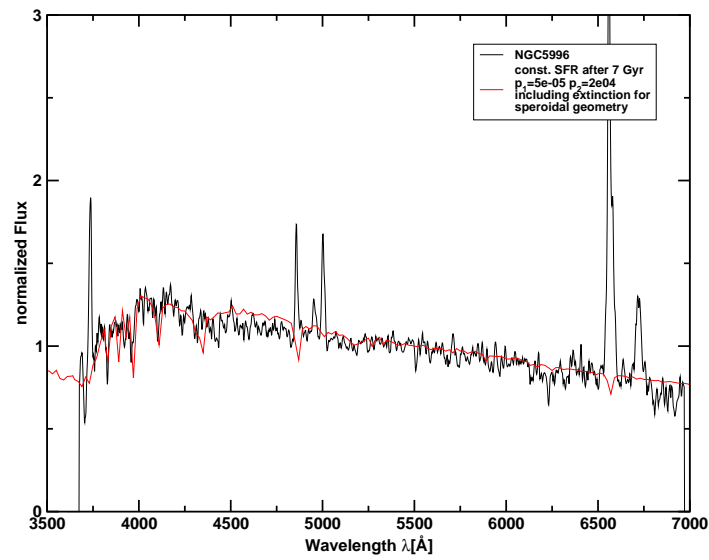
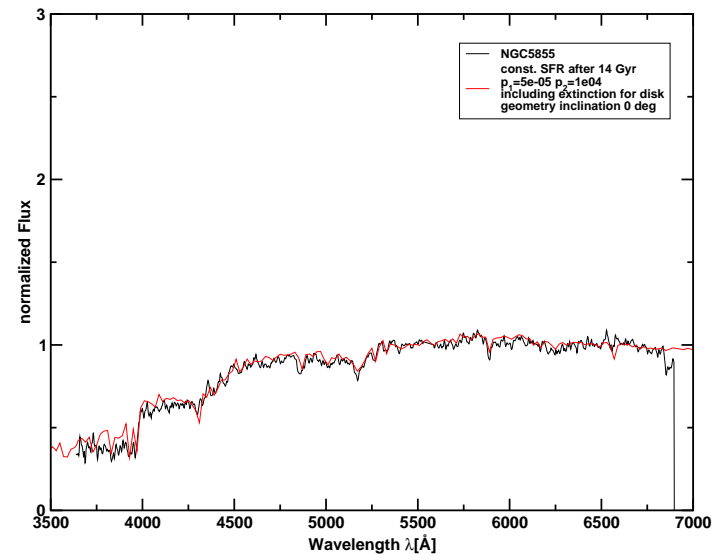
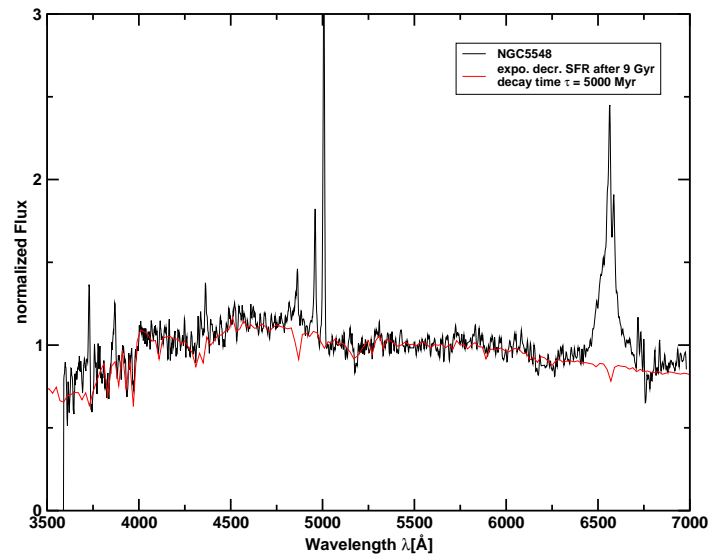
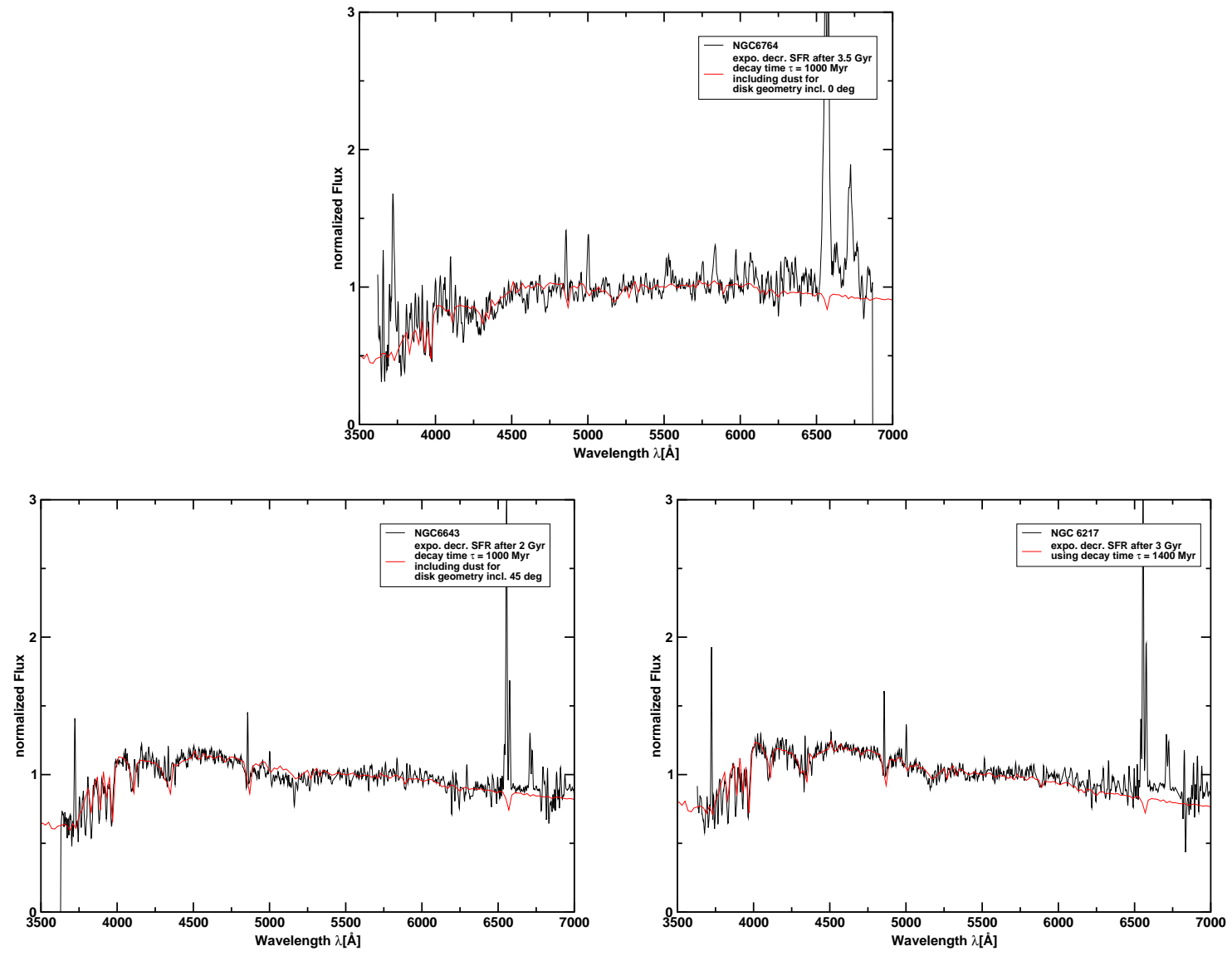


Figure C.6: NGC5548, NGC5866, NGC5996, NGC6181

Figure C.7: NGC6217, NGC6643, NGC6764



Bibliography

- Aparicio, A. & Gallart, C. 1995, *AJ*, 110, 2105
- Armandroff, T. E., Davies, J. E., & Jacoby, G. H. 1998, *AJ*, 116, 2287
- Beijersbergen, M., de Blok, W. J. G., & van der Hulst, J. M. 1999, *A&A*, 351, 903
- Bell, E. F., Barnaby, D., Bower, R. G., de Jong, R. S., Harper, D. A., Hereld, M., Loewenstein, R. F., & Rauscher, B. J. 2000, *MNRAS*, 312, 470
- Bertin, E. & Arnouts, S. 1996, *A&A*, 117, 393
- Binggeli, B., Sandage, A., & Tammann, G. A. 1985, *AJ*, 90, 1681
- Blain, A. W., Smail, I., Ivison, R. J., Kneib, J. ., & Frayer, D. T. 2002, *ArXiv Astrophysics e-prints*
- Bothun, G. D., Impey, C. D., Malin, D. F., & Mould, J. R. 1987, *AJ*, 94, 23
- Bruzual, G. & Charlot, S. 2003, *MNRAS*, 344, 1000
- Calzetti, D., Kinney, A. L., & Storchi-Bergmann, T. 1994, *ApJ*, 429, 582
- Charlot, S. & Bruzual, A. G. 1991, *ApJ*, 367, 126
- Cimatti, A. 2003, *Ap&SS*, 285, 231
- Dalcanton, J. J., Spergel, D. N., Gunn, J. E., Schmidt, M., & Schneider, D. P. 1997, *AJ*, 114, 635
- Davies, J. I., Phillips, S., & Disney, M. J. 1989, *Ap&SS*, 157, 299
- de Blok, W. J. G., McGaugh, S. S., & Rubin, V. C. 2001, *AJ*, 122, 2396
- de Blok, W. J. G. & van der Hulst, J. M. 1998a, *A&A*, 335, 421
- . 1998b, *A&A*, 336, 49

- de Blok, W. J. G., van der Hulst, J. M., & Bothun, G. D. 1995, *MNRAS*, 274, 235
- de Jong, R. S. 1996, *A&AS*, 118, 557
- Dell'Antonio, I., Jannuzi, B. T., Smith, M., & Dey, A. . 1999, submitted
- Disney, M. & Phillipps, S. 1983, *MNRAS*, 205, 1253
- Disney, M. J. 1976, *Nat*, 263, 573
- Driver, S. P., Phillipps, S., Davies, J. I., Morgan, I., & Disney, M. J. 1994, *MNRAS*, 266, 155
- Eggen, O. J., Lynden-Bell, D., & Sandage, A. R. 1962, *ApJ*, 136, 748
- Erben, T., Schirmer, M., Dietrich, J. P., Cordes, O., Habertzettl, L., Hetterscheidt, M., Hildebrandt, H., Schmithuesen, O., Schneider, P., Simon, P., Cuillandre, J. C., Deul, E., Hook, R. N., Kaiser, N., Radovich, M., Benoist, C., Nonino, M., Olsen, L. F., Prandoni, I., Wichmann, R., Zaggia, S., Bomans, D. J., Dettmar, R.-J., & Miralles, J. M. 2005, *ArXiv Astrophysics e-prints*
- Faber, S. M. 1972, *A&A*, 20, 361
- Ferguson, H. C. 1989, *AJ*, 98, 367
- Ferguson, H. C. & Sandage, A. 1988, *AJ*, 96, 1520
- Ferrini, F., Franco, J., & Matteucci, F., eds. 1990, *Chemical and dynamical evolution of galaxies*
- Filippenko, A. V. 1982, *PASP*, 94, 715
- Fioc, M. & Rocca-Volmerange, B. 1997, *A&A*, 326, 950
- Fouque, P., Durand, N., Bottinelli, L., Gouguenheim, L., & Paturel, G. 1990, *A&AS*, 86, 473
- Freeman, K. C. 1970, *ApJ*, 160, 811
- Gallagher, J. S., Littleton, J. E., & Matthews, L. D. 1995, *AJ*, 109, 2003
- Guiderdoni, B. & Rocca-Volmerange, B. 1987, *A&A*, 186, 1
- Habertzettl, L. 1999, Master's thesis, Ruhr-University Bochum
- Habertzettl, L., Bomans, D. J., & Dettmar, R.-J. 2003, *American Astronomical Society Meeting Abstracts*, 203,
- Hamuy, M., Walker, A. R., Suntzeff, N. B., Gigoux, P., Heathcote, S. R., & Phillips, M. M. 1992, *PASP*, 104, 533
- Hoeppe, G., Brinks, E., Klein, U., Giovanardi, C., Altschuler, D. R., Price, R. M., & Deeg, H.-J. 1994, *AJ*, 108, 446

-
- Hopkins, A. M., Miller, C. J., Nichol, R. C., Connolly, A. J., Bernardi, M., Gómez, P. L., Goto, T., Tremonti, C. A., Brinkmann, J., Ivezić, Ž., & Lamb, D. Q. 2003, *ApJ*, 599, 971
- Hubble, E. & Tolman, R. C. 1935, *ApJ*, 82, 302
- Impey, C. & Bothun, G. 1989, *ApJ*, 341, 89
- Impey, C., Bothun, G., & Malin, D. 1988, *ApJ*, 330, 634
- Impey, C. D., Sprayberry, D., Irwin, M. J., & Bothun, G. D. 1996, *ApJS*, 105, 209
- Kauffmann, G., Charlot, S., & White, S. D. M. 1996, *MNRAS*, 283, L117
- Kauffmann, G., White, S. D. M., & Guiderdoni, B. 1993, *MNRAS*, 264, 201
- Kennicutt, R. C. 1983, *ApJ*, 272, 54
- . 1989, *AJ*, 344, 685
- . 1992a, *ApJS*, 79, 255
- . 1992b, *ApJ*, 388, 310
- King, I. 1962, *AJ*, 67, 471
- Koo, D. C. 1985, *AJ*, 90, 418
- Kraan-Korteweg, R. C. & Huchtmeier, W. K. 1992, *A&A*, 266, 150
- Kroupa, P., Tout, C. A., & Gilmore, G. 1993, *MNRAS*, 262, 545
- Landolt, A. U. 1992, *AJ*, 104, 340
- Lilly, S. J., Le Fevre, O., Crampton, D., Hammer, F., & Tresse, L. 1995, *ApJ*, 455, 50
- Liu, C. T. & Green, R. F. 1998, *AJ*, 116, 1074
- Loh, E. D. & Spillar, E. J. 1986, *ApJ*, 303, 154
- Longair, M. S. 1998, *Galaxy Formation* (Springer-Verlag Berlin Heidelberg New York)
- Longmore, A. J., Hawarden, T. G., Goss, W. M., Mebold, U., & Webster, B. L. 1982, *MNRAS*, 200, 325
- Massey, P. 1997, *A User's Guide to CCD Reductions with IRAF*
- Massey, P., Valdes, F., & Barnes, J. 1992, *A User's Guide to Reducing Slit Spectra with IRAF*
- Matthews, L. D. & Gallagher, J. S. 1997, *AJ*, 114, 1899
- Matthews, L. D. & Gao, Y. 2001, *ApJ Lett.*, 549, L191

- Matthews, L. D., Gao, Y., Uson, J. M., & Combes, F. 2005, *AJ*, 129, 1849
- McGaugh, S. S. 1991, *ApJ*, 380, 140
- . 1994, *ApJ*, 426, 135
- . 1996, *MNRAS*, 280, 337
- McGaugh, S. S., Bothun, G. D., & Schombert, J. M. 1995, *AJ*, 110, 573
- McGaugh, S. S., Rubin, V. C., & de Blok, W. J. G. 2001, *AJ*, 122, 2381
- Miller, G. E. & Scalo, J. M. 1979, *ApJS*, 41, 513
- Nilson, P. 1973, *Uppsala general catalogue of galaxies (Acta Universitatis Upsaliensis. Nova Acta Regiae Societatis Scientiarum Upsaliensis - Uppsala Astronomiska Observatoriums Annaler, Uppsala: Astronomiska Observatorium, 1973)*
- Norberg, P., Cole, S., Baugh, C. M., Frenk, C. S., Baldry, I., Bland-Hawthorn, J., Bridges, T., Cannon, R., Colless, M., Collins, C., Couch, W., Cross, N. J. G., Dalton, G., De Propris, R., Driver, S. P., Efstathiou, G., Ellis, R. S., Glazebrook, K., Jackson, C., Lahav, O., Lewis, I., Lumsden, S., Maddox, S., Madgwick, D., Peacock, J. A., Peterson, B. A., Sutherland, W., & Taylor, K. 2002, *MNRAS*, 336, 907
- O'Neil, K. 2000, *ArXiv Astrophysics e-prints*
- O'Neil, K. & Bothun, G. 2000, *ApJ*, 529, 811
- O'Neil, K., Bothun, G. D., & Cornell, M. E. 1997a, *AJ*, 113, 1212
- O'Neil, K., Bothun, G. D., Schombert, J., Cornell, M. E., & Impey, C. D. 1997b, *AJ*, 114, 2448
- O'Neil, K., Hofner, P., & Schinnerer, E. 2000, *ApJ Lett.*, 545, L99
- O'Neil, K., Schinnerer, E., & Hofner, P. 2003, *ApJ*, 588, 230
- Osterbrock, D. 1989, *Astrophysics of Gaseous Nebulae and Active Galactic Nuclei (University Science Books, Sausalito California)*
- Palunas, P., Collins, N. R., Gardner, J. P., Hill, R. S., Malumuth, E. M., Smette, A., Teplitz, H. I., Williger, G. M., & Woodgate, B. E. 2000, *ApJ*, 541, 61
- Peng, C. Y., Ho, L. C., Impey, C. D., & Rix, H. 2002, *AJ*, 124, 266
- Pickering, T. E., Impey, C. D., van Gorkom, J. H., & Bothun, G. D. 1997, *AJ*, 114, 1858
- Rana, N. C. & Basu, S. 1992, *A&A*, 265, 499
- Roennback, J. & Bergvall, N. 1995, *A&A*, 302, 353

-
- Romanishin, W., Krumm, N., Salpeter, E., Knapp, G., Strom, K. M., & Strom, S. E. 1982, *ApJ*, 263, 94
- Rosenbaum, S. D. & Bomans, D. J. 2004, *A&A*, 422, L5
- Salpeter, E. E. 1955, *ApJ*, 121, 161
- Schechter, P. 1976, *ApJ*, 203, 297
- Schlegel, D. J., Finkbeiner, D. P., & Davis, M. 1998, *ApJ*, 500, 525
- Schombert, J. M., Bothun, G. D., Impey, C. D., & Mundy, L. G. 1990, *AJ*, 100, 1523
- Schombert, J. M., Bothun, G. D., Schneider, S. E., & McGaugh, S. S. 1992, *AJ*, 103, 1107
- Searle, L., Sargent, W. L. W., & Bagnuolo, W. G. 1973, *ApJ*, 179, 427
- Skillman, E. D., Bomans, D. J., & Kobulnicky, H. A. 1997, *ApJ*, 474, 205
- Skillman, E. D., Tolstoy, E., Cole, A. A., Dolphin, A. E., Saha, A., Gallagher, J. S., Dohm-Palmer, R. C., & Mateo, M. 2003, *ApJ*, 596, 253
- Spergel, D. N., Verde, L., Peiris, H. V., Komatsu, E., Nolta, M. R., Bennett, C. L., Halpern, M., Hinshaw, G., Jarosik, N., Kogut, A., Limon, M., Meyer, S. S., Page, L., Tucker, G. S., Weiland, J. L., Wollack, E., & Wright, E. L. 2003, *ApJS*, 148, 175
- Spinrad, H. & Taylor, B. J. 1971, *ApJS*, 22, 445
- Springel, V. & Hernquist, L. 2003, *MNRAS*, 339, 312
- Steinmetz, M. 2003, *Ap&SS*, 284, 325
- Swaters, R. A., Madore, B. F., & Trewhella, M. 2000, *ApJ Lett.*, 531, L107
- Teplitz, H. I., Hill, R. S., Malumuth, E. M., Collins, N. R., Gardner, J. P., Palunas, P., & Woodgate, B. E. 2001, *ApJ*, 548, 127
- Terlevich, A. I. & Forbes, D. A. 2002, *MNRAS*, 330, 547
- Tinsley, B. M. 1972a, *A&A*, 20, 383
- . 1972b, *ApJ*, 178, 319
- van den Bergh, S. 1959, *Publications of the David Dunlap Observatory*, 2, 147
- van Dokkum, P. G. 2001, *PASP*, 113, 1420
- van Zee, L., Haynes, M. P., & Salzer, J. J. 1997, *AJ*, 114, 2497
- White, S. D. M. & Rees, M. J. 1978, *MNRAS*, 183, 341

Woosley, S. E. & Weaver, T. A. 1995, ApJS, 101, 181

Worthey, G., Faber, S. M., Gonzalez, J. J., & Burstein, D. 1994, ApJS, 94, 687

Zackrisson, E., Bergvall, N., & Ostlin, G. 2005, ArXiv Astrophysics e-prints

Zwicky, F. 1957, Morphological astronomy (Berlin: Springer, 1957)

Acknowledgments

At this point I like to thank all people who helped me to finish this thesis. Especially I like to thank Prof. Dr. R.–J. Dettmar for providing me the topic of the thesis. With his support it was often possible to participate at astronomical conferences as well as carrying out observing programs. I also like to thank Priv. Doz. Dr. D.J. Bomans for his very good supervision. From him I've learned a lot about astronomy and research in general. I enjoyed much the science discussions with him which help to bring this project forward. I hope, I did not disappoint their trust. Thanks also to Dr. K. Weis for having always time to discuss my astronomical questions.

A special thanks goes to all colleges at the Astronomical Institute of the Ruhr–University Bochum. They always created a pleasant surrounding which made it more easy to concentrate on my work. Thanks to Dr. M. Jütte, Dipl. Phys. V. Knierim, Dipl. Phys. G. Aronica, and many others I enjoyed much our lunch meetings, which often ends in long discussion about mostly non astronomical topics. Especially, I like to mention Dipl. Phys. O. Schmithüsen. His work as a computer administrator—especially in the final phase of my thesis—helped me a lot. I also enjoyed to work with him in the Bonn/Bochum project about the development of a reduction pipeline for the analysis of wide field imaging data. I am also very thankful to Dipl. Phys. D. Rosenbaum who provided me with the large scale distribution plot of the LSB galaxies. I also enjoyed our collaboration in the LSB galaxy working group. Here I also have to thank Dipl. Phys. C. Trachternach for his collaboration in the group. A special thanks goes to my room mate Dipl. Inform. K. Polsterer. I enjoyed our discussions also about non astronomical topics.

A special thanks goes to Dipl. Phys. E. Manthey and Dipl. Phys. J. van Eymeren for reading the thesis very carefully.

At this place I like to thank especially our secretary Ms. D. Menger–Münstermann. She always have an open door for the problems of the Diploma and PhD students in the institute.

I also like to thank Prof. Dr. P. Schneider and Dr. T. Erben for the good collaboration in the Bonn/Bochum pipeline project.

Finally I like to thank my family. Without the support of my parents it would never be possible to study physics and to finish this dissertation. A special thanks goes to my wife Petra Haberzettl. She always gave me the power to follow on my research and created a place where I could feel at home. Especially I enjoyed our discussion about our two different research topics. I also thank her for reading the first draft versions of this thesis.

This thesis has been founded by the Bonn/Bochum Graduiertenkolleg “Magellanic System, Galaxy Interaction and Evolution of Dwarf Galaxies” as well as the DESY/BMBF project 05 AE2PD/8 “Infrastruktur zur Auswertung von Weitwinkel–Photometrie Daten”.

This project has been performed based on observations made with ESO Telescopes at the La Silla under program ID 66.A-0154(A). This research has made use of NASA's Astrophysics Data System (ADS) and the NASA Astronomical Data Center. I acknowledge the use of the reduction software package IRAF, which is written and supported by the IRAF programming group at the National Optical Astronomy Observatories (NOAO) in Tucson Arizona.

Curriculum Vitae

Personal Info:

Name: Haberzettl
Firstname: Lutz
day of birth: 05.08.69
place of birth: Burgstädt / Sachsen
Nationality: German
Private Adress: Merkurstr. 42
40223 Düsseldorf
marital status: married
since: 08.07.1994

Education:

1976 – 85: Polytechnische–Oberschule/Limbach–Oberfrohna
(elementary and junior high school)
1986: 10. year Gymnasium Horkesgath/Krefeld (junior high school)
1986 – 87: 10. year Realschule Horkesgath/Krefeld–Hüls (junior high school)
qualification: “Fachoberschulreife”
1986 – 90: 10. – 13. grade Gymnasium Horkesgath/Krefeld (High School)
qualification: “allgemeine Hochschulreife” (University entrance qualification)
1990 – 00: Ruhr–University Bochum, study of physics
2000: Diploma in Physics (Master of Science equiv.)
degree awarded with grade 2 (good)
Diploma thesis at the Astronomical Institute Ruhr–University Bochum
Title of thesis:
“Low Surface Brightness Galaxies in Deep CCD Surveys”
supervisors: Prof. Dr. R.–J. Dettmar and Dr. D.J. Bomans
since 2000: Ph.D. Student at the Astronomical Institute Ruhr–University Bochum
Title of thesis:
“Star Formation History of Low Surface Brightness Galaxies in the HDF–S”
supervisor: Prof. Dr. R.–J. Dettmar and Dr. D.J. Bomans

Positions:

10/1998 – 02/2000 Administration of the Graduiertenkolleg
*“Magellanic System, Galaxy Interaction
and Evolution of Dwarf Galaxies”* Bonn/Bochum
03/2000 – 08/2000 graduate research assistant at the Astronomical Institute
of the Ruhr–University Bochum

03/2000 – 08/2000	graduate research assistant at the Astronomical Institute of the Ruhr–University Bochum
09/2000 – 12/2000	research assistant at the Astronomical Institute of the Ruhr–University Bochum
01/2001 – 12/2001	scholarship by the Graduiertenkolleg <i>“Magellanic System, Galaxy Interaction and Evolution of Dwarf Galaxies”</i> Bonn/Bochum
01/2002 – 03/2002	research assistant at the Astronomical Institute of the Ruhr–University Bochum
01/2002 – 03/2005	research assistant at the Astronomical Institute of the Ruhr–University Bochum, in the framework of the Bonn–Bochum colaborative project <i>“Infrastructure for the Analysis of Wide–Field Photometric Data”</i>